Dissertation

submitted to the

Combined Faculties for the Natural Sciences and for Mathematics

of the Ruperto-Carola University of Heidelberg, Germany

for the degree of

Doctor of Natural Sciences

presented by

M.Sc. Linda-Isabella Viol

born in Köln, Germany

Oral examination: 13th of September 2019

Behavior and regulation of centriolar appendage proteins during mitosis

Referees: Prof. Dr. Gislene Pereira

Prof. Dr. Elmar Schiebel

Summary

The centrosome is a small non-membranous organelle composed of two centrioles and surrounded by the pericentriolar material. The two primary functions of the centrosome are first, to act as the main microtubule-organizing center in interphase and mitosis and second, to generate the primary cilium. The primary cilium is a microtubule-based structure that projects from the plasma membrane, where it acts as a signaling hub to transfer extracellular signals into intracellular responses. Thereby, the cilium coordinates diverse signaling pathways implicated in development, tissue homeostasis and disease. The primary cilium originates from the older centriole of the pair, called the mother centriole. This mother centriole is decorated at its distal tip with a nine-fold symmetric ring of distal and subdistal appendage proteins. Both centrioles duplicate once per cell cycle to generate one copy of themselves and hence one of the centriole contains the oldest appendages. Studies in model organisms proposed that those inherently asymmetric centrosomes potentially work as a scaffold for asymmetric distribution of cell fate determinants during mitosis and thereby acting as an intrinsic cue for asymmetric cell division. Yet, how centrosome asymmetry is established and how, if at all, influences asymmetric cell division in human stem cells remains unclear. Thus, one aim of this study was to characterize centrosome asymmetry in somatic and stem cells. I observed centrosomal asymmetry during mitosis for a subset of appendages, while others dispersed from the centrosome upon the G2/M transition. My data show that an appendage core (composed of ODF2, Cep83 and SCLT1) remained at the mother centriole from interphase to mitosis, whereas a sub-set of appendages including Ninein, Centriolin, Cep123, Cep164 and LRRC45 detached from the mother centriole during mitosis. The behavior of appendages was similar in differentiated cells and human stem cells.

The second aim was to unravel whether centrosome asymmetry regulates asymmetric stem cell division. I found that ODF2 can be used as a marker for centrosome asymmetry during mitosis in human hematopoietic stem and progenitor cells (HSPCs). Here, I correlated the position of the daughter and mother centrosome, visualized by ODF2, with the asymmetric distribution of the stem cell marker CD133 in dividing HSPCs using imaging flow cytometry. Although a role for centrosomes in the asymmetric cell division of HSPCs cannot fully be excluded, I could not observe a clear correlation between centrosome age and CD133 segregation. Further, reversion of

centrosome asymmetry by ODF2 depletion had no impact on the differentiation potential of HSPCs.

The third aim concentrated on the regulation of appendage behavior. Distal appendages, which are required for initial steps of ciliogenesis, are released from centrosomes before mitosis by a mechanism that is currently unknown. Therefore, I aimed to elucidate the regulation of the cell cycle-dependent behavior of appendages and the consequence of perturbed appendages regulation with special regards to their function in ciliogenesis. Here, I show that the mitotic kinase Nek2 regulates the distal appendage removal at the mother centriole at the onset of mitosis. Ectopic overexpression of Nek2 but not kinase-dead Nek2 prematurely displaced those appendages in interphase, indicating a kinase-specific function. This phenotype was recapitulated in breast cancer cells with high levels of Nek2. Conversely, in Nek2 knockout (KO) cells, appendages remained associated with the older centrosome during mitosis. I could show that persistence of distal appendages on the mother centrosome in mitotic Nek2 KO cells did not allow the cells to fully disassemble their cilia before mitosis, resulting in a ciliary remnant during mitosis. This triggered asymmetric inheritance of ciliary signaling components and asynchronous cilium reassembly after cell division. Asynchronous cilium growth may have consequences for cell fate determination by allowing sister cells to differentially detect environmental signals. Therefore, a ciliary remnant during mitosis might be restricted to asymmetrically dividing stem cells, which need asymmetric cilium re-assembly as a tool for differential responding to environmental signals after cell division. Together, my data established the kinase Nek2 as a central regulator of distal appendages.

Zusammenfassung

Das Zentrosom ist ein kleines nicht-membranöses Organell, welches aus zwei Zentriolen besteht und von einer perizentriolären Matrix umgeben ist. Die beiden Hauptfunktionen des Zentrosoms bestehen darin, erstens als Hauptzentrum für die Organisierung von Mikrotubuli in der Interphase und Mitose zu dienen und zweitens das primäre Zilium zu erzeugen. Das primäre Zilium ist eine auf Mikrotubuli basierende Struktur, die aus der Plasmamembran herausragt und als Signalzentrale für die Übertragung extrazellulärer Signale in intrazelluläre Reaktionen fungiert. Dabei koordiniert das Zilium verschiedene Signalwege, die an der Entwicklung, Gewebehomöostase und Erkrankung beteiligt sind. Das primäre Zilium stammt aus dem älteren Zentriol des Paares, dem Mutterzentriol. Jenes Mutterzentriol ist an seiner distalen Spitze mit einem neunfach symmetrischen Ring aus distalen und subdistalen Protein Fortsätzen verziert. Beide Zentriolen duplizieren einmal pro Zellzyklus indem sie eine Kopie von sich selbst zu erzeugen. Daher enthält eine der Zentriolen die ältesten Fortsätze. Studien an Modellorganismen schlugen vor, dass diese inhärent asymmetrischen Zentrosomen als Gerüst für die asymmetrische Verteilung von Zellschicksalsdeterminanten während der Mitose dienen und somit als intrinsischer Anhaltspunkt für die asymmetrische Zellteilung fungieren. Es bleibt jedoch unklar, wie Zentrosomen Asymmetrie festgelegt wird und wie sie, wenn überhaupt, die asymmetrische Zellteilung in menschlichen Stammzellen beeinflusst.

Ein Ziel dieser Studie war es daher, die Zentrosomen Asymmetrie in somatischen Zellen und Stammzellen zu charakterisieren. Ich beobachtete eine zentrosomale Asymmetrie während der Mitose für eine Untergruppe von Fortsätzen, während sich andere bei der G2/M-Transition vom Zentrosom lösten. Meine Daten zeigen, dass ein Kern der Fortsätze (bestehend aus ODF2, Cep83 und SCLT1) von der Interphase bis zur Mitose am Mutterzentriol verblieb, während sich eine Untergruppe von Fortsätzen, einschließlich Ninein, Centriolin, Cep123, Cep164 und LRRC45, während der Mitose vom Mutterzentriol löste. Das Verhalten der Fortsätze in differenzierten Zellen ähnelte dem in menschlichen Stammzellen.

Das zweite Ziel war es aufzuklären, ob die Zentrosomen Asymmetrie die asymmetrische Stammzellteilung reguliert. Ich fand heraus, dass ODF2 als Marker für die Zentrosomen Asymmetrie während der Mitose in menschlichen hämatopoetischen Stamm- und Vorläuferzellen (HSPCs) verwendet werden kann. Daher korrelierte ich die Position des Tochter- und Mutterzentrosoms, die durch ODF2 sichtbar gemacht

wurde, mit der asymmetrischen Verteilung des Stammzellmarkers CD133 in teilenden HSPCs unter Verwendung der bildgebenden Durchflusszytometrie. Obwohl eine Rolle von Zentrosomen bei der asymmetrischen Zellteilung von HSPCs nicht vollständig ausgeschlossen werden kann, konnte ich keine eindeutige Korrelation zwischen dem Alter von Zentrosomen und der CD133-Segregation beobachten. Darüber hinaus hatte die Umkehrung der Zentrosomen Asymmetrie durch ODF2-Depletion keinen Einfluss auf das Differenzierungspotential von HSPCs.

Das dritte Ziel konzentrierte sich auf die Regulierung des Verhaltens der zentrosomalen Fortsätze. Distale Fortsätze, die Schlüsselfaktoren für das Andocken von Ziliarvesikeln bei den ersten Schritte der Ziliogenese sind, werden vor der Mitose durch einen derzeit unbekannten Mechanismus aus den Zentrosomen freigesetzt. Daher beabsichtigte diese Arbeit die Regulation des zellzyklusabhängigen Verhaltens der Fortsätze und die Konsequenz einer gestörten Regulation unter besonderer Berücksichtigung ihrer Funktion in der Ziliogenese zu erklären. Hier zeige ich, dass die mitotische Kinase Nek2 zu Beginn der Mitose die Entfernung der distalen Fortsätze am Mutterzentrum reguliert. Ektopische Überexpression von Nek2, aber nicht von einer Kinase-inaktiven Mutante hat diese Fortsätze in der Interphase vorzeitig verdrängt, was auf eine Kinase-spezifische Funktion hinweist. Dieser Phänotyp wurde in Brustkrebszellen mit hohen Nek2-Werten rekapituliert. Umgekehrt blieben in Nek2-Knockout (KO) Zellen während der Mitose die zentrosomalen Fortsätze mit dem älteren Zentrosom assoziiert. Schließlich zeigte ich, dass eine beeinträchtigte Freisetzung der zentrosomalen Fortsätze in Nek2-Knockout Zellen zu einem Ziliarrest am Zentrosom mitotischer Zellen führt. Dies löste eine asymmetrische Vererbung ziliarer Signal Komponenten und ein asynchrones Wachstum von Zilien der resultierenden Tochterzellen aus. Asynchrones Zilienwachstum kann Konsequenzen für die Bestimmung des Zellschicksals haben, indem es Schwesterzellen ermöglicht wird, Umweltsignale unterschiedlich zu erfassen. Aus diesem Grund kann ein Ziliarrest während der Mitose auf die asymmetrische Teilung von Stammzellen beschränkt sein, die eine asymmetrische Zilienbildung benötigen, um nach der Zellteilung differenziell auf Umweltsignale reagieren zu können. Zusammen haben meine Daten die Kinase Nek2 als zentralen Regulator für distale Fortsätze etabliert.

Table of contents

1. Introduction

1.1 The centrosome: structure and composition

The centrosome was initially discovered by the cell biologists Walther Flemming and Edouard van Beneden in the 1870s (Beneden, 1876; Flemming, 1875). In 1888, Theodor Boveri termed this small organelle “centrosome” based on its central position in the cell (Boveri, 1888) and described it as the ‘material of inheritance’ (Wilson, 1925). The centrosome is a small non-membranous organelle of 1-2 µm and is positioned in the cytoplasm, usually near the nucleus. It is the main microtubule-organizing center (MTOC) of most animal cells in interphase and determines the two poles of the microtubule-based mitotic spindle (Bornens, 2002; Doxsey, 2001; Kellogg et al., 1994). While the centrosome was present in the last common eukaryotic ancestor, it has been lost in the evolution of higher plants and was replaced by a functional equivalent in fungi, the so-called spindle pole body (SPB) (Moens and Rapport, 1971). Each centrosome comprises two cylindrical, orthogonally arranged centrioles surrounded by a non-membranous, electron-dense matrix known as the pericentriolar matrix (PCM) (Bornens, 2002). A mature centrosome of a first gap phase (G1) cell is represented in Figure 1A. It is composed of two centrioles, daughter and mother. Their names are derived from their genesis, which occurred either in the preceding cell cycle (daughter centriole) or earlier (mother centriole). The mother centriole also contains appendages (see 1.2.). The two centrioles are connected by interconnecting fibers mainly composed of centrosomal never in mitosis A-related kinase 2 (Nek2)-associated protein 1 (C-Nap1) and rootletin (Fry et al., 1998; Yang et al., 2002). The cylindrical shape of the centrioles is formed by nine tubulin microtubule triplets (Figure 1B). The most central and only complete microtubule in the triplet is the A-tubule, while the B- and C-tubules are incomplete and do not form a full microtubule ring (Paintrand et al., 1992). In the mother centriole, the C-tubules terminate ~100 nm before the end of the A- and B-tubules at the distal ends. Hence, the proximal part of the centriole contains microtubule triplets, while the distal end contains only microtubule doublets. Daughter centrioles, in contrast to mother centrioles, exhibit cartwheels surrounded by nine sets of triplet microtubules. Upon formation during interphase, the A-, B-, and C-tubules of daughter centrioles continue to elongate together to a length of ~400 nm beyond the cartwheel stack (Gupta and Kitagawa, 2018).

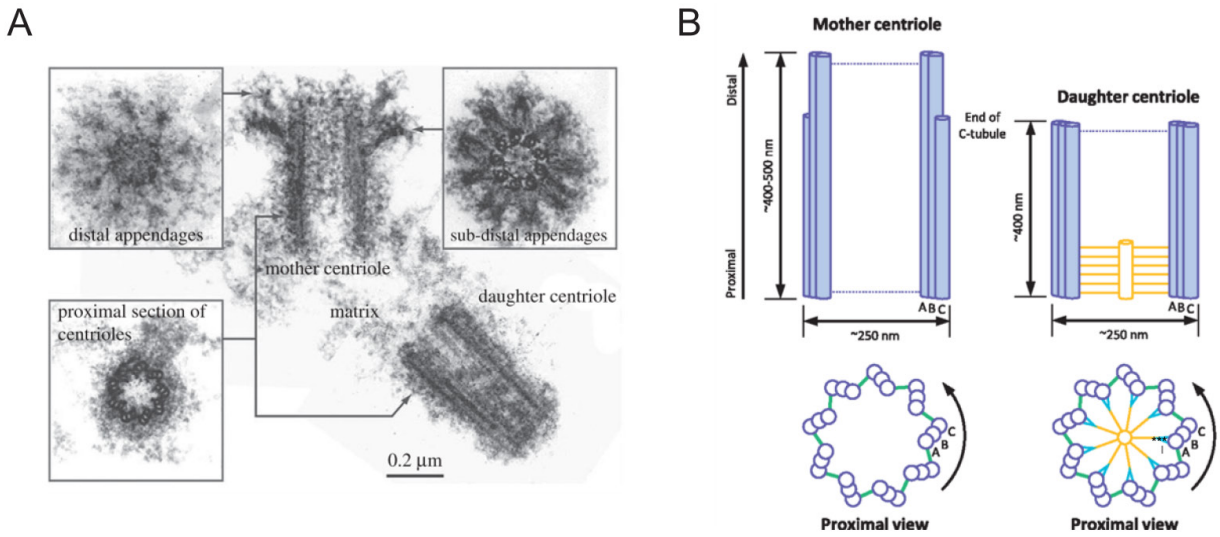

Figure 1. Structure of the mammalian centrosome. (A) Electron micrograph of a longitudinal section of centrioles in isolated centrosomes and cross sections highlighting the distal and subdistal appendages [adapted from Winey and O'Toole 2014]. (B) Schematic representation of a human centriole showing the ninefold symmetric arrangement of the microtubule triplets. Cartwheels are depicted in yellow, centriolar microtubules in purple, the pinhead connecting the cartwheel to the microtubules in blue and the A–C linker in green. Distal and subdistal appendages are not shown in this representation. A-, B- and C-tubules are indicated on the longitudinal and cross-sections of the centrioles [adapted from Gupta and Kitagawa 2018].

Although the newly assembled centriole reaches its full length in early mitosis, it cannot duplicate or nucleate PCM until it has passed through mitosis (Fu et al., 2015; Wang et al., 2011). The PCM embeds the centrioles and acts as the primary MTOC (Gould and Borisy, 1977; Woodruff et al., 2014). The PCM consists of a structural scaffold of fibrous proteins, including several large coiled-coil proteins (Salisbury, 2003), such as pericentrin (Dictenberg et al., 1998; Doxsey et al., 1994), Cep152 (Cizmecioglu et al., 2010), Cep192 (Gomez-Ferreria et al., 2007; Zhu et al., 2008) and Cyclin dependent kinase 5 (Cdk5)-regulatory subunit associated protein 2 (CDK5RAP2) (Fong et al., 2008). Subdiffraction imaging defined the higher order PCM organization revealing that the PCM has a layered structure made of fibers and matrices (Lawo et al., 2012; Mennella et al., 2012). The fibrous meshwork embeds the γ-tubulin ring complex, a ring-shaped multiprotein complex required for nucleating and anchoring microtubules (Moritz and Agard, 2001; Moritz et al., 1995; Moritz et al., 2000; Stearns and Kirschner, 1994; Zheng et al., 1998). The γ-tubulin ring complex also acts as a protecting cap of the microtubule's minus-ends, while they continue to grow from their plus end (Wiese and Zheng, 2000).

Other components of centrosomes are centriolar satellites, visible by electron microscopy (EM) as small electron-dense granules of approximately 70 to 100 nm that cluster around the centrosome. They were observed next to newly forming daughter

centrioles, associated with microtubules originating from the centrosome or around assembling basal bodies of motile cilia in epithelial cells. These structures have been viewed as vehicles for protein trafficking towards the centrosome (Anderson and Brenner, 1971; Bernhard and de Harven, 1960; Berns et al., 1977; De-Thé, 1964; Sorokin, 1968; Steinman, 1968). However, recent studies revealed their importance in regulating ciliogenesis, neurogenesis and as a signaling hub for dynamic remodeling in response to a variety of cues (Tollenaere et al., 2015).

1.2 Subdistal and distal appendage proteins

The two centrioles within a centrosome vary in age and morphology and thus have different functions. As mentioned beforehand, only the older, mother centriole is decorated with appendage proteins that are acquired at the subdistal and distal ends of the centriole (Chrétien et al., 1997; Ibrahim et al., 2009; Paintrand et al., 1992; Vorobjev and Chentsov, 1982). In cross sections of EM images, subdistal appendages appear as triangular structures attached to centriolar microtubule blades at the distal end (Figure 1A). While the number of subdistal appendages varies, distal appendages are always present in an amount of 9 - one for each triplet (doublet) of MT of the mother centriole. The distal appendage proteins play a key role for initial steps of cilia biogenesis (Graser et al., 2007; Schmidt et al., 2012; Tanos et al., 2013), while subdistal appendages are more relevant for microtubule organization (Vorobjev and Nadezhdina, 1987). Since the beginning of this century, many proteins of the distal and subdistal appendages have been characterized. Their interactions were described and the sequence of their appearance on the centriole was established (Kurtulmus et al., 2018; Mazo et al., 2016; Tanos et al., 2013). Figure 2A shows a schematic of a centrosome with the appendages analyzed in this study.

The assembly pathway of subdistal appendages is depicted in Figure 2B: Coiled-Coil And C2 Domain Containing 2A (CC2D2A) and C2 Calcium Dependent Domain Containing 3 (C2cd3) were shown to be required for outer dense fiber protein 2 (ODF2) recruitment and ciliation in mouse cells (Thauvin-Robinet et al., 2014; Veleri et al., 2014). However, other studies disputed a role of C2cd3 for subdistal appendage recruitment (Cortés et al., 2016; Ye et al., 2014), therefore C2cd3 was left out of the scheme (Figure 2B). The subdistal appendage protein ODF2 is critical for the formation of subdistal appendages. In retinal pigment epithelial (RPE1) ODF2 knockout (KO) cells, the other subdistal appendages Cep128 and Centriolin are lost from the

centrosome, as well as the distal part of Ninein, Kif2a, dynactin subunit p150glued and Cep170. Cep128 loss has a partial effect on ODF2 recruitment. The assembly hierarchy follows the order ODF2, Cep128, Centriolin, followed by the Ninein group (Figure 2B) (Kashihara et al., 2019; Mazo et al., 2016). Of those, Ninein is the subdistal appendage critical for microtubule anchoring and retains the γ-tubulin ring complex at the N-terminus (Delgehyr et al., 2005). Cilia formation was impaired upon depletion of the subdistal appendage Ninein (Graser et al., 2007) but not in Ninein knockout cells (Mazo et al., 2016). Huang et al. in 2017 described two new subdistal appendages: Coiled-Coil Domain-Containing Proteins (CCDCs) CCDC120 and CCDC68, which are also important for microtubule anchoring. According to their scheme, CCDC120 is recruited to subdistal appendages by ODF2 and recruits both Cep170 and Ninein through two distinct domains. ODF2 affects the recruitment of CCDC68, likely indirectly, to the centrosome. There, CCDC68 competes with CCDC120 in recruiting Cep170 (Huang et al., 2017).

Originally, it has been proposed that ODF2 localizes to both subsets of appendages and is essential for their assembly (Ishikawa et al., 2005; Tateishi et al., 2013). However, these studies used mouse cells and contradictory results were observed for distal appendages by small interfering ribonucleic acid RNA (siRNA) depletion of ODF2 in human RPE1 cells (Kuhns et al., 2013). In the absence of ODF2 in mouse cells, primary cilia formation was completely suppressed (Ishikawa et al., 2005; Tateishi et al., 2013). Kuhns et al. 2013 and Graser et al. 2007 observed a decrease of ciliated cells in serum-starved RPE1 cells upon siRNA mediated depletion of ODF2. In contrast, Mazo et al. 2013, using ODF2 KO cells, did neither measure a decline in ciliation nor an effect in ciliary length. It remains to be solved if ODF2 is required for distal appendage and cilia assembly in human cells and if the discrepancies in results are a result of interspecies variability, residual ODF2 levels upon depletion or off-target effects.

Previously, Cep164 was the only protein shown to associate with the distal appendages by immunofluorescence and immune-EM studies (Graser et al., 2007; Schmidt et al., 2012). In the past decade, other proteins of the distal appendages Cep123/Cep89 (Sillibourne et al., 2013), Cep83, fas-binding factor 1 (FBF1), Sodium channel and clathrin linker 1 (SCLT1) (Tanos et al., 2013), LRRC45 (Kurtulmus et al., 2018) and C2cd3 (Ye et al., 2014) have been characterized. Depletion experiments revealed a hierarchical network of distal appendage proteins assembly: C2cd3,

together with Talpid3, is critical for the assembly of distal appendages (Wang et al., 2018; Ye et al., 2014). Cep83 targets Cep164, FBF1, Cep123 and SCLT1 to the mother centriole (Tanos et al., 2013). Additional, SCLT1 recruits LRRC45 and LRRC45 recruits FBF1 to the centriole (Kurtulmus et al., 2018) (Figure 2C). It was further shown that removal of specific daughter centriole proteins, namely Cep120 and Centrobin, is a prerequisite for the acquisition of distal appendages during the maturation of the future mother centriole (Wang et al., 2018).

Cep164 is crucial for ciliogenesis (Graser et al., 2007; Schmidt et al., 2012) and it triggers cilia formation by mediating vesicular docking through recruitment of Rabin8 and Rab8 (Schmidt et al., 2012) and targeting the Tau tubulin kinase 2 (TTBK2) to the centrosome via its WW domain (Cajánek and Nigg, 2014). Additionally, knockout mice revealed that Cep164 is essential for multiciliogenesis (Siller et al., 2017). C2cd3 was shown to be critical for vesicle docking in mouse embryonic fibroblasts (Ye et al., 2014). The suppression of each Cep123, Cep83, SCLT1 and FBF1 blocked ciliogenesis (Tanos et al., 2013). SCLT1 and Cep83 depletion, like Cep164, resulted in defective initiation of ciliation. Opposed to this, depletion or KO of FBF1 showed that initiation steps are independent of FBF1. Yet, this appendage is required for ciliary gating of transmembrane proteins (Tanos et al., 2013; Yang et al., 2018). LRRC45 is also not essential for docking of early ciliary vesicles. Rather, this appendage promotes cilia biogenesis by organizing centriolar satellites, establishing the transition zone and promoting the docking of Rab8 GTPase-positive vesicles (Kurtulmus et al., 2018). The architecture of distal appendages was recently resolved in super-resolution: C2cd3 localizes to the centriolar lumen, Cep83 form the inner core outside the centriole, followed by Cep123, Cep164, SCLT1 and a second pool of Cep164 (Yang et al., 2018, Figure 2D).

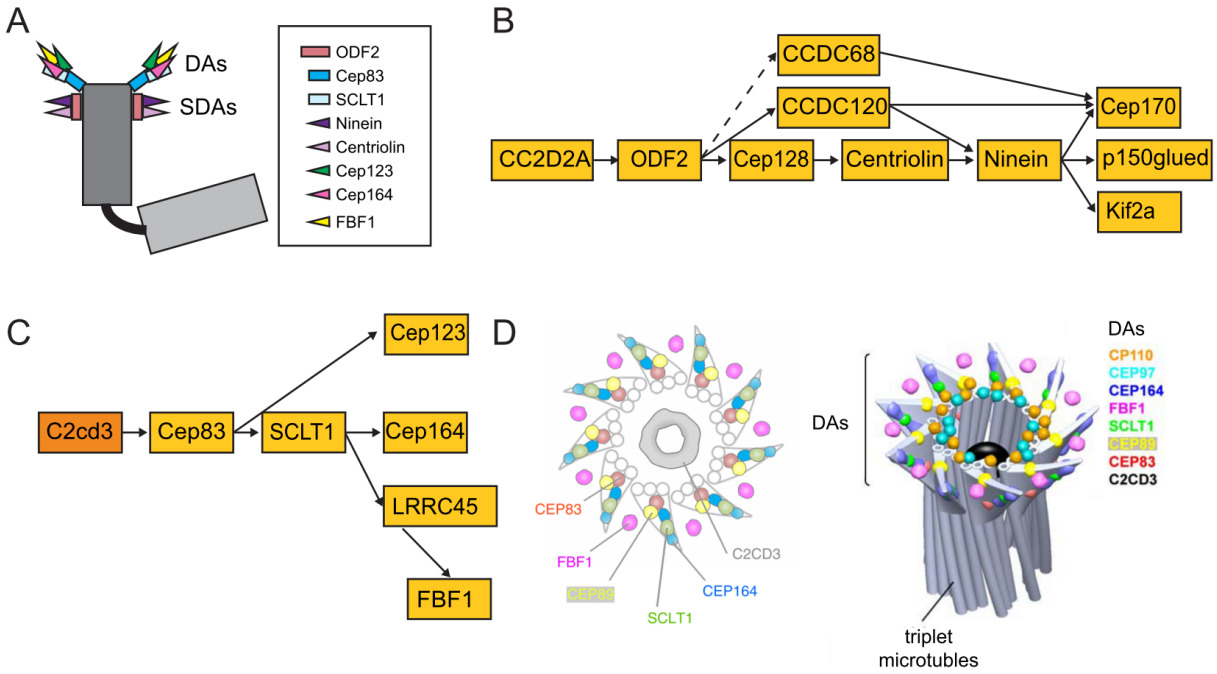

Figure 2. The assembly hierarchy of subdistal and distal appendage components. (A) Scheme of a gap phase 1 (G1) centrosome showing those appendage components, which were analyzed in this study. DA= distal appendage, SDA= subdistal appendage (B) Schematic model of SDA assembly. (C) model for the hierarchy of DA assembly. Appendage proteins are shown in a yellow box. C2cd3 is shown in an orange box as a non-appendage protein. (D) Model and a 3D computational model illustrating the positioning of proteins at the DAP region. FBF1 occupies the gaps between DAP blades, whereas C2CD3 localizes to the centriolar lumen (Yang et al., 2018).

1.3 The duplication cycle of the centrosome

Due to the centrosomes importance for mitotic spindle nucleation, genomic stability, and cilia formation, the numbers of centrosomes in the cell and thus its duplication process must be tightly regulated. Although the centrosomes at both spindle poles usually seem identical, the age of their individual centriole pairs is different. The centrosome duplicates once per cell cycle in a semi-conservative manner like the genetic material (Figure 3). In G1 both centrioles are still connected by a flexible linker (Bryan Tsou and Stearns, 2006; Mardin and Schiebel, 2012). The separation of centrioles, also termed as ‘centriole disengagement’, takes place in telophase/G1 (Piel et al., 2000). It is promoted by the activity of Polo-like kinase 1 (PLK1) and the cysteine protease separase (Schöckel et al., 2011; Tsou et al., 2009). After centriole disengagement, the flexible linker connecting both centrioles is established (O’regan et al., 2007). As mentioned previously, C-Nap1 and rootletin are main components of the linker. At G1/S transition, concurrent with initiation of deoxyribonucleic acid (DNA) replication, both centrioles start nucleating new daughter centrioles. Here, the cartwheel, a nine-fold symmetric, self-assembling structure serves as a template for the tubulin-microtubule triplets, which will constitute the procentriole (Kitagawa et al.,

2011; van Breugel et al., 2011). Spindle assembly abnormal protein 6 homolog (SAS6) and SCL-interrupting locus protein's (STIL) intrinsic oligomerization properties serve as a template for the cartwheels nine-fold symmetry. The formation of the cartwheel is initiated by an activation of Polo-like kinase 4 (PLK4) (Dzhindzhev et al., 2014; Kim et al., 2013; Ohta et al., 2014) that precedes the recruitment of SAS6 (Kitagawa et al., 2011; Nakazawa et al., 2007; van Breugel et al., 2011) and SCL-interrupting locus protein's (STIL) (Cottee et al., 2015; Stevens et al., 2010). Here, PLK4 phosphorylates STIL to link the procentriole cartwheel to the microtubule wall of the old centriole (Moyer and Holland, 2019). SAS-6 is not only required for the initiation of centriole formation, but also for the stabilization of centriole intermediates (Yoshiba et al., 2019). Additionally, Cep135/Bld10p is important for centriole formation by forming a coiled-coil (CC) structure that binds tubulin, protofilaments, and microtubules (Kraatz et al., 2016). Centrosomal P4.1-associated protein (CPAP) helps to elongate the centriole by deposition of centriolar microtubules (Kohlmaier et al., 2009; Tang et al., 2009). To control centriole length, centriolar coiled-coil protein of 110 kDa (CP110) caps the distal centriole end to limit microtubule extension (Schmidt et al., 2009; Spektor et al., 2007).

At the gap phase 2 (G2), the two pairs of centrioles separate from each other becoming two centrosomes. The centrosomes are separated when the kinase activity of Nek2 exceeds the phosphatase activity of type 1γ phosphatase and leads to the phosphorylation of the centriole linker proteins C-Nap1 and rootletin (Fry et al., 1998; Helps et al., 2000; Mardin et al., 2011). The timely activation of Nek2 in centrosome separation is under direct control of the cell cycle machinery. Upon mitotic entry, Aurora A and Plk1 kinases promote centrosome separation by stimulating the phosphorylation and displacement of linker proteins at the centrosome (Mardin et al., 2011). Centrosome maturation in late G2 involves the acquisition of PCM with enhanced recruitment of γ-tubulin ring complexes. This process increases microtubule nucleation activity required for spindle formation. Once the linker is broken, the two centrosomes are separated through the recruitment of the kinesin-related motor Eg5 to the centrosomes (Bertran et al., 2011).

In mitosis, each centrosome pair consists of one old and one new centriole. Consequently, in the next cell cycle, one pair will consist of recently synthesized centrioles, while the other will contain one centriole that can be many cell cycles old. Thus, after cytokinesis, the two daughter cells inherit centrosomes of different age and

protein composition (Paintrand et al., 1992). If, after mitosis, the cell exits the cell cycle and remains quiescent, cells can form cilia (Plotnikova et al., 2009; Seeley and Nachury, 2010). It was shown that cilia are formed by the centrosome containing the oldest centriole (Anderson and Stearns, 2009).

According to previous studies, the incorporation of appendage proteins starts at the G2/M transition and is only fully completed in the G1-phase of the next cell cycle by mechanisms that remain to be elucidated (Nigg and Stearns, 2011). In contrast, De Harven & Dustin in 1960 first noted that subdistal appendages are exclusively detected on interphase centrioles and never on mitotic ones (De Harven and Dustin, 1960). In addition to this, an ultrastructural study revealed that they disappear during the G2 phase and reappear on centrosomes at the beginning of the post-mitotic G1 phase (Vorobjev and Chentsov, 1982). Although the importance of centrosome distal appendages for cilia biogenesis is known for a long time (Graser et al., 2007; Schmidt et al., 2012; Tanos et al., 2013), their behavior during mitosis is poorly understood. Even less is known about mechanistic basics and how this process is regulated at G2/M transition. Independent of the here performed analysis (Results, 3.1.1.), a recent study using high-resolution microscopy published that the outer distal components are lost upon mitosis, while inner distal appendages are maintained (Bowler et al., 2019). However, a comparative investigation of the cell cycle behavior of centrosome appendages with regards to its regulation and asymmetry in somatic versus stem cells and is missing.

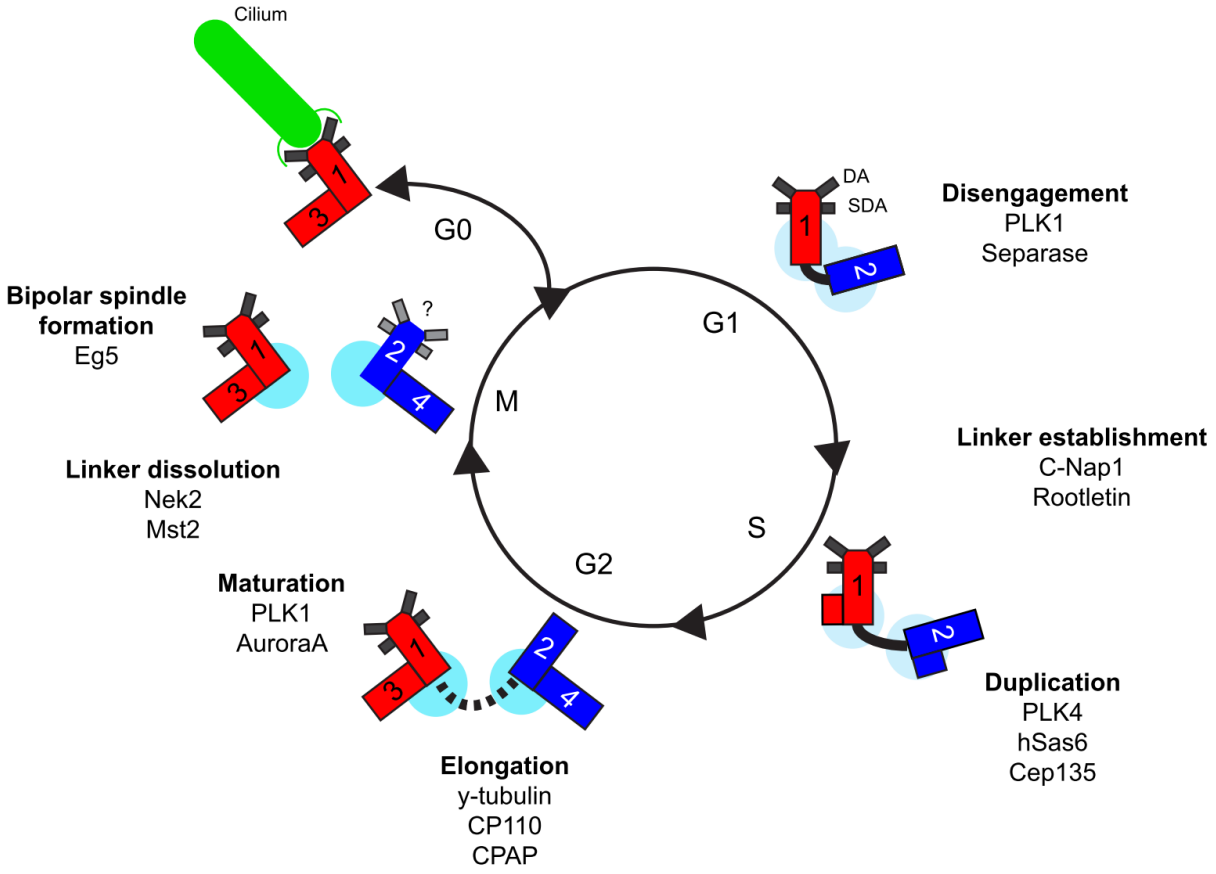

Figure 3. The centrosome duplication cycle. At the G1 phase, the sole centrosome is composed of a mother (1) and a daughter (2) centriole. Beginning in S phase and extending in the G2 phase, two new daughter centrioles (3 and 4) are generated. The daughter centriole (2) acquires appendage proteins later in the cell cycle, whereas the newly formed daughters are devoid of appendages. Consequently, the centrosome containing the grandmother centriole (1) is the older centrosome in mitosis. A comprehensive understanding of the mitotic behavior of different appendage complexes remains elucidated. If after mitosis cells enter a quiescent phase, the so-called exit of G1 (G0) phase, they can form a primary cilium (green). PCM is depicted with blue circles.

1.4 The primary cilium

Cilia can be assembled on almost all cell types in the human body (Olsen, 2005). Hematopoietic cells, which are in suspension, are believed to lack cilia. However, one study conflicted this assumption and showed short cilia in human blood and bone marrow cells (Singh et al., 2016).

The primary, non-motile, cilium is a microtubule-based projection and serves as an ‘antenna’ for detecting and responding to external signals. Primary cilia formation occurs when cells enter to quiescence, for example upon differentiation, but can also occur in proliferating cells (Seeley and Nachury, 2010). The primary cilium arises from the mother centriole that differentiates into the basal body of the cilium (Figure 4). It consists of a microtubule-based core, named the axoneme. The axoneme is composed of a nine-fold symmetric arrangement of duplet tubulin microtubules. Motile and primary cilia differ in their axoneme structure. In motile cilia, the axonemal microtubules

are decorated with dynein complexes and radial spokes that act in a coordinated fashion to achieve ciliary movement (Lindemann and Lesich, 2010). Besides, motile cilia have a central tubulin microtubule doublet in the center of the axoneme in a so-called 9+2 arrangement. Primary cilia lack the central microtubule doublet and have a 9+0 arrangement. Further, dynein motor proteins are missing on the axoneme of primary cilia (Goetz and Anderson, 2010; Nigg and Raff, 2009). While motile cilia are only found on a few specialized epithelial cell types and on sperms, primary cilia are present on almost every vertebrate cell.

A ciliary membrane encloses the axoneme, which is continuous with the plasma membrane but differs in its lipid and protein composition (Rohatgi and Snell, 2010). The membrane curvature, which is created at the membrane at the cilium base is described as the ‘‘ciliary pocket’’ (Molla-Herman et al., 2010).

Although, one would expect that cilia as “cellular antennas” are located on the cell surface, fully surfaced cilia are only found in protozoans such as Trypanosoma and primary cilia in epithelial cells of kidney tubules (Benmerah, 2013; Field and Carrington, 2009; Latta et al., 1961; Molla-Herman et al., 2010). In many cell types, cilia are confined in a deep narrow pit created by a membrane invagination, sensing the environment only through the narrow opening at the end of the structure (Sorokin, 1962). These so-called "submerged cilia" are found in many vertebrate cells, including RPE1 cells, fibroblasts, and neurons (Baudoin et al., 2012; Mazo et al., 2016; Sorokin, 1962).

Once attached to membrane structures, the mother centriole is referred to as a basal body. The tubulin microtubules of the axoneme provide the scaffold of the cilium around which intraflagellar transport (IFT) systems, membrane interacting proteins, septins, and other proteins shape the cilium (Malicki and Johnson, 2017). The transition zone is located where the axoneme, the basal body, the plasma, and the ciliary membranes intersect. Structurally, the transition zone is composed of transition fibers, Y-links and the ciliary pocket (Garcia-Gonzalo and Reiter, 2017; Nachury et al., 2010; Reiter et al., 2012; Ringo, 1967). The transition fibers are derived from the distal appendages and interact directly with ciliary vesicles and the ciliary membrane, mediating the contact between the centrosome and the ciliary membrane (Joo et al., 2013; Schmidt et al., 2012; Sillibourne et al., 2013; Tanos et al., 2013). The Y-links were described by EM as multiple rows of complex structures, but only some proteins were hypothesized so far to compose them (Garcia-Gonzalo and Reiter, 2012).

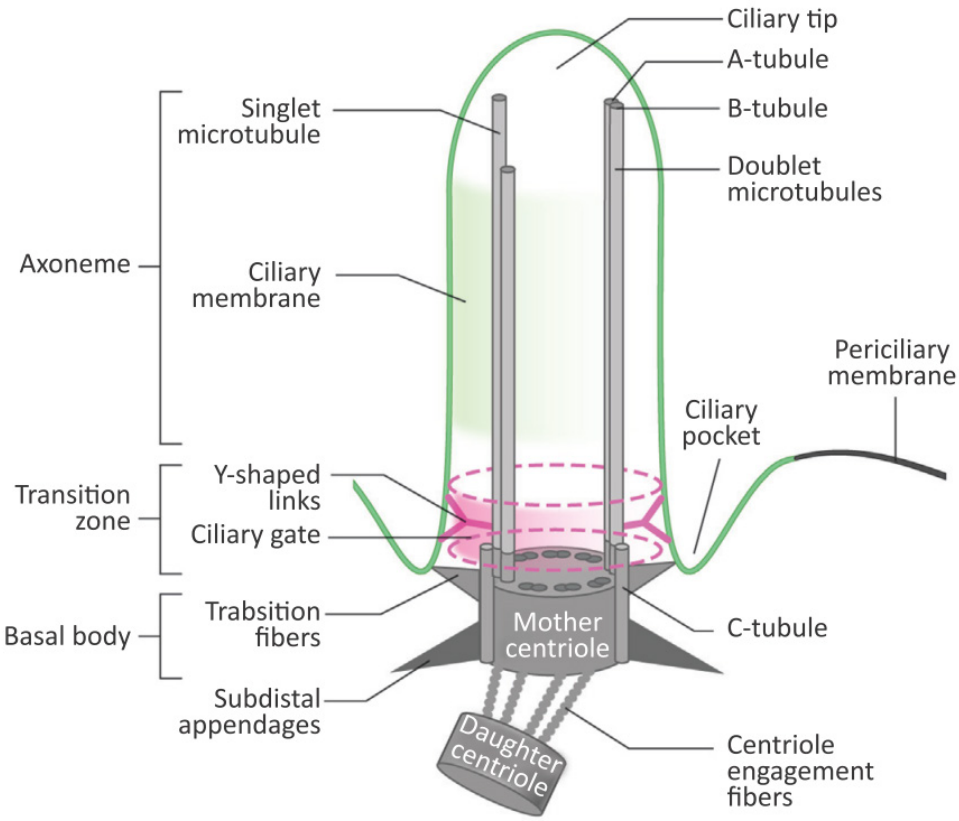

Figure 4. Simplified schematic of cilium ultrastructure (individual components are not in scale). For the purposes of clarity, two doublets of microtubules represent the ciliary axoneme (the A- and B-tubules; grey rods), and the nine-fold symmetry is indicated by dark grey ovals in the mother centriole. The axoneme is bound by the ciliary membrane (green line and shading). The mother and daughter centrioles are indicated by the grey cylinders, with the third C-tubule extending from the mother centriole towards the ciliary transition zone. The transition zone is also characterized by Y-shaped links (pink) that mediate interactions with the ciliary membrane. Transition fibers (light grey) extend from the distal appendages of the mother centriole. The permeability barrier called the 'ciliary gate' is indicated by the dashed pink ovals and pink shading [adapted from Malicki and Johnson 2017].

1.4.1 Regulation of primary cilia assembly and disassembly

Studies have shown that the assembly of primary cilia in mammalian cells is triggered by mitogen deprivation or differentiation, leading to cell cycle exit (Aughsteen, 2001; Choksi et al., 2014; Fu et al., 2014; Marion et al., 2009; Wheatley et al., 1996). Still, many questions about the regulation of ciliogenesis and the intracellular signaling events that promote it remain to be solved at the molecular level. Nonetheless, in the last decade, sophisticated cell biology and time-lapse microscopy experiments showed that ciliogenesis occurs sequentially through a series of well-orchestrated events, involving several intrinsic and extrinsic control mechanisms (Figure 5). Depending on the type of cilium, surfaced or submerged, ciliogenesis proceeds through two distinct pathways, termed the extracellular and intracellular pathways, respectively. In either pathway, membrane biogenesis and vesicular trafficking are required.

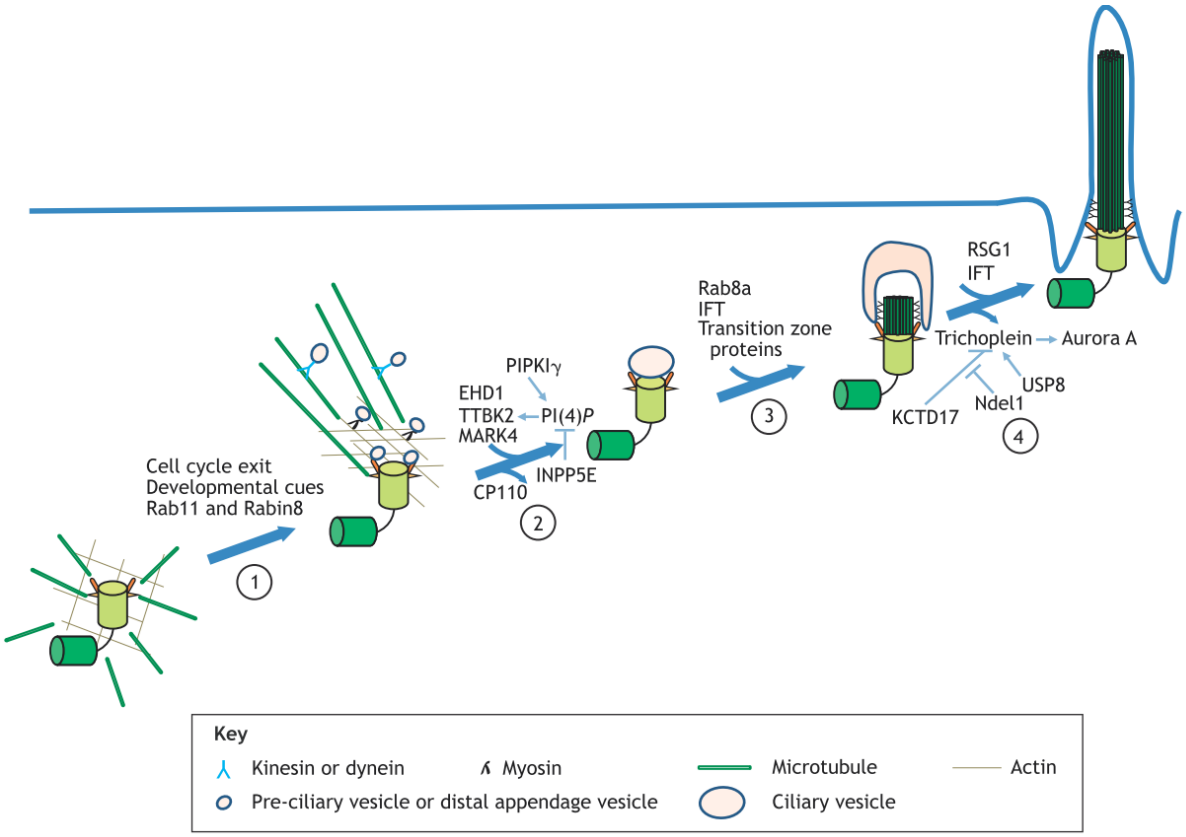

Figure 5. Stages and key players in primary cilium assembly. (1) Upon cell cycle exit or after receiving developmental signals, cilia formation starts with the recruitment of Rabin8, a guanine nucleotide exchange factor (GEF), to the recycling endosome. Here, Rabin8 is activated by Rab11, which in turn leads to recruitment of Rab8a. Those small pre-ciliary vesicles are transported via microtubule-actin networks to the distal end of the mother centriole, where Rab8a facilitates the docking of vesicles by interacting with a group of distal appendages, including Cep164. Next, the vesicles fuse into a larger ciliary vesicle. (2) EHD1 facilitates the fusion of the vesicles into a large ciliary vesicle. After ciliary vesicle formation, the tau tubulin kinase TTBK2 is recruited by Cep164 and triggers the removal of the CP110-CEP97 inhibitory complex. The kinase MAP/microtubule affinity-regulating kinase 4 (MARK4) is another catalyst for CP110 removal. Recruitment of TTBK2 by Cep164 is negatively regulated by phosphatidylinositol 4-phosphate [PI(4)P]. The centrosomal pool of PI(4)P is in turn negatively regulated by phosphatidylinositol 5-phosphatase (INPP5E) and positively by the PtdIns(4)P 5-kinase PIPKIγ. (3) Next, IFT complexes are continuously recruited to the ciliary base to elongate the axoneme. Simultaneously, Rab8a is recruited to the mother centriole to facilitate ciliary membrane extension. The transition zone is then assembled. (4) Subsequently, axoneme elongation and membrane fusion follow. RSG1 is required to initiate axoneme elongation. During axoneme elongation, free tubulin enters the cilium from the cytoplasm by diffusion and via IFT, the motor-dependent bi-directional cargo transport mechanism. Inhibition of the ciliary disassembly pathway also allows outgrowth of the cilium [Adapted from (Wang and Dynlacht, 2018)].

Assembly of a primary cilium starts with the conversion of the mother centriole to a basal body. First, basal feet assemble from the subdistal appendages that are anchored to cytoplasmic microtubules (Kunimoto et al., 2012). Additionally, transition fibers originate from the distal appendages (Anderson, 1972; Anderson and Brenner, 1971; Dawe et al., 2007; Fisch and Dupuis-Williams, 2011). The distal appendages are key players for cilia formation (Graser et al., 2007; Schmidt et al., 2012; Tanos et al., 2013). The centriole to basal-body transition is marked by the association of small

ciliary vesicles near distal appendages (Kobayashi et al., 2014; Lu et al., 2015b; Schmidt et al., 2012). Cep164 promotes the association with ciliary vesicles via interaction with the small GTPase Rab8. Rab8 is controlled by its guanine exchange factor (GEF) Rabin 8 (Graser et al., 2007; Schmidt et al., 2012). Rab proteins regulate distinct steps in membrane trafficking through the control of vesicularization of the donor membrane and fusion with the acceptor membrane. Rab8a has this function in the case of the ciliary membrane assembly. Upon serum starvation, it is redistributed from the trans-Golgi network to the mother centriole (Westlake et al., 2011; Yoshimura et al., 2007). Rab11-positive recycling endosomes transport Rabin8 and the membrane-tethering complex TrappII, which regulates vesicle tethering to the basal body (Westlake et al., 2011). After docking to the mother centriole, the small vesicles fuse to a large ciliary vesicle (Sánchez and Dynlacht, 2016). Ehd1 and Ehd3, as well as the SNARE component SNAP-29, are recruited for the fusion into large vesicles. Those elongate through continuous fusion with vesicles to produce the primary cilium membrane (Lu et al., 2015b).

Together with ciliary vesicle establishment, a negative regulator of ciliogenesis, the CP110/Cep97 complex, which caps the distal end centrioles, is removed by targeted protein degradation at the mother centriole (Kobayashi et al., 2011; Schmidt et al., 2009; Spektor et al., 2007). TTBK2 is recruited by Cep164 and triggers the removal of CP110/Cep97 (Cajánek and Nigg, 2014; Goetz et al., 2012). The recruitment of TTBK2 by CEP164 is regulated by phosphatidylinositol 4-phosphate [PI(4)P] levels at the centrosome/ciliary base. PI(4)P binds to Cep164 and TTBK2 and inhibits their interaction in proliferating cells. The balance of the activity of the Phosphatidylinositol (PtdIns) kinase (PIPKIγ) and the opposing phosphatidylinositol 5-phosphatase (INPP5E) fine-tunes PtdIns(4)P and PtdIns(4,5)P^2 levels. Once INPP5E leaves the centrosome in quiescent cells, PIPKIγ promotes TTBK2 recruitment by consuming the PI(4)P at the centrosome (Xu et al., 2016). A second kinase, MARK4, regulates cilia assembly by displacing CP110/Cep97 (Kuhns et al., 2013). CP110/Cep97 removal then allows the extension of microtubules to form the ciliary axoneme (Kobayashi et al., 2011).

Since cilia are compartmentalized, they require a machinery for the transport of material required for proper growth. This task is performed by the IFT, which transports proteins and structural building blocks into the axoneme. Here, the IFT-B complex loads and transports the cargo to the ciliary tip (anterograde transport), while the IFT-

A complex returns turnover products or signaling components back to the cell body (retrograde transport) (Pedersen and Rosenbaum, 2008).

Furthermore, the amount of soluble tubulin as axonemal building blocks promotes ciliary length (Sharma et al., 2011). Rab8a also facilitates ciliary membrane extension (Nachury et al., 2007). Rab8a recruitment, and hence vesicle fusion and extension, is further regulated by Cep290. Cep290 localizes to the centriolar satellites and the ciliary transition zone (Kim et al., 2008; Tsang et al., 2008).

Additionally, the WD-repeat containing protein 8 (WDR8) functions together with SSX2IP and Cep135 in the assembly of centriolar satellites and vesicle docking (Gupta et al., 2015; Klinger et al., 2014; Kurtulmus et al., 2016). Once assembled and elongated, the cilium holds its composition partly by gating mechanisms at the base of the cilium: a soluble protein barrier and the transition zone (for comprehensive reviews, see (Jensen and Leroux, 2017; Nachury, 2018). Recent data suggest that the protein RSG1 has a role in the final maturation and membrane extension of the cilium (Agbu et al., 2018). Lastly, it should be noted that cilium length is also under the control of cilium disassembly pathways, which counteract assembly pathways during the cell cycle.

When cells re-enter the cell cycle, cilia must be removed, since this structure seems incompatible with the mitotic spindle. The molecular mechanisms responsible for synchronizing cilium disassembly with the cell cycle are only partly understood (Izawa et al., 2015; Ke and Yang, 2014; Kim et al., 2015). Cilia disassemble in a biphasic manner, with the first major ‘wave’ occurring in G1 and a second wave occurring before mitosis (Pugacheva et al., 2007; Tucker et al., 1979). Cilium disassembly requires the destabilization and depolymerization of axonemal microtubules. Ciliary tubulins are distinguished by a set of post-translational modifications. Especially ones govern axoneme stability should be removed during the disassembly of the cilium (Kim and Tsiokas, 2011).

The mechanisms govern cilia disassembly a summarized in Figure 6. Cilium disassembly and resorption are mainly activated by Aurora A, which stimulates HDAC6-mediated deacetylation and destabilization of microtubules. Aurora A is regulated by complex signaling pathways, which accompany cell cycle re-entry, during cilia disassembly. Aurora A is activated by calcium-calmodulin (CaM) and hence under control of pathways that induce calcium influx (Nielsen et al., 2015; Plotnikova et al., 2012). Platelet-derived growth factor receptor β (PDGFR β) activates PLCγ causing

the release of intracellular calcium and activation of CaM and Aurora A (Nielsen et al., 2015). Calcium influx further induces the binding of Aurora A to the scaffolding protein NEDD9 (also known as HEF1) promoting Aurora A activation (Plotnikova et al., 2012). Another histone deacetylase, HDAC2, influences cilium disassembly and positively activates Aurora A (Kobayashi et al., 2017).

Further, activation of non-canonical Wnt signaling promotes Aurora A activation. Wnt5a induces the phosphorylation of Dishevelled 2 (Dvl2), leading to the formation of a Dvl2-PLK1 complex. This complex, in turn, stabilizes the NEDD9(HEF1)/Aurora A complex (Lee et al., 2012).

Additionally, Pitchfork (Pifo) and the subdistal appendage assembly regulator trichoplein collaborate to activate Aurora A (Inoko et al., 2012; Kinzel et al., 2010).

The nuclear distribution element (NDE)-like 1 (Ndel1) blocks ciliogenesis by stabilizing trichoplein at the basal body by protecting it from ubiquitin-mediated destruction (Inaba et al., 2016). Aurora A activity is further controlled by phosphoinositide signaling promoting its interaction with NEDD9(HEF1). Additionally, the interaction of the phosphatidylinositol phosphatase INPP5E with Aurora A supports transcriptional down-regulation of Aurora A (Hamze-Komaiha et al., 2016; Plotnikova et al., 2015). At the onset of cilium disassembly, the protein CRAP acts as a negative regulator of ciliary length by providing a scaffold for the formation of a cilium disassembly complex, comprising Aurora A, Nde1, and OFD1 at the ciliary base (Gabriel et al., 2016).

A second kinase involved in cilia disassembly is PLK1. PLK1 phosphorylates and activates the depolymerizing kinesin Kif2a. Kif2a localizes to the proximal ends of both centrioles and subdistal appendages. In quiescent cells, Kif2a is degraded through anaphase-promoting complex/cyclosome (APC/C)-mediated destruction to facilitate ciliogenesis. However, upon proliferative signals, phosphorylation by PLK1 facilitates the de-polymerization of ciliary microtubules (Miyamoto et al., 2015).

A third kinase regulating cilia formation is Nek2 (DeVaul et al., 2017; Endicott et al., 2015; Spalluto et al., 2012). Overexpression of Nek2 reduces ciliation and depletion of Nek2 via siRNA led to the observation of ciliated cells after centrosome separation (G2) and in prophase (Kim et al., 2015; Spalluto et al., 2012). It was shown that Nek2 regulates cilium disassembly via phosphorylation of another microtubule depolymerizing kinesin Kif24 (Kim et al., 2015). Kif24 was identified through its association with CP110 (Kobayashi et al., 2011). Upon serum starvation and in G1, Nek2 levels are barely detectable, concomitant with loss of phosphorylated Kif24 and

occurrence of ciliation (Kim et al., 2015). It must be noted, that most of the studies indicate that Nek2 acts to prevent assembly and nucleation of new cilia at the G2/M transition but does not disassemble fully formed cilia (DeVaul et al., 2017; Kim et al., 2015). In contrast, Spalluto et al. (2012) proposed Nek2 functions in cilia disassembly. Regulation of ciliation by Nek2 was shown to be independent of the Aurora A pathway in assembling cilia. However, both kinases seem to be required for the resorption of assembled cilia and Aurora A and Nek2 functionally interact in cilia reabsorption in ARPE-19 cells (DeVaul et al., 2017).

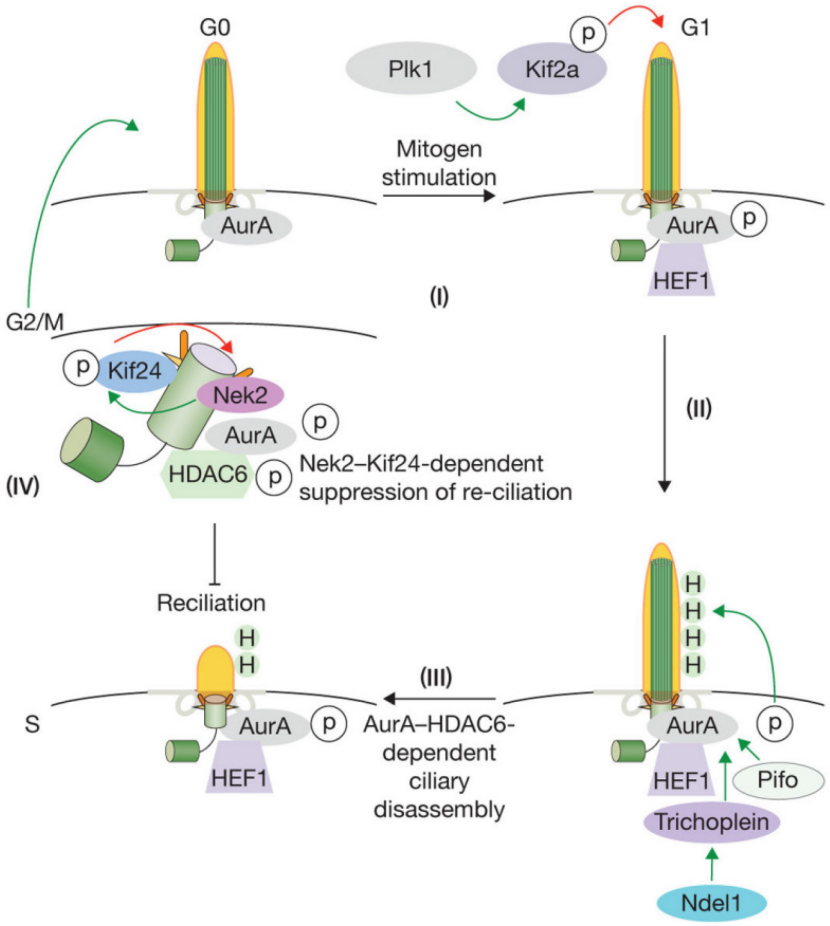

Figure 6. The regulation of cilium disassembly. Cell cycle re-entry induced by several signaling pathways or serum growth factors trigger cilium disassembly in G1 phase via activation of Aurora A. NEDD9(HEF1) complexes with and activates Aurora, which then stimulates the histone deacetylase HDAC6. HDAC6 de-acetylates and destabilizes microtubules within the axoneme. Pitchfork (Pifo) and trichoplein collaborate to activate AurA, and Ndel1 stabilizes trichoplein at basal bodies to suppress ciliogenesis. During cilium disassembly, PLK1 and Nek2 activate the kinesins Kif2a and Kif24, respectively. Those are required for the depolymerization of microtubules. Activation of Kif24 provides a sustained block to re-ciliation throughout G2/M [adapted from Sanchez and Dynlacht 2016].

1.4.2 Primary cilia in signaling

The main function of the cilium is being a signaling hub to transfer extracellular signals into intracellular responses. Therefore, it is associated with receptors of important signaling pathways. Hedgehog (Hh) signaling was one of the first pathways linked with

primary cilia, fulfilling a central role in development (Corbit et al., 2005; Huangfu and Anderson, 2005; Huangfu et al., 2003; Lee et al., 1992). The receptor of Hh ligand, the 12 transmembrane domain receptor Patched 1, is located at the ciliary membrane at the base of the cilium in the unstimulated state. In the absence of the Hh ligand, Patched1 excludes and represses Smoothened (Smo) from the cilium. In this case, Gli transcription factors (Gli1, Gli2, and Gli3) of the Hh target genes are sequestered and suppressed by Suppressor of Fused (SuFu) at the tip of the primary cilium (Haycraft et al., 2005; Zeng et al., 2010) When the Hh ligand reaches its target cell, Patched 1 leaves the cilium, allowing Smo to translocate into the cilium (Corbit et al., 2005; Rohatgi et al., 2007).

There, Smo represses SuFu, relieving the inhibition of Gli. Once Gli is freed, it is post-translationally modified to form Gli activator form (GliA). GliA is then transported to the nucleus to activate the expression of target genes (Kogerman et al., 1999; Tukachinsky et al., 2010) (Figure 7A).

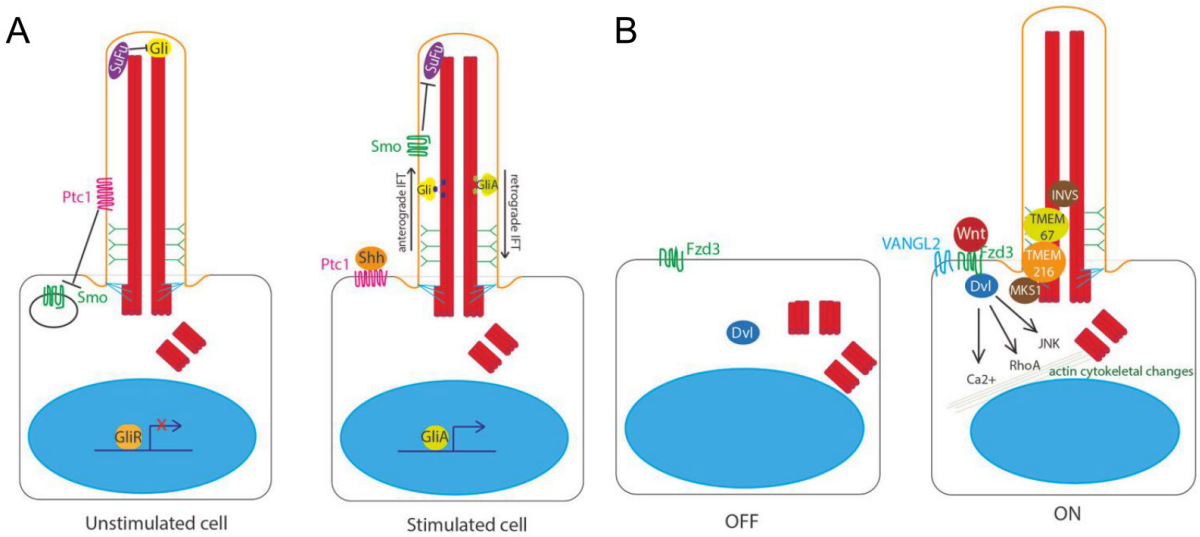

Figure 7. Hedgehog and Wnt signaling at the primary. (A) In the unstimulated state, Patched1 sits in the ciliary membrane and represses and excludes Smoothened (Smo) from the cilium. Gli transcription factors are sequestered and repressed by Suppressor of Fused (SuFu) at the tip of the cilium. Upon binding of the ligand Sonic Hedgehog (Shh) to Patched1, it leaves the cilium allowing Smo to enter the cilium. There, Smo represses SuFu, relieving suppression of Gli. Free Gli is post-translationally modified to become Gli activator (GliA). GliA is transported out of the cilium to the nucleus to activate gene expression. (B) Non-canonical Wnt ligands bind to Frizzled 3 (Fzd3) receptor, triggering asymmetric localization of Vangl2 in the cell. This pathway acts through Dishevelled (Dvl) to activate RhoA, the JNK pathway, and calcium release to stimulate remodeling of the actin cytoskeleton. The migration of the basal body to the apical cell surface is regulated by Dvl, by transition zone proteins meckelin (TMEM67) and TMEM216 and by basal body protein MKS1. Inversin targets cytoplasmic Dvl for proteasomal degradation [adapted from (Wheway et al., 2018)].

The role of cilia in canonical Wnt signaling is still controversial. On the one hand, several cell and animal studies show that defects in cilia lead to massive over-

activation of Wnt signaling (Abdelhamed et al., 2013; Cano et al., 2004; Lin et al., 2003; Wheway et al., 2013). On the other hand, others disagree on a connection between canonical Wnt signaling and cilia (Huang and Schier, 2009; Ocbina et al., 2009; Sugiyama et al., 2011). Whereas the role of cilia in canonical Wnt signal transduction is disputed, it is well acknowledged that cilia are important players in the planar cell polarity (PCP) non-canonical Wnt signaling pathway [(Gómez-Orte et al., 2013), Figure 7B]. The PCP pathway was first established in *Drosophila* (Ciruna et al., 2006). Cell polarity establishment is dependent upon the migration of the basal body to the apical cell surface to define apicobasal polarity (Jones et al., 2008). The apical positioning of the basal body in the establishment of PCP is highly conserved across evolution (Carvajal-Gonzalez et al., 2016). Dvl is essential for basal body docking, ciliogenesis and PCP (Park et al., 2008; Wallingford et al., 2000) as are transition zone transmembrane proteins (TMEM) TMEM67 and TMEM216, and basal body protein MKS1 (Adams et al., 2012; Dawe et al., 2007; Dawe et al., 2009; Valente et al., 2010). Contrasting to restricting canonical Wnt signaling, Inversin enhances non-canonical Wnt, and is assumed to control the switch between canonical and non-canonical Wnt signaling in *Xenopus* (Simons et al., 2005). The importance of migration of the basal body to the apical cell surface during PCP and non-canonical Wnt signaling is highlighted by the diseases that occur when critical signaling components are mutated (see next chapter). Besides Hh and Wnt signaling, primary cilia are crucial for many other pathways. Examples include the PDGFα signaling pathway (Christensen et al., 2008; Schneider et al., 2005), transforming factor beta (TGF-β) receptor signaling (Clement et al., 2013; Vestergaard et al., 2016), and Notch (Ezratty et al., 2011).

Signaling pathways are often presented as linear, isolated cascades. Yet, there are complex cross-talks and dynamic fluctuations in signaling, dependent on cell type and genetic background. The key to our understanding of cilia in cellular signaling might be to differentiate the roles of cilia in various cells, tissues, and organs.

1.4.3 Primary cilia in development and disease

Dysfunctions in cilia formation and thus impaired cell signaling and/or embryonic development cause a wide range of diseases known as ciliopathies (Reiter and Leroux, 2017) (See overview in Figure 8). Additionally, loss of ciliation is associated with multiple types of cancer (Emoto et al., 2014; Hassounah et al., 2013; Nobutani et al., 2014).

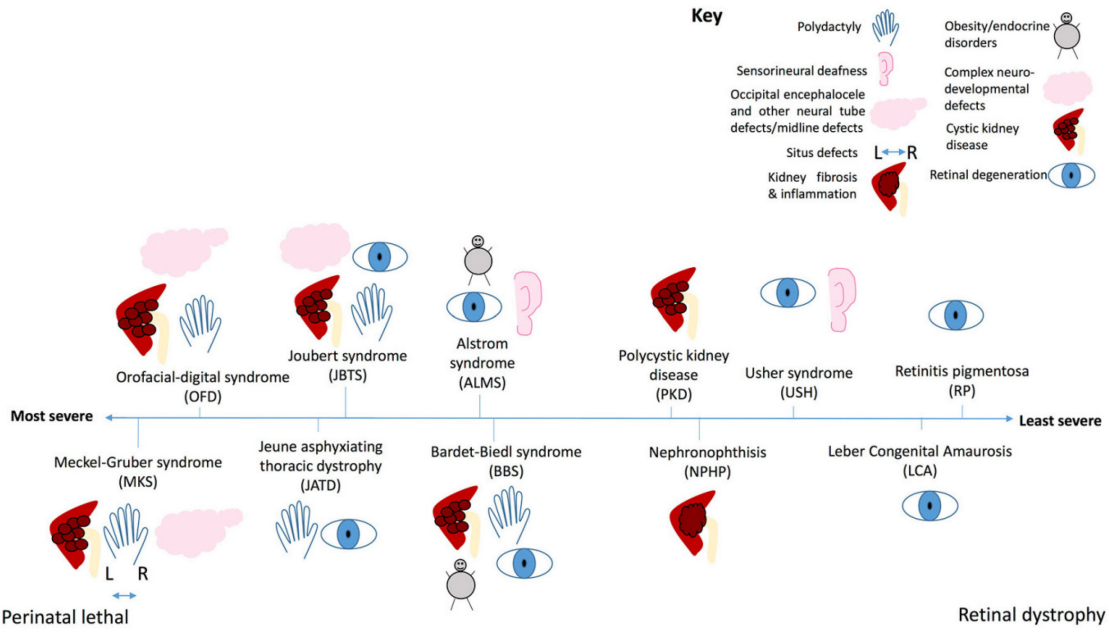

Figure 8. Graphic of typical features of ciliopathies. The severity of each ciliopathy is shown along a spectrum from perinatal lethal to isolated retinal dystrophy. Key shows which phenotype is represented by each symbol. ALMS, Alström syndrome; BBS, Bardet-Biedl syndrome; JATD, Jeune asphyxiating thoracic dystrophy; JBTS, Joubert syndrome; LCA, Leber congenital amaurosis; MKS, Meckel-Gruber syndrome; OFD, Oro-facial-digital syndrome; PKD, Polycystic kidney disease; RP, retinitis pigmentosa; SLS, Senior-Løken syndrome; USH, Usher syndrome [adapted from (Wheway et al., 2018)].

Defects in motile cilia often result in chronic bronchitis, sinusitis, male sterility and situs inversus or immotile ciliary syndromes, such as Kartagener's Syndrome, that lead to persistent respiratory infections (Afzelius, 1976; Dhar et al., 2009; Gerdes et al., 2009; Leigh et al., 2009). They are referred to as primary ciliary dyskinesias or PCDs. The presence of motile cilia in the brain, oviduct, the sperm flagellum likely provides an explanation of why ciliary defects cause infertility and neurological diseases. Further, the loss of nodal cilia function leads to laterality defects in terms of body patterning, such as heart development (Koefoed et al., 2014). We got insights about the role of motile, as well as primary cilia in breaking left-right asymmetry in the embryo from the mouse model (Hamada, 2016).

Diseases associated with primary cilia are genetically heterogeneous disorders that share clinical manifestations. Despite the signaling pathways mentioned in the last chapter, G-protein coupled receptors on olfactory cilia allow detection of smell (Jenkins et al., 2009). Further, primary cilia can sense fluid movement across the cell surface, like urine flow within kidney tubules. Mutations in the genes encoding this pathway are responsible for autosomal dominant polycystic kidney disease (ADPKD) (Shillingford et al., 2006). Besides, retinal photoreceptors have primary cilia, which are loaded with membranes loaded with phototransducing pigments (Valdés-Sánchez et al., 2013).

Both Hedgehog and Wnt signaling are crucial for tissue patterning during embryogenesis, stressing why their loss results in developmental defects. Still, these pathways also have key roles in tissue maintenance and homeostasis, and their deregulation is implicated in degenerative diseases and cancer progression (Briscoe and Thérond, 2013; Goggolidou, 2014).

Puzzlingly, some defects in primary cilium interfere with the function of a single organ. Among these are PKD, retinopathies, such as retinitis pigmentosa (RP) and Leber congenital amaurosis (LCA). However, of special scientific relevance are the recessive ciliopathy syndromes, which affect a range of organs with differing severity. These include Alstrom Syndrome (ALMS), Bardet Biedl Syndrome (BBS), Joubert Syndrome (JBTS), Meckel-Gruber Syndrome (MKS), Jeune Syndrome (also known as asphyxiating thoracic dysplasia, ATD), Senior-Løken Syndrome (SLS), Nephronophthisis (NPHP), Oral-Facial-Digital Syndrome (OFD), Ellis-van Creveld Syndrome (EVS), and Short Rib-Polydactyly Syndrome (SRPS). They affect the kidneys, liver, eyes, ears, brain, bones, and reproductive system and therefore can involve a combination of symptoms ranging from cystic kidneys, liver fibrosis, blindness, deafness, to infertility, mental retardation, obesity, and diabetes (Reiter and Leroux, 2017). The pleiotropy in severity and organ involvement is striking in the NPHP-like ciliopathies that, although being rare, are the most common cause of end-stage renal disease in children and young adults (Hildebrandt et al., 2009; Hurd and Hildebrandt, 2011).

In Meckel-Gruber syndrome, JBTS, BBS, and NPHP, many of the same genes are mutated, but the severity of the disease depends on how severely the mutation affects protein production or function. The less severe ciliopathies tend to be caused by mutations, which do not prevent ciliogenesis entirely, sometimes in multiple organs, sometimes in specific organs. Table 1 summarizes these ciliopathy phenotypes and their underlying signaling defect resulting from cilia loss or dysfunction.

Table 1. Ciliopathy phenotypes, causing ciliopathies, and the signaling pathway underlying the phenotype [adapted from Wheway et al. 2018].

Ciliopathy phenotype	Ciliopathy	Underlying signaling defect resulting from cilium loss or dysfunction
Polydactyly	BBS, JATD, JBTS, MKS, OFD	Shh
Sensorineural deafness	ALMS, USH	Wnt PCP
Occipital encephalocele and other neural tube defects/midline defects	MKS, OFD	Shh, Wnt PCP, Notch
Situs defects	MKS	Notch, LR
Kidney fibrosis and inflammation	NPHP, SLS	Hippo
Obesity/endocrine disorders	ALMS, BBS	GPCR (gonadotropin hormone receptor)
Complex neurodevelopmental defects including cerebellar vermis hypoplasia, ataxia, and psychomotor delay	JBTS	GPCR (ARL13B), PDGFR (INPP5E), Shh, Wnt
Cystic kidney disease	BBS, JBTS, MKS, OFD, PKD	mTOR, canonical Wnt
Retinal degeneration	ALMS, BBS, JATD, JBTS, LCA, RP, SLS, USH	GPCR (rhodopsin/opsin)

Besides ciliopathies, recent studies linked cilia loss to a multitude of tumors, including pancreatic ductal adenocarcinoma, renal cell carcinoma, thyroid cancer, breast cancer, ovarian cancer, prostate cancer, cholangiocarcinoma, glioblastoma and melanoma (Egeberg et al., 2012; Gradilone et al., 2013; Han et al., 2009; Hassounah et al., 2013; Lee et al., 2016; Menzl et al., 2014; Moser et al., 2009; Schraml et al., 2009; Seeley et al., 2009; Yuan et al., 2010). Both, the loss or the persistence of cilia were shown to have consequences for tumor development and progression, depending on the type of tumor.

As discussed above, primary cilia are important for Hh signaling, which plays a crucial role in development. In a breast cancer model, inhibition of ciliogenesis resulted in increased Hh signaling, followed by tumor formation and malignancy (Hassounah et al., 2017). Additionally, cilia loss promotes pancreatic intraepithelial neoplasia formation during tumorigenesis (Seeley et al., 2009). Another study using a pancreatic cancer model found that cilia loss triggers the mevalonate pathway through β catenin-TCF signaling, which further increases oncogenic Ras-Erk signaling (Deng et al., 2018). Noteworthy, a recent study proposes the loss of cilia promotes tumor survival after chemotherapy. In medulloblastomas, depletion of OFD1 and ciliogenesis led to resistance to Smo inhibition by achieving a cilium-independent transduction Hh signaling. This can enhance more-aggressive tumor growth (Zhao et al., 2017) (Figure 9). In contrast, restoring ciliation would not be a suitable therapy for other cancer types. Contrary to the examples above, cilia persist in several tumors and can increase malignancy (Fu et al., 2014; Yasar et al., 2017). In a medulloblastoma mouse model, tumorigenesis is driven by constitutively active Smo and can be blocked by genetic ablation of cilia or INPP5P inactivation. As a result, oncogenic Hh signaling and tumor growth are reduced (Conduit et al., 2017; Han et al., 2009). Further, in glioblastoma

lysophosphatidic acid signaling and thus increased mitosis is regulated through the primary cilium. In these cells, the cilium is the location for receptors of this pathway (Loskutov et al., 2018). Lastly, cells resistant to cancer therapy are characterized by a higher number and/or length of cilia. Interestingly, increasing cilia length by Kif17 knockdown leads to *De Novo* drug resistance (Jenks et al., 2018).

The examples show that the presence or non-presence of primary cilia in tumors can mediate hijacked Hh signaling, promote the formation of tumors or lead to drug resistance. Nevertheless, whether ciliary dysfunction is a cause or a consequence of cellular transformation remains to be clarified.

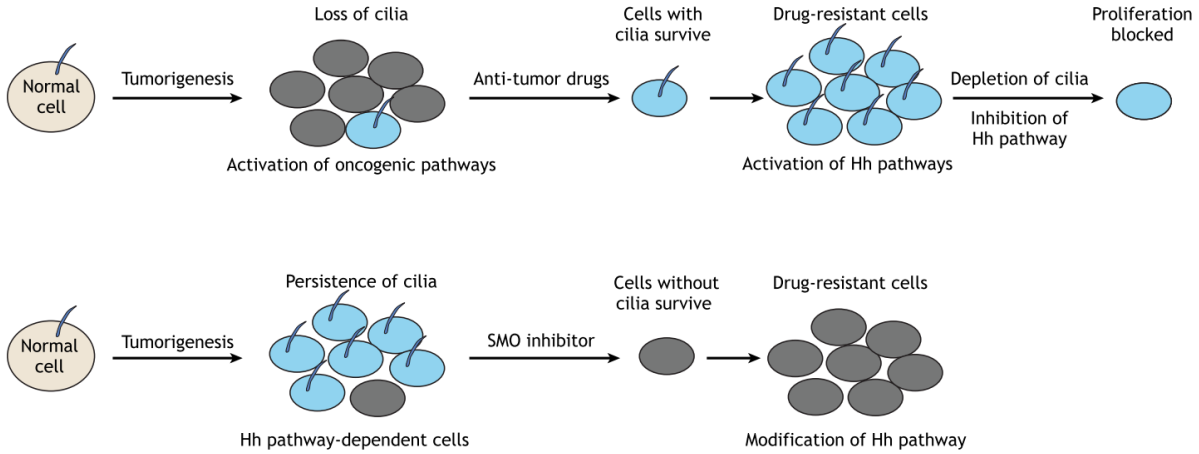

Figure 9. Cilia de-regulation in cancer. (A) Many cancer cells display a loss or reduction of ciliated cells. In addition, mutations lead to the activation of oncogenic pathways and possibly also abnormal Hh signaling. However, cancer cells show increased ciliogenesis and cilia signaling upon becoming drug resistant. Depletion of cilia or Hh inhibition can block the proliferation of these drug-resistant cells. (B) In other tumors, cilia can persist and seem to help them maintaining an oncogenic Hh pathway. After Smo inhibition, cells without cilia survive but become drug-resistant by a modified Hh pathway [adapted from Wang and Dynlacht 2018].

1.5 Centrosome asymmetry and asymmetric cell division (ACD)

The special property of stem cells is that their expansion is asymmetric (Wolpert, 1988). A cell division is defined asymmetric when the two daughter cells have different size, cellular constituents are preferentially segregated into only one of the two daughter cells, or when the two arising daughter cells differ in their future cell fate (Hirsch, 1977; Horvitz and Herskowitz, 1992). A just recently arising, but potentially fundamental aspect of the ACD mechanism in stem cells is the asymmetric property of centrosomes during cell division. Several studies suggest that the two distinctly segregating centrosomes can provide an efficient intrinsic mechanism for asymmetric segregation of cell fate determinants. Pioneering work in stem cell models correlated centrosome age and unequal cell fate (Figure 10).

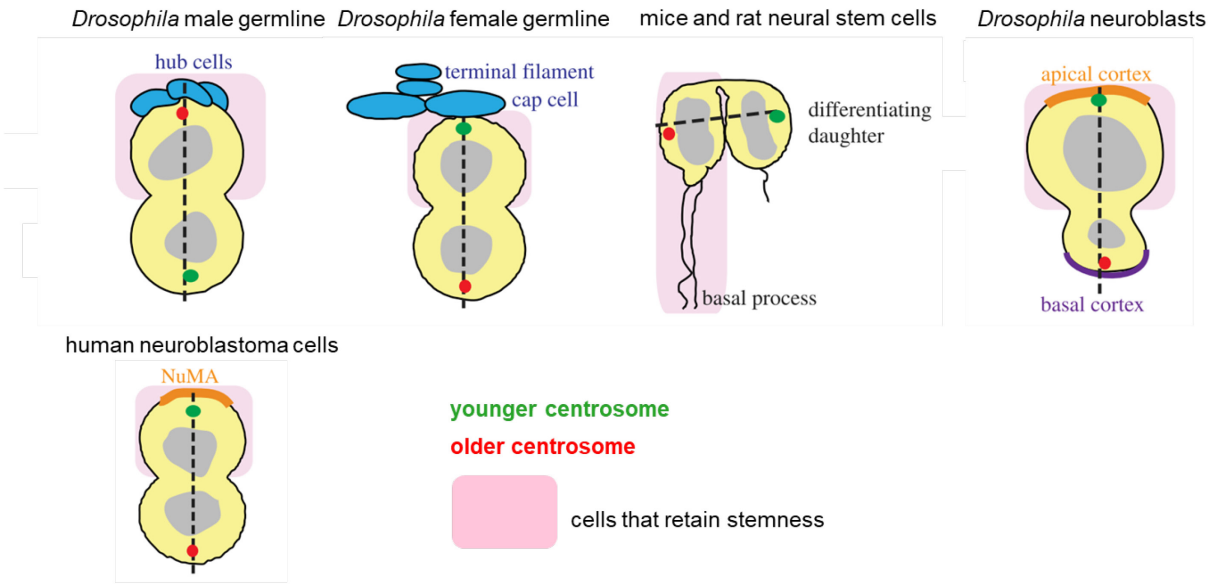

Figure 10. Centriole age and fate during ACD in stem cell models. Position of mother (red) and daughter (green) centrosomes during ACD in *Drosophila* male GSC (hub/niche cells are labeled blue), *Drosophila* female GSC (niche cells in blue), mice and rat neuronal stem cells, *Drosophila* neuroblast (apical and basal cortex labeled brown and purple), and the Neuroblastoma cell line (the NuMA crescent is labeled brown). Pink areas mark the cells that retain stemness and dotted lines represent the stemness/differentiation axes that [modified after (Reina and Gonzalez, 2014)].

1.5.1 In yeast

Asymmetric separation of MTOCs was first studied in yeast (Pereira et al., 2001). Despite being unicellular, budding yeast clearly divides asymmetrically: The mother cell generates the smaller bud cells and only the mother cell will change the mating type after cell division, resulting in fate asymmetry. In contrast to centrosomes, the yeast's equivalent, the SPB, does not replicate semi-conservatively. Here, the entire SPB is duplicated each cell cycle, resulting in one old and one new SPB (Rüthnick and Schiebel, 2016). Asymmetric SPB inheritance was demonstrated by Pereira et al. (2001), showing that the daughter cells nearly always inherit the old SPB, while the newly synthesized SPB remains in the mother cell.

To coordinate cell polarity and cell division axis, budding yeast have the spindle position checkpoint (SPOC) (Bloecher et al., 2000; Pereira et al., 2000; Wang et al., 2000; Yeh et al., 1995). The SPOC inhibits the mitotic exit network (MEN) until one SPB enters the bud. This bud-bound SPB is usually the older SPB, while the daughter SPB stays in the mother cell (Pereira et al. 2001). Components of SPOC and MEN localize at the bud-bound older SPB, by this means coordinating cell cycle progression (D'Aquino et al., 2005; Huisman and Segal, 2005; Pereira and Schiebel, 2005; Pereira et al., 2002; Piatti et al., 2006). Studies showed that the old SPB nucleates more and longer astral microtubules than the other (Liakopoulos et al., 2003). Those

microtubules interact with the bud cortex and orientate the SPB toward the future daughter cell (Korinek et al., 2000; Lee et al., 2000; Yin et al., 2000).
It is assumed that an additional signaling network, the SPB Inheritance Network (SPIN), controls SPB specification. Here, the Swe1 kinase (Wee1 in other eukaryotes), phosphorylates the SPB outer plaque protein Nud1 (Centriolin orthologue) on the old SPB during G1 phase. Subsequent, inactivation of Swe1 protects the newly assembling SPB from being marked. Consequently, the relative timing of Swe1 inactivation and SPB assembly ensures that only the preexisting old SPB carries the phosphorylation mark (Lengefeld et al., 2017).

1.5.2 In Drosophila

In higher organisms, the link between centrosome age and unequal cell fate was first established by Yamashita et al. (2007). In *Drosophila* male germline stem cells (mGSCs), the older centrosome is exclusively inherited by the daughter cell possessing stem characteristics. This cell stays connected with the niche, while the daughter centrosome is inherited by the differentiating daughter cell. At EM level, in these cells, the mother centrosome always connects with astral microtubules, while the daughter is associated with only a few astral microtubules. Those connect the mother centrosome in the stem cell to the interface between their niche, so-called hub cells (Yamashita et al., 2007). Interestingly, the opposite is true for *Drosophila* female germline stem cells (fGSCs): The daughter cell, which stays as a GSC inherits the daughter centrosome and the mother centrosome segregates into the cell assigned for differentiation (Salzmann et al., 2014). In *Drosophila* larval neuroblasts, the same behavior of mother and daughter centrosome as in fGSCs was observed (Conduit and Raff, 2010; Januschke et al., 2011). Live imaging using the PCM reporter CNN-green fluorescent protein (GFP) revealed that centrosome size asymmetry in *Drosophila* neuroblasts is generated by differential Cnn incorporation into the PCM at mother and daughter centrioles. Cnn incorporation is downregulated at the mother centriole, while it is maintained at the daughter centriole. As a result, the daughter centrosome maintains PCM and microtubules, ensuring the connection to the apical cell cortex (Conduit and Raff, 2010). Gambarotto et al. (2019) reported that PLK4 regulates this asymmetry of PCM, microtubule nucleation on the daughter versus mother centrosome and proper spindle orientation in Drosophila NSCs. The study showed that PLK4, the master centriole duplication kinase, phosphorylates the PCM protein Spd2 at the

mother centrosome resulting in less microtubule nucleation and the displacement of Fzr, a protein that promotes apical anchoring. In contrast, PLK4 is inactivated at the daughter centrosome by a yet unknown mechanism, resulting in unphosphorylated Spd2 and maintenance of Fzr and hence microtubule nucleation and apical anchoring of the daughter centrosome (Gambarotto et al., 2019). A surveillance mechanism, like SPOC in yeast, exists in mGSCs, named centrosome orientation checkpoint (COC). The COC stops cells upon centrosome/spindle misorientation. Although centrosome and cell polarity components seem to play a central role for COC function, the molecular mechanism remains still largely unknown (Pereira and Yamashita, 2011).

1.5.3 In the mouse system

In mouse brains (Wang et al., 2009) reported that the radial glial progenitor cell, which stays connected to the stem cell niche, retains the older mother centrosome. Furthermore, they showed that depletion of the subdistal appendage protein Ninein in these cells disrupted the asymmetric inheritance of mother and daughter centrosomes. This resulted in a loss of radial glial progenitor cells, indicating defects in the regulation of ACD. The same effect was observed upon depletion of Ninein in rat embryos (Delgehyr et al., 2005).

Furthermore, in mouse neural stem cells, the older mother centriole is associated with a ciliary remnant (Paridaen et al., 2013). In most differentiated somatic cells, the primary cilium is disassembled prior to mitosis and is assembled again in G1 following division (Pugacheva et al., 2007; Spalluto et al., 2012). In contrast, a part of neuronal stem cells keeps a ciliary remnant on the older centrosome during mitosis but lose it upon differentiation. The older centrosome and associated remnant usually segregate to the stem cell in an asymmetric division. The cell receiving the remnant makes a cilium first and is responsive to Sonic hedgehog ligand. Here, additional it was shown that centrosomal association of ciliary membrane in dividing neural stem cells decreased at late neurogenesis when these cells differentiate (Paridaen et al., 2013). Further, Centriolin plays a role in the ACD of mouse meiotic oocytes. Knockdown of Centriolin in oocytes resulted in a failure of peripheral meiotic spindle migration, large polar body emission, and 2-cell like oocytes (Sun et al., 2017). Additionally, ODF2 modulates microtubule organization, required for cortical nuclear mitotic apparatus (NuMA) localization in MDCK cells. Therefore, depletion leads to spindle orientation defects in these cells (Hung et al., 2016). The authors observed similar defects in

spindle orientation upon ODF2 depletion in the human cell line U2OS. Notably, a recent study analyzing the role of centrosome inheritance in neuronal progenitors in the developing cerebellum of the mouse failed to observe any correlation between cell fate and asymmetric centrosome inheritance (Chatterjee et al., 2018).

1.5.4 In human cells

Finally, in human cancer cells, namely neuroblastoma cells, the daughter cell, which assembled a NuMA crescent, preferentially inherits the daughter centrosome. The authors distinguished the daughter centrosome by weaker or no staining of the mother specific appendage ODF2. The authors speculated, based on the knowledge about the NuMA homolog in *Drosophila* neuroblasts, that the NuMA and daughter centrosome-retaining cell has more self-renewing capacity (Izumi and Kaneko, 2012). (Gasic et al., 2015) found that, in Henrietta Lacks (HeLa) and RPE1 cells, differential stability of kinetochore–microtubule attachments depends on the presence of ODF2, which is kept at the oldest centriole. This asymmetry in stability influences the fate of non–disjoined chromosomes to co–segregate mostly with the older centrosome.
Despite these studies hint towards a correlation between centrosome inheritance and ACD, mechanistic insights how centrosome asymmetry is established and how it can influence stem cell fate, especially in mammalian cells, remain largely unknown.

1.6 The Nek2 kinase

Besides Cdks, PLKs and Aurora kinases, the family of Never in mitosis A (NIMA)-related kinases is emerging as an additional regulator of the cell cycle and centrosome function. The use of temperature-sensitive mutant strains of the filamentous fungus *Aspergillus nidulans* identified the founding member, NIMA. Initial studies demonstrated that NIMAs function is required at the G2/M transition (Bergen et al., 1984; Oakley and Morris, 1983; Osmani et al., 1987). Structural relatives of NIMA have been identified in *S. cerevisiae* and *S. pombe* and *Chlamydomonas reinhardtii* termed Kin3, Finl and Fa2p, respectively (Jones and Rosamond, 1990; Krien et al., 1998; Mahjoub et al., 2002). Several vertebrate Neks have been identified termed Nek1-Nek11, however, they differ in their sequence compared to NIMA despite the catalytic domain (Fry et al., 2012).
Nek2 represents the closest structural relative of NIMA in the human genome and for this reason, Nek2 has become the most extensively studied of the vertebrate Neks

(Fry, 2002). Nek2 homologs have been identified in mouse, pig, human and *Xenopus*. In vertebrates, Nek2 is expressed as two splice variants, Nek2A, and Nek2B (Hames and Fry, 2002; Uto et al., 1999). In human somatic cells, Nek2A is the predominant isoform but Nek2B is still present (Hames and Fry, 2002). Nek2A comprises an N-terminal catalytic domain and a C-terminal regulatory domain containing a leucine zipper dimerization motif, a binding site for protein phosphatase 1 (PP1) and two destruction motifs that are recognized by the APC/C (Fry, 2002). Nek2B lacks the PP1 binding site and destruction motif (Hames and Fry, 2002) (Figure 11). The catalytic domain contains motifs typical of serine/threonine protein kinases (Fry et al., 1995; Hanks and Hunter, 1995). The leucine zipper promotes homodimerization, which leads to trans-autophosphorylation within the C-terminal region (Fry et al., 1999). The destruction sites in Nek2As C-terminus are required for the degradation of Nek2A upon mitotic entry. Nek2B, lacking the motifs, stays throughout mitosis (Hames et al., 2001).

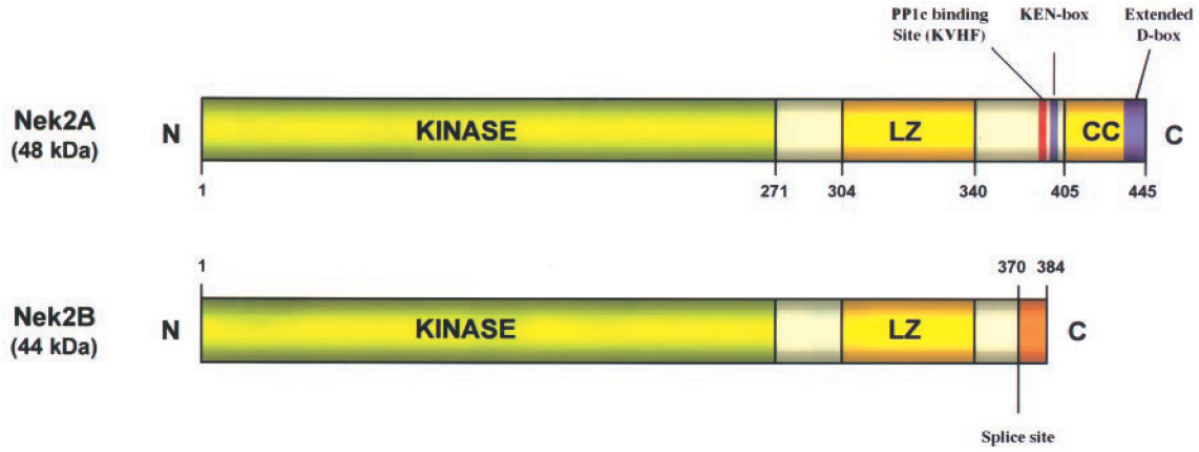

Figure 11. Structure and domains of Nek2A and B. The relative positions of the catalytic domain (kinase), leucine zipper (LZ), coiled-coil (CC), splice site, PP1c binding site, KEN-box (APC/C recognition) and extended cyclin A-type destruction box (proteasomal degradation) are indicated in the scheme. Numbers above and below the structures indicate amino acid positions [from Fry et al., 2002].

1.6.1 Nek2 functions and interactions

The first established function of Nek2 was the promotion of centrosome separation and hence subsequent bipolar spindle formation (See 1.3.). It does so by phosphorylation of the linker proteins C-Nap1 and rootletin at the G2/M transition when the levels of Nek2 peak (Fry et al., 1998; Fry et al., 2012; Hames and Fry, 2002; Hames et al., 2001; Whitfield et al., 2002). Nek2 regulates cilia formation via phosphorylation of Kif24, resulting in enhanced microtubule depolymerization at the cilium via Kif24 (Kim et al., 2015, see 1.4.1.). During cilia resorption in ARPE-19 cells, Nek2 physically interacts with Aurora A and both kinases act additively (DeVaul et al., 2017; Kim et al., 2015).

Despite its role in ciliogenesis and centrosome cohesion, Nek2 has further targets, indicating a role for controlling microtubule nucleation. Additional to its localization at the proximal ends of both mother and daughter centrioles (Fry et al., 1998), Nek2 localizes to the distal ends of the centriole and the basal body. Its accumulation at this site is cell cycle-dependent and appears to peak in late G2 (Kim et al., 2015; Spalluto et al., 2012). Here, it acts on Ninein like protein (Nlp), a mother centriole-specific protein, implicated in microtubule anchoring. As mitotic entry requires a major reorganization of the microtubule cytoskeleton, Nlp is banished from the centrosome upon mitotic entry. Nlp was shown to be displaced from interphase centrosomes upon overexpression of active Nek2 or hyperactive PLK1 without significant additive effect in human U2OS cells. Kinase-inactive Nek2 prevented PLK1 dependent Nlp replacement and *in vitro* activity of Nlp phosphorylation by PLK1 increased in combination with Nek2. Therefore, the authors suggested that Nek2 phosphorylation primes Nlp for PLK1 phosphorylation (Rapley et al., 2005).

Another centrosomal target of Nek2 is centrobin, a daughter centriole specific protein. Nek2 suppression resulted in enhanced centrobin levels at the centrosome, suggesting Nek2 controls centrosomal levels of centrobin (Jeong et al., 2007). The authors further revealed by knockdown experiments that centrobin is involved in microtubule organization in interphase cells and spindle assembly in mitotic cells.

Additionally, a recent automated study using literature-based algorithm followed by experimental validation identified p53 as a target of Nek2. Nek2 phosphorylates p53, resulting in p53 inhibition and thus promotion of cell division (Choi et al., 2018).

In summary, studies indicate that the main function of Nek2 is to phosphorylate proteins at the right time, resulting in their controlled dispersal from the centrosome and proper cell cycle progression.

1.6.2 Regulation of Nek2

As outlined above, Nek2 is involved in centrosome separation, bipolar spindle formation and ciliation (Faragher and Fry, 2003; Spalluto et al., 2012). Hence, the activity of Nek2 needs to be tightly controlled to ensure proper cell function. To ensure that its levels and activity only peak at specific time points of the cell cycle (G2/M) Nek2 is degraded in mitosis by proteasomal degradation mediated by APC/C (Fry et al., 1995; Hames et al., 2001). Nek2 levels drastically decrease in G1 and in G0 upon serum starvation, concomitant with loss of phosphorylated Kif24 (Kim et al., 2015;

Spalluto et al., 2012). This is likely because Nek2A is destroyed by the proteasome upon mitotic entry, persisting throughout G1 and G0 (Hames et al., 2001). Further, in G0 and early G1 cells, the transcription factor E2F4 functions as a transcriptional repressor of Nek2 (Ren et al., 2002).

The activity of Nek2 is enhanced by autophosphorylation (Rellos et al., 2007) and negatively regulated by PP1 (Eto et al., 2002; Hames et al., 2001). When another G2/M Kinase, PLK1, is active, one of its targets, Mst1, reverts the inhibitory association of Nek2 and PP1 (Fry et al., 1999; Golsteyn et al., 1995; Helps et al., 2000; Mardin et al., 2011). The centrosomal level of Nek2 is controlled by rapid turned over at the centrosome owing to a careful balance of transport via satellites, microtubules and localized proteasomal degradation (Hames et al., 2005).

1.6.3 Nek2's function in development and disease

Nek2's role in important cellular processes, particularly the regulation of ciliation and thus signaling already hints towards the assumption that de-regulation of this kinase has severe consequences. As described in 1.4.3., cilia play a crucial role in left-right symmetry breaking during development. In *Xenopus*, overexpression or knockdown of Nek2 resulted in abnormal development, combined with premature cilia resorption and modified signaling. The data showed that Nek2 is a switch balancing ciliogenesis and resorption in the development of left-right asymmetry (Endicott et al., 2015). Recently, it was uncovered that Nek2 regulates planar cell polarity via Dvl, another phosphorylation target. In *Drosophila*, APC/C regulates Nek2, which in turn regulates Dvl localization and proteasomal degradation. Dvl is a core target of APC/C during PCP establishment (Weber and Mlodzik, 2017).

Further, Nek2 regulates B cell development immune response in the mouse. In transgenic mice, overexpression of Nek2 likely shifted B cell development towards self-renewal, indicated by more immature B cells in the bone marrow and decreased differentiated B cells in the peritoneal cavity. In the same study, Nek2 transgenic mice had an enhanced T cell-dependent immune response (Gu et al., 2014).

Notably, Nek2 is a proto-oncogene that is overexpressed in several forms of cancer, including breast cancer. Nek2 overexpression leads to increased proliferation and drug resistance of cancer cells, while depletion of Nek2 reverts these effects. Still, the mechanistic role of Nek2 in cancer development is mainly unknown (Cappello et al., 2014; Hayward et al., 2004; Zhou et al., 2013).

Nek2 is overexpressed in more than 24 cancer types, contributes to drug resistance, and is associated with tumor progression and poor prognosis. Hence, it can serve as a cancer biomarker and effective target for cancer therapy (Fang and Zhang, 2016; Kokuryo et al., 2019; Wang et al., 2019; Yao et al., 2019). Therefore, is of medical relevance to uncover how Nek2 influences tumor progression and if it is cause or consequence of cancer. One of the many cancer types with Nek2 overexpression is hepatocellular carcinoma. Here, it was found that epithelial to mesenchymal transition plays a crucial role in Nek2-mediated cell invasion. The study further suggested that the phenotype results from alterations in signaling including Wnt, NF-κB overexpression and p53 (Zhang et al., 2018).

Further insight into how Nek2's role in ciliation affects cancer progression was given by Kim et al. 2015. Mammary epithelial cells lose primary cilia as they undergo oncogenic transformation (Menzl et al., 2014; Seeger-Nukpezah et al., 2013; Yuan et al., 2010). Nek2 and Kif24 are overexpressed in breast cancer cells and abrogating the defective Nek2/Kif24 activation can restore primary cilia formation and restrict proliferation in breast cancer cells (Kim et al., 2015).

The evolving role of Nek2 as a cancer biomarker and promising target for drug development hopefully increases efforts to entangle its role in the progression of diverse cancer types on the molecular level.

2. Aims of this study

The focus of this study is to analyze the behavior and regulation of appendage proteins at the centrioles in human differentiated and stem cells. Appendage proteins are associated with the older of the two centrioles. In mammalian cells, the centrosome duplicates semi-conservatively before mitosis and new centrioles are formed from the two existing centrioles. Therefore, one of the two centrosomes carries the oldest centriole. Recent studies showed that those inherently asymmetric centrosomes potentially work as a scaffold for the asymmetric distribution of cell fate determinants. Therefore, asymmetrically assembled appendage protein complexes at mitotic centrosomes might be critical for this process in stem cells. Yet, how centrosome asymmetry is established and how, if at all, it influences asymmetric cell division in human stem cells remains unclear. Moreover, the molecular details underlying the behavior of appendages during the cell cycle with regard to asymmetry, maturation, and regulation remain to be clarified.

Therefore, the three main aims of this study were:

(I) To characterize centrosome asymmetry in somatic and stem cells. Here, I analyzed how different appendages and associated centrosomal proteins behave during the cell cycle in differentiated cells (human retina epithelial RPE1 and the hematopoietic cell line KG1a) and hematopoietic stem and progenitor cells (HSPCs).

(II) To decipher whether centrosome age controls asymmetric cell division. Therefore, I correlated the distribution of the old and new centrosomes (as determined in aim I) regarding the asymmetric segregation of stem cell markers in HSPCs.

(III) To elucidate how the cell cycle-dependent behavior of appendages is regulated. Distal appendages are known to have important functions in cilia formation and it must be tightly regulated when ciliogenesis occurs during cell cycle progression. Hence it is tempting to speculate that the assembly of appendages and cilia are functionally and temporally coordinated. Because some distal appendages were reported to lose their centrosomal localization during mitosis, I analyzed if a kinase is required for this process and the consequence of perturbed appendage regulation with special regards to their function in ciliogenesis.

This study provides insight into the regulation of appendage behavior by the kinase Nek2. Moreover, this study connects the regulation of centrosome appendages to the symmetric versus asymmetric outcome of two progenies after cell division.

3. Results

3.1 Analysis of the cell type specific behavior of centrosomal proteins

3.1.1 Analysis of centrosomal appendages in human somatic and progenitor cells

To achieve a better understanding of the cell cycle behavior of centrosome appendages with regards to asymmetry, maturation, and regulation, I started investigating the behavior of a subset of appendages throughout the cell cycle. I systematically analyzed the behavior of the key distal appendage components Cep83, SCLT1, Cep164, FBF1, and Cep123 and subdistal components ODF2, Centriolin and Ninein in differentiated cell lines and hematopoietic stem and progenitor cells (HSPCs). As an example for a differentiated, adherent and ciliating cell line RPE1 cells were chosen. Immunofluorescence microscopy to detect appendage proteins at different stages of the cell cycle revealed a drastic reduction of Cep164, Cep123, LRRC45, Ninein and Centriolin levels at mother and daughter centrosome (centrosome 1 and 2) during mitosis in RPE1 cells (Figure 12A and B). EM proofed that ODF2 is a marker for the older centrosome during (Kong et al. 2014, Bowler et al. 2019). To verify that centrosome 1 and 2 can be referred to as the older and younger centrosome in this analysis, Cep164 and Cep83 intensities were quantified at the ODF2 high and ODF2 low centrosome, as an example for appendages that are removed or retained during mitosis, respectively. The resulting quantifications indicate that the centrosome with higher intensity (centrosome 1) can be referred to as the older (mother) centrosome (Figure 13).

Quantitative imaging showed that Cep164, Cep123, LRRC45, Ninein and Centriolin began to disappear from centrosomes in prophase and the reduced levels were maintained until telophase. Only Cep164, LRRC45, and Ninein displayed a slight increase in telophase with still significant lower levels compared to interphase. To determine if appendage release occurs before or after nuclear envelope breakdown (NEB), cells were co-stained with anti-nuclear pore complex proteins antibody Mab414. Cep123, Cep164, LRRC45, and Ninein are released in prophase/G2 (before NEB). The subdistal appendage Centriolin showed the first drastic reduction during prometaphase, while e.g. Cep164 is released before NEB (Figure 14). It must be noted, that the release of Centriolin was variable (Figure 12A). Its levels on the centrosome decreased before NEB in a population of cells, while it stayed until mitosis in another. In RPE1 cells, ODF2, Cep83, and SCLT1 and FBF1 remained on one centrosome and

displayed asymmetry throughout the cell cycle (Figure 12). ODF2 intensity increased on one centrosome (mother centrosome) at the beginning of mitosis, returned to interphase levels during prometa- and metaphase and decreased in ana- and telophase. Similarly, FBF1 retained interphase levels on one centrosome, most likely the mother centrosome, in mitosis and slowly matured on the second (younger) centrosome. The asymmetry is strongly visible throughout the cell cycle for those two appendages in RPE1 cells. Thus, ODF2 and FBF1 can serve as a marker for the older centrosome during mitosis in these cells. Likewise, Cep83 and SCLT1 average signal intensities stayed strong at the mother centrosome in mitosis (centrosome 1). In contrast to ODF2 and FBF1, Cep83 and SCLT1 signal intensity on the younger centrosome (centrosome 2) increased early during mitosis. This indicates an earlier acquirement of SCLT1 and Cep83 on the younger centrosome compared to ODF2.

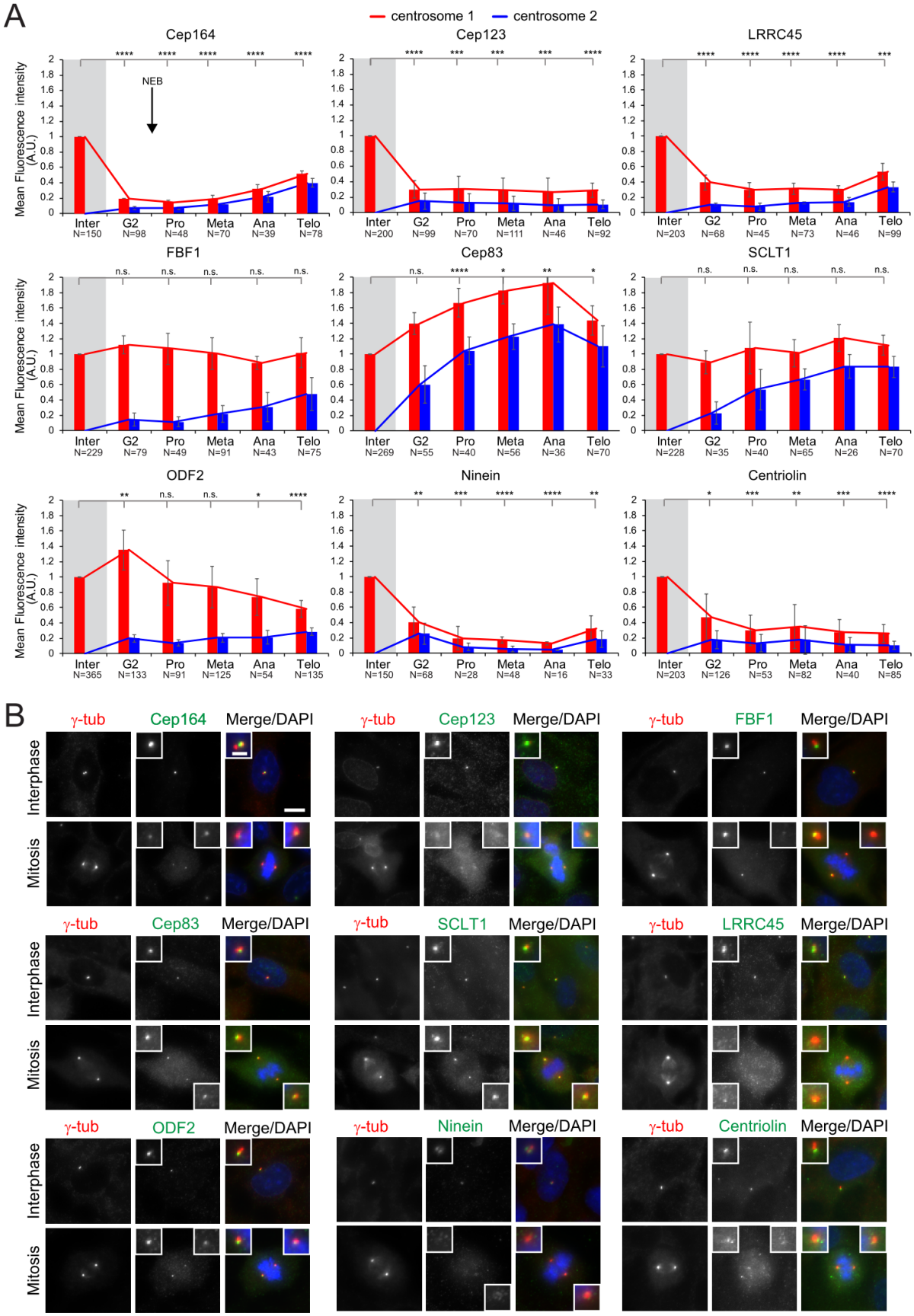

Figure 12. Quantification of the cell cycle-dependent behavior of appendage proteins in RPE1 cells. (A) The levels (pixel intensities) of the indicted appendage protein were measured at each centrosome (centrosome 1 and centrosome 2) during interphase (inter), G2, prometaphase (pro), metaphase (meta), anaphase (ana) and telophase (telo) and normalized to the average of interphase.

Interphase is marked by a gray shading to highlight exit to mitosis. For interphase, the average intensity was set to one. Here the values for the second centrosome were set to zero because just one centrosome and appendage signal exists (Figure 14). The different phases of the cell cycle were determined based on centrosome distance and DNA condensation. Graphs depict fluorescence intensity in arbitrary units (A.U.) and show the average ± standard deviation of all performed repetitions for each protein in each cell cycle phase. Numbers below the bars represent the total number of cells analyzed for each condition. NEB=nuclear envelope breakdown. Students's t-test was performed to determine if intensity values of centrosome 1 in each phase differ significantly from interphase levels. Significance probability: ns: $P > 0.05$, *: $P \leq 0.05$, **: $P \leq 0.01$, ***:$P \leq 0.001$, ****: $P \leq 0.0001$. (B) Representative images for the cell cycle behavior of appendage proteins in RPE1 cells. Appendage proteins were labeled with specific antibodies and γ-tubulin served as a centrosome marker. 4'6-diamidino-2-phenylindole (DAPI) stained the DNA. Scale bars are 10 µm and 2 µm.

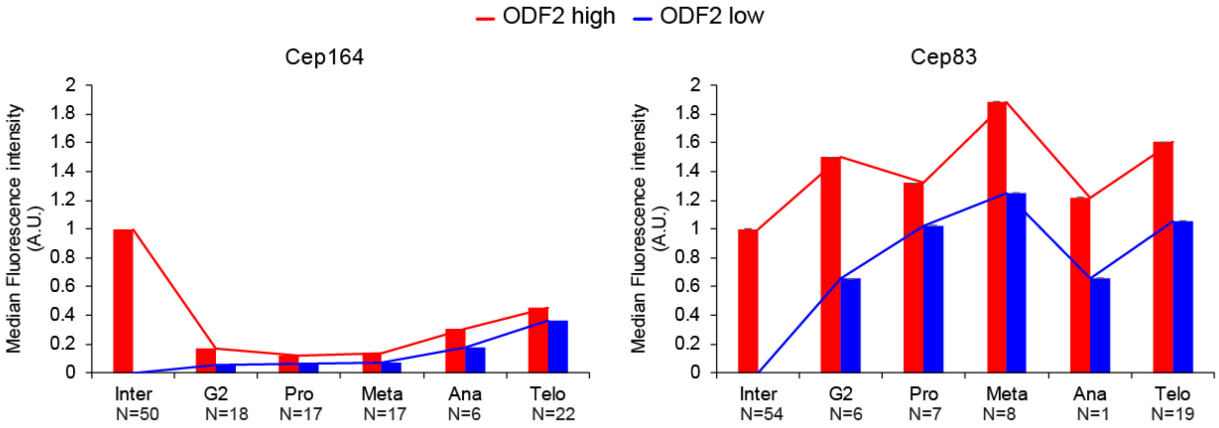

Figure 13. Quantification of Cep164 and Cep83 on the ODF2 high (mother) and ODf2 low (daughter) centrosome in RPE1 cells. Appendage proteins were labeled with specific antibodies and γ-tubulin served as a centrosome marker. The levels (pixel intensities) of the indicted appendage protein were measured at the centrosome with high (red) and low (blue) ODF2 intensity during interphase (inter), G2, prometaphase (pro), metaphase (meta), anaphase (ana) and telophase (telo) and normalized to the average of interphase. The different phases of the cell cycle were determined based on centrosome distance and DNA condensation. Graphs depict fluorescence intensity in arbitrary units (A.U.). Numbers below the bars represent the total number of cells analyzed for each condition.

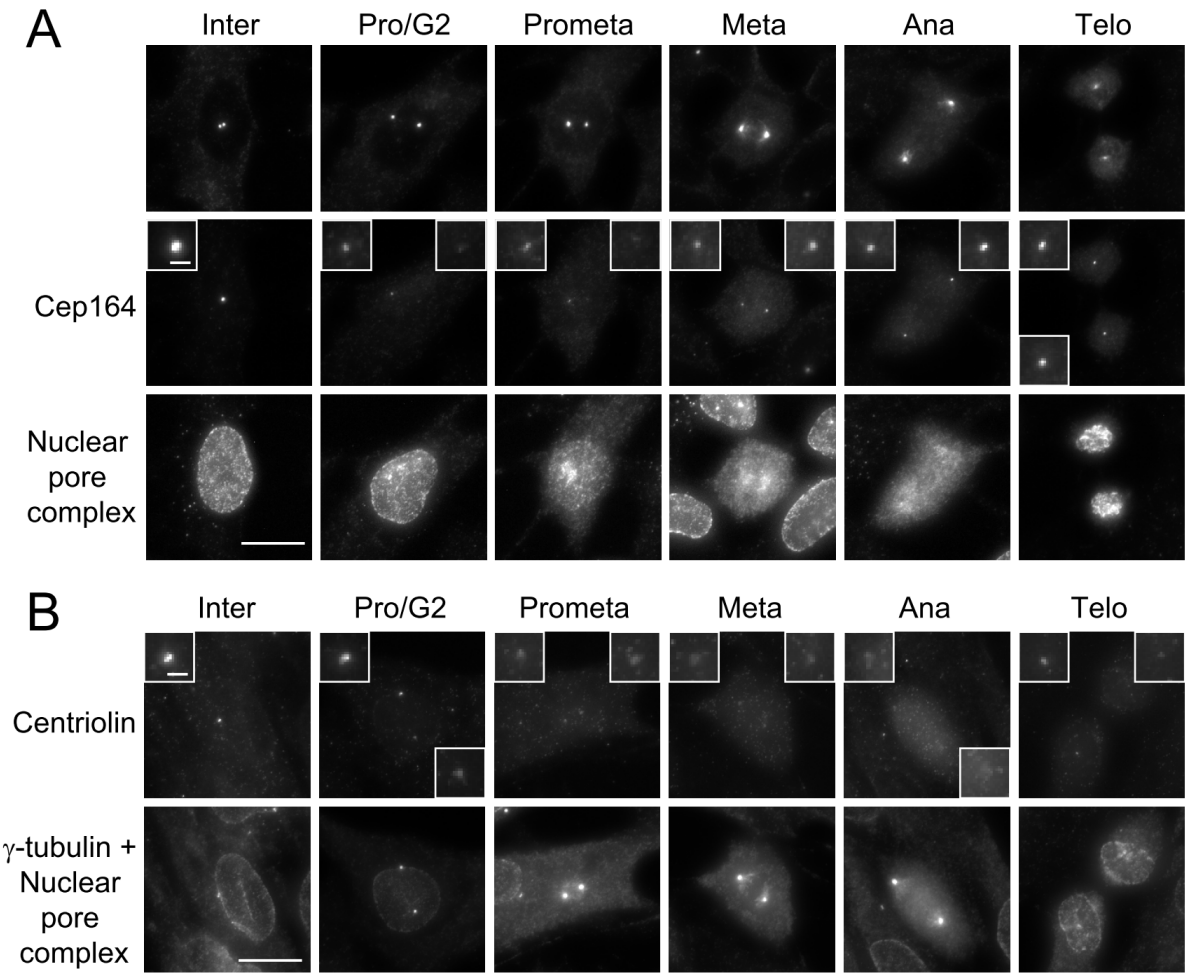

Figure 14. Localization of the distal appendage protein Cep164 (A) and subdistal appendage protein Centriolin (B) at the centrosome in different cell cycle phases in RPE1 cells. γ-tubulin was used as a centrosome reference. Nuclear pore complex antibody Mab414 was used two identify the nuclear envelope breakdown (NEB). Cep164 release from the centrosome starts before NEB, Centriolin release after NEB. Scale bars are 20 µm and 2 µm.

One aim of this study was to analyze whether appendage asymmetry is present in human stem cells and if it regulates ACD.

Therefore, I addressed if I observe differences in appendage behavior during mitosis in stem and progenitor cells. Here, I analyzed the same appendages as in RPE1 cells in primary CD34+ (stemness maker in HSPCs) HSPCs. HSPCs were used because they are one of the few primary multipotent cells that can be isolated from living humans. Additionally, the acute myelogenous leukemia (AML) cell line KG1a, which is also CD34+ and displays progenitor-like properties (Civin et al., 1984) was used (Figure 16 and 17).

I set the intensity of the second centrosome in all my analysis to 0. Therefore, I first verified the lack of signal on the daughter centriole during interphase in hematopoietic cells. Both centrioles, distinguished by γ-tubulin, were measured in HSPCs. Fluorescence signal intensities of all proteins displayed median intensity close to zero on the younger centriole, although γ-tubulin was found on both centrosomes in interphase (Figure 15). It should be noted that studies using higher resolution showed Ninein and Centriolin colocalizing at the open end of the centrosome tube and the proximal end of both centrioles in interphase (Ou et al., 2002). In contrast, in this study, the resolution was not sufficient to resolve Ninein and Centriolin localization at the centrosome tube.

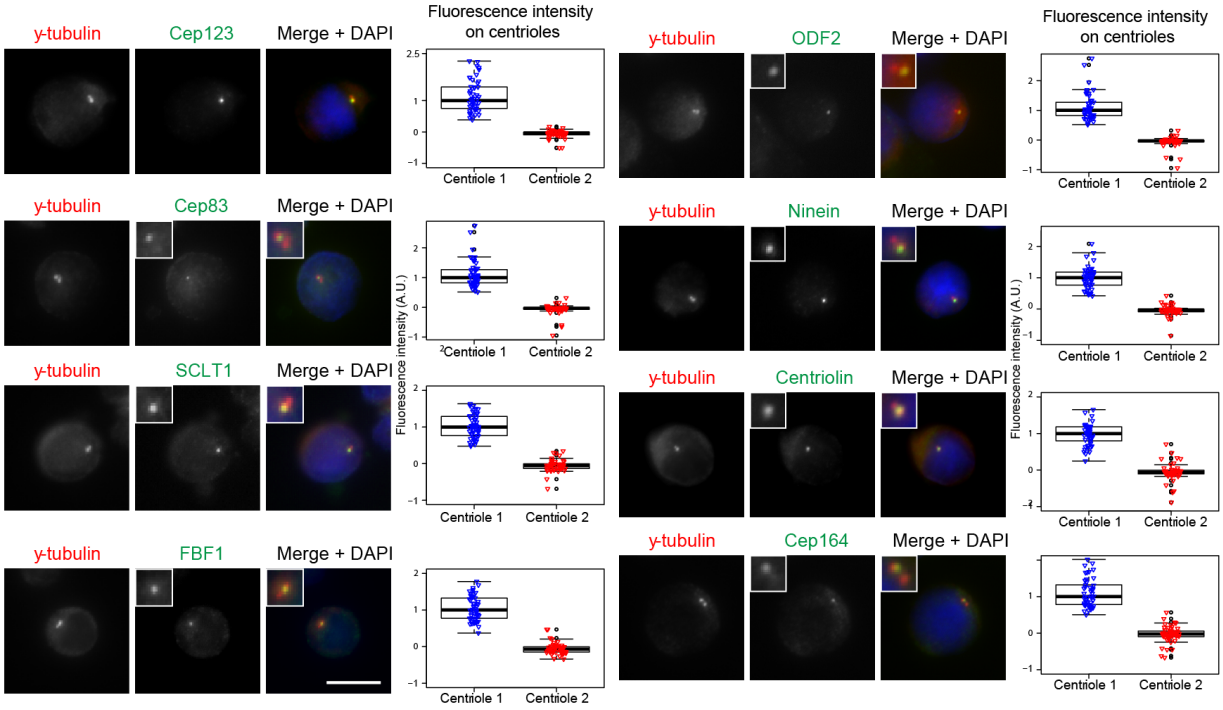

Figure 15. The analyzed centrosomal appendage proteins are only present on one of the two centrioles. Representative pictures show indirect immunofluorescence in HSPCs cells using antibodies against the indicated proteins (scale bar is 10 μm). The graphs show fluorescence intensities on both centrioles normalized to the median of the stronger interphase signal. For each staining 50 cells were analyzed.

The same cell cycle-dependent analysis as shown before for RPE1 cells (Figure 12) revealed similar results in HSPCs and KG1a cells (Figure 16 and 17). The localization of Cep123 and Centriolin differed from RPE1 (Figure 12) and the reported localization in other mammalian somatic and stem cells (Sillibourne et al. 2013). In HSPCs and KG1a cells, their levels did decline on the spot corresponding to the centrosome marker, but additionally Cep123 and Centriolin positive dots localized surrounding the centrosome once the cells entered mitosis. The nature of the structures to which

Cep123 localizes in mitotic HSPCs remains to be defined but are reminiscent of centriolar satellites. This phenotype varied between experimental repetitions and was observed in 66-72% of mitotic HSPCs and between 51-88% of mitotic KG1a cells. These granule-like structure sometimes localized very close to the centrosome, which disturbed some measurements. This is likely the cause for higher mitotic Centriolin and Cep123 levels in HSPCs compared to the other cell types (Figure 16). In contrast to RPE1, average ODF2 levels stayed high on centrosome 1 in KG1a cells, while they even increased until telophase in HSPCs. Association of SCLT1 and Cep83 with mitotic centrioles in the analyzed cell types is similarly like RPE1 cells, although the intensity increase of Cep83 in on the mitotic mother centrosome is less drastic in HSPCs and not even present in KG1a cells.

Notably, FBF1 differed in hematopoietic cells compared to RPE1 cells and maintained low levels on both centrosomes during mitosis, indicating a cell-type specific regulation of this appendage proteins.

Interestingly, the mitotic behavior of appendage proteins observed in the here analyzed cell types (Figure 12, 16 and 17) reflects the hierarchical network of their assembly (Introduction, Figure 2C): The assembly of appendage proteins, which were released from the centrosome in mitosis (Cep164, FBF1, Cep123), was shown to be dependent on the components that stay on the mother centrosome in mitosis (ODF2, Cep83, and SCLT1) (Ishikawa et al., 2005; Tanos et al., 2013).

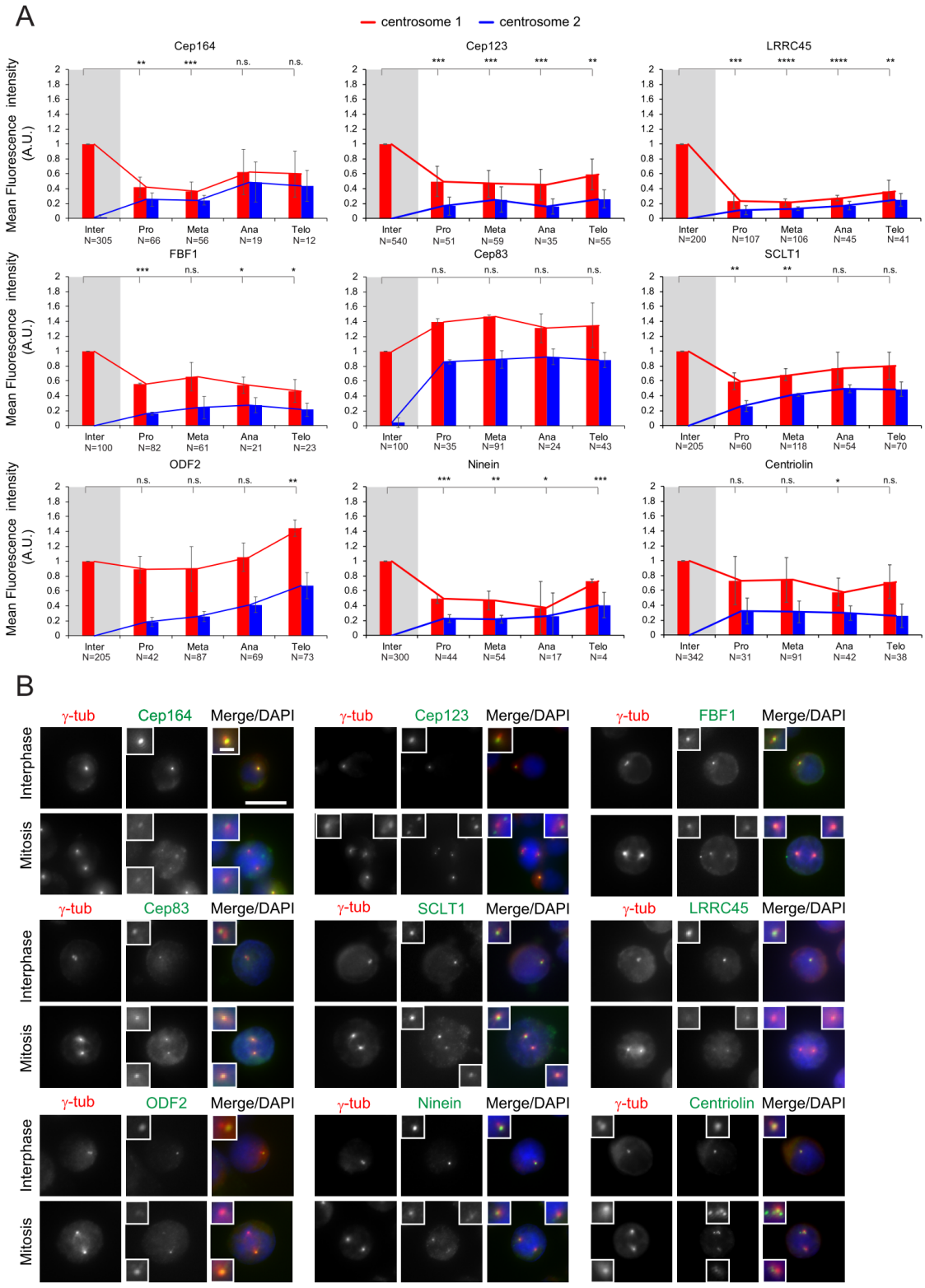

Figure 16. Cell cycle behavior of appendage proteins in primary HSPCs is comparable to RPE1 cells, except for FBF1. (A) The levels (pixel intensities) of the indicted appendage protein were measured at each centrosome (centrosome 1 and centrosome 2) during interphase (inter), G2, prometaphase (pro), metaphase (meta), anaphase (ana) and telophase (telo) and normalized to the average of interphase. Interphase is marked by a gray shading to highlight exit to mitosis. For interphase, the average intensity was set to one. Here the values for the second centrosome were set to zero because just one centrosome and appendage signal exists (Figure 14). The different phases of the cell cycle were determined based on centrosome distance and DNA condensation. Graphs depict fluorescence intensity in arbitrary units (A.U.) and show the average ± standard deviation of all performed repetitions for each protein in each cell cycle phase. Numbers below the bars represent the

total number of cells analyzed for each condition. NEB=nuclear envelope breakdown. (A) Student's t-test was performed to determine if intensity values of centrosome 1 in each phase differ significantly from interphase levels. Significance probability: ns: P > 0.05, *: P ≤ 0.05, **: P ≤ 0.01, ***:P ≤ 0.001, ****: P ≤ 0.0001. (B) Representative images for the cell cycle behavior of appendage proteins in HSPCs. Appendage proteins were labeled with specific antibodies and γ-tubulin served as a centrosome marker. DAPI stained the DNA. Scale bars are 10 μm and 2 μm.

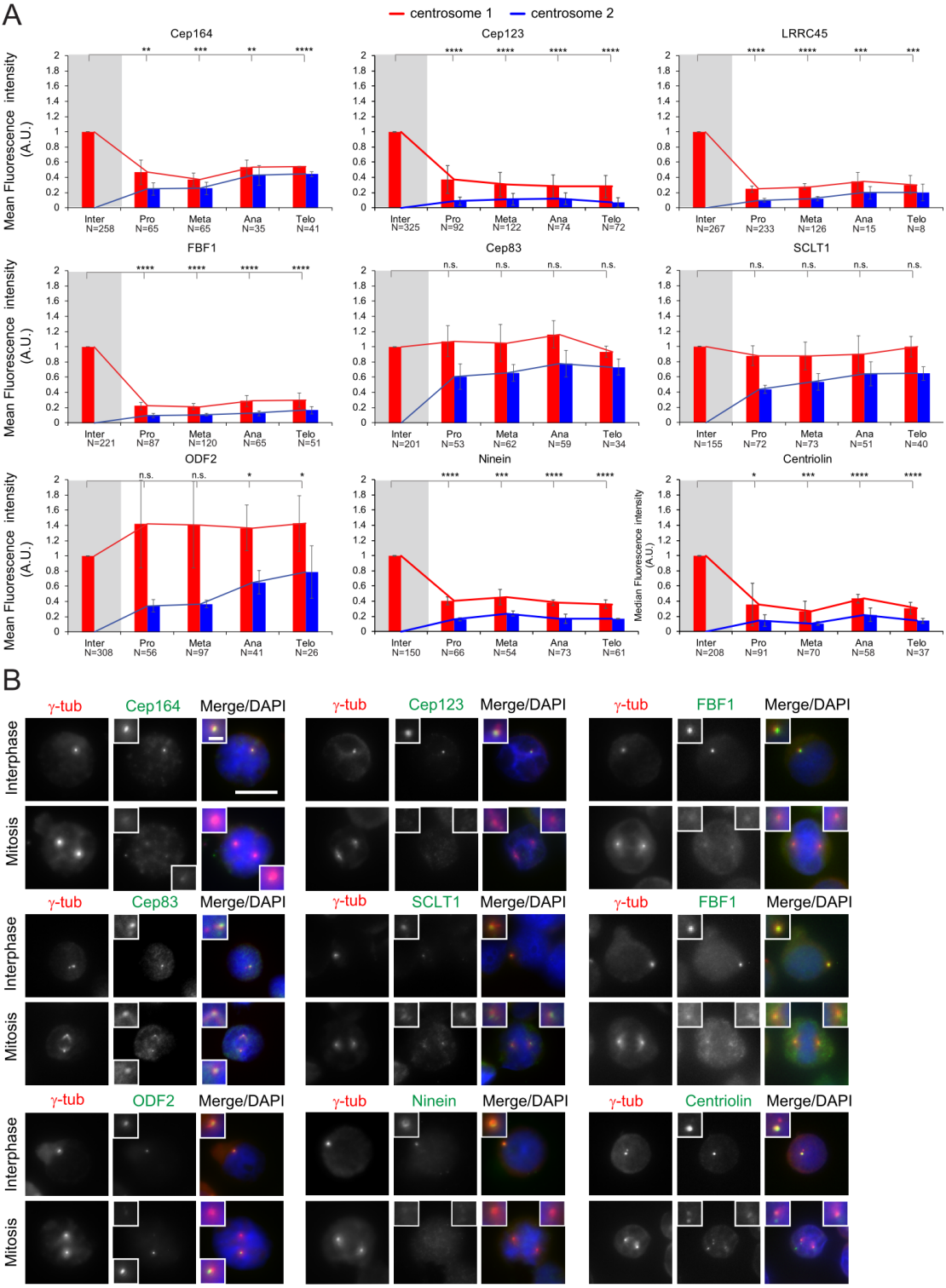

Figure 17. Cell cycle behavior of appendage proteins in KG1a cells is comparable to RPE1 cells, except for FBF1. (A) The levels (pixel intensities) of the indicted appendage protein were measured at each centrosome (centrosome 1 and centrosome 2) during interphase (inter), G2, prometaphase (pro), metaphase (meta), anaphase (ana) and telophase (telo) and normalized to the average of interphase. Interphase is marked by a gray shading to highlight exit to mitosis. For interphase, the average intensity

was set to one. Here the values for the second centrosome were set to zero because just one centrosome and appendage signal exists (Figure 14). The different phases of the cell cycle were determined based on centrosome distance and DNA condensation. Graphs depict fluorescence intensity in arbitrary units (A.U.) and show the average ± standard deviation of all performed repetitions for each protein in each cell cycle phase. Numbers below the bars represent the total number of cells analyzed for each condition. NEB=nuclear envelope breakdown. Student's t-test was performed to determine if intensity values of centrosome 1 in each phase differ significantly from interphase levels. Significance probability: ns: $P > 0.05$, *: $P \leq 0.05$, **: $P \leq 0.01$, ***:$P \leq 0.001$, ****: $P \leq 0.0001$. (B) Representative images for the cell cycle behavior of appendage proteins in KG1a cells. Appendage proteins were labeled with specific antibodies and γ-tubulin served as a centrosome marker. DAPI stained the DNA. Scale bars are 10 µm and 2 µm.

3.1.2 Analysis of other centrosome components in human somatic and progenitor cells

3.1.2.1 Analysis of the daughter centriole specific protein centrobin

The primary goal of the cell cycle-dependent localization analysis was to identify appendage proteins, which specifically mark the older mother centrosome during mitosis. There, ODF2 was established as a for centrosome asymmetry on the mother centrosome in all three analyzed cell types. Additionally, I studied the daughter centrosome specific protein centrobin regarding centrosome asymmetry as a potential marker for the younger centrosome during mitosis. Centrobin was identified as a centriole-associated protein that asymmetrically localizes to the younger daughter centriole. In somatic cells (76NTert) it stains only one centriole in most cells in the G0/G1 state. In G1/S, S, and G2/M phase cells, there are usually two strongly stained centrobin dots, correlating with the two newly synthesized daughter centrioles (Zou et al., 2005).

Here, I wanted to test the mitotic behavior of centrobin in mitotic HSPCs or KG1a cells. In my analysis, the staining in mitotic cells differed from the more gradual asymmetry observed for asymmetrically distributed mother appendage proteins. First, centrobin had a much higher intensity on mitotic centrosomes than interphase centrosomes. Secondly, in the majority of cells, it was completely symmetric. Conversely, in a section of cells, it was either only present on one centrosome or very weakly stained on one of the two centrosomes. 28% of HSPCs and 35% of KG1a cells displayed a centrobin intensity ratio of the strong/weak centrosome higher than 1.5 (Figure 18).

I did not consider this protein as a useful marker for centrosome asymmetry in mitotic cells because of two reasons: First, only a few cells showed visible centrobin asymmetry. Second, I did not observe any clear correlation when I double-stained daughter specific centrobin and mother specific ODF2 in mitotic cells (data not shown).

In about half of the cells, strong centrobin was observed opposite to the ODF2 strong centrosome. On other mitotic cells, both strong signals overlapped on the same site.

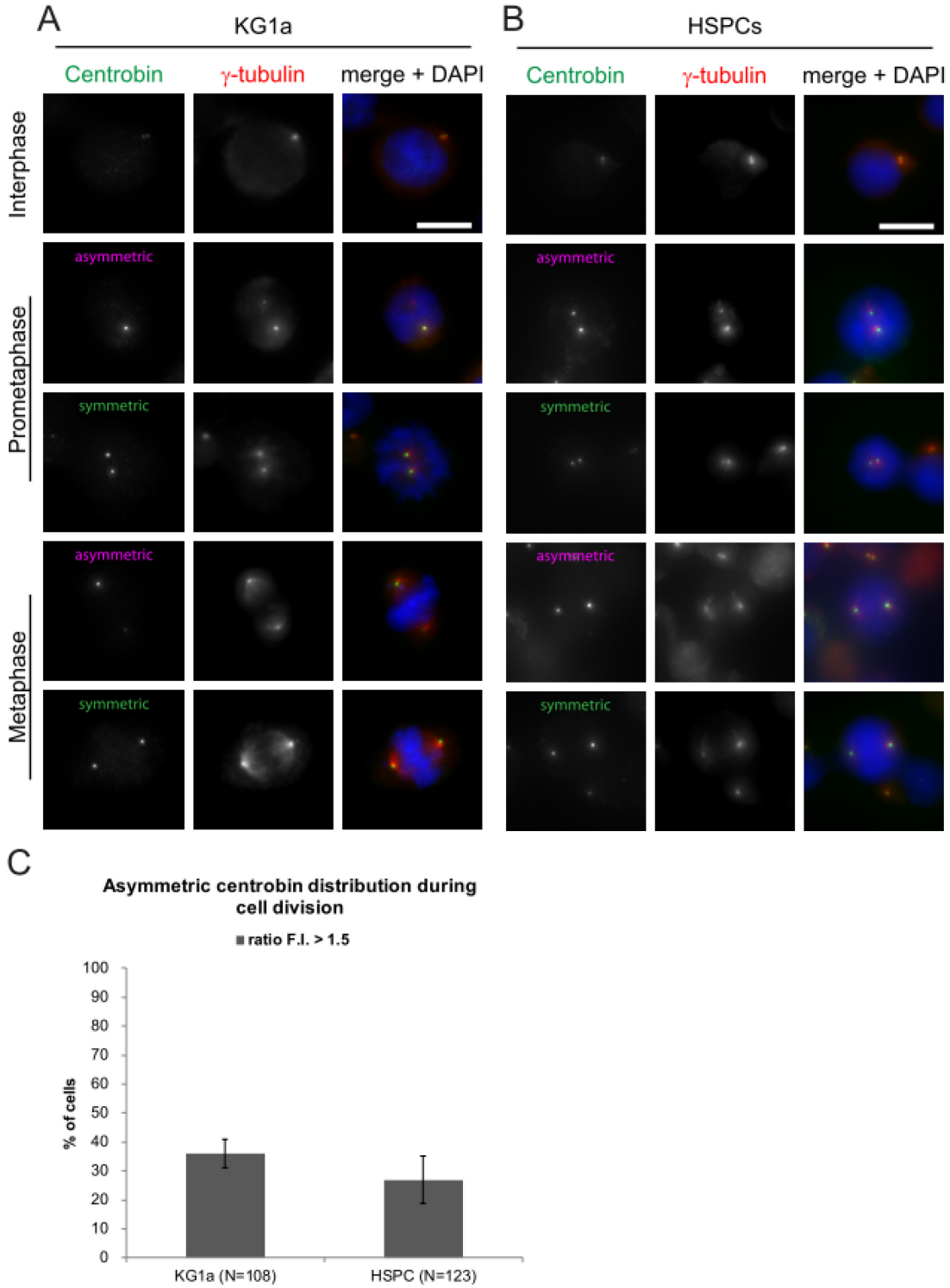

Figure 18. Subcellular localization of centrobin in HSPCs and KG1a cells at different cell cycle phases. Immunofluorescence images of KG1a cells (A) and HSPCs (B) stained with a specific anti-centrobin antibody. γ-tubulin (red) and DAPI (blue) serve as markers for centrosomes and nuclei, respectively. Scale bar is 10 µm. Examples of prominent phenotypes are shown. (C) The graph shows a quantification of HSPCs and KG1a cells with asymmetric centrobin staining in different phases of mitosis, defined as a fluorescence ratio of the stronger vs weaker centrobin signal > 1.5. The data is from three experiments each. Graphs show the average ± standard deviation of all performed repetitions. Numbers below the bars represent the total number of cells analyzed for each condition.

3.1.2.2 Analysis of regulators of ciliary proteins and regulators of ciliogenesis in hematopoietic cells: Cep97, CP110, TTBK2, and Arl13B

It is mostly assumed that cilia are absent in hematopoietic cells, although one study disputes this (Singh et al., 2016). As the primary cilium serves as a signaling antenna for the cell, I reasoned that ciliary proteins and regulators are either absent or may still be important for differential signaling in dividing HSPCs despite their lack of the cilium. I was further interested whether these proteins still have a centrosomal localization in hematopoietic cells. Thus, I analyzed cilia proteins and regulators like CP110, Cep97, and ADP-ribosylation factor-like protein 13B (Arl13B) in HSPCs and KG1a cells compared to the ciliating RPE1 cell line. CP110 and Cep97 localize to the distal end of the mother and daughter centriole and are key negative regulators of ciliogenesis by capping the mother centriole (Spektor et al., 2007).

Indeed, both proteins localized at the centrosome in interphase and mitosis. The localization pattern did not differ compared to RPE1 cells (Figure 19). As both proteins were not visibly asymmetric during mitosis, they are not further relevant for my examination of centrosome asymmetry in ACD.

Next, I investigated the ciliogenesis regulating kinase TTBK2, which removes CP110/Cep97 (Cajánek and Nigg, 2014; Goetz et al., 2012). TTBK2 localized in a similar way in hematopoietic cells (HSPCs and KG1a) and RPE1 cells (Figure 20A-C). TTBK2 displayed weak centrosomal staining in interphase cells. Cep164 recruits TTBK2 (Cajánek and Nigg, 2014). Hence, it disappeared from the centrosome in mitotic cells like its target Cep164 (Figure 12, 16, 17). As reported before in RPE1 cells (Chaki et al., 2012), TTBK2 accumulated at the midzone in anaphase cells and the midbody in telophase cells in all three here analyzed cell types. Interestingly, TTBK2 additionally appeared in cytoplasmic aggregates in 23% of the AML cell line KG1a (Figure 20D). The phenotype was more prominent in double and multinucleated KG1a cells (not shown). Similar TTBK2 aggregates were observed in the human neuroblastoma-derived cell line SH-SY5Y and Human embryonic kidney cells 293 (HEK293) cells upon TTBK2-GFP overexpression. There, the aggregates colocalized with phosphorylated TDP-43. The TAR DNA binding protein, TDP-43, plays a pathogenic role in amyotrophic lateral sclerosis and frontotemporal dementia (Mackenzie and Rademakers, 2008). The authors suggest that abnormal TTBK2 activity increases TDP-43 phosphorylation and aggregation, a hallmark of

neurodegenerative disease (Afroz et al., 2019). Future studies might reveal if TTBK2 aggregates also correlate with cancer and could serve as a biomarker.

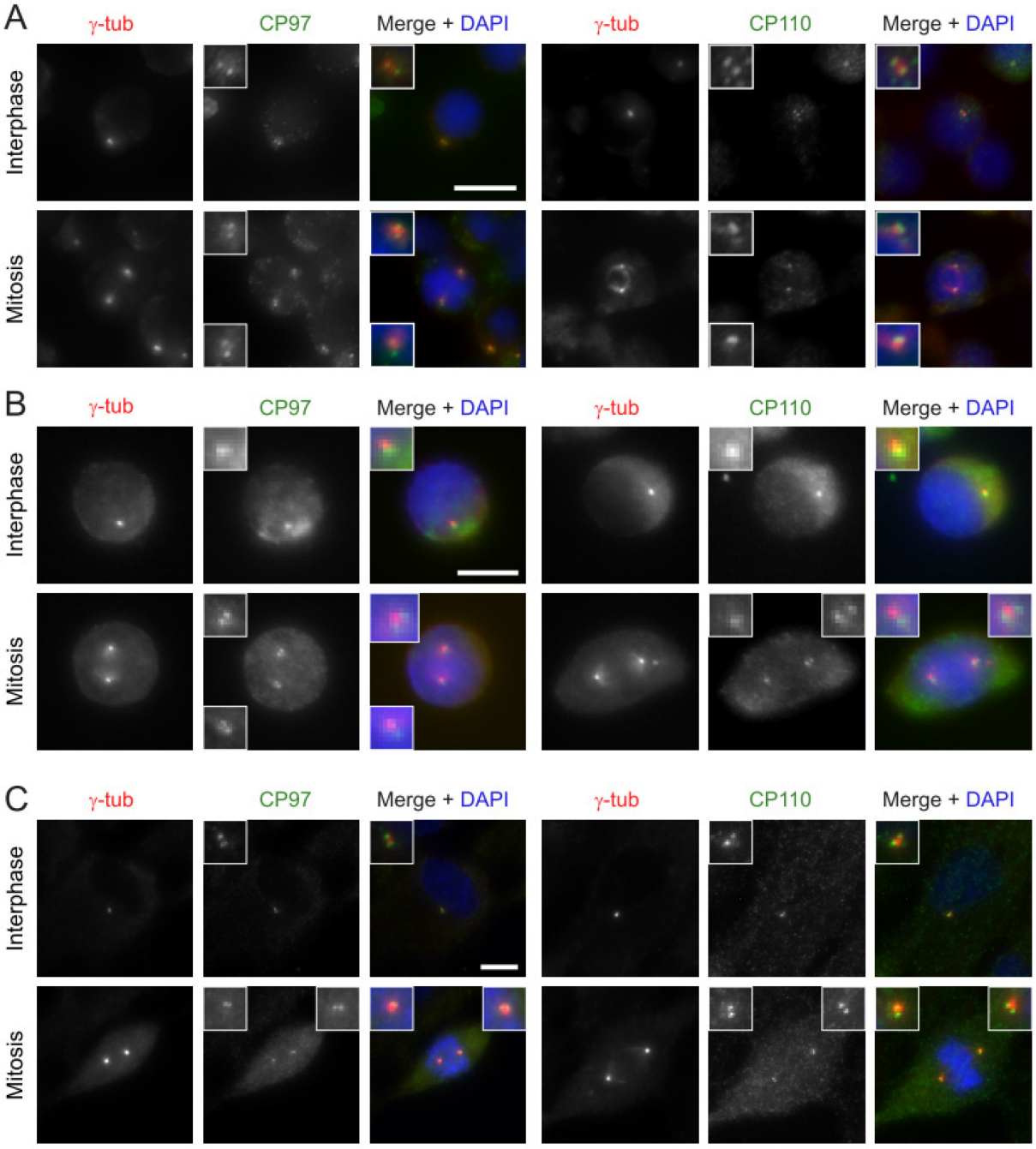

Figure 19. Subcellular localization of Cep97 and CP110. Immunofluorescence images of HSPCs (A), KG1a (B) and RPE1 (C) cells stained with specific and anti-Cep97 or CP110 primary antibodies. γ-tubulin and DAPI were used as a centrosome and nucleus reference, respectively. Examples of prominent phenotypes are shown. Scale bar is 10 μm. Inlets are 3 times enlargements of indicted centrosomes. In all analyzed cases no centrosome asymmetry was observed.

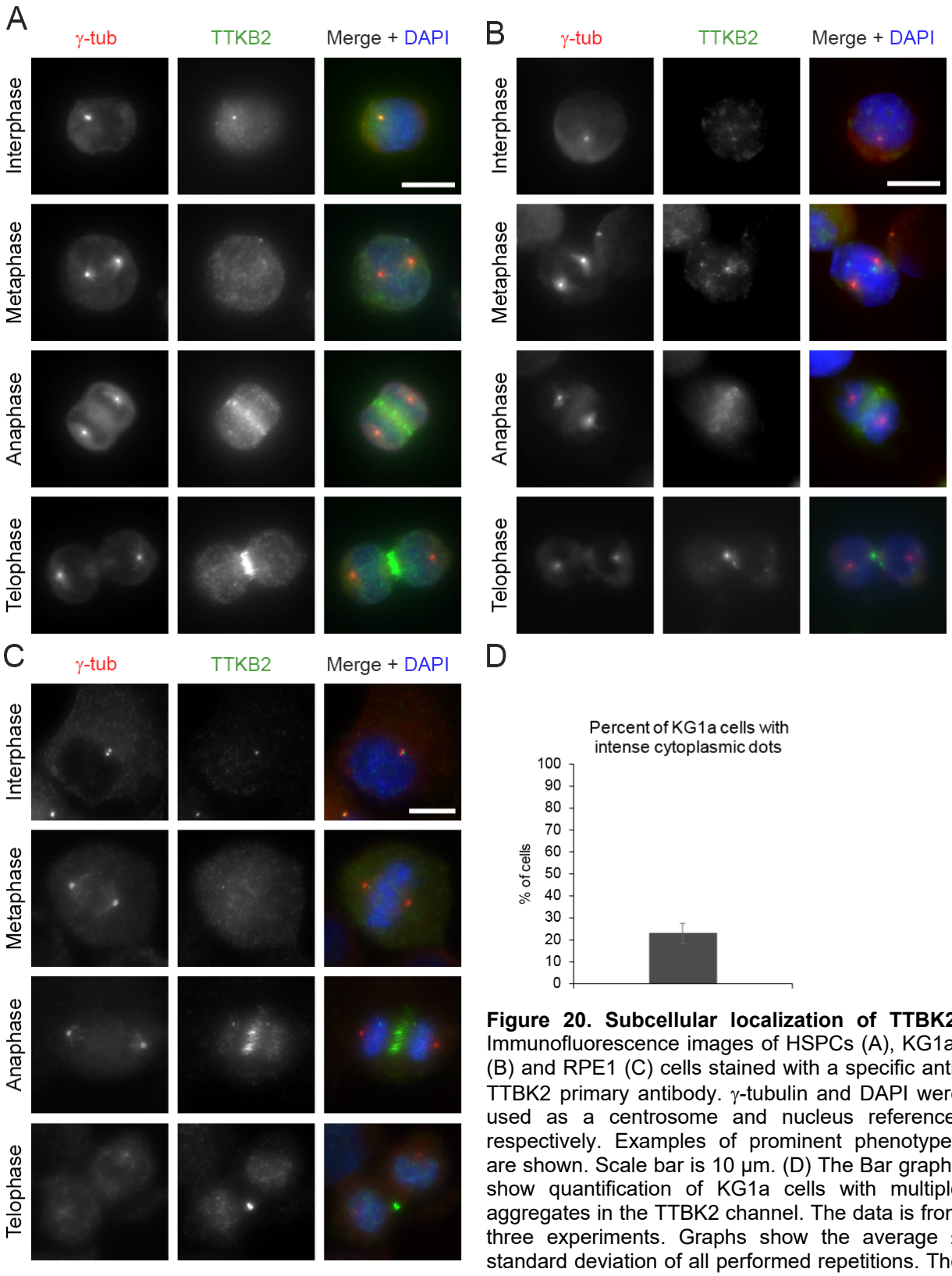

Figure 20. Subcellular localization of TTBK2. Immunofluorescence images of HSPCs (A), KG1a- (B) and RPE1 (C) cells stained with a specific anti-TTBK2 primary antibody. γ-tubulin and DAPI were used as a centrosome and nucleus reference, respectively. Examples of prominent phenotypes are shown. Scale bar is 10 µm. (D) The Bar graphs show quantification of KG1a cells with multiple aggregates in the TTBK2 channel. The data is from three experiments. Graphs show the average ± standard deviation of all performed repetitions. The total number of cells analyzed was N=327.

Next, I studied the ciliary membrane specific protein Arl13B (Cantagrel et al. 2008). Hereby, I aimed to reveal if HSPCs and KG1a cells can form cilia or if this protein may display a differing localization and function. Arl13B is a small GTPase that localizes to the ciliary matrix (the compartment between the membrane and the axoneme). It plays

a role in the formation and maintenance of cilia and regulates endocytic-recycling traffic (Barral et al., 2012; Cantagrel et al., 2008; Lu et al., 2015a). Interestingly, Arl13B localized not on the centrosome but in a polarized manner in most of KG1a cells (Figure 21B). The most prominent localization in interphase was an accumulation in the uropod in KG1a cells (Figure 21B and D). Uropods refer to the hind part of polarized cells during cell migration that stabilize and move the cell (Sanchez-Madrid and Serrador, 2009). Others observed a similar pattern by comparing peripheral blood mononuclear cells of healthy donors and patients with chronic myelogenous leukemia (CML) (Lee et al. 2014). In this analysis, the polarized Arl13B staining was rarely observed in HSPCs obtained from healthy donors (Figure 21A and D).

Even without serum starvation, a part of RPE1 interphase cells is always ciliated (Figure 21C). Sigh et al. 2016 found that 97-99% of hematopoietic blood and bone marrow cells and 10-36% of KG1a cells were ciliated upon serum withdrawal. I could not reproduce this observation. In contrast, neither cilia nor an Arl13B stained ciliary membrane remnant was observed in KG1a and HSPCs. Even after following the same protocol as Singh et al. for HSPCs and KG1a or additionally serum starvation in KG1a cells I did not observe ciliated cells (data not shown). This difference could be due to different sources of primary cells and cell lines, different markers used for cilia (Arl13B versus acetylated tubulin) or the cilia were too short to be recognized by the imaging techniques used in this study.

During mitosis, Arl13B was always dispersed but showed clear staining in the midzone during telophase and cytokinesis. The function of Arl13B at the midbody is unknown yet but points towards a role during cell division. Sometimes one of the two daughter cells retained the midbody remnant after cytokinesis in HSPCs and KG1a cells (data not shown).

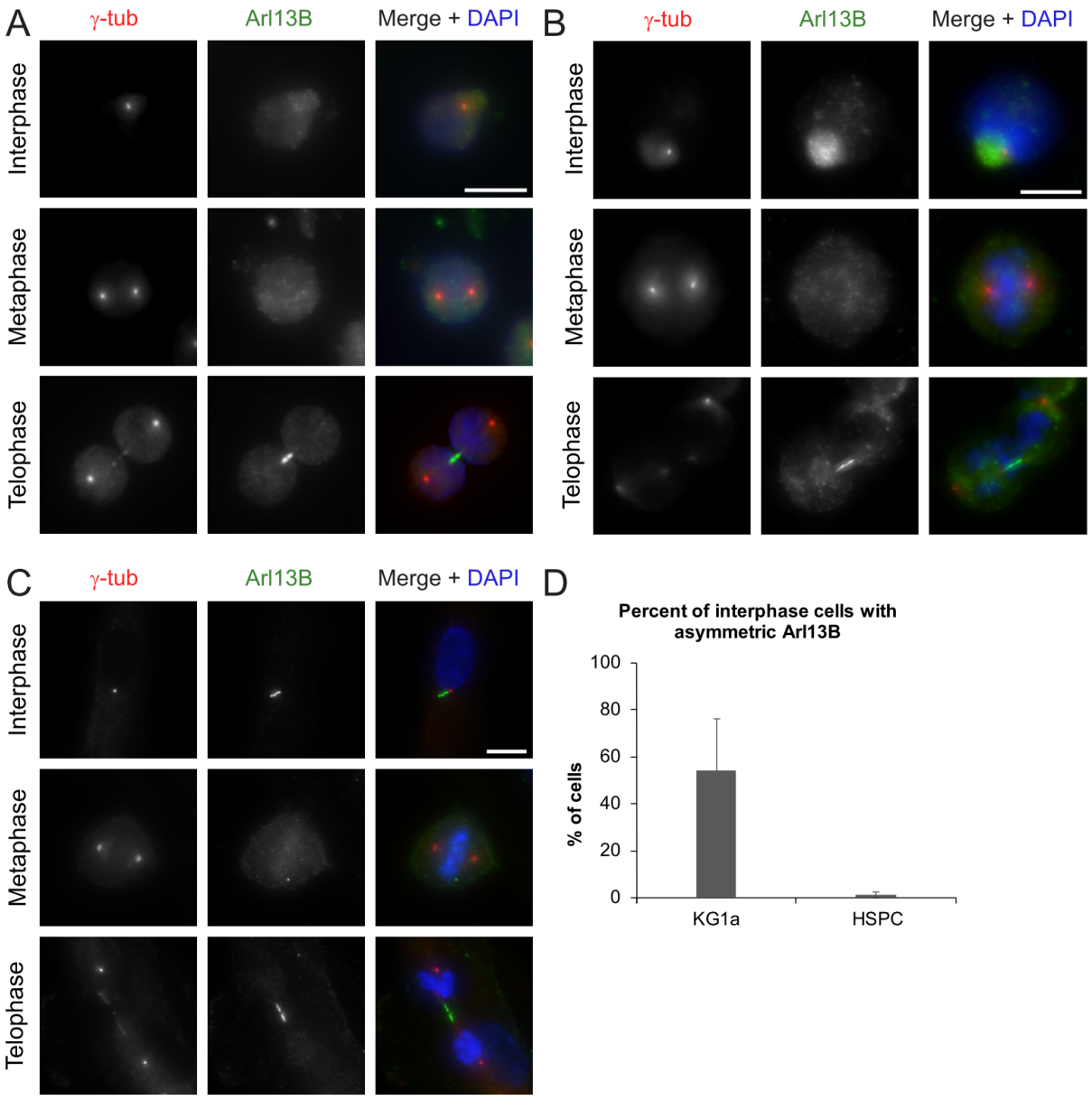

Figure 21. Subcellular localization of Arl13B at different cell cycle phases. Immunofluorescence images of HSPCs (A), KG1a- (B) and RPE1 (C) cells stained with a specific anti-Arl13B primary antibody. γ-tubulin was used as a centrosome reference. DAPI stained the DNA. Examples of prominent phenotypes are shown. Scale bar is 10 µm. (D) The Bar graphs show quantification of KG1a cells and HSPCs with asymmetric/polarized Arl13B in interphase cells. The data is from three experiments. Graphs show the average ± standard deviation of all performed repetitions. The total number of cells analyzed was N=600 for HSPCs and N=1260 for KG1a.

3.1.2.3 Localization of the satellite and linker marker PCM1 and Rootletin in hematopoietic cells

Finally, I was interested in the cell cycle-dependent behavior of two other centrosome components in hematopoietic cells: the localization of satellites marked by PCM1 and the centrosomal linker, marked by rootletin.

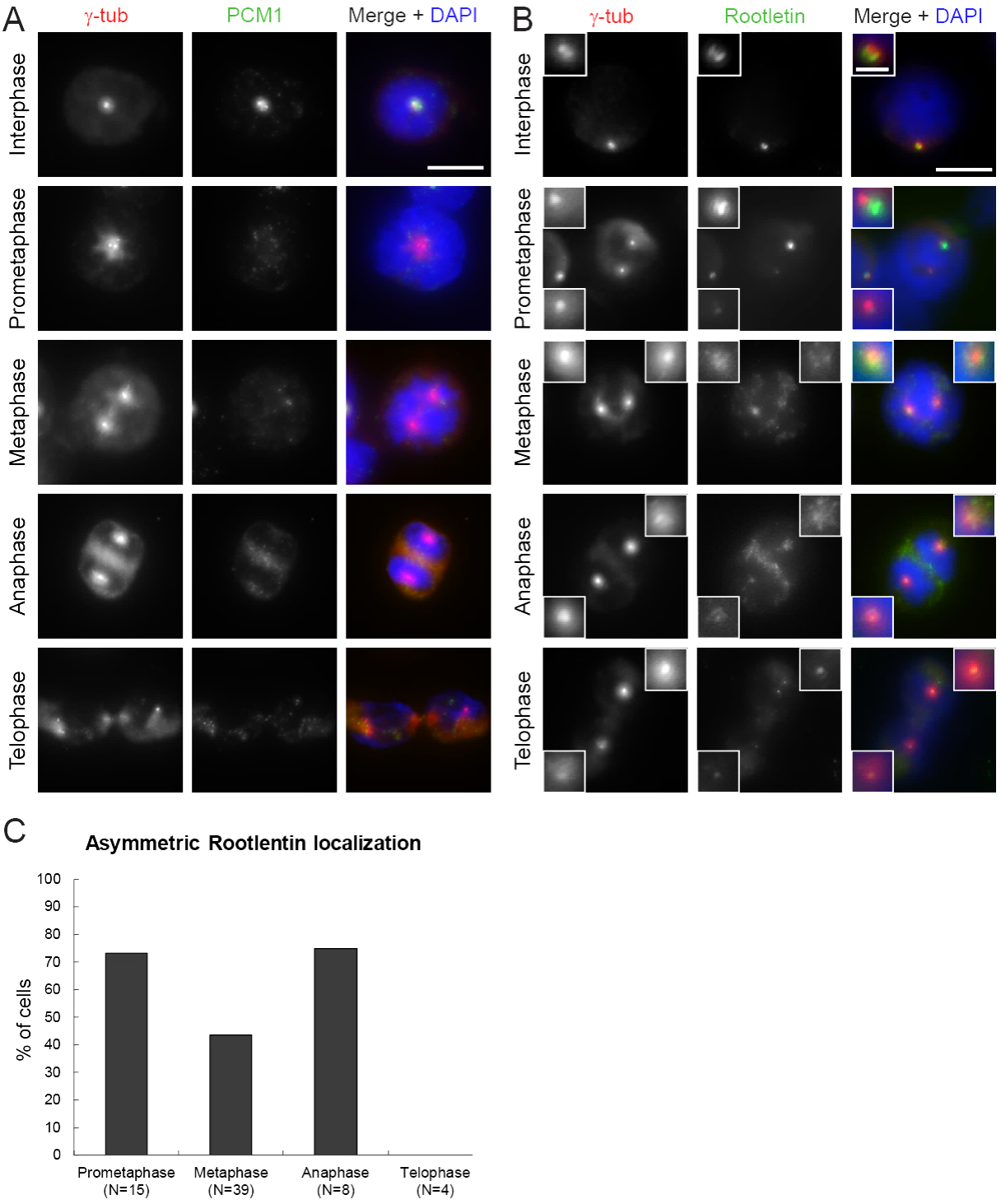

Figure 22. Subcellular localization of PCM1 and Rootletin at different cell cycle phases in KG1a cells. Immunofluorescence images of KG1a cells stained with specific antibodies against PCM1 (A) and Rootletin (B) in different cell cycle phases. The brightness/contrast of the rootletin channel was increased for mitotic cells for observation of the asymmetric distribution of the remaining signal. γ-tubulin (red) and DAPI (blue) serve as markers for centrosomes and nuclei, respectively. Examples of prominent phenotypes are shown. Scale bars are 10 µm and 2 µm. (C) The graphs show the quantification of KG1a cells with asymmetric Rootletin. The data is from one experiment. Numbers below the bars represent the total number of cells analyzed for each condition.

PCM1 localized granule-like surrounding the centrosome in interphase KG1a cells and dispersed and lost centrosomal proximity in mitotic cells (Figure 22A). The same was

observed by others in RPE1 cells (Lopes et al., 2011). In KG1a cells, the linker protein rootletin localized on interphase centrosomes as published previously (Bahe et al., 2005) (Figure 22B). As the linker is dissolved during mitosis, this protein leaves the centrosome, which is in line with a previous report in U2OS cells (Bahe et al. 2005). Still, I was interested whether the remaining rootletin close to mitotic centrosomes has a bias for segregating to the older or younger centrosome. Therefore, I increased the brightness/contrast for the PCM1 channel and quantified visibly asymmetric rootletin. In a preliminary analysis, 50-70% of prometa, meta and anaphase cells showed asymmetrically distributed rootletin (Figure 22C).

Table 2 summarizes the common behavior of the centrosomal proteins analyzed in this section. I focused my further analysis on the behavior of the appendage proteins. Based on my observations I defined two major questions I aim to answer: First, does centrosome age correlate with cell fate in human stem cells and second, how and why many of the other appendages are released from the mitotic centrosome? The next sections show my approaches to answer these questions, beginning with the first aim.

Table 2. Summary of the common localization in mitosis of centrosomal proteins analyzed in HSPCs, KG1a- and RPE1 cells

Behavior during mitosis	Proteins
Reduction/elimination from centrosome	Cep164, Cep123, FBF1 (in HSPCs/KG1a), LRRC45, Centriolin, Ninein, TTBK2, PCM1, Rootletin
Stays on centrosome: Mostly symmetric	SCLT1, Cep83, CP110, Cep97, Centrobin
Stays on centrosome: Asymmetric	ODF2, FBF1 (in RPE1)
Midzone during telophase	Arl13B, TTBK2

3.2 Correlation of centrosome asymmetry and ACD in HSPCs

3.2.1 The search for intracellular markers with differential distribution during mitosis in HSPCs

I identified ODF2 as the best marker for centrosome asymmetry among all here analyzed appendages. It stays at the older centrosome during mitosis and has a slow maturation on the new centrosome. Therefore, it displays the most obvious asymmetry throughout mitosis in the studied cell types.

The next prerequisite to investigate the role of centrosome asymmetry in ACD of HSPCs was the identification of a marker for this mode of division. A hallmark of ACD

is the differential distribution of cellular constituents like proteins or messenger RNA (mRNA) into the two arising daughter cells (Introduction, 1.5.).

I thus first searched in the literature for markers that segregate asymmetrically in HSPCs and then tested if I could reproduce the published asymmetric segregation.

One possible candidate is the endocytic protein and cell fate determinant Numb. The Notch pathway supports the maintenance of primitive hematopoietic cell fates (Suzuki and Chiba, 2005). The protein Numb directly binds to the intracellular domain of membrane-bound Notch. It is postulated that Numb acts as a negative regulator by mediating Notch degradation via binding to AP-2, which targets proteins for clathrin-mediated endocytosis (Berdnik et al., 2002; Hutterer and Knoblich, 2005). In muscle stem cells (Shinin et al., 2006) and T lymphocytes (Chang et al., 2007), Numb segregates asymmetrically during mitosis. Importantly, in mouse hematopoietic progenitor cells this behavior was also observed in 44% of the cells (Wu et al., 2007). By tracking dividing HPCs and their individual daughters via time-lapse imaging, the authors observed divisions after which only one daughter maintained activated Notch signaling, while decreased signaling indicated differentiation of the other daughter.

The group of Bernd Giebel found another connection between the endosomal system and ACD in human HPSCs (Beckmann et al., 2007). The tetraspanins CD53 and CD63 and the transferrin receptor CD71, which are associated with endosomal traffic, were enriched in vesicular structures. Those segregated differentially in ~20% of dividing cells in stroma-free conditions. This rate fits very well to the rate of ACD defined in the analysis of division kinetics of primitive hematopoietic cells *in vitro* (Huang et al., 1999). Further, CD133 was identified as a surrogate stem-cell marker (Beckmann et al., 2007) and is one of the genes with the greatest overexpression in the primitive slow dividing fraction of hematopoietic stem cells (HSCs) (Wagner et al., 2004). Thus, this marker can also give a hint if the older/younger centrosome stays in the more primitive cell. Görgens et al. (2014) found asymmetric segregation of CD133 in 28% of human HSPCs. In addition to those published marker for ACD in HSCs, I analyzed if ß-catenin is asymmetrically distributed in HSCs because Wnt signaling is involved in self-renewal and expansion of stem cells (Perry et al., 2011). Further, in mouse embryonic stem cells, localized Wnt signaling was shown to control the mitotic spindle orientation and therefore ACD (Habib et al., 2013).

Next, I analyzed these proteins in HSPCs to identify a suitable marker for ACD. Figure 23 and Table 3 summarize my analysis for the potential ACD marker in HSPCs and

KG1a cells. I focused the analysis on anaphase and telophase cells, as only then the polarity of the future daughter and mother cell is defined.

Table 3. Asymmetric distribution of reported markers for ACD in HSPCs and KG1a cells. The distribution was regarded as asymmetric with a fluorescence intensity ratio of the two protein poles higher than 1.5. The data is from one experiment for each staining.

Protein	% asymmetric HSPC	% asymmetric KG1a
Numb	< 5% (N=46)	< 5% (N=39)
Notch	< 5% (N=35)	< 5% (N=28)
CD53	Not analyzed	15% (N=26)
CD63	17 % (N=35)	50 % (N=38)
ß-Catenin	Not analyzed	< 5% (N=17)
CD133	31 % (N=100)	Not expressed

In contrast to the observed asymmetry in murine HSCs, asymmetric Numb or Notch distribution was not found in mitotic HSPCs (Figure 23A).

Although 15% of KG1a cells showed an intensity ratio of the two poles >1.5, CD53 displayed a similar symmetric distribution as Numb during division and was therefore not promising enough for analysis in HSPCs (Figure 23B). In contrast, asymmetric distribution of CD63 was observed in 50% of KG1a cells (Table 3, Figure 23C). Thus, asymmetric segregation of late endosomes, which are marked by CD63, was higher in KG1a cells than reported for HSPCs (Beckmann et al. 2007). I observed a lower frequency of asymmetric CD63 segregation in 17% of HSPCs. This is in line with published results (Beckmann et al., 2007) (Table 3, Figure 23C). ß-catenin always localized on the cell surface in KG1a cells and was never asymmetric in mitosis (Figure 23D). Consequently, I did not perform an analysis in HSPCs. Additionally, cell division control protein 42 (CDC42) was analyzed because of reported asymmetry in HSCs (Florian et al., 2012; Florian et al., 2018). In my analysis, no dividing cell displayed asymmetry of this protein (data not shown).

Lastly, I could reproduce the asymmetric segregation of the surrogate stem cell marker CD133 in HSPCs found by Görgens et al. (2014). In collaboration with the group of Bernd Giebel (University Clinic Essen), I used the CD133 surface antibody HC7 in indirect immune-fluorescence (Figure 23E) and live cell imaging (data not shown). I could observe an asymmetric distribution in 30% of HSPCs (Table 3), which is in line with the analysis of Görgens et al. (2014).

In summary, in this analysis, the only clearly asymmetrically distributing markers are CD63 and CD133. Those can be further used to correlate centrosome asymmetry with unequal cell division.

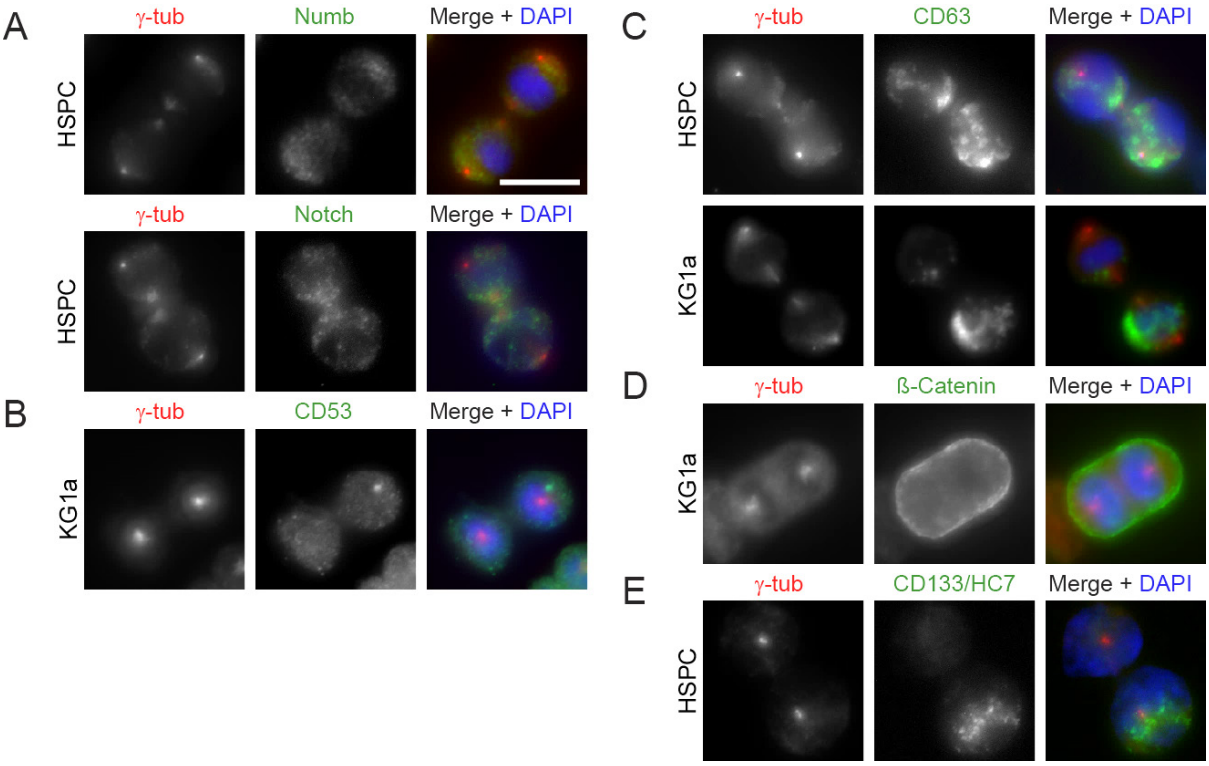

Figure 23. Subcellular localization of Numb, Notch, Cd53, CD63, and CD133 in dividing KG1a cells. Cells were fixed and co-stained with γ –tubulin and Numb/Notch (A), CD53 (B), CD63 (C), ß-Catenin (D) and CD133 (E) in the indicated cell types. γ-tubulin (red) and DAPI (blue) serve as markers for centrosomes and nuclei, respectively. Scale bar is 10 µm.

3.2.2 Analysis of centrosome asymmetry with respect to asymmetrically distributing marker in hematopoietic cells

Previous work in stem cell models found a correlation between stemness and inheritance of the older or younger centrosome in polarized stem cells (Introduction part 1.5.). I hypothesized that centrosome age and daughter cell fate likewise have a connection in non-polarized stem cells, like HSPCs. Two prerequisites to analyze the role centrosomes in asymmetric divisions of HSPCs were met: ODF2 as a marker for centrosome asymmetry during mitosis and CD133 and CD63 as differentially segregating components. For simplicity, I started with a co-staining of ODF2 and CD63 in KG1a. In KG1a cells with asymmetric CD63 segregation, 28% of the cells showed a co-segregation of CD63 to the ODF2 positive pole (mother centrosome). In contrast, in a preliminary analysis in HSPCs (N=35), 69% of CD63 segregated to the ODF2 positive pole. Therefore, and because I reproduced the asymmetric segregation of the

more promising surrogate stem cell marker CD133 in HSPCs (Görgens et al., 2014), I did not continue further investigations with CD63 in HSPCs.

The CD34+ population comprises different progenitors, including multipotent progenitors (MPPs). Those MPPs divide asymmetrically into lympho-myeloid (LMs) and erythro-myeloid progenitors (EMs). The daughter cell differentiating into the LM lineage inherits CD133 during this division, while EM progenitors are depleted of CD133 (Figure 24A, Görgens et al., 2014). In a first analysis using immunofluorescence microscopy, a distribution of 60% co-segregation with the younger and 40% co-segregation with the older centrosome was obtained (data not shown).

As only 30% of dividing CD34+ sorted cells showed an asymmetric distribution of CD133 and the frequency of mitosis is low in these cells, I conclude that a more sophisticated method is needed to capture a large number of cells. In contrast to normal immunofluorescence of fixed cells, imaging flow cytometry allows a high throughput analysis. It combines the sample size of cytometry with the resolution of microscopy on a single cell level. Thus, I started to use imaging flow cytometry in cooperation with the group of Bernd Giebel. Here, I was able to correlate centrosome asymmetry, marked by ODF2, with the stem cell marker CD133 and differentiation markers in up to 12 channels for each cell in a population (Figure 24B and C). Cord blood CD34+ cells were cultured for 2 days to monitor initial divisions shown in Figure 24A.

An analysis strategy was established including the identification of telophase cells, recognizing ODF2 intensity on the centrosome and correlating it with the intensity of CD133 in each daughter cell compartment.

While the additional staining for differentiation marker (CD34, CD45RA) is still under optimization, preliminary data suggests that the more stem cell-like cell (CD133+) has a higher tendency to inherit the older centrosome (39 vs 61 %) (Figure 24D).

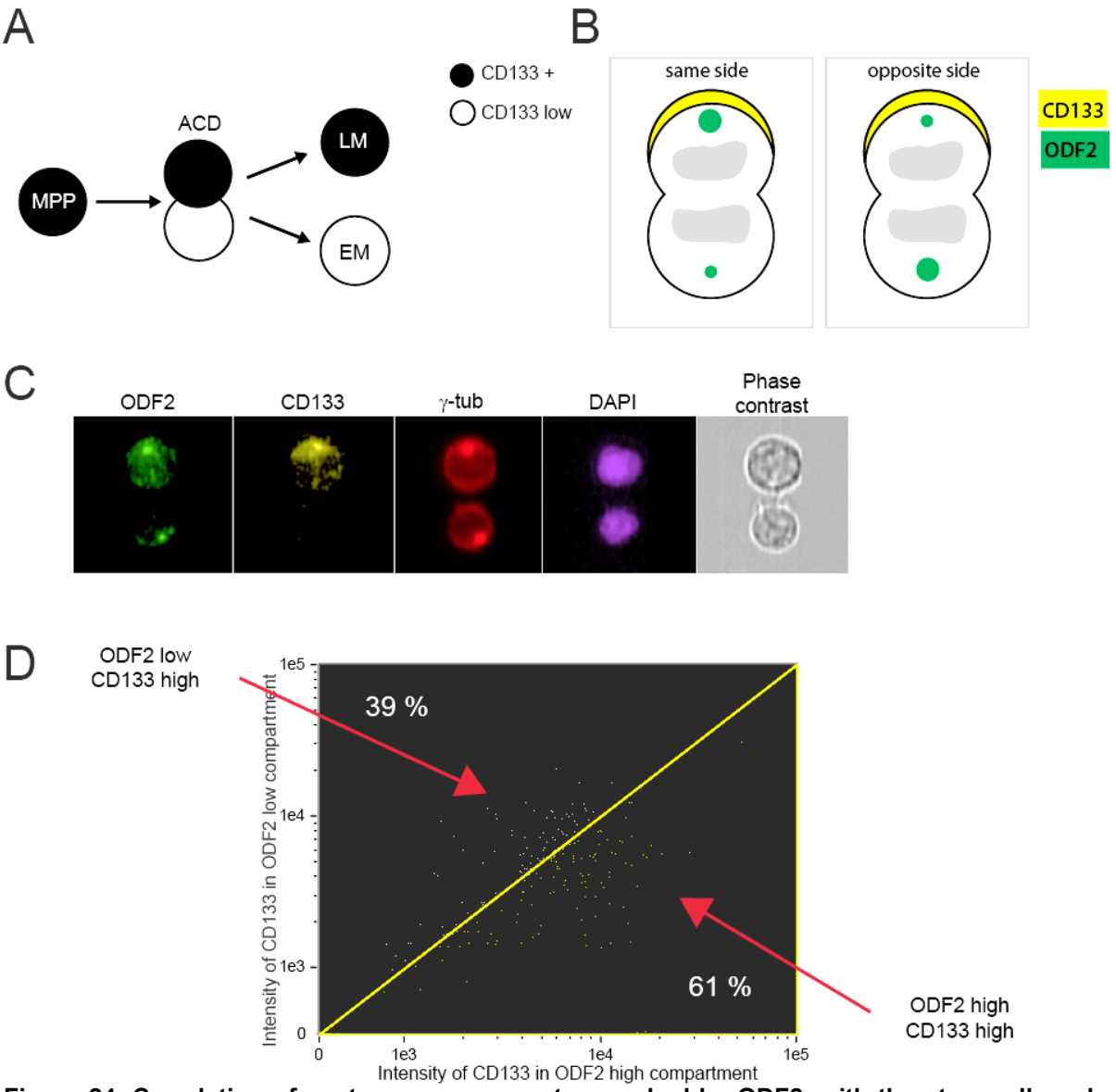

Figure 24. Correlation of centrosome asymmetry, marked by ODF2, with the stem cell marker CD133 using imaging flow cytometry. (A) Multipotent progenitors (MPPs) divide asymmetrically into CD133 positive lympho-myeloid (LM) and CD133 negative erythro-myeloid (EM) progenitors. (B) Scheme showing the rationale: We aim to identify if the more primitive cell (CD133 positive) inherits the older (stronger ODF2 signal) or younger centrosome (weak ODF2 signal). Condensed nuclei are depicted in grey (C-D) CD34+ cells were analyzed after 2 days to monitor initial divisions. Cells were fixed, and proteins were labeled with specific antibodies before processing by imaging flow cytometry. An analysis strategy was established including identification of dividing cells, identifying ODF2 intensity on the centrosome and correlating it with the intensity of CD133 in each daughter cell compartment. We developed an analysis function using the Amnis software, in which daughter cells can be separated into those which have a higher intensity of CD133 in the ODF2 low or high compartment. N=263 telophase cells. Data is representative of one from three experiments.

Additionally, I analyzed within the cooperation with the group of Bernd Giebel if knockdown of ODF2 causes changes in differentiation and renewal of HSPCs. In case centrosome asymmetry affects ACD, knockdown of ODF2 should affect the HSPCs differentiation. Therefore, CD34+ cells were sorted for MPPs and transduced with ODF2 shRNA and the control plasmid (GFP). The cells were cultivated in HSPC media

and analyzed regarding their differentiation into LM, EM, MP, and late progenitors (LP) using flow cytometry on day 3, 7 and 12 post-transduction (1 day after isolation).

At day 12 of cultivation, the CD34+ cells expressing ODF2 shRNA had higher frequencies of LPs and lower frequencies of EMs in comparison to the control (Figure 25A). In 6 experimental repetitions, these differences were not significant.

The amount of sorted MPPs was too small to allow quantification of knockdown efficiency. Therefore, the efficiency of the shRNA construct was verified in KG1a cells (Figure 25B), where a knockdown efficiency of ~60% was achieved. Thus, either ODF2 has no effect on HSPC differentiation or an effect could not be seen because of the incomplete knockdown.

In conclusion, these data suggest that ODF2 may not be a main player involved in asymmetric segregation of CD133 and ACDs in the hematopoietic system.

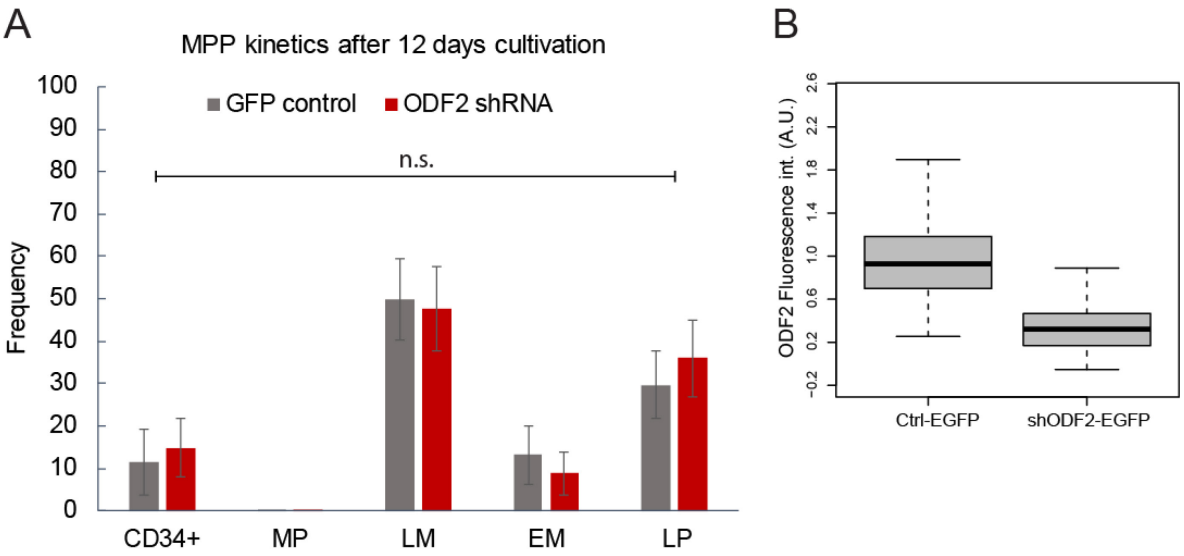

Figure 25. Differentiation potential of HSPCs is not affected by ODF2 knockdown. (A) Frequency [%] of HSPC populations after 12 days of cultivation. CD34+ cells were sorted for multipotent progenitors (MPs) and transduced with ODF2 shRNA and the control plasmid (GFP). The cells were analyzed regarding their differentiation into lympho- (LP) and erythro- myeloid (EM) progenitors, and late progenitors (LP) using flow cytometry. Graphs show the average ± standard deviation of all performed repetitions. N=6 repetitions. (B) Verification of ODF2 knockdown using shRNA in KG1a cells. Fluorescence intensity measurement of ODF2 using indirect immunofluorescence in control (Ctrl-EGFP) transduced KG1a cells vs. cells transduced with EGFP-ODF2 shRNA after FACS sorting for GFP positive cells. Cumulative data from two independent experiments is shown. Normalization to the Ctrl treatment was performed. N=150 centrosomes were quantified per condition.

3.2.3 Analysis of the division mode of HSPCs vs. leukemic cell lines

It is still unclear why or how asymmetrically dividing cells developed mechanisms to retain either the mother or daughter centrosome. So far, I only analyzed if centrosome asymmetry serves as an intrinsic cue for asymmetric divisions. In this case, the different composition and properties of the older and younger centrosome would

actively influence polarity, e.g. by impacting on the asymmetric segregation of components as analyzed in the previous section. However, stem cells, also HSCs, are in niches that were shown to influence the mode of division (Hoggatt et al., 2016). Hence, another mechanism of how centrosomes influence polarized divisions could be, for example, the differential ability of the two centrosomes to nucleate astral microtubules. These can interact with cortical cues, which might be connected to adhesion factors on the surface of niche cells (Morin and Bellaiche, 2011). In this case, centrosome asymmetry would primarily be used to ensure proper coordination of spindle orientation and the localization of fate determinants.

So far it is not possible to analyze human HSPC division with respect to their niche *in vivo*. Therefore, it is necessary to develop reliable *in vitro* assays to study oriented cell division in a controlled way. For this purpose, I collaborated with the laboratory of Motomu Tanaka (University Heidelberg), an expert in biointerphase models, such as supported membranes (Tanaka and Sackmann, 2005). Here, we developed an *in vitro* assay, using chamber slides, which were coated with biomembranes supplemented with the surface glycoprotein ICAM-1. Niche cells express ICAM-1, which binds to the integrin alpha-L (LFA-1A) expressed by HSPCs (Gunji et al., 1992). We performed live cell imaging using ICAM-1 coated chambers and quantified dividing cells with respect to their orientation towards the surface.

Here, we identified three modes of division by analyzing HSPCs on ICAM-1 coated surfaces (Figure 26). I considered divisions as symmetric if both daughter cells had a horizontal orientation to the surface during the whole division process (Figure 26A, Figure 27A). The mode of division was considered as polarized if the division started with one daughter cell vertical to the surface (Figure 26B, Figure 27B) or if one daughter cell detached later during the division process (horizontal to vertical divisions, Figure 26C, Figure 27C).

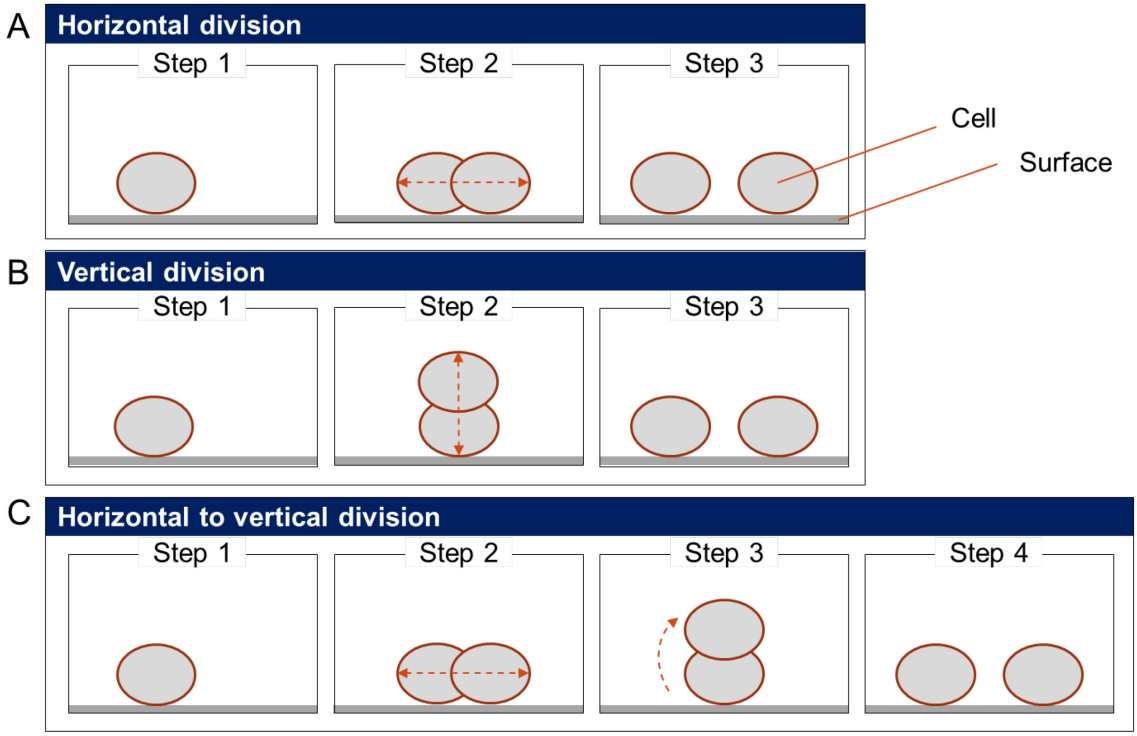

Figure 26. Three modes of cell division on ICAM-1 coated slides were identified for HSPCs. The scheme shows the three types of HSPC division observed on ICAM-1 coated slides.

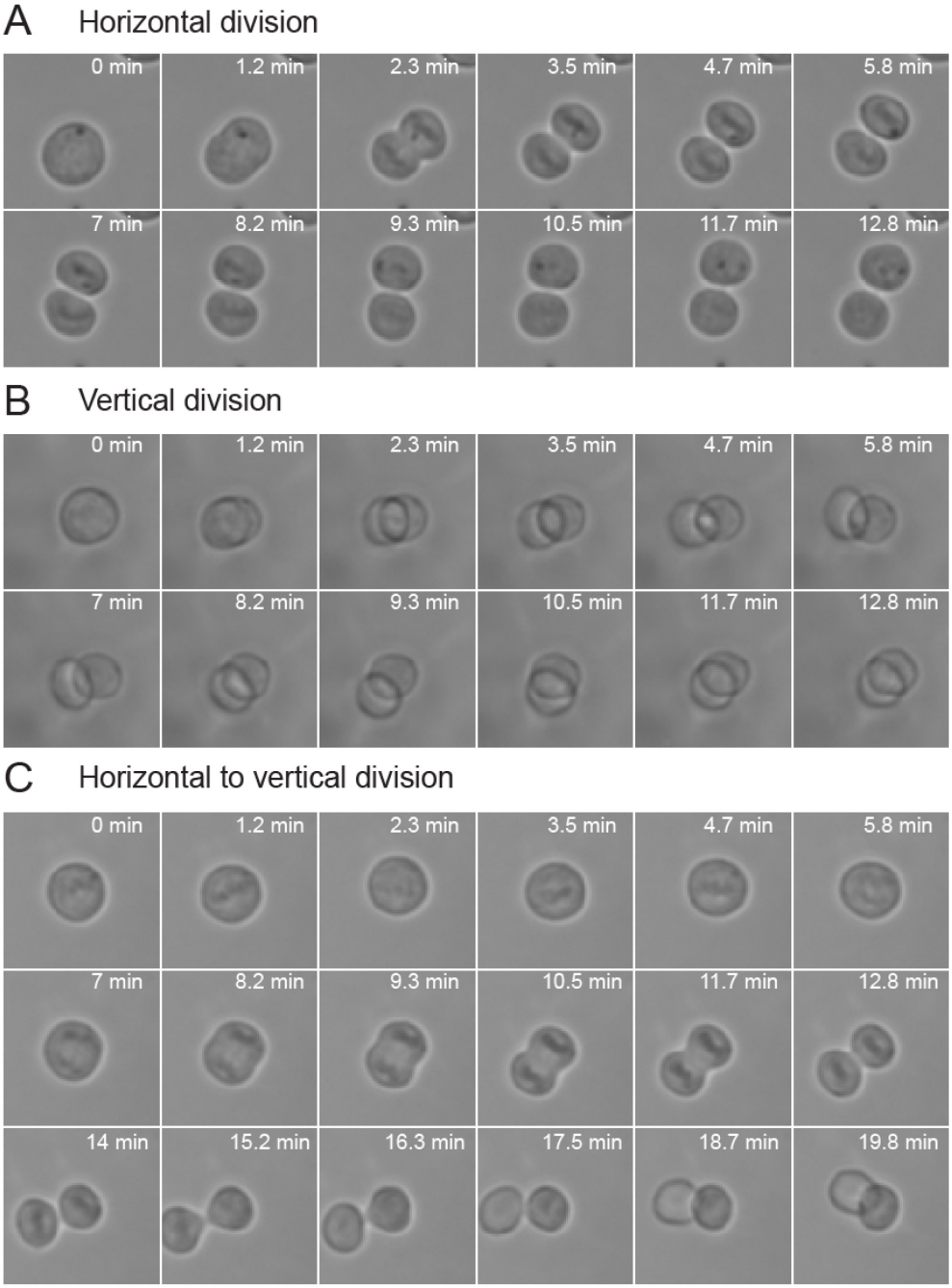

Figure 27. Examples of dividing HSPCs for the three modes of cell division on ICAM-1 coated slides. Cells were seeded in ICAM-1 coated channels and live cell imaging using a Kayence microscope was performed for 12-14 h. Pictures were taken all 70 s. (A) Example of an HSPC dividing horizontally. (B) Example of an HSPC dividing vertically. (C) Example of an HSPC dividing first horizontally with the concomitant detachment of one daughter cell leading to a vertical type of division.

In HSPCs, 23% of the cells had polarized (vertical) types of division. 16% of the cells divided directly vertical and 7% horizontal to vertical (Figure 28).

The leukemic cell lines KG1a and K562 were compared to HSPCs from healthy donors. Despite their leukemic origin, KG1a cells are still CD34+ and display many undifferentiated features (Civin et al., 1984). We wanted to test, whether KG1a cells can be used as a model to study the regulation of ACD because of their greater

availability than primary cells. As KG1a and K562 cells are derived from leukemia patients, the study of the division mode on ICAM-1 coated slides can additionally support the analysis if the amount of symmetric vs asymmetric divisions changed in leukemic cell lines. KG1a cells never divided vertically on ICAM-1 coated chamber slides (Figure 28). Conversely, vertical divisions were overserved in 17% of the AML cell line K562. Of those, 9% were directly vertical and 8% of the horizontal to vertical type (Figure 28). In summary, this method seems as a promising tool to mimic the stem cell niche in directing asymmetric divisions *in vitro*. In the future, this tool could be used to study oriented divisions by combining the analysis of division axis with differential protein segregation in healthy versus leukemic donor HSPCs to analyze the process and its potential deregulation in cancer mechanistically.

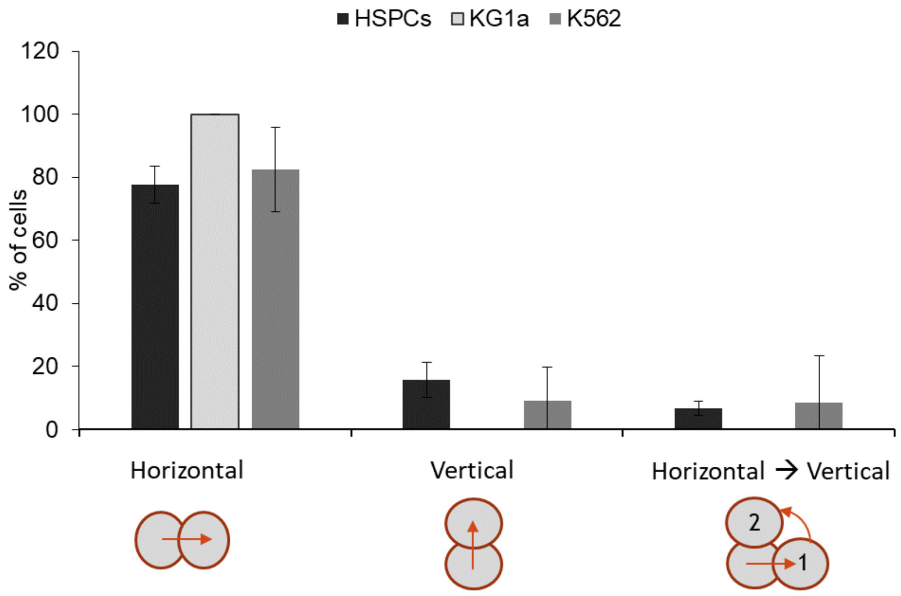

Figure 28. Division type in primary CD34+ cells vs. leukemic cell lines. Quantification of the division axis in HSPCs, KG1a, and K562 cells. Live cell imaging was performed for 12-13.6 hours, all 70 s, on the Kayence microscope. Graphs show the average ± standard deviation of all performed repetitions. The five repetitions for HSPCs were from different CD 34+ resources (three times cord blood, two times peripheral blood), N=564. For KG1a, four independent experiments were performed, N=292. Four independent experiments were performed with K562 cells, N=85.

3.3 The Nek2 kinase: A novel function in the regulation of centrosome appendages

The second aim, which arose upon the analysis of the mitotic behavior of appendage proteins, was to understand the molecular mechanisms involved in the regulation of appendages during mitosis. Consequently, I started to elucidate how specific appendages lose their centrosomal localization upon the G2/M transition. Many kinases peak in their expression and/or activity during the G2/M transition (Fry et al., 1995; Gheghiani et al., 2017; Golsteyn et al., 1995; Marumoto et al., 2002; Schmidt et

al., 2017; Wright et al., 1999). Hence, I asked whether a kinase could be involved. The Nek2 kinase was a bona fide candidate. Its activity peaks at the G2/M transition and concomitant with appendage release, Nek2 accumulates in cells and at centrosomes prior to mitosis (Figure 29A). As a subset of appendages begins to disappear from the centrosome during this time, I speculated that Nek2 could be responsible for this process.

3.3.1 The kinase Nek2 colocalizes with appendages

Previous studies did not define the overlap of Nek2 with appendages, as conventional fluorescence microscopy was used (Spalluto et al., 2012, Kim et al. 2015). To better define the localization-overlap of Nek2 with distal and subdistal appendages, I performed 3D-structural illumination microscopy (3D-SIM) with RPE1 cells co-stained with Nek2 and either Cep164 or ODF2 (Figure 29B-D). I found that in addition to its proximal localization, Nek2 fully colocalized with the distal appendage protein Cep164. There, Nek2 decorated a part of the ring formed by the appendage in 49% of analyzed cells (Figure 29B). Additionally, I found a partial colocalization with the distal part of the subdistal appendage protein ODF2 in 60% of cells (Figure 28B). The Nek2 signal was specific as it was absent in Nek2 knockout (KO) cells (Figure 29C).

The intensity of Nek2 was much stronger on the proximal pool, compared to the distal pool (Figure 28B). Therefore, I analyzed Nek2 localization in C-Nap1 KO cells lacking the proximal Nek2 pool (Hardy et al., 2014; Panic et al., 2015; Spalluto et al., 2012). Here, the colocalization of Nek2 with either Cep164 or ODF2 in interphase cells persisted (Figure 29D). This indicates that Nek2 binds to the distal ends of the mother centriole independently of the proximal pool. On top views, Nek2 appeared as dots or incomplete rings (Figure 29D). This may indicate that Nek2 associates with appendages in a transient manner.

In summary, Nek2 fully colocalizes with a part of the ring formed by the distal appendage Cep164 and partly with the subdistal appendage ODF2 (Figure 29E). Its colocalization with appendages suggests that Nek2 is a potential kinase that regulates appendages.

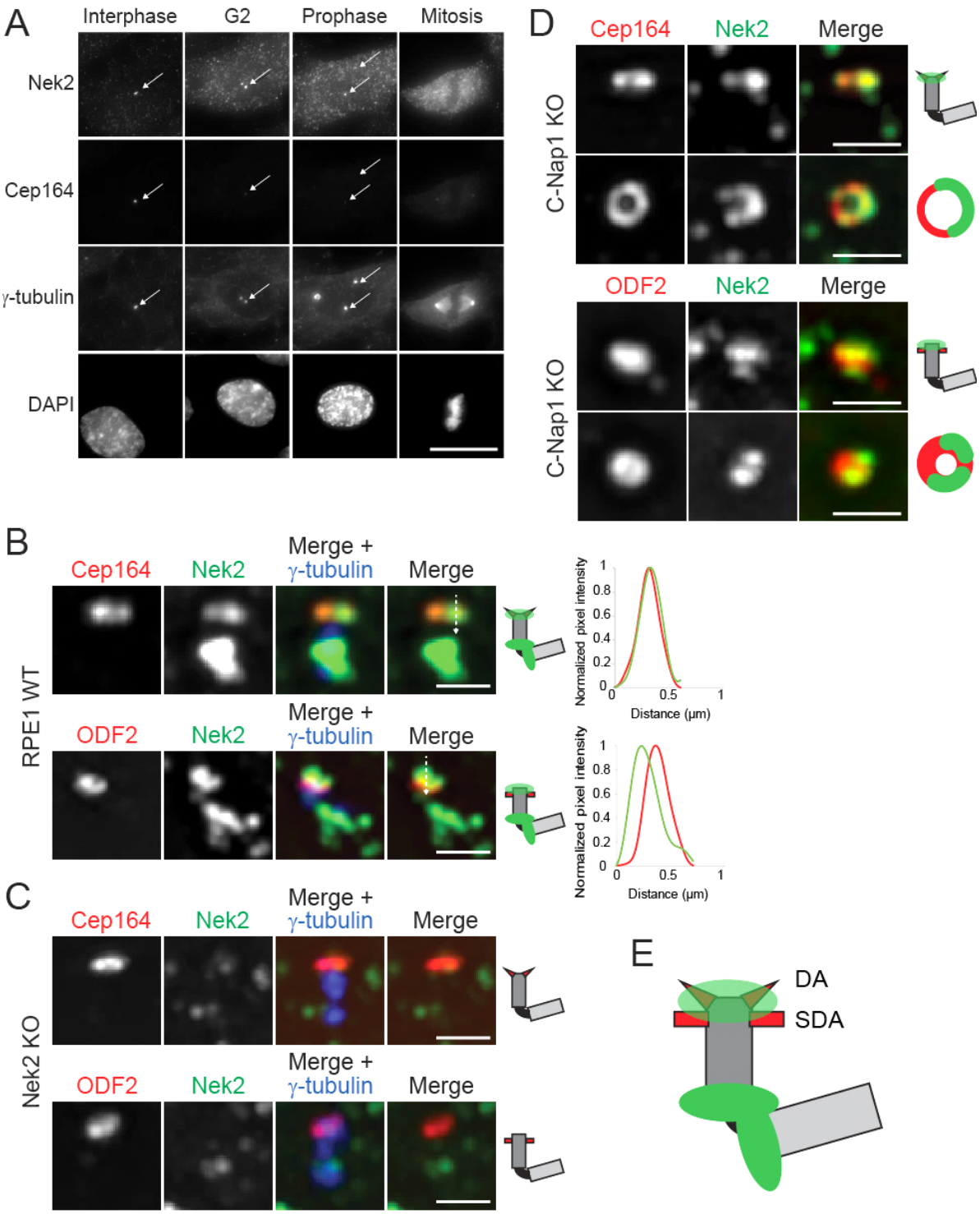

Figure 29. Colocalization of the kinase Nek2 with appendages. (A) Representative immunofluorescence images show localization of the distal appendage protein Cep164 and Nek2 in interphase, G2, prophase and mitosis. Nek2 intensity is highest in G2/prophase, the time when specific distal appendages (here Cep164) start disappearing from the centrosome. Arrows indicate the centrosomes. γ-tubulin and DAPI serve as markers for centrosomes and nuclei, respectively. Scale bar is 20 μm. (B) Representative images of Cep164 and ODF2 co-stainings with Nek2 using 3D SIM microscopy in RPE1 wild type (WT) cells. Line graphs show the plot profile of Cep164 and ODF2 (red) and Nek2 (green). Sketches represent the intensity of indicated proteins plotted according to the line shown in the merge picture. (C) Representative images of Cep164 and ODF2 co-stainings with Nek2 using 3D SIM microscopy in RPE1 Nek2 KO cells. (D) Representative images of Cep164 and ODF2 co-stainings with Nek2 using 3D SIM microscopy in RPE1 C-Nap1 KO cells. Scale bar is 1 μm. (E) Schematic representation of the distal appendage (DA) Cep164 and subdistal appendage (SDA) ODF2 in relation to Nek2.

3.3.2 Nek2 is required for removal of Cep164, Cep123, and LRRC45 prior to mitosis

I hypothesized that if Nek2 is responsible for the mitotic removal of appendages from the centrosome, this process should be reversed upon loss of the kinase. To test this idea, I monitored fluorescence levels of the appendages throughout the cell cycle in an RPE1 Nek2 KO cell line. KO of Nek2 was verified using an antibody against endogenous Nek2 (Figure 30).

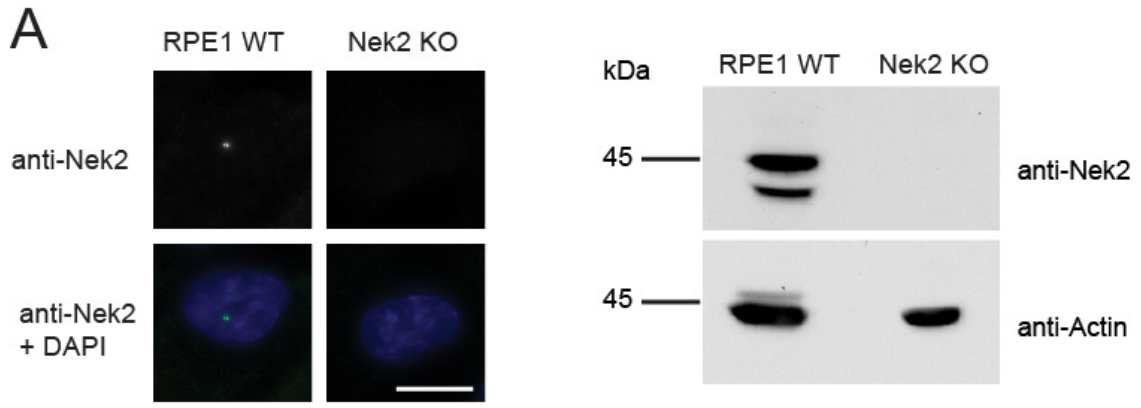

Figure 30. Verification of the Nek2 KO line. Representative images showing fixed RPE1 WT and RPE1 Nek2 KO cells and western-blot using the same cell lines. A specific antibody against Nek2 was used to visualize the loss of Nek2 in the KO cell line. γ-tubulin was used as a centrosome reference and DAPI stained the DNA. Actin was used as a loading control. Scale bar is 20 µm.

In interphase cells, Cep123 levels were slightly higher in Nek2 KO, while there was no intensity difference for the other appendages (Figure 31A). Notably, those appendages, which declined in RPE1 wild type (WT) cells during mitosis, remained at the mother centrosome in Nek2 KO cells, except for Ninein (Figure 31B). In the case of Ninein, only the G2- and prophase levels were higher in Nek2 KO cells compared to WT cells, while the mitotic release of Ninein still occurred in Nek2 KO cells.

The cell cycle-dependent behavior of Cep164 in RPE1 WT vs. Nek2 KO cells is shown as an example for the reversion of appendage release in Figure 31C. In Nek2 KO cells, Cep64 remained attaches to the ODF2 positive older centrosme (Figure 31C). The mitotic attachment of normally decreasing distal appendages on the mother centrosome in Nek2 KO cells could be rescued upon inducible expression of Nek2 in the Nek2 KO background (Figure 32).

Because Ninein was not affected and because I focused my later analysis on distal appendages and their role in ciliogenesis, rescue analysis for Ninein and Centriolin were not performed.

Together, my data indicates that Nek2 is required for the release of a subset of distal appendages prior to mitosis.

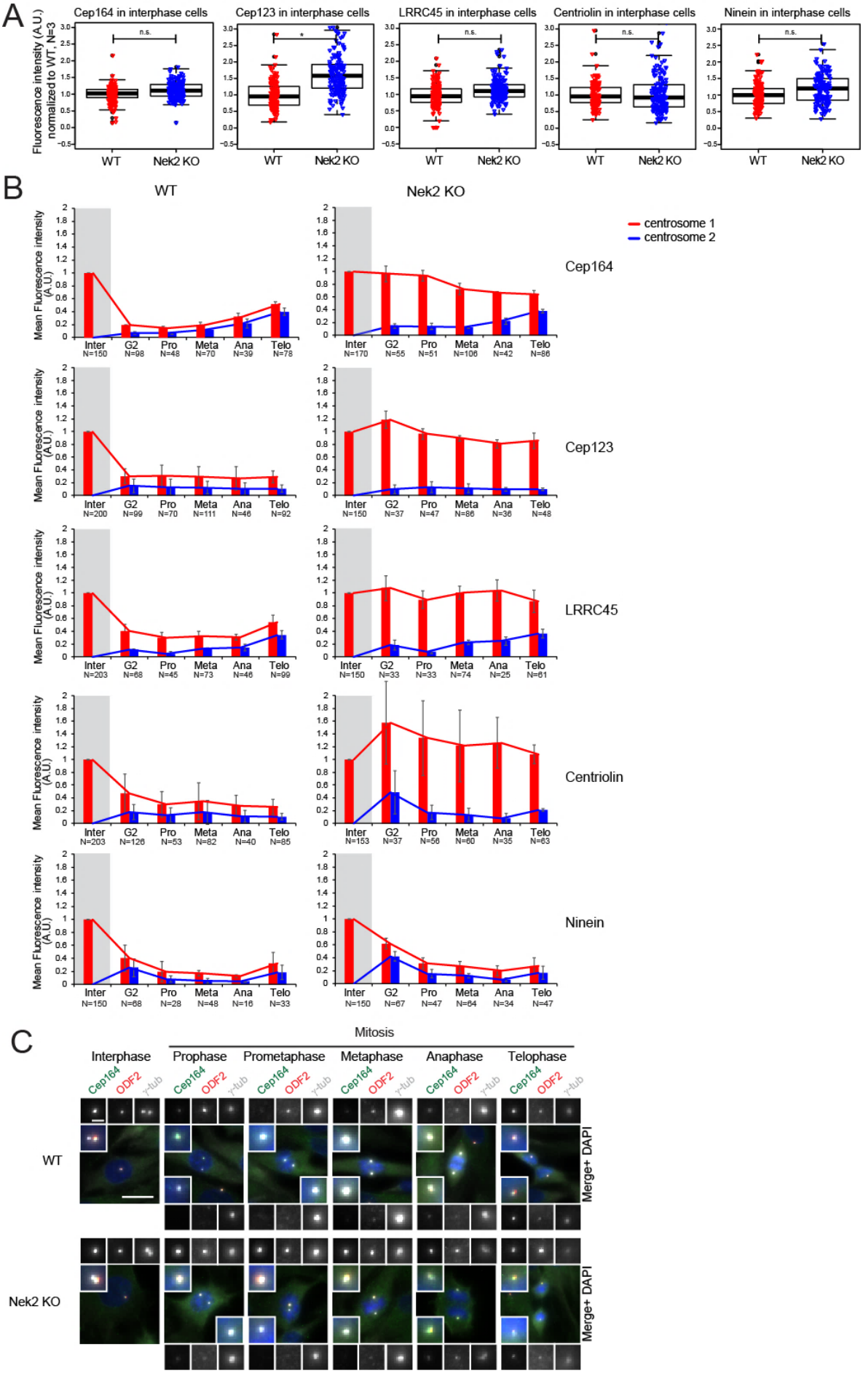
A
Cep164 in interphase cells
Cep123 in interphase cells
LRRC45 in interphase cells
Centriolin in interphase cells
Ninein in interphase cells
Fluorescence intensity (A.U.) normalized to WT, N=3
n.s.
*
WT
Nek2 KO
B
WT
Nek2 KO
centrosome 1
centrosome 2
Mean Fluorescence intensity (A.U.)
Cep164
Cep123
LRRC45
Centriolin
Ninein
Inter
G2
Pro
Meta
Ana
Telo
C
Mitosis
Interphase
Prophase
Prometaphase
Metaphase
Anaphase
Telophase
Cep164
ODF2
γ-tub
WT
Nek2 KO
Merge+ DAPI

Figure 31. Appendage-asymmetry is maintained in Nek2 KO cells. (A)The box/dot plots show Cep164, Cep123 and LRRC45 fluorescence intensity (arbitrary unit) measured at the interphase centrosome in RPE1 WT and Nek2 KO cells. The graph shows the normalized combination of three independent experiments. Statistical analyses of fluorescence intensity measurements were performed using two-tailed student's t-test; Number of centrosomes quantified was at least 50 per cell type per experimental repetition. (B) Quantification of the cell cycle-dependent behavior of appendages in RPE1 WT vs. Nek2 KO cell. Quantifications for RPE1 WT same as Figure 12A. The levels (pixel intensities) of the indicted appendage protein were measured at each centrosome (centrosome 1 and centrosome 2) during the indicated. Interphase is marked by a gray shading to highlight exit to mitosis. The average intensity of the interphase staining was set to one and the values for the second centrosome were set to zero in interphase because just one centrosome and appendage signal exists in this cell cycle phase. The different phases of the cell cycle were determined based on centrosome distance and DNA condensation. Graphs depict fluorescence intensity in arbitrary units (A.U.). Graphs show the average ± standard deviation of all three repetitions for each protein in each cell cycle phase. Numbers below in the bars represent the total number of cells analyzed for each condition. (C) Representative pictures show Cep164 and ODF2 co-stainings in RPE1 WT and Nek2 KO cells throughout the cell cycle. γ-tubulin was used as a centrosome reference and DAPI as a nuclear marker. Scale bars are 20 µm and 2 µm.

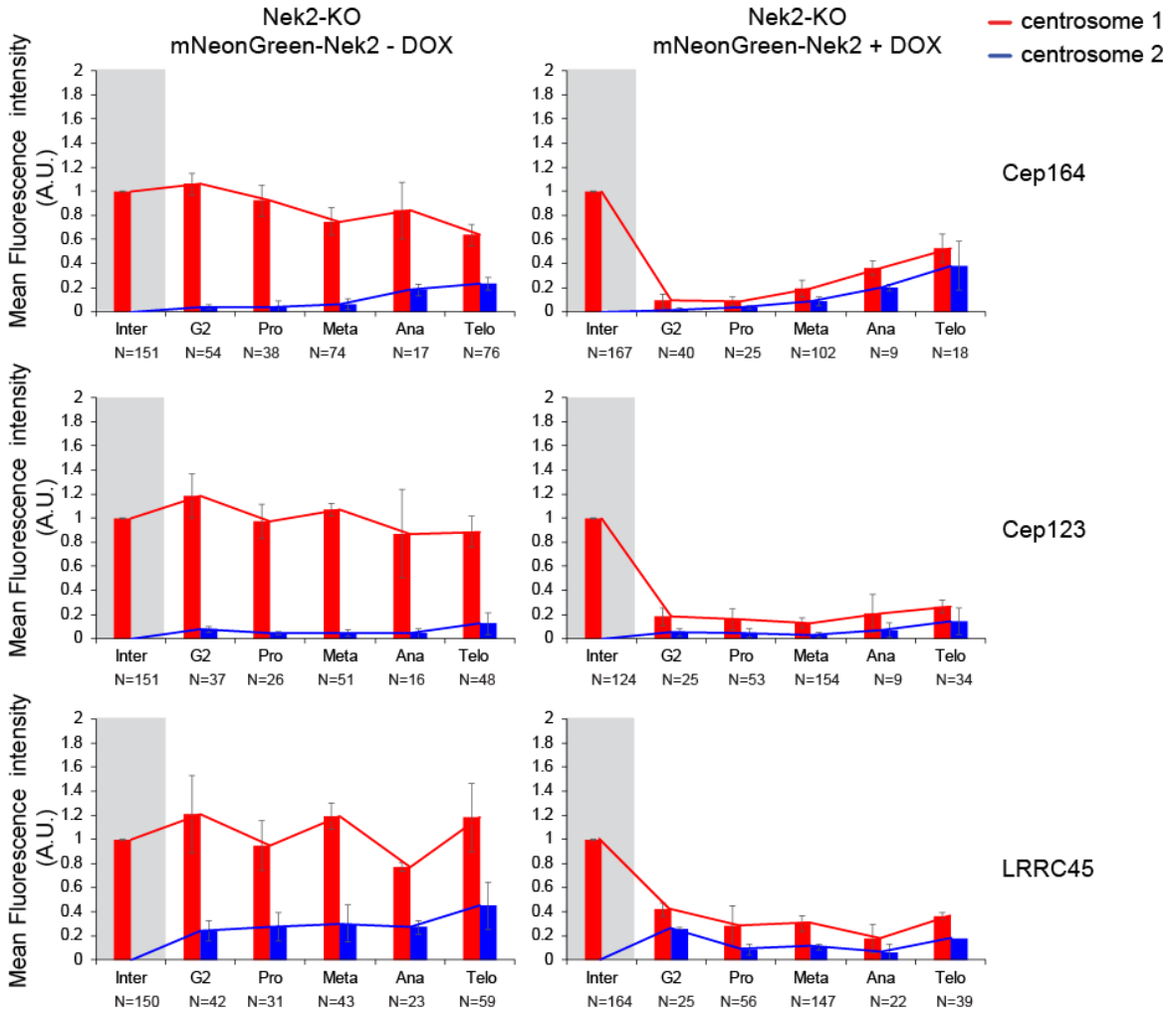

Figure 32. The mitotic attachment of appendages on the mother centrosome in Nek2 KO cells can be rescued. Quantification of the cell cycle-dependent behavior of Cep164, Cep123 and LRRC45 in the rescue cell line RPE1 Nek2 KO clone with doxycycline (DOX) inducible mNeonGreen-Nek2 expression with and without DOX induction. Quantifications were performed as described in Figure 31. The number of quantified cells per cell cycle phase is below the bar graph.

3.3.3 The distal pool of Nek2 releases appendages from interphase centrosomes independently of the proteasome

Previous work showed that mother centriole-specific Nlp is displaced from interphase centrosomes upon overexpression of active Nek2 or hyperactive PLK1 in human U2OS cells. Therefore, together with its temporarily colocalization with appendages and peak at G2/M transition (Hames and Fry, 2002), I asked whether ectopic overexpression of active Nek2 prematurely displaces distal appendages from the mother centriole. To address this question, I analyzed appendages in RPE1 cells stably expressing doxycycline-inducible WT Nek2 (Nek2-WT) or kinase-dead (KD) Nek2 (Nek2-KD) with a K37R substitution (Fry et al., 1995) fused to mNeonGreen (Figure 33 and 34). Doxycycline induction led to a mNeonGreen-Nek2 and -Nek2- KD overexpression in ~75% of cells in the stable cell line (Figure 33A, B), while no signal was visible in the GFP channel without doxycycline induction (Figure 33A). I only considered mNeonGreen-Nek2 positive cells for the quantifications as shown in Figure 33A. More than 60% of these cells had decreased appendage levels.

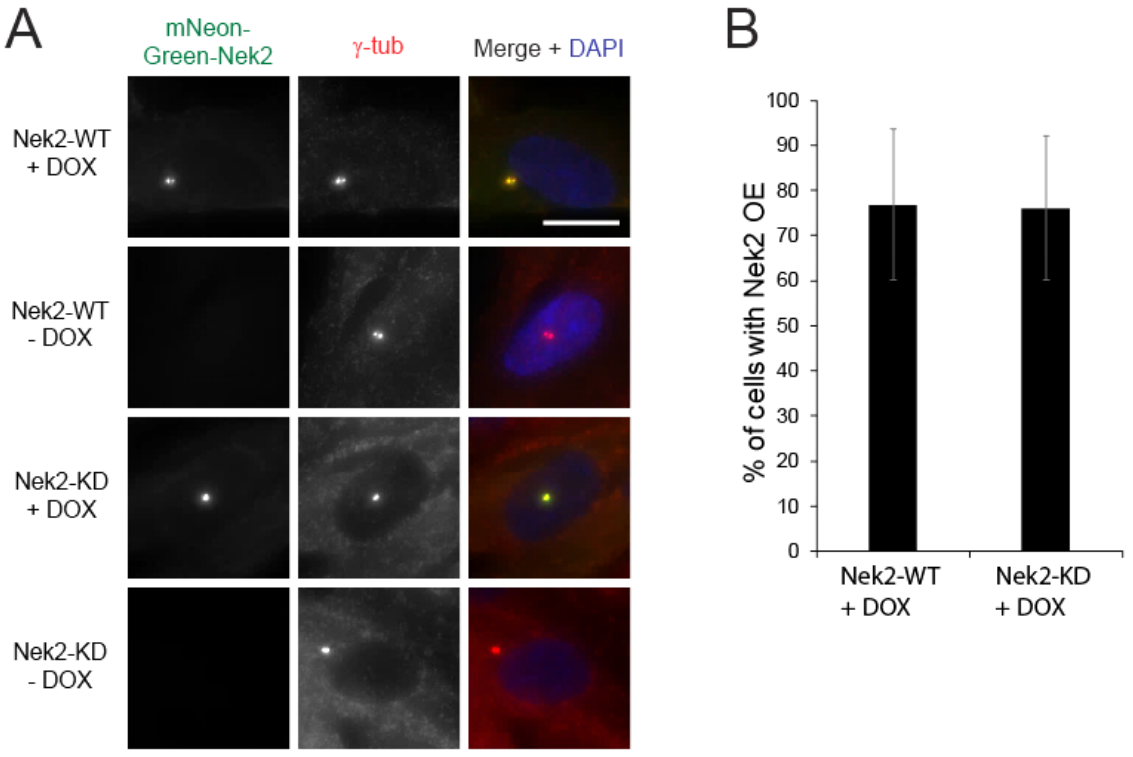

Figure 33. Nek2mNeonGreen overexpression in RPE1 cells. (A) Representative images showing Nek2-WT- and Nek2-KD-mNeonGreen overexpressing cell lines with and without doxycycline (DOX) induction. γ-tubulin was used as a centrosome reference. DAPI stained the DNA. Scale bar is 20 µm. (B) Quantification of Nek2-WT- and Nek2-KD-mNeonGreen overexpressing cells after 24 h of DOX induction. N=335 Nek2-WT and N=424 Nek2-KD cells were quantified in three independent repetitions. Results show the average ± standard derivation.

The overexpression of active but not inactive Nek2 led to a significant reduction of Cep164, Cep123, FBF1, LRRC45, Centriolin and Ninein from the mother centriole in interphase (Figure 34A). Those are the appendages, which usually decrease during mitosis. As expected, the appendages that stay on the centrosome in mitosis (ODF2, SCLT1, and Cep83) were not released from the centrosome in interphase upon Nek2 overexpression (Figure 34). FBF1 decreased only in hematopoietic, but not in RPE1 cells during mitosis, but still was reduced upon Nek2 overexpression in RPE1 cells (Figure 34). The reason for this bipartite behavior of FBF1 remains unclear. For LRRC45, I analyzed the protein levels in RPE1 C-Nap1 depleted cells. This allowed to exclusively detect the distal pool of LRRC45 (Hardy et al., 2014; Panic et al., 2015; Spalluto et al., 2012). Nek2 overexpression led to a reduction of LRRC45 interphase, while the overexpression of Nek2-KD had a dominant effect upon LRRC45 and led to a significant increase of intensity at the interphase centriole (Figure 34A).

Next, I asked, whether the release of the distal appendages is in general only dependent on the distal pool of Nek2. Like LRRC45, the levels of Cep164, Cep123, and FBF1 were still significantly reduced upon C-Nap1 depletion, indicating that the centrosomal release upon Nek2 overexpression is independent of its proximal pool (Figure 35).

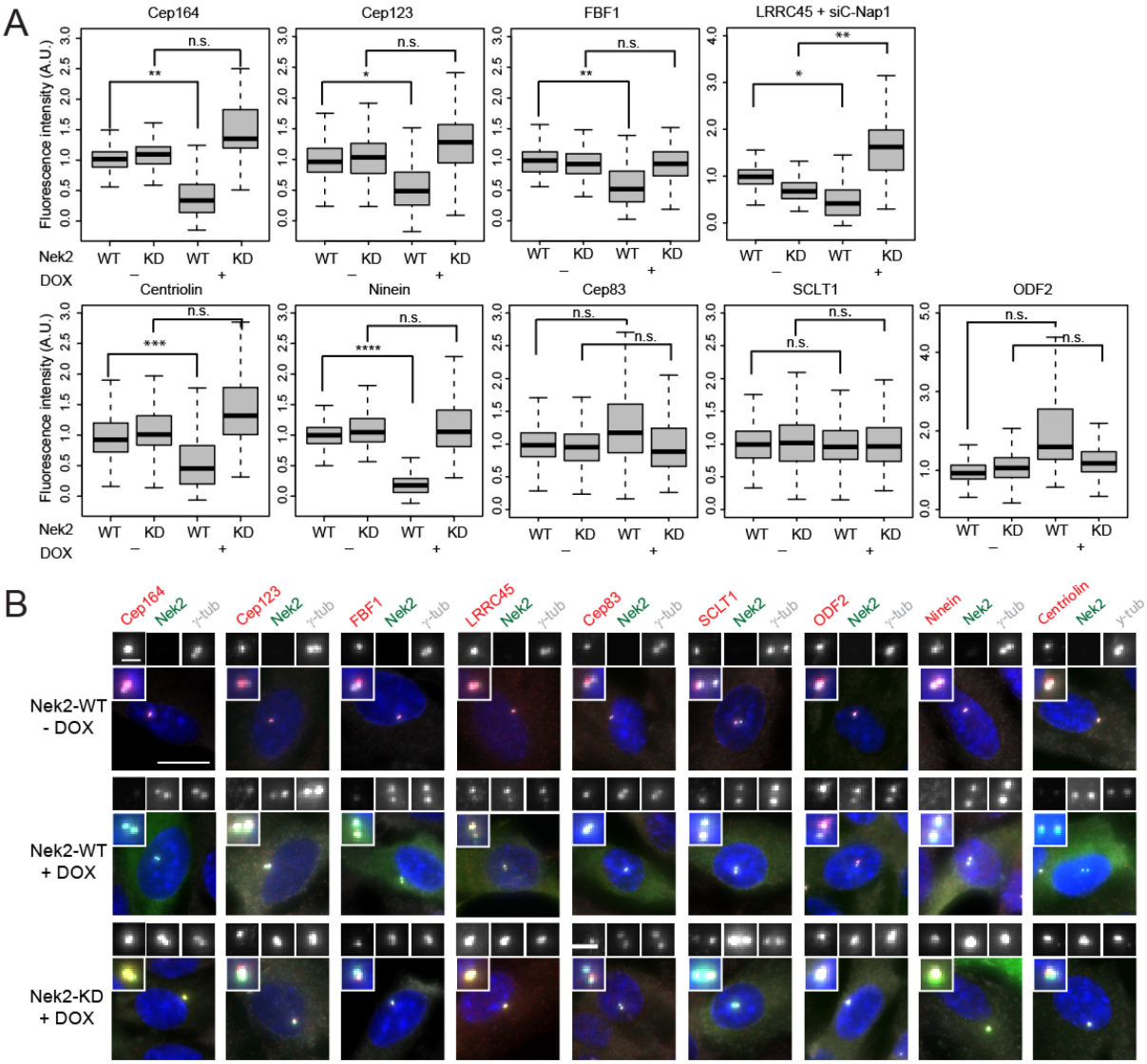

Figure 34. Appendages are released from interphase centrosomes after ectopic Nek2 overexpression. (A) Whisker-Box Plots representing the quantification of appendage signal at the centrosome after normalization to the average RPE1 WT signal. The plots show the normalized combination of three different experiments. At least 50 cells were analyzed per condition in each of three independent experiments. Doxycycline (DOX) inducible RPE-1 cell line was used for mNeonGreen-Nek2 (WT) and -Nek2-K37R (KD) overexpression. To analyze only the distal pool of LRRC45, I depleted C-Nap1 for the staining of this protein. Appendage intensities of Cep164, Cep123, and FBF1 were significantly decreased after Nek2-WT but not Nek2-KD overexpression. Student's t-test was performed for the average of the independent experiments. Significance levels: ns $P > 0.05$, *: $P \leq 0.05$, **: $P \leq 0.01$, ***:$P \leq 0.001$, ****: $P \leq 0.0001$. (B) Representative pictures show indirect immunofluorescence of the analyzed appendages in RPE1 WT conditions (-DOX) and upon Nek2 and Nek2-KD overexpression (+DOX) using the indicated antibodies. γ-tubulin was used as a centrosome reference and DAPI as a nuclear marker. Scale bars are 20 µm and 2 µm.

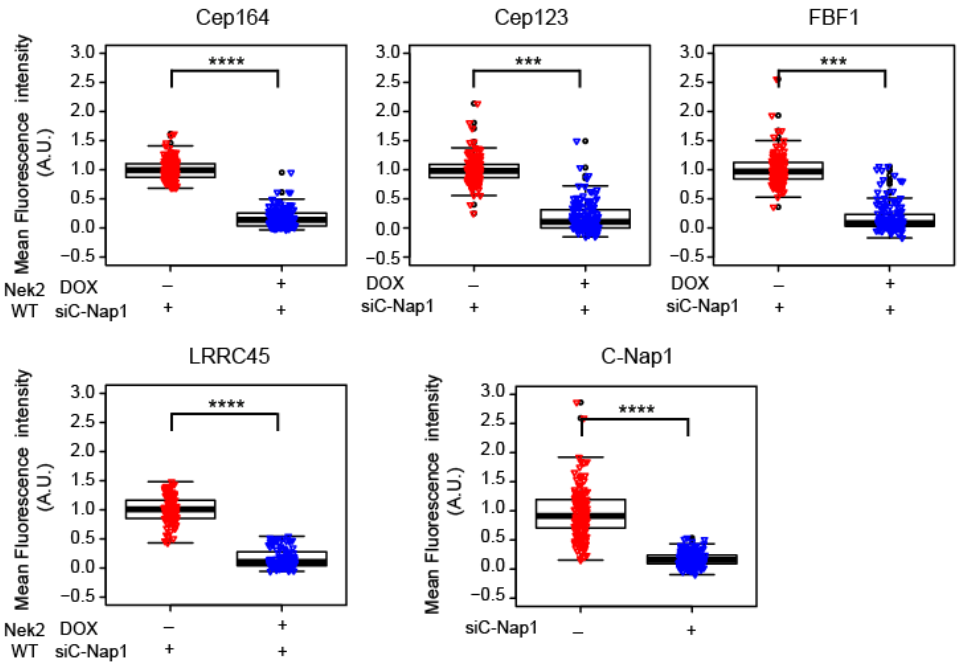

Figure 35. Release of appendages after Nek2 overexpression depends on the distal pool of Nek2. Box/dot plot shows quantification of the fluorescence intensity from the indicated proteins upon C-Nap1 siRNA with and without DOX-induced Nek2-WT expression. Cumulative data from three different experiments are shown. N=150 cells for each condition. Significance levels: ns $P > 0.05$, *: $P \leq 0.05$, **: $P \leq 0.01$, ***:$P \leq 0.001$, ****: $P \leq 0.0001$.

Next, I wanted to unravel if local protein degradation is involved in the mitotic regulation of appendages. Therefore, I used the proteasome inhibitor MG132 to analyze if proteasome inhibition reverts the release from interphase centrosomes (Figure 36). As described previously (Hames et al., 2005), cells treated with MG132 had an increase in the centrosomal intensity of endogenous Nek2 and overexpressed Nek2 compared to untreated cells, showing an effective treatment (Figure 36A). The fluorescence intensity of Cep164, Cep123, FBF1, LRRC45, and Centriolin was still significantly decreased upon WT Nek2 overexpression on top of proteasome inhibition. Likewise, SCLT1, ODF2, and Cep83 were not diminished (Figure 36B). This data indicates that protein degradation is not the underlying mechanisms leading to appendage removal by overproduced Nek2.

To note, ODF2 and Cep83 had an increased intensity on the centrosome upon Nek2 overexpression. Further analysis is needed to show how higher levels of Nek2 trap these proteins on the centrosome.

Together, my data indicate that higher levels of Nek2 are sufficient to promote the ectopic displacement of a sub-set of distal appendages from the mother centriole.

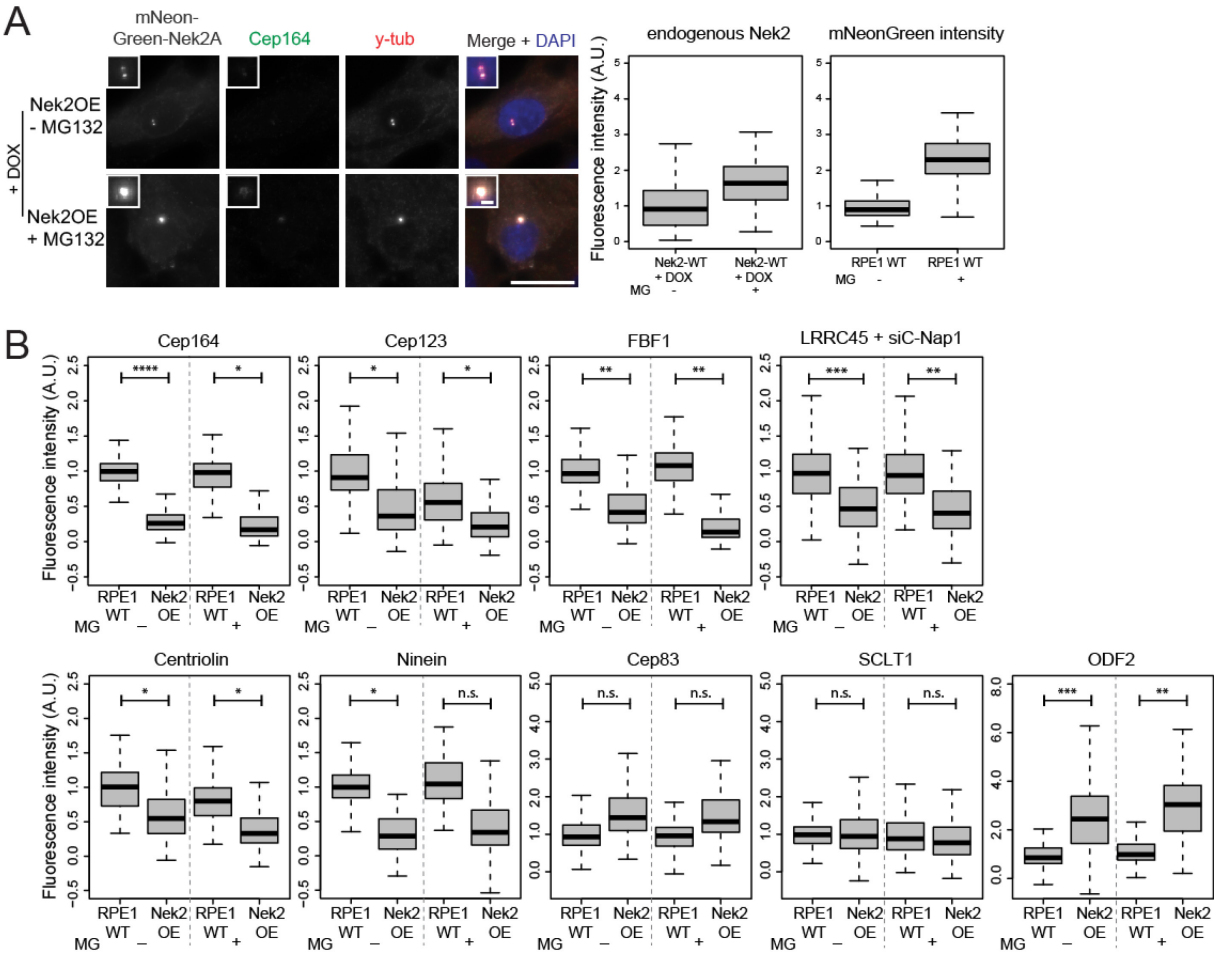

Figure 36. The release of appendages upon Nek2 overexpression is not a result of local degradation. (A) Representative images of the fixed Nek2-WT-mNeonGreen overexpressing cell line with and without proteasome inhibition using MG132. A specific antibody against Cep164 was used to visualize the reduction of this appendage protein upon overexpression. γ-tubulin was used as a centrosome reference and DAPI stained the DNA. Scale bars are 20 µm and 2 µm. Proteasome inhibition was controlled by quantification of endogenous Nek2 in RPE1 WT cells using a specific antibody and of the mNeonGreen-Nek2 signal in Nek2-WT overexpressing cells. Whisker-Box Plots represent the quantification of the signal at the centrosome after normalization to the average of the - MG treatment. N=50 cells per condition. As published (Spalluto et al., 2012), Nek2 accumulates at the centrosome after proteasome inhibition. (B) The same phenotype as described in Figure 34 was still observed after treatment with the proteasome inhibitor MG132 (MG). Because I wanted to analyze only the distal pool of LRRC45, I depleted C-Nap1 for the staining of this protein. Used cell lines: RPE1 WT, Nek2 OE= RPE1 Nek2-WT plus DOX. 50 cells were analyzed per condition in each of three the independent experiments (two for Ninein and Centriolin). Significance levels: ns P > 0.05, *: P ≤ 0.05, **: P ≤ 0.01, ***:P ≤ 0.001, ****: P ≤ 0.0001

3.3.4 PLK1 is not required for the Nek2 dependent release of distal appendages

Previously, Nek2 and PLK1 were suggested to work synergistically to remove the subdistal component, ninein-like protein (Nlp), from centrosomes prior to mitosis (Rapley et al., 2005). I next tested if PLK1 is also involved in subdistal appendage removal. Therefore, I analyzed if PLK1 inhibition using the inhibitor BI-2536 on top of Nek2 overexpression diminishes the effect of Cep164 displacement from the

centrosome upon Nek2 overexpression (Figure 37A). An increase of rounded metaphase-arrested cells in the BI-2536 treated sample without doxycycline induction confirmed the effectiveness of PLK1 inhibition (Figure 37B). PLK1 inhibition on top of Nek2 overexpression did not significantly compromise Cep164 displacement from interphase centrosomes compared to solely overexpressing Nek2 (Figure 37A). This indicates that Nek2 does not require PLK1 for its action on distal appendages.
Furthermore, inducible overexpression of the hyperactive (T210D mutation) form of PLK1 did not change the levels of Cep164, Cep123, LRRC45 or FBF1 at interphase centrosomes (Figure 37C-D), indicating that PLK1 does not phenocopy Nek2 in respect to distal appendage removal. Furthermore, the overexpression of hyperactive PLK1 resulted in the premature recruitment of appendage proteins on the daughter centrioles (Figure 37D), as previously published for HeLa cells (Kong et al. 2014).
Starting with this analysis, Ninein and Centriolin were not analyzed any longer because Ninein was still released from the mitotic centrosome in Nek2 KO cells (Figure 31) and only distal appendages are key players in cilia formation, which is the main focus of my further analysis.

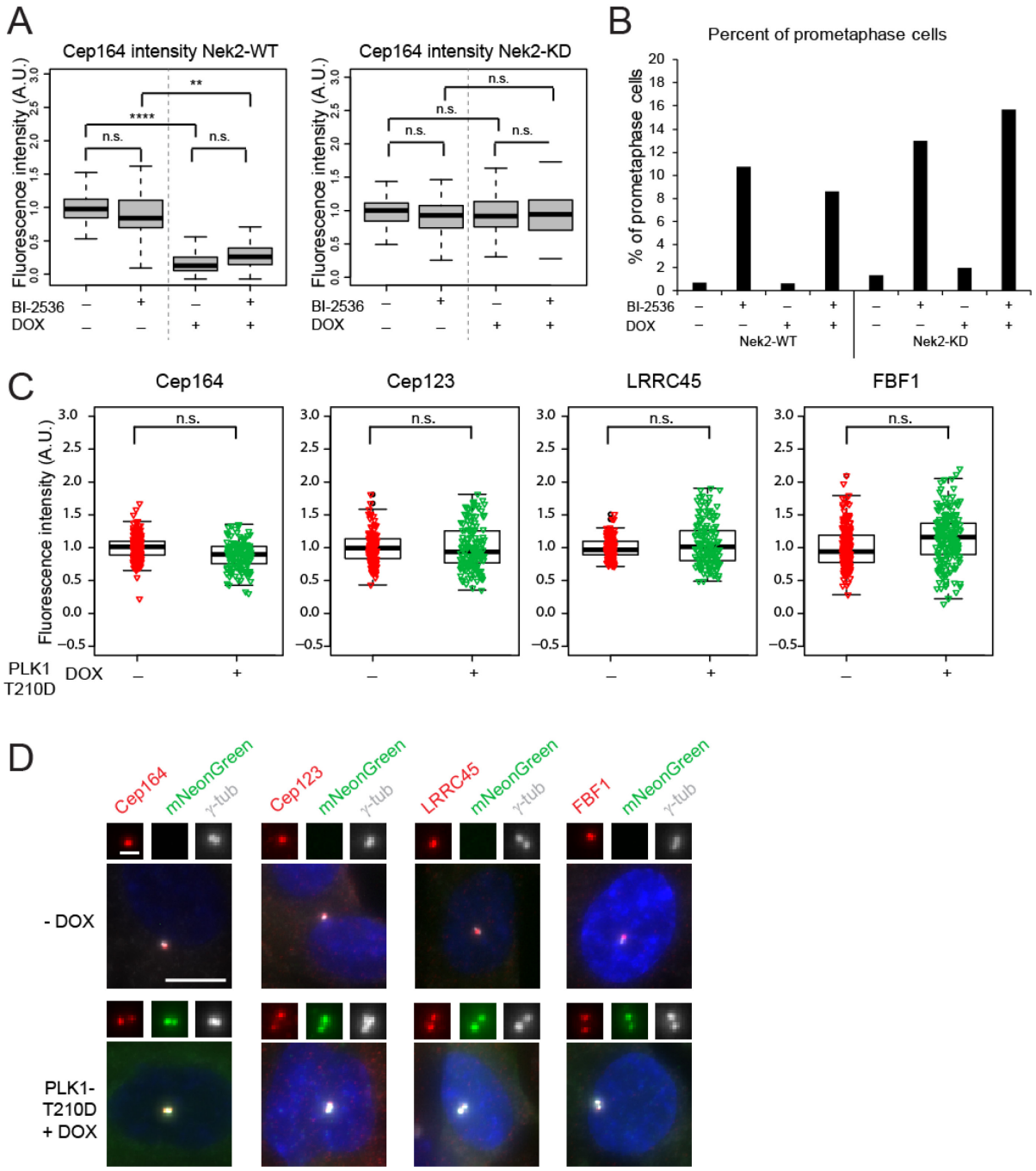

Figure 37. Nek2 dependent release of distal appendages is independent of PLK1. (A) Boxplots representing combined data from 3 independent experiments for Cep164 appendage signal at the centrosome after normalization to the - DOX and - BI-2536 signal. A DOX-inducible RPE-1 cell line was used for Nek2-WT and -KD overexpression and BI-2536 was used as a PLK1 inhibitor. N>250 cells were analyzed for each condition. Student's t-test was performed for the average of three independent experiments. (B) Percentage of prometaphase cells was quantified as a control for PLK1 inhibition (Sumara et al., 2004). At least 70 cells were quantified per condition. (C) Dot/box plots show the normalized fluorescence intensities of the indicated proteins in doxycycline (DOX) inducible mNeonGreen-PLK1 or hyperactive mutant PLK1-T210D expressing cell lines with and without DOX from 2-4 repetitions. In total, N=100-200 cells were analyzed. Significance levels: ns P > 0.05, *: P ≤ 0.05, **: P ≤ 0.01, ***:P ≤ 0.001, ****: P ≤ 0.0001. (D) Quantification of PLK1-WT and PLK1-T210D overexpressing cells after DOX induction. In three independent experiments, a total of 218 cells and 199 cells were quantified for PLK1-WT and -T210D, respectively. (E) Representative images showing the signal of the indicated appendages (red) in PLK1-WT and -T210 mNeonGreen overexpressing (green) cell lines compared to PLK1-WT without DOX induction. γ-tubulin (gray) and DAPI (blue) serve as a marker for centrosomes and nuclei, respectively. Scale bar is 10 µm

3.3.5 Impairment of ciliogenesis upon Nek2 overexpression correlates with reduction of distal appendages

Distal appendages are required for the initial steps of cilia formation (Graser et al., 2007; Schmidt et al., 2012; Tanos et al., 2013; Yang et al., 2018). Therefore, I hypothesized that the diminished levels of distal appendages induced by overproduced Nek2 have an influence on ciliogenesis. It was shown that Nek2 regulates cilium disassembly via phosphorylation of Kif24, which prevents the outgrowth of cilia in proliferating cells (Kim et al., 2015). I wanted to investigate if the removal of appendages is an additional Kif24 dependent or independent event influencing ciliation upon Nek2 overexpression in ciliating cells. Primary cilium assembly and disassembly can be recapitulated *in vitro* in RPE1 cells, where 48 h of serum starvation leads to robust ciliation, while re-stimulation of cells with serum-containing media tempts cilium disassembly (Pugacheva et al., 2007).

In line with Kim et al. (2015), ciliation was not decreased if overexpression of Nek2 was induced after cells were serum starved (Figure 38B) reinforcing the conclusion that Nek2 is unlikely to act on assembled cilia. Further, in this setting, Cep164 levels were only very mildly reduced, despite Nek2 overexpression (Figure 38C). Hence, already assembled cilia might prevent the action of Nek2 on centrosomal appendages. To note, upon Nek2 overexpression in serum-containing medium and induced ciliogenesis through serum-withdrawal for 48 h, the overexpressed Nek2 levels were drastically reduced (Figure 38D), as previously noted for endogenous Nek2 levels (Kim et al., 2015).

In agreement with previous reports (DeVaul et al., 2017; Kim et al., 2015; Spalluto et al., 2012), ciliation was modest but significantly reduced after overexpression of Nek2 followed by serum starvation (Figure 38E). To address if the loss of ciliation correlates with Cep164 removal, I quantified Cep164 intensities after 24 h doxycycline-induced overexpression, followed by 48 h of serum starvation in ciliated vs. non-ciliated cells. The levels of Cep164 were significantly reduced in ciliated and non-ciliated Nek2 overexpressed cells in comparison to WT cells (Figure 38F). However, Cep164 intensity did not decrease as drastically in ciliated Nek2 overexpressing cells compared to non-ciliated cells (Figure 38F). This implies that the unciliated population of cells upon 48h of serum starvation was not capable of cilia formation or had premature cilium disassembly due to the reduction of appendages after Nek2 overexpression.

To better understand why the reduction of ciliation is only moderate despite prolonged overexpression, I classified the heterogeneously Nek2 overexpressing cells into different groups: High levels, medium levels and very low levels (Figure 38G and H). Nek2 was still detectable at the centrosomes with medium to higher levels, although, upon serum starvation, most cells had low levels or no detectable Nek2 (Figure 38H). Cells with higher Nek2 levels at the centrosomes upon serum starvation showed more frequently a Cep164 reduction (Figure 38I) and a stronger reduction in cilia formation (Figure 38J).

Together, this data indicates that the persistence of high Nek2 levels upon serum starvation correlates with distal appendage removal and cilia loss.

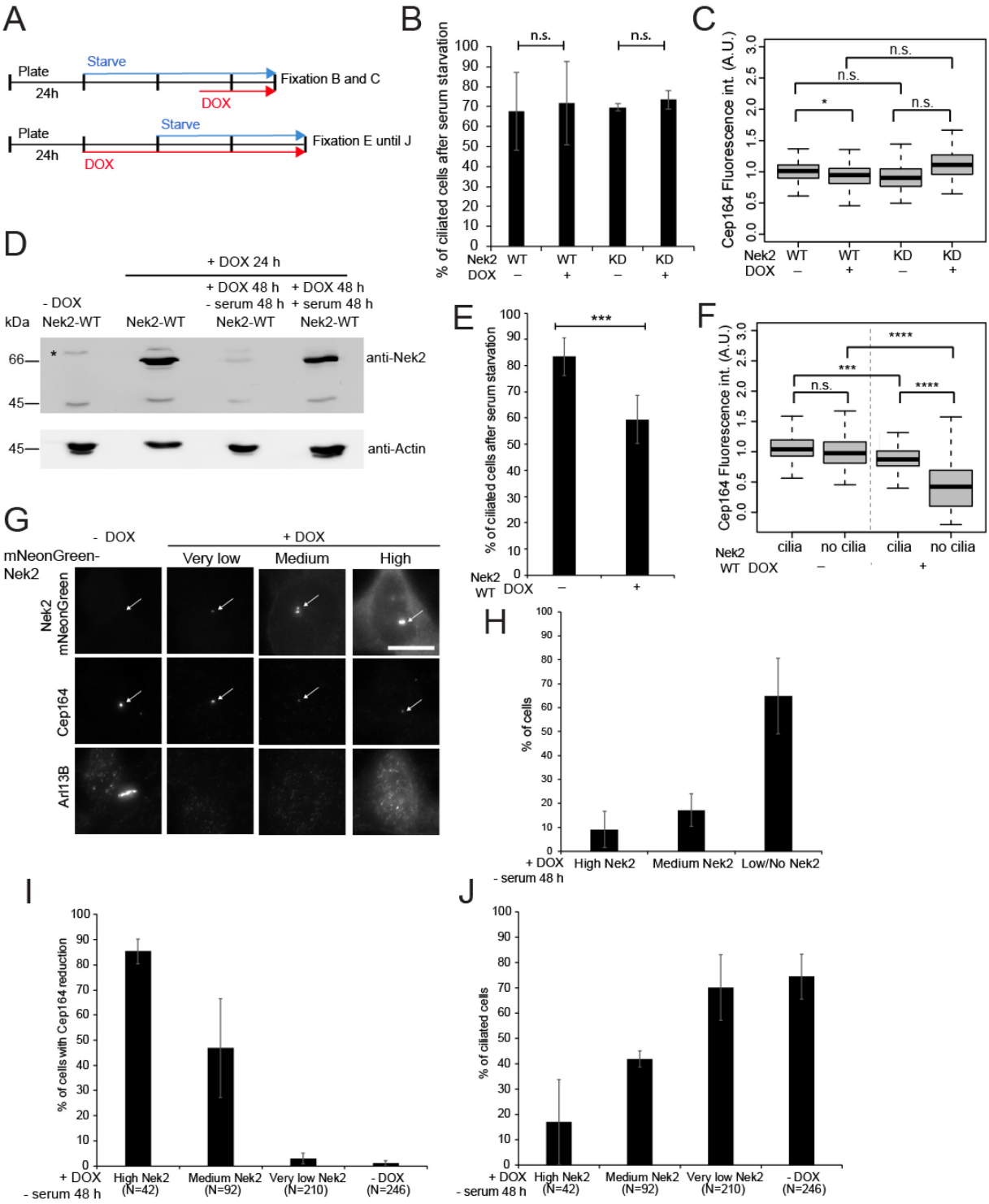

Figure 38. Subdistal appendage release is implicated in reducing ciliation upon Nek2 overexpression. (A) Diagram indicates the timing of doxycycline (DOX) induction and serum starvation. (B) Ciliation was examined after 60 h of serum starvation and DOX inducible Nek2 overexpression for the last 24 h with and without DOX. Arl13B was used as a cilia marker. Results show the average ± standard derivation. N>60 cells were quantified per condition in two independent experiments. (C) Whisker-Box Plots show the quantification of Cep164 signal at the centrosome after normalization to the average of the Nek2-WT -DOX signal with and without Nek2 overexpression. The plots show the normalized combination of two different experiments. Total N>110 cells per condition were quantified. (D) Representative western-blot showing the decrease of total Nek2 mNeonGreen levels using an anti Nek2 antibody and Actin as a loading control. Asterix indicates an unspecific band. The lower Nek2 band (~45 kDa) is the size of endogenous Nek2 and the upper band the fusion of Nek2 and mNeonGreen. Cells were treated with or without DOX and serum as indicated in the figure. (E) Ciliation

was examined in RPE1 WT and Nek2 overexpressing (72 h dox) RPE1 cells after 48 h of serum starvation. Arl13B was used as a cilia marker and γ–tubulin as a basal body marker. N>500 cells were quantified in five independent experiments. (F) Whisker-Box Plots show the quantification of Cep164 signal at the centrosome after normalization to the average of ciliated Nek2-WT -DOX signal. Ciliated vs. non-ciliated cells were distinguished using Arl13B as a cilia marker. The plots show the normalized combination of six different experiments. Total N>195 cells per condition were quantified. (G) Representative images showing the heterogeneity of Nek2 overexpression levels. Immunofluorescence using specific antibodies against Cep164 and Arl13B was performed in Nek2mNeonGreen overexpressing cells. Scale bar is 20 µm. (H) Quantification of the proportion of cells with high, medium and low or no Nek2 overexpression. Results show the average ± standard derivation of four independent repetitions. Total N=469. (I) Percentage cells with low or undetectable Cep164 levels were quantified using indirect immunofluorescence and antibodies against Cep164 and γ-tubulin as a centrosome marker. Results show the average ± standard derivation of four independent repetitions. Numbers below in the bars represent the total number of cells analyzed for each condition. (J) Percentage of ciliated cells was quantified using indirect immunofluorescence and antibodies against Arl13B and γ–tubulin as cilia and centrosome marker. Results show the average ± standard derivation of four independent repetitions. Numbers below in the bars represent the total number of cells analyzed for each condition. Significance levels: ns P > 0.05, *: P ≤ 0.05, **: P ≤ 0.01, ***:P ≤ 0.001, ****: P ≤ 0.0001.

3.3.6 Ciliation is not impaired in Nek2 KO cells

Depletion of Nek2 in RPE1 cells has been reported to reduce cilia formation upon serum starvation (Graser et al., 2007), while others saw no effect or only a modest increase of ciliation upon serum starvation (Spalluto et al., 2012). As previous studies used siRNA, I investigated if Nek2 influences serum-starvation induced ciliogenesis in two different Nek2 KO clones (Figure 39). Ciliation was not increased in the Nek2 KO clone used for most of the shown studies (clone 18) and only a modest increase was visible in the other cell line (clone 27) compared to WT cells (Figure 39A). This observation is in line with the study of Spalluto et al. (2012). According to my hypothesis that the effect of Nek2 on ciliation is through appendage levels, ciliation should not be affected in Nek2 KO cells because appendages are not affected in Nek2 KO interphase cells (Figure 31). However, slightly increased levels, as seen in one of the clones, may reflect a suppressive role of Nek2 for cilium assembly as suggested by Kim et al. (2015). While depletion of Nek2 in cycling cells drastically increased ciliation in the study of Kim et al. (2015), the study of Spalluto et al. (2012) showed that only one of six tested siRNAs led to an increase of ciliation compared to the control. Here, using Nek2 KO cells lines no significant increase of ciliation in cycling cells was observed (Figure 39B). This observation raises the possibility that the increase of ciliation in cycling cells upon Nek2 siRNA treatment in the study of Kim et al. (2015) represents an off-target effect. To test this idea, I depleted Nek2 using the same siRNAs used in the named study in RPE1 WT cells and in the Nek2 KO clone 18. Although the tendency to ciliate was generally higher in cycling WT cells compared to the KO clone in these experiments, both cell lines had a higher percentage of cilia after

Nek2 siRNA treatment (Figure 39C). Overall, these data suggest that Nek2 does not affect cilia formation in interphase cells.

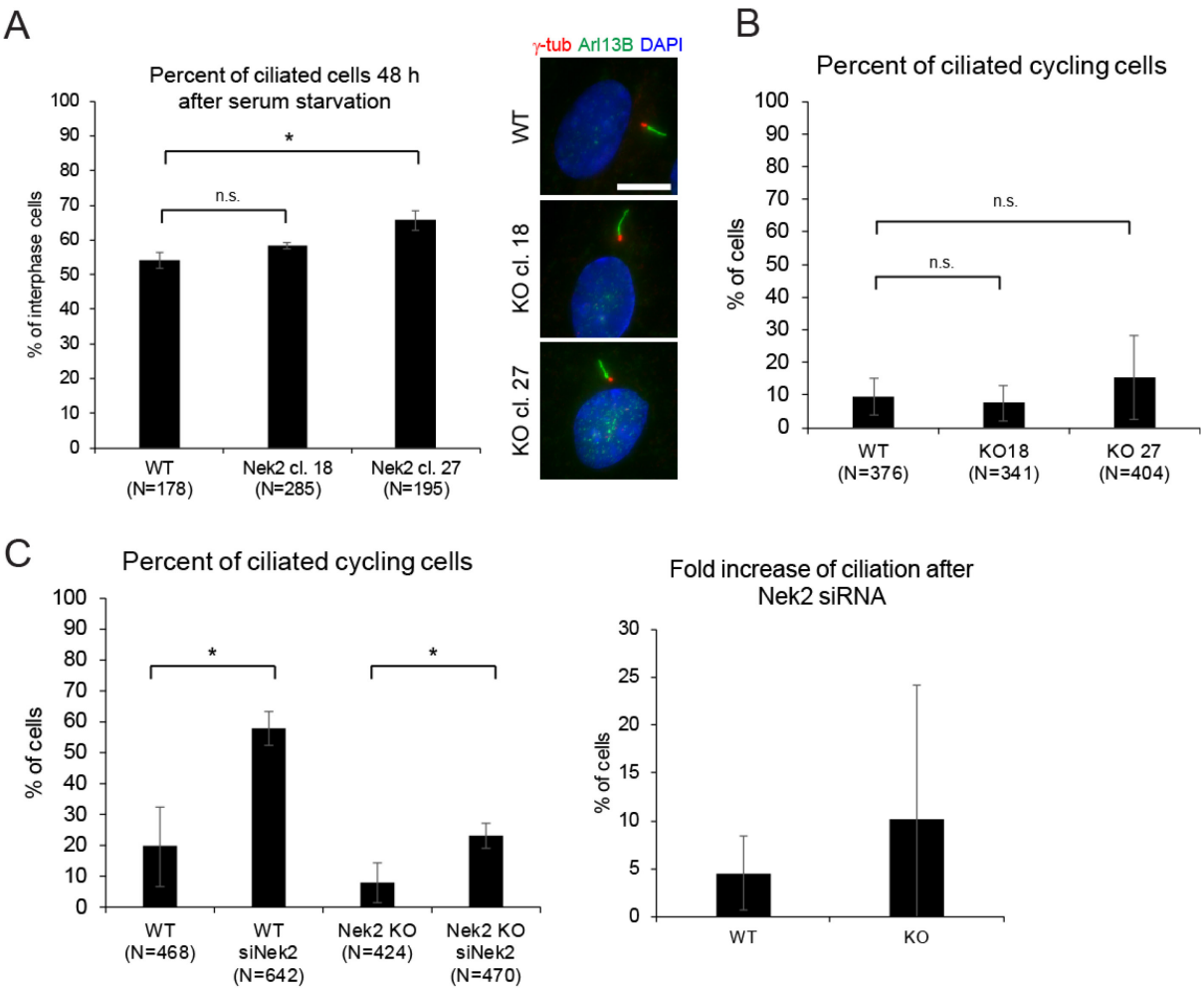

Figure 39. Ciliation in RPE1 WT vs. Nek2 KO cell lines. (A) Ciliation was examined in RPE1 WT cells and two different Nek2 KO clones after 48 h of serum starvation. Results show the average ± standard derivation of three independent repetitions. Numbers below the bars represent the total number of cells analyzed for each condition. Representative images on the right side. Arl13B was used as a cilia marker and γ–tubulin as a basal body marker. Scale bar is 10 µm. (B) Ciliation was examined in cycling RPE1 WT cells and two different Nek2 KO clones. Results show the average ± standard derivation of two independent repetitions. Numbers below in the bars represent the total number of cells analyzed for each condition. (C) Increase of ciliation was examined in cycling RPE1 WT cells and the Nek2 KO clone 18 after Nek2 siRNA treatment. Results show the average ± standard derivation of three independent repetitions. Numbers below in the bars represent the total number of cells analyzed for each condition. Significance levels: ns P > 0.05, *: P ≤ 0.05, **: P ≤ 0.01, ***:P ≤ 0.001, ****: P ≤ 0.0001.

3.3.7 Cep164 removal by Nek2 is independent of Kif24

I next asked whether Nek2 could regulate appendages via Kif24. To address this hypothesis, I analyzed if the centriolar removal of Cep164 upon Nek2 overexpression required Kif24. Cep164 levels were similarly reduced upon Kif24 depletion on top of Nek2 overexpression compared to Nek2 overexpressing cells treated with control siRNA (Figure 40A). The efficiency of Kif24 depletion was verified using real-time-PCR (Figure 40B). This suggests that Nek2 does not require Kif24 to remove appendages

from the centrosome upon overexpression. Additionally, I observed that Cep164 centrosomal levels decreased during mitosis upon Kif24 depletion like in REP1 WT cells, indicating that Kif24 is not essential for appendage removal from the centrosome prior to mitosis (Figure 40C).

Moreover, I analyzed if Kif24 overexpression influenced appendage levels by transiently overexpressing Kif24-*Aequorea coerulescens* GFP (AcGFP) and quantifying Cep164 levels in Kif24-AcGFP positive transfected cells compared to control transfected cells (Figure 40D-F). Kif24 overexpression had no effect on Cep164 levels (Figure 40E and F), yet it reduced ciliogenesis (Figure 40G) as reported previously (Kim et al., 2015). Therefore, I concluded that Kif24 is dispensable for appendage regulation by Nek2 and increased Nek2 levels affect ciliation via appendages independent of the pathway via Kif24.

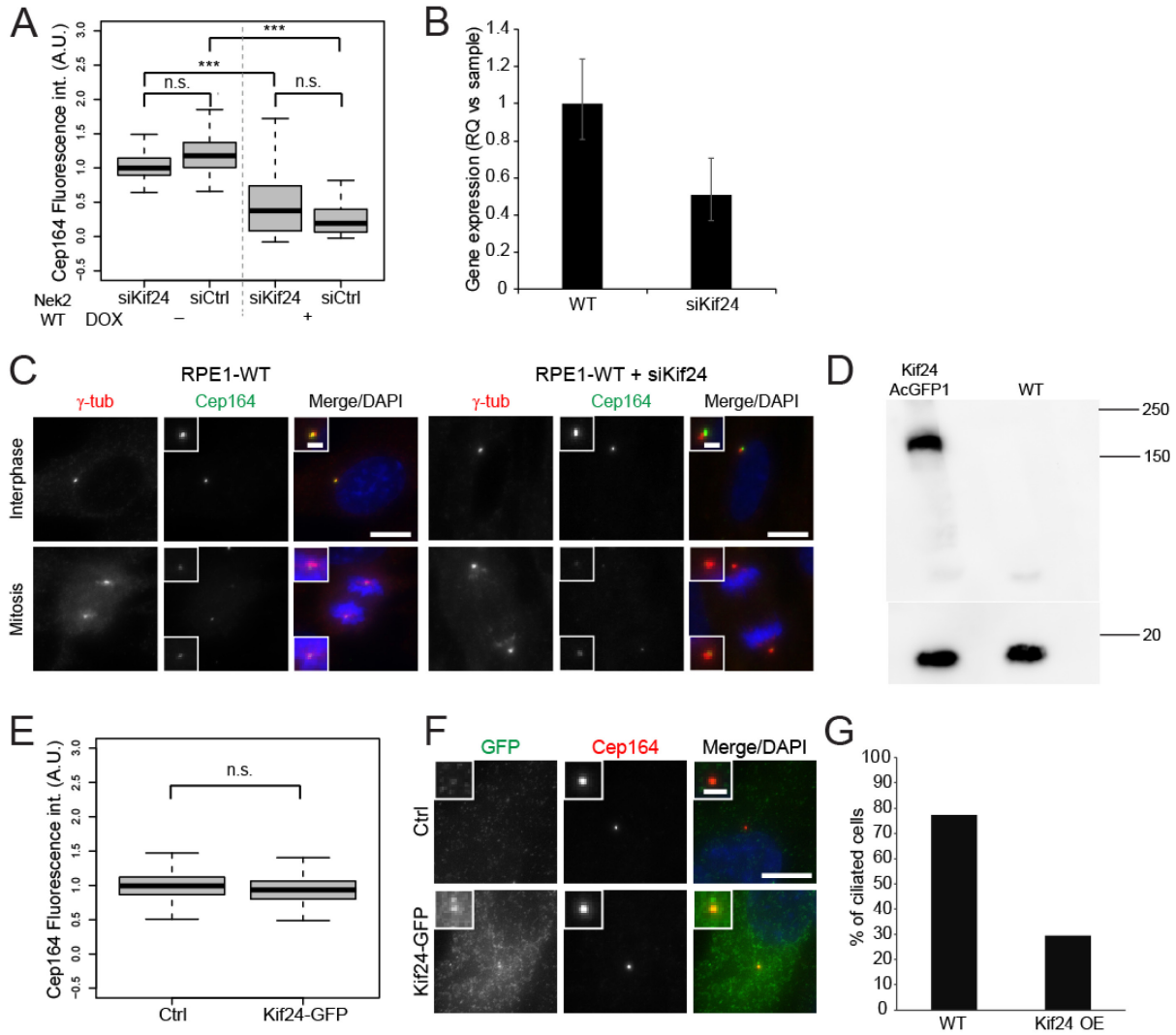

Figure 40. Appendage release via Nek2 is independent of the Kif24 pathway. (A) Fluorescence intensity measurement of Cep164 using indirect immunofluorescence after control (Ctrl) or Kif24 depletion in inducible Nek2 overexpressing cells minus and plus doxycycline (DOX). Three independent experiments were performed. Normalization to the –DOX siKif24 treatment was performed. N=175

centrosomes were quantified per condition. (B) qPCR was used to quantify Kif24 mRNA levels after Kif2 siRNA in RPE1 cells compared to RPE1 WT cells. Results show the RQ value for the respective treatment and error bars the respective maximum and minimum RQ value for each sample. Results display one out of two representative experiments. (C) Representative images of mitotic RPE1 WT and siKif24 treated cells using a specific antibody against Cep164. Scale bars are 10 µm and 2 µm. (D) Verification of the AcGFP1-Kif24 overexpressing cell line (Miyamoto et al. 2015). HEK273T cells transfected with AcGFP1-KIF24 were compared to WT HEK273T cells. A specific anti-GFP antibody was used to visualize the fusion construct of Kif24 (152 kDa) and GFP (27 kDa) on western-blot. Cofilin was used as a loading control. (E) Fluorescence intensity measurement of Cep164 using indirect immunofluorescence in control (Ctrl) transfected RPE1 WT cells vs. cells transfected with the AcGFP1-Kif24 containing plasmid. Cumulative data from three independent experiments is shown. Normalization to the Ctrl treatment was performed. N=150 centrosomes were quantified per condition. (F) Representative images of control (Ctrl) transfected RPE1 WT cells and cells transfected with an AcGFP1-KIF24 containing plasmid. (G) Ciliation was quantified in AcGFP1-Kif24 positive cells compared to control transfected cells to confirm the functionality of the construct. Kif24 overexpression induces the reduction of ciliated cells (Kim et al., 2015). N=62 RPE1 WT cells and N=29 AcGFP1-Kif24 positive cells.
Significance levels: ns $P > 0.05$, *: $P \leq 0.05$, **: $P \leq 0.01$, ***:$P \leq 0.001$, ****: $P \leq 0.0001$.

3.3.8 Interphase Cep164 levels are affected in Nek2 overexpressing breast cancer cell lines

I next asked whether a decrease in appendage levels in cells with high Nek2 expression other than RPE1 could be observed. Nek2 is a proto-oncogene that was shown to be overexpressed in several forms of cancer, including breast cancer (Cappello et al., 2014; Hayward et al., 2004; Zhou et al., 2013). Therefore, I tested whether I find a decrease in appendage levels in cancer cells with high Nek2 expression. To analyze whether Nek2 positive breast and breast cancer cells have reduced appendage levels, I analyzed Cep164 centrosomal protein levels in cell lines, derived from MCF10A cells, that have been transformed with oncogenic Ras (V12G) and clonally selected after passage in mice (Dawson et al., 1996; Miller et al., 2000; Santner et al., 2001). These cell lines, MCF10AT (pre-malignant mammary cells) and MCF10CA1 (invasive, metastatic carcinoma), represent increasing grades of malignancy. Although they are non-tumorigenic MCF10A cells are immortal and hyperplastic and also display enhanced expression of Nek2 (Kim et al., 2015; Neve et al., 2006; Yuan et al., 2010).

The appendage protein Cep164 normally stays on the interphase centrosome in Nek2 positive RPE1 interphase cells, as observed before and is only reduced upon entry into the G2/M phase (Figure 12A). However, an increased amount of MCF10A, -AT and- CA1 breast cells had reduced Cep164 levels even in interphase compared to normal epithelial RPE1 cells as a control (Figure 41A). Consequently, cells with low Cep164 centrosomal levels ranged between 24 and 37% in the MCF10A, -AT and -CA1 cells, compared to only 7% in interphase RPE1 WT cells.

The decrease in interphase Cep164 levels in MCF10-derived cell lines was due to Nek2 because depletion of Nek2 using specific siRNA reverted the phenotype, while siRNA against Nek2 had no effect in RPE1 cells (Figure 41B). Nek2 depletion did not fully rescue the Cep164 decrease. This could be due to remaining Nek2 levels upon incomplete knockdown of Nek2 (Figure 41C).

The effect of Nek2 upon appendages could be more pronouncedly seen when Nek2 positive and negative cells within the same cell line were scored separately (Figure 41D). Cep164 levels were especially reduced in interphase MCF10A, -AT and -CA1 cells, which were Nek2 positive compared to Nek2 negative cells of each cell line (Figure 41D and E). It has to be mentioned that MCF10CA1 cells had the highest amount of cells with Cep164 reduction (Figure 41A), while the reduction of Cep164 on the centrosome was least pronounced (Figure 41D). This could be explained by the fact that in some MCF10CA1 cells Nek2 levels were higher in the cytoplasm, but not at the centrosome. These cells were only considered for phenotypic quantifications in Figure 41A and B but not for the plots shown in Figure 41D.

Interestingly, the Nek2 intensity, neither measured at the centrosome (Figure 41F), nor in the total cell lysate (Figure 41G) were significantly higher in the MCF10A derived cell lines compared to RPE1 cells. This indicates that disturbed or increased activity rather than augmented levels of Nek2 cause premature Cep164 release in interphase in the analyzed breast cell lines.

On the other hand, once Nek2 intensity was correlated against Cep164 intensity for each cell line, I observed a negative correlation for the MCF10A derives cell lines and not RPE1 cells (Figure 41H). This was noticeable by a declining regression line and higher correlation coefficient (R) in the MCF10A and derived cell lines, while there was no correlation in RPE1 cells (Figure 41H).

Furthermore, siRNA against Nek2 partly rescued reduced ciliation as described before (Kim et al., 2015). Reduced ciliation is associated with oncogenic transformation in mammary epithelial cells (Menzl et al., 2014; Seeger-Nukpezah et al., 2013; Yuan et al., 2010). This raises the possibility that not only abrogating the defective Nek2/Kif24 pathway (Kim et al. 2015), but also normalizing appendage levels in interphase might restore primary cilia formation and restrict proliferation in breast cancer cells.

My data thus indicate that high Nek2 levels diminish distal appendage association with the mother centriole in hyperplastic and cancer mammary cell lines.

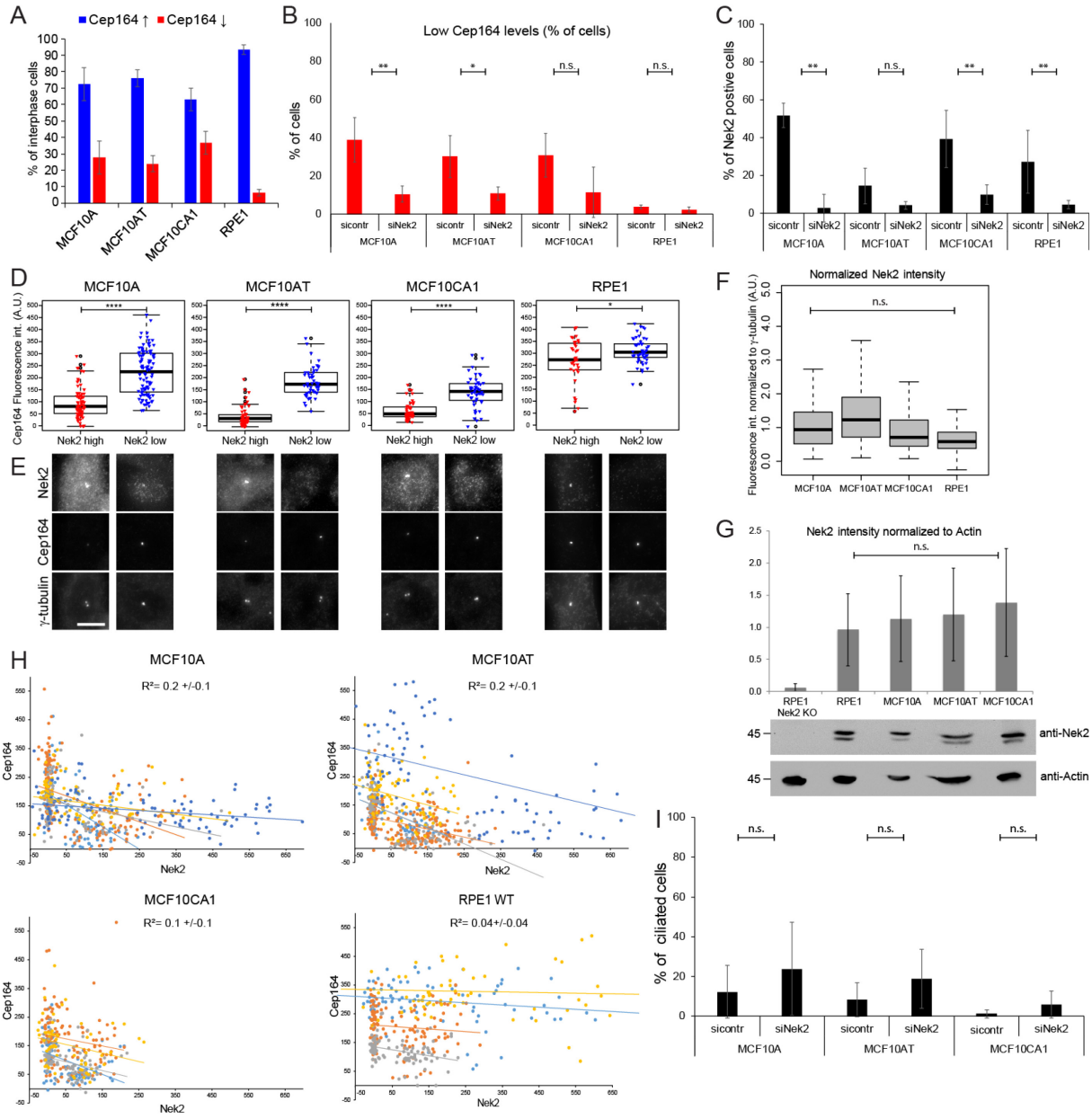

Figure 41. Interphase Cep164 levels are affected in Nek2 overexpressing breast cancer cell lines. (A) Percentage of interphase cells with low and high Cep164 levels were quantified using indirect immunofluorescence. A specific Cep164 antibody and γ-tubulin was used as a reference for the centrosome. DAPI was used as a nuclear marker and to distinguish mitotic from interphase cells. N>130 cells were analyzed per experiment and cell type per repetition in five independent experiments. The bar graph indicates the average ± standard derivation for all experiments. (B) Decreased Cep164 levels in interphase epithelial breast cancer and precursor cells could be rescued upon siRNA of Nek2. N>80 cells were analyzed per cell type and condition in each experimental repetition. Results show the average ± standard derivation in four independent experiments (three for MCF10CA1). (C) Quantification of Nek2 positive interphase epithelial breast cancer and precursor cells and RPE1 with and without siRNA against Nek2. N>450 cells were analyzed per cell type and treatment in a total of four independent experiments (three in the case of MCF10CA1). Results show the average ± standard derivation. (D) Box/dot plots show Cep164 fluorescent intensity (arbitrary unit) measured at the centrosome in Nek2 positive and negative interphase cells. The graph is representative of one experiment out of five. N>80 cells were analyzed per experimental repetition for each cell type. (E) Representative immunofluorescence images for Nek2 positive and negative cells for each cell type using specific antibodies against Nek2, Cep164 and γ-tubulin. Scale bar is 10 µm. (F) The box plots show Nek2 fluorescent intensity (arbitrary unit) measured at the centrosome in Nek2 positive interphase cells normalized to the γ-tubulin signal of each cell line to adjust to the staining efficiency of each cell line. The graph shows cumulative data from four independent experiments (three for RPE1). N>150 cells

were analyzed for each cell type. (G) Representative western-blot out of five independent experiments (four for RPE1) showing the protein level of total Nek2 using an anti Nek2 antibody and Actin as a loading control. Bar graphs show the average ± standard derivation for the intensity quantification of all repetitions. (H) Graphs show Cep164 intensity plotted against Nek2 fluorescence intensity for each cell line. Different colors indicate different experimental repetitions. Trendlines for each repetition are shown. Correlation factor R is shown above the plot. (I) Percent of ciliated interphase cells were quantified using Arl13B as a marker for ciliary membrane. At least 100 cells were quantified per cell type and condition in each of three independent replications. Student's t-test was performed for the average of all independent experiments.
Significance levels: ns P > 0.05, *: P ≤ 0.05, **: P ≤ 0.01, ***:P ≤ 0.001, ****: P ≤ 0.0001.

3.3.9 Influence of Nek2 overexpression on the differentiation of hematopoietic progenitor cells

Due to Nek2's role in development and disease (part 1.6.3.) and because overexpression of Nek2 influenced the differentiation of B cells (Gu et al., 2014), I next wanted to analyze if Nek2 influences the differentiation of hematopoietic progenitors. Therefore, I used similar techniques as described in part 3.2.2 for ODF2 within the cooperation with the group of Bernd Giebel. To this issue, CD34+ cells were sorted for MPPs and transduced with Nek2- and Nek2-KD-enhanced GFP (EGFP) overexpression and the control plasmid expressing only EGFP. As described previously (3.2.2), the cells were analyzed regarding their differentiation potential into LM, EM, MP, and LPs using flow cytometry. At day 12 of cultivation, the population of LMs was visibly reduced and the population of EMs increased, however not significantly (Figure 42A). Still, results were reproducible and suggest that HSPCs tend to differentiate into the CD133 negative erythro-myeloid direction with high Nek2 levels (Figure 42B). Notably, the observed effect seems independent of Nek2's kinase function, as overexpression of the kinase-dead version mimicked Nek2-WT overexpression (Figure 42A). As the amount of sorted MPPs is too small to allow quantification of knockdown efficiency, the overexpression constructs were verified in RPE1 cells using indirect immunofluorescence (Figure 42C).

In parallel to the flow cytometric analysis, the granulocyte, macrophage and erythrocyte differentiation capacity of the transduced cells were studied. For this purpose, GFP+ LMs and EMs were sorted into the CFC assay during the flow cytometric read-out on day 3 post-transduction. In this analysis (Figure 42D), more late differentiation colonies and less early progenitors suggested a faster differentiation. Yet, the also these differences were not significant.

Further, in the flow cytometric analysis, the GFP+ frequency of the transduced cells was followed to identify impacts of the inserted cassette on the proliferation rate. Upon Nek2 and Nek2-KD overexpression cell numbers are significantly reduced after 12

days (GFP ratio), demonstrating less self-renewal or a strong reduction of proliferation capacity (Figure 42E).

Together, the flow cytometric analysis and the CFC analysis indicate that Nek2 does not drastically influence cell-fate decisions or colony-forming properties in HSPCs. Though, Nek2 and Nek2-KD overexpression resulted in both assays with a reduction of more primitive cell types, combined with a significantly lower proliferation rate. This might be caused by enhanced differentiation to more mature progenitor types and/or vice versa by a reduction of self-renewal potential.

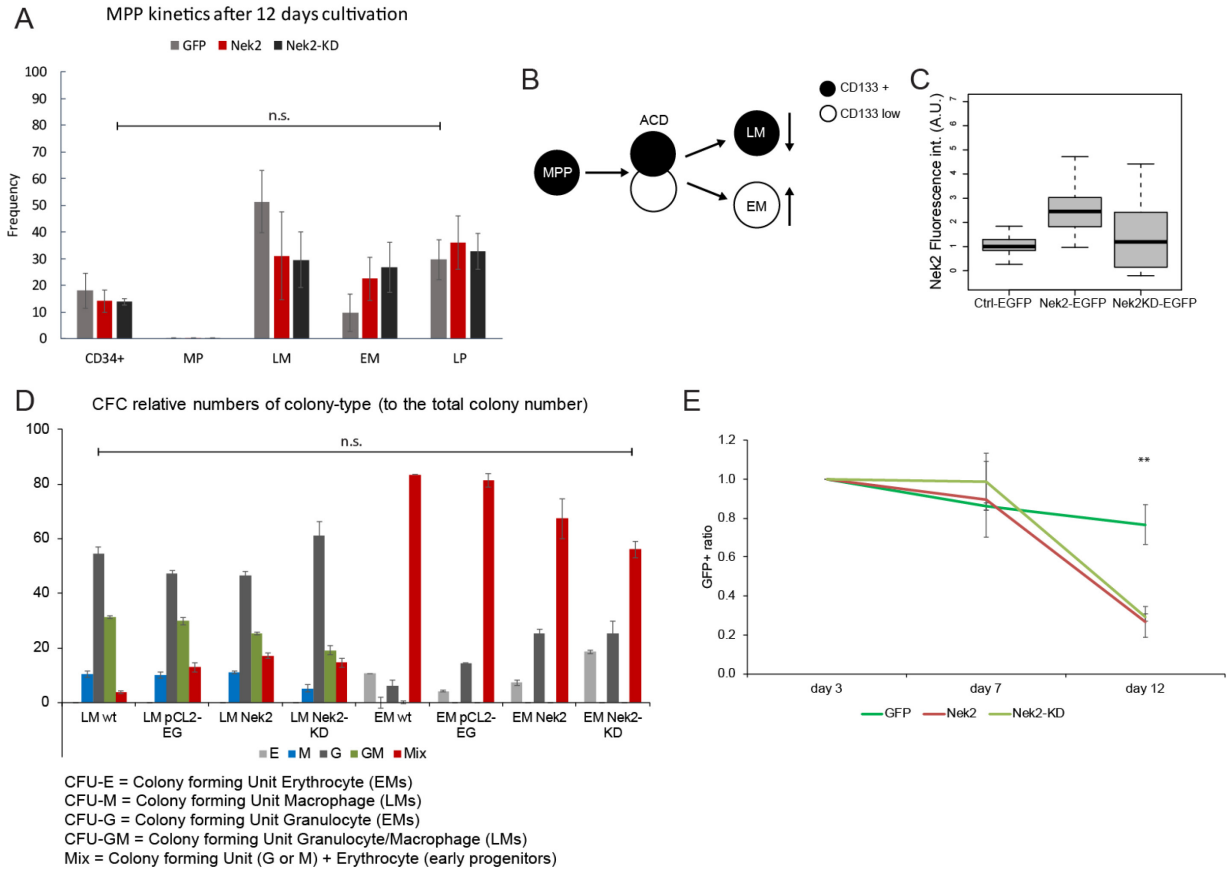

CFU-E = Colony forming Unit Erythrocyte (EMs)
CFU-M = Colony forming Unit Macrophage (LMs)
CFU-G = Colony forming Unit Granulocyte (EMs)
CFU-GM = Colony forming Unit Granulocyte/Macrophage (LMs)
Mix = Colony forming Unit (G or M) + Erythrocyte (early progenitors)

Figure 42. Analysis of hematopoietic progenitor cell differentiation upon Nek2 overexpression. (A) Frequency [%] of HSPC populations after 12 days of cultivation. CD34+ cells were sorted for multipotent progenitors (MPs) and transduced with Nek2-GFP, Nek2-KD-GFP overexpression- and the control plasmid (GFP). The cells were cultivated in HSPC media and analyzed regarding their differentiation into lympho- (LP) and erythro- myeloid (EM) progenitors, and late progenitors (LP) using flow cytometry. Data is from three independent experiments. Results show the average +/- standard derivation. Students-T test was performed. (B) Multipotent progenitors (MPPs) divide asymmetrically into CD133 positive lympho-myeloid (LM) and CD133 negative erythro-myeloid (EM) progenitors. The frequency of LM differentiation was lower and EM differentiation was higher upon Nek2 overexpression. (C) Verification of Nek2 overexpression in RPE1 cells. Fluorescence intensity measurement of Nek2 using indirect immunofluorescence in control (Ctrl-EGFP) transfected cells vs. cells transfected with an EGFP-Nek2 and -Nek2-KD containing plasmid. Normalization to the Ctrl treatment was performed. N=108, 79 and 29 for Ctrl, Nek2 and Nek2-KD centrosome intensities were quantified, respectively. (D) CFC-colony frequency normalized to the number of seeded cells. Results show the average +/- standard derivation of three independent experiments. Legend for colony types is shown in the figure. (E) GFP+ ratio of day 7 and day 12 in comparison to day 3. Results show the average +/- standard derivation of three independent experiments.
Significance levels: ns $P > 0.05$, *: $P \leq 0.05$, **: $P \leq 0.01$, ***:$P \leq 0.001$, ****: $P \leq 0.0001$.

3.3.10 A ciliary remnant in mitotic Nek2 KO cells leads to the asymmetric inheritance of ciliary signaling components and asynchronous cilium reassembly

Next, I asked for the consequence of disturbed appendage regulation in the Nek2 KO cells line. In explanation, what is the reason that specific appendages like Cep123 and Cep164 are released during mitosis and what happens if this process is reverted as in the case of the Nek2 KO cell line?

As the primary cilium is an important signaling hub, controlling which cells can form a cilium and the timing of the process are critical. In somatic cells, e.g. RPE1 (Spalluto et al. 2012), the primary cilium is resorbed before entry into mitosis and is assembled again in G1 following division. In contrast, specific stem cells keep a ciliary remnant on the older centrosome (Paridaen et al. 2013). The distal appendages, which are removed during normal mitosis in RPE1 cells are required for cilia formation (Graser et al., 2007; Schmidt et al., 2012; Tanos et al., 2013). Hence, I hypothesize that the removal of appendages during mitosis is another mechanism of Nek2 to regulate the timely controlled disassembly of cilia. To test this idea, I asked whether ciliary membrane resorption before mitosis is prevented in Nek2 KO cells and if the residual of the appendages on the mother centrosome is responsible for inhibited cilium membrane resorption.

Remarkably, nearly half of the mitotic cells showed the cilia-membrane marker Arl13B as vesicle-like staining at the mother centriole decorated by Cep164, after serum starvation, followed by serum-re-stimulation (Figure 43A). In contrast, no cilium or ciliary membrane was observed in WT cells. This indicates that an Arl13B-associated ciliary membrane (referred as ciliary remnant) remained associated with the mother centriole during mitosis, as previously reported for prophase cells with reduced levels of Nek2 (Spalluto et al., 2012).

No mitotic remnant was detected after siRNA of the distal appendage protein Cep164 (Figure 43B), confirming that Arl13B docked at the mother centriole in a Cep164-dependent manner. The phenotype was specific to Nek2 loss, as the inducible expression of Nek2 in the Nek2 KO background rescued it (Figure 43C).

Subsequently, I generated Arl13B-GFP cell lines in the background of RPE1 WT and Nek2 KO cells to analyze the observed phenotype using live cell imaging. This revealed that ciliated Nek2 KO cells shortened the cilium to a remnant during mitosis, from which a new cilium could be formed after division (Figure 43D). Arl13BGFP RPE1-

WT cells never kept a remnant during mitosis (not shown) as displayed before via indirect immunofluorescence (Figure 43A).

Because of ciliary remnant inheritance, the daughter cell retaining the “older” centrosome and the ciliary remnant was able to prematurely form cilia in Nek2 KO cells. The daughter cell that retained the cilia remnant reformed a cilium in 2 +/- 2.6 h after cell division. I did not observe cilia reformation in the daughter cell that inherited the younger centrosome (not decorated by Cep164) during the remaining imaging time (in average approximately 9 h/up to 19.3 h) (Figure 43E and F).

This data suggests that the presence of distal appendages during mitosis in Nek2 KO cells contribute to cilia remnant maintenance during mitosis and faster cilia reformation after cell division.

To test whether synchronous primary cilium formation in RPE1 cells allows sister cells to respond differentially to an environmental signal I examined sonic hedgehog (Shh) pathway activity (Introduction part 1.4.2.). The pathway component Smo localizes to cilia when stimulated by Shh ligand or by pathway agonists such as N-Methyl-N′-(3-pyridinylbenzyl)-N′-(3-chlorobenzo[b]thiophene-2-carbonyl)-1,4-dia-minocyclohexane (SAG). To determine whether the mitotic cilia remnant contains Smo, I induced SMO-eGFP expression via doxycycline in RPE1 WT and Nek2 KO cell lines (Figure 44). Cells were treated with the Shh pathway agonist SAG during the 24 h serum re-stimulation after 24 h of serum starvation.

In contrast to a previous report (Seo et al., 2011), the percentage of Smo-eGFP positive cilia was similar in SAG treated interphase Nek2KO and RPE1 WT cells compared to untreated cells (Figure 44A). During mitosis, like Arl13B, a remnant containing SMO-eGFP was visible in live cell imaging (not shown) and immunofluorescence (Figure 44B-D) in Nek2 KO SMO-eGFP cells. Remarkably, SAG treatment increased the number of mitotic cells with ciliary membrane marked by Arl13B by ~20% (Figure 44B). Moreover, the number of fully ciliated mitotic cells by 20% after SAG treatment (Figure 44C), suggesting Shh stimulation may pronounce premature cilia formation in mitotic Nek2KO cells. This data demonstrates that the sister cell with the ciliary remnant can become responsive to Shh while the other sister cell is not.

In summary, the consequence of asymmetric ciliary remnant inheritance in Nek2 KO cells was that the sister cell keeping the remnant reformed a signaling proficient cilium earlier after mitosis. This can be viewed as a type of ACD: Asynchronous cilium growth

might have consequences for cell fate determination by allowing sister cells to differentially detect environmental signals. Therefore, a ciliary remnant during mitosis might be restricted to asymmetrically dividing stem cells, which need a tool to respond contrarily to environmental signaling (Paridaen et al. 2013).

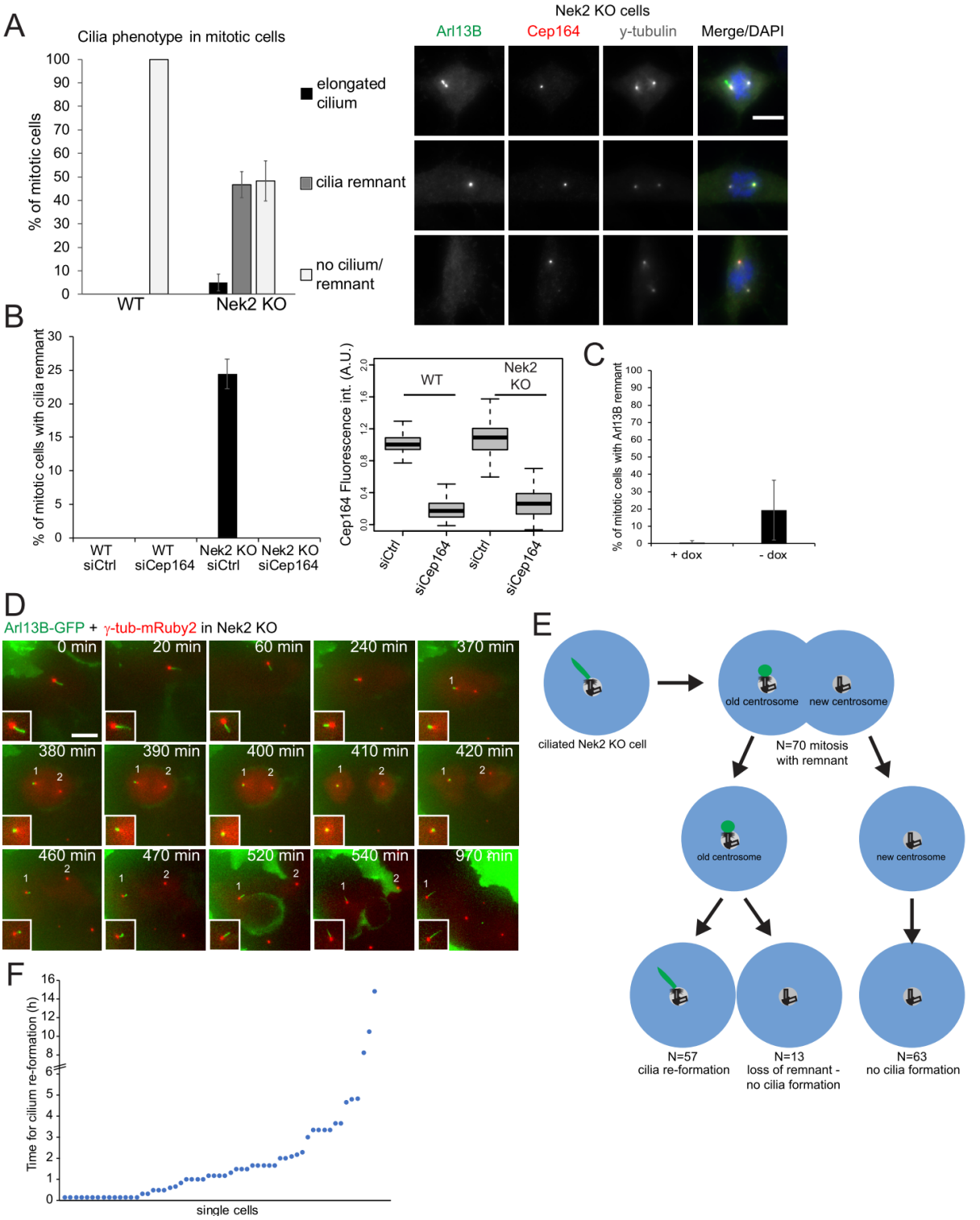

Figure 43. A ciliary remnant in mitotic Nek2 KO cells leads asynchronous cilium reassembly. (A) RPE1 WT and Nek2 KO cells were fixed and analyzed via indirect immunofluorescence using the indicated antibodies. Arl13B was used as a marker for the ciliary membrane. Scale bar is 10 µm. The percentage of ciliated cells following serum-starvation (24 h), and subsequent serum-stimulation (24 h)

is shown. In N=3 repetitions, an average of 47% of cells had a dot marked for cilia membrane (Arl13B) during mitosis, which was not observed in RPE1 WT cells. In total, 161 mitotic RPE1 WT and 232 RPE1 Nek2 KO cells were quantified. (B) Upon siRNA of Cep164, mitotic cells did not remain a cilia remnant in the background of Nek2 KO cells. WT siCtrl (N=125), WT siCep164 (N=150), Nek2 KO siCtrl (N=164), Nek2 KO siCep164 (N=125). Whisker-Box Plots represent the quantification of Cep164 appendage signal at the centrosome in RPE1 WT and Nek2 KO cells with and without Cep164 siRNA treatment. Cumulative data from three different experiments are shown. N=150 cells were analyzed for each condition. (C) Quantification of cells with Arl13B remnant in the rescue cell line for the Nek2 KO with DOX-inducible mNeonGreen-Nek2 expression with and without DOX induction. N>290 mitotic cells were quantified per condition in three independent experiments. (D) Representative still images of live cell imaging using Arl13bGFP and γ-tubulin-mRuby2 expressing Nek2 KO cells. (E) Quantification of Arl13B-GFP remnant inheritance using live cell imaging in a total of three independent experiments. (F) Duration of cilia re-formation in cells, which kept a ciliary remnant during mitosis plotted for the individual cells. T_0=after cytokinesis.

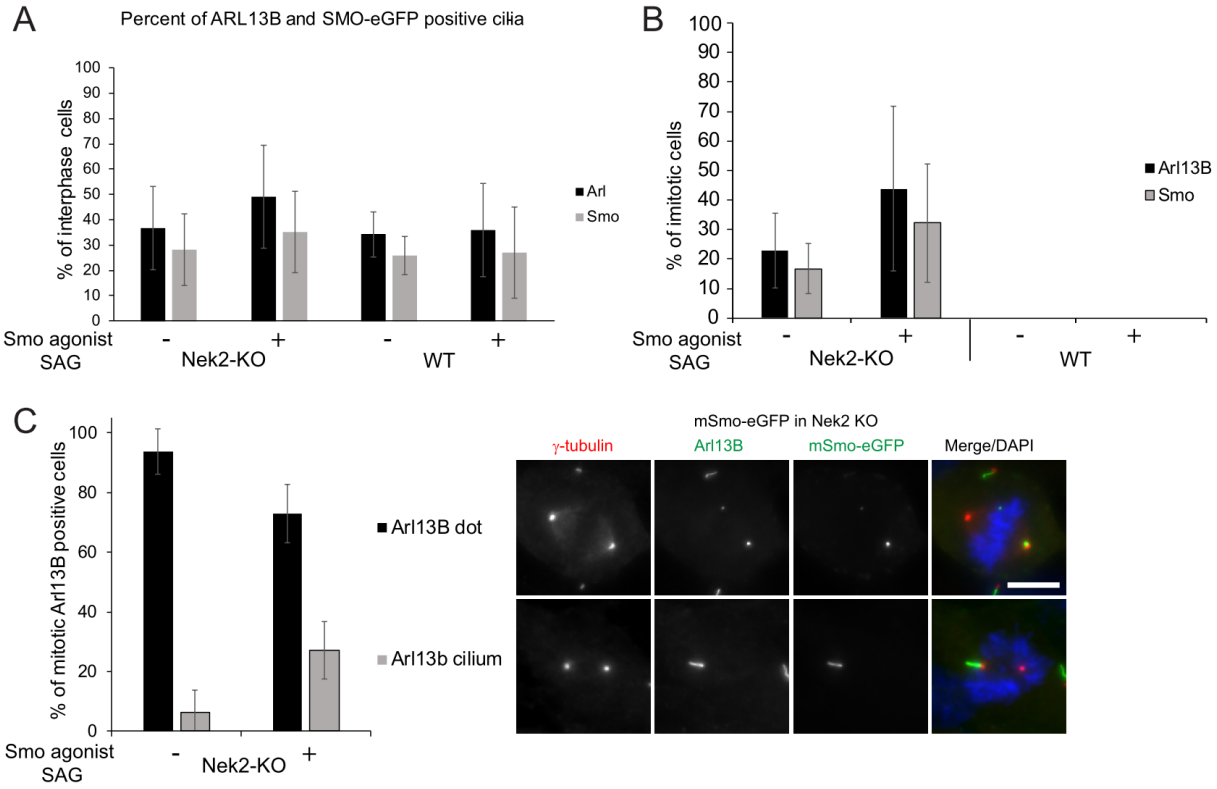

Figure 44. A ciliary remnant in mitotic Nek2 KO cells leads to the asymmetric inheritance of ciliary signaling components. (A) Percent of interphase cells with an Arl13B or SMO-eGFP positive cilium. SMO-eGFP expression was induced in Nek2 KO and WT RPE cells with and without SAG treatment. Cells were fixed and stained for Arl13B. Nek2 KO without SAG (N=658), Nek2 KO SAG (N=1236), WT without SAG (N=334), WT SAG (N=696). (B) Inheritance of SMO-eGFP as a remnant was quantified in inducible SMO-eGFP expressing Nek2 KO and WT RPE cells with and without SAG treatment. Cells were serum starved for 24 h, followed by 24 h serum re-stimulation to stimulate the formation of a ciliary remnant. SAG treatment was combined with the serum re-stimulation for 24 h. Cells were fixed and stained for Arl13B. Three independent experiments were performed. Nek2 KO without SAG (N=367), Nek2 KO SAG (N=522), WT without SAG (N=124), WT SAG (N=298). (C) Additionally, it was distinguished between cells inheriting a dot-like remnant or a cilium like structure. Nek2 KO without SAG (N=84), Nek2 KO SAG (N=262). Cells were fixed and stained for Arl13B. γ-tubulin was used as a centrosome reference and DAPI stained the DNA. Scale bar is 10 µm.
All results show the average ± standard derivation of the performed repetitions.

Lastly, I was interested if the ciliary remnant in Nek2 KO cells is a result of disturbed CP110 removal. During cilia formation in G1 and G0 cells, TTBK2 recruitment by

Cep164 induces removal of the CP110-CEP97 inhibitory complex (Introduction part 1.4.1., Figure 5). I hypothesized that the remanence of Cep164 on the mother centrosome during mitosis might trigger TTBK2 dependent CP110 removal. This could cause the ciliary remnant and premature cilia assembly in Nek2 KO cells. To test this idea, I analyzed the ciliogenesis inhibitor CP110 in RPE1 WT compared to Nek2 KO cells throughout the cell cycle (Figure 45). Quantitative image analysis revealed no difference between RPE1 WT and Nek2 KO cells concerning the behavior of CP110. CP110 stayed on both centrosomes in WT and Nek2 KO cells. Neither was it removed, nor displayed it a higher asymmetry on one centrosome in Nek2 KO cells (Figure 45A). In contrast to its target Cep164, TTBK2 diminished from the mitotic centrosomes in both cell types (Figure 45B), as described previously for RPE1 WT cells (Figure 20C). It must be noted, that in both, WT and Nek2 KO cells, a few mitotic cells displayed one CP110 dot on one centrosome but two on the other. However, in those Nek2 KO cells having this phenotype, I could not observe a correlation of removal of one of the CP110 dots and Arl13B remnant occurrence (data not shown). Together, this indicates that regulation of CP110 removal is not connected with the Nek2 dependent prevention of cilia assembly or cilia disassembly prior to mitosis.

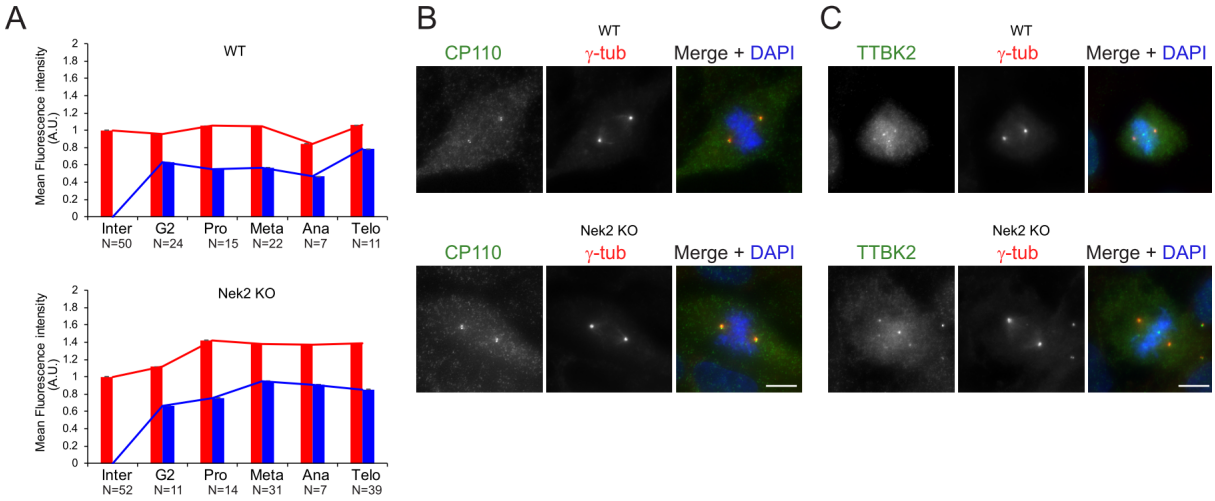

Figure 45. Nek2 KO cells keep a ciliary remnant despite the presence of CP110 on the mother centrosome. (A) Quantification of cell cycle-dependent behavior of CP110 in RPE1 WT vs. Nek2 KO cell. The levels (pixel intensities) of the indicted appendage protein were measured at each centrosome (centrosome 1 and centrosome 2) during the indicated cell cycle phases. The average intensity of the interphase staining was set to one and the values for the second centrosome were set to zero because just one centrosome exists in this cell cycle phase. The different phases of the cell cycle were determined based on centrosome distance and DNA condensation. Graphs depict fluorescence intensity in arbitrary units (A.U.). Numbers below in the bars represent the total number of cells analyzed for each condition. (B) Cells were fixed and stained for CP110. γ-tubulin was used as a centrosome reference and DAPI stained the DNA. Scale bar is 10 µm. (C) RPE1 WT and Nek2 KO cells were fixed and stained for TTBK2. γ-tubulin was used as a centrosome reference and DAPI stained the DNA. Scale bar is 10 µm.

3.3.11 Interaction studies for Nek2 and appendages

The results shown above clearly indicate Nek2's involvement in the mitotic release of distal appendages. Therefore, I next asked if the centrosome appendages are direct targets of Nek2. I employed the yeast two-hybrid system for the first screen of interactions. I analyzed the interaction between Nek2, Nek2-KD, and the non-catalytic C-terminus of Nek2 (Nek2-C) (Introduction, Figure 11) and several truncations plus full-length versions of the centrosome appendages (Figure 46). Truncations were chosen dependent on functional domains. Here, LRRC45, Cep123, SCLT1, and Cep83 constructs were obtained from Bahtyiar Kurtulums and Jakob Schuy. FBF1 and ODF2 constructs were generated in this study. For Cep164, in addition to the full-length construct, the N- and C-terminal domains were used because the coiled-coil domains in the middle of the protein frequently yield false positives in yeast two-hybrid screenings due to nonspecific interactions with other coiled-coils (sub-cloned truncations obtained from Schmidt et al. 2012).

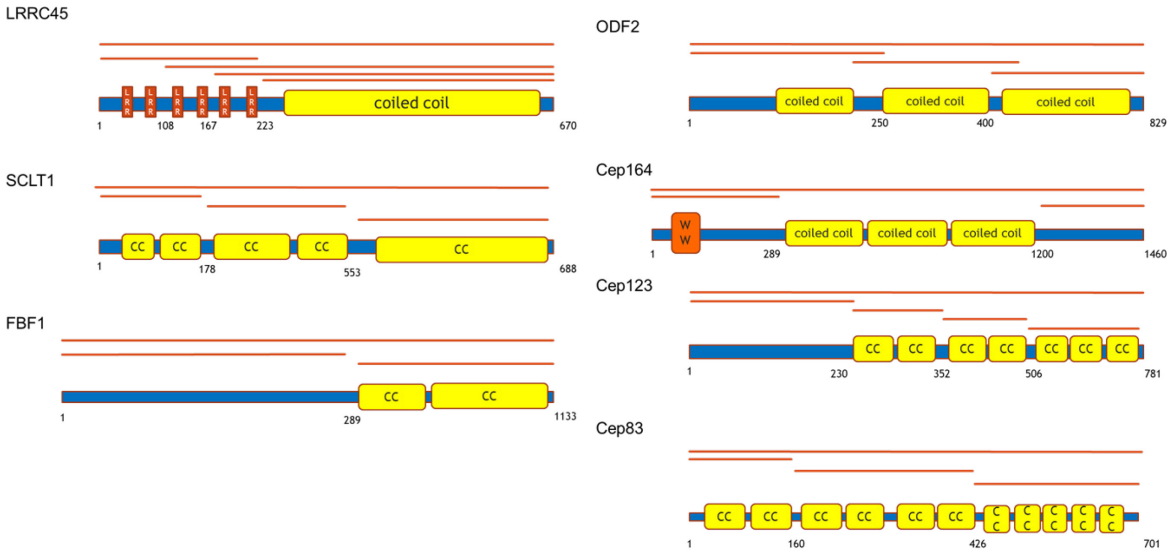

Figure 46. Full-length construct and truncations of appendages used for the yeast two-hybrid screen to find Nek2 interactors. Schematic representation of existing domains in appendage proteins. Numbers represent amino acid positions. The orange lines indicate the yeast two-hybrid truncated constructs created. Coiled-coil (if abbreviated =CC), WW= tryptophan/tryptophan domain, LRR= Leucine reach repeat. LRRC45, Cep123, SCLT1, and Cep83 constructs were a kind gift from Bahtyiar Kurtulums and Jakob Schuy.

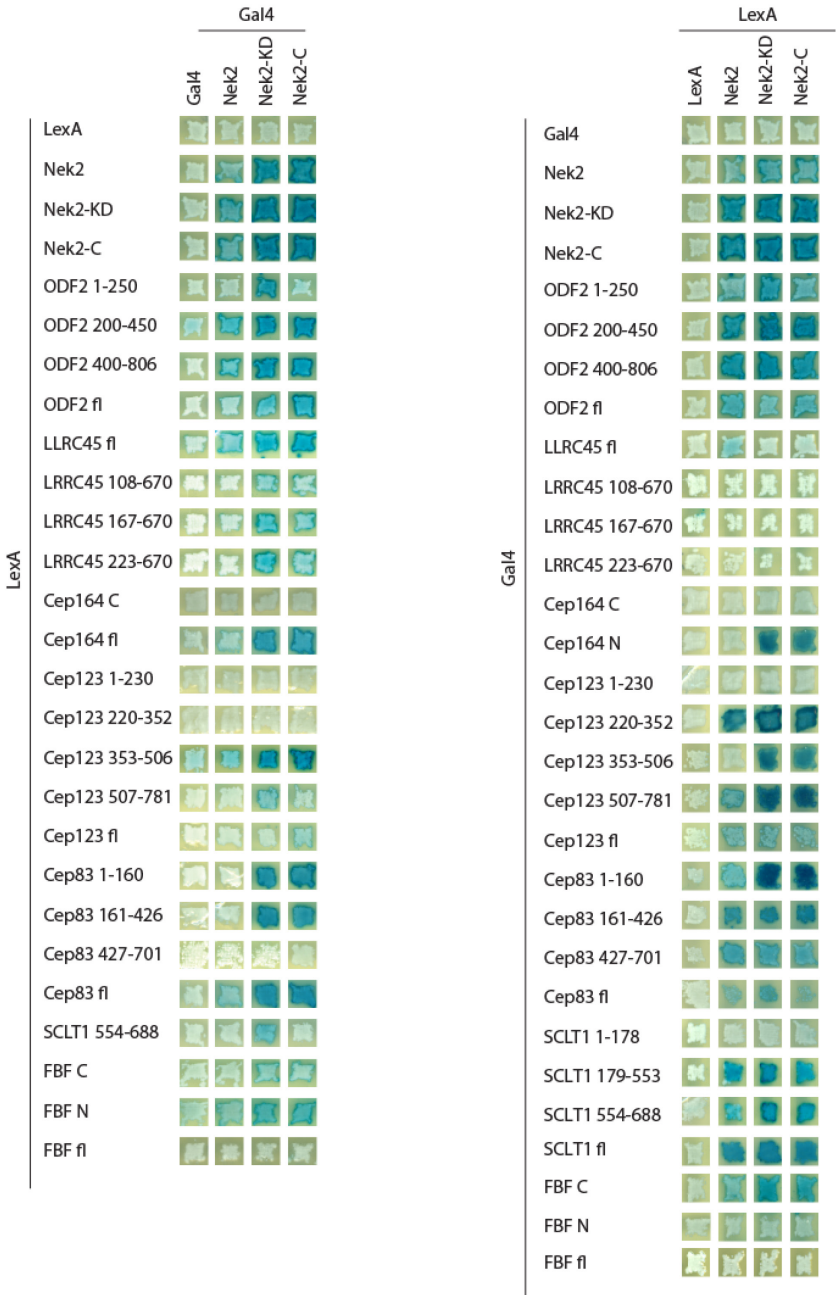

Figure 47. Nek2 directly interacts with appendages in a yeast two-hybrid screen. Yeast two-hybrid assay for mapping the interactions between LexA and Gal4 fusion proteins, as indicated. Development of blue color indicates protein interaction. A representative experiment out of two independent repetitions is shown.

In summary, one or more truncations of all appendages displayed interaction with Nek2 in a yeast two-hybrid screen (Figure 47). Many interactions were stronger with the kinase-dead version of Nek2 than with the WT version. This is in line with the dominant-negative effect and the stronger accumulation of Nek2-KD at the centrosome observed upon overexpression in RPE1 cells (Part 3.3.3). All ODF2 truncations interacted with the Nek2 constructs in both directions, except the N-terminal region (codons 1-250), which interacted with Nek2-KD in one direction. LRRC45 was used as a positive control (He et al., 2013). Although full-length LRRC45 interacted in both directions with Nek2, the truncated versions interacted with Nek2-KD and the Nek2 C-terminus only in one direction.

The full-length and N-terminal region of Cep164 interacted with Nek2-KD and Nek2-C. Only one region of Cep123 (codons 353-506) interacted in both directions with Nek2-KD and Nek2C. Cep83 full-length interacted in both directions with all Nek2 constructs and two of the truncations interacted in both directions with Nek2-KD and Nek2-C. The

C-terminal region of SCLT1 interacted in both directions with Nek2-KD. The N-terminus of FBF1 interacted in one direction with Nek2, while FBF-C interacted in the other direction in the yeast two-hybrid screen. The results for interactions in both directions are summarized in Table 4.

Table 4. Summary of positive interactions between Nek2 and appendages in both directions via yeast two-hybrid

Interaction in both directions?	Nek2	Nek2 KD	Nek2-C
ODF2 1-250			
ODF2 200-450			
ODF2 400-806			
ODF2-fl			
Cep164-C			
Cep164-N			
Cep164-fl			
Cep123 1-230			
Cep123 220-352			
Cep123 353-506			
Cep123 507-781			
Cep123 fl			
Cep83 1-160			
Cep83 161-426			
Cep83 427-701			
Cep83 fl			
SCLT1 1-178			
SCLT1 179-553			
SCLT1 554-688			
FBF-C			
FBF-N			
FBF-fl			

To note, many of the appendage proteins contain coiled-coil domains, which could produce false positives. Hence, I complemented my analysis with other strategies to find true interaction partner. Therefore, I analyzed interactions via Co-immunoprecipitation (Co-IP) and started optimizing a kinase assay to find true phosphorylation partner and sites. In contrast to the yeast two-hybrid screen, Nek2 and Nek2-KD, tagged with GFP, were only co-immunoprecipitated with ODF2-FLAG and not with Cep83, Cep123 (Figure 48A), Cep164 and SCLT1 (not shown).

Additionally, I optimized a kinase assay for Nek2 and Nek2-KD using Nek2 kinase isolated from HEK cells. In parallel, first appendage constructs were purified, which can be used in follow-up studies to find Nek2 interactors (Figure 48B and C). Expressed Nek2-Flag was efficiently immunoprecipitated with M2 beads and purification of the active construct could be shown by its autophosphorylation (Fry et al., 1999) in the radioactive blot (Figure 48D). In Figure 48D, LRRC45 C-terminus (codons 223-260), tagged with MBP was used as a positive control (He et al., 2013). However, the loading amount of this protein was too small to allow detection and must be optimized.

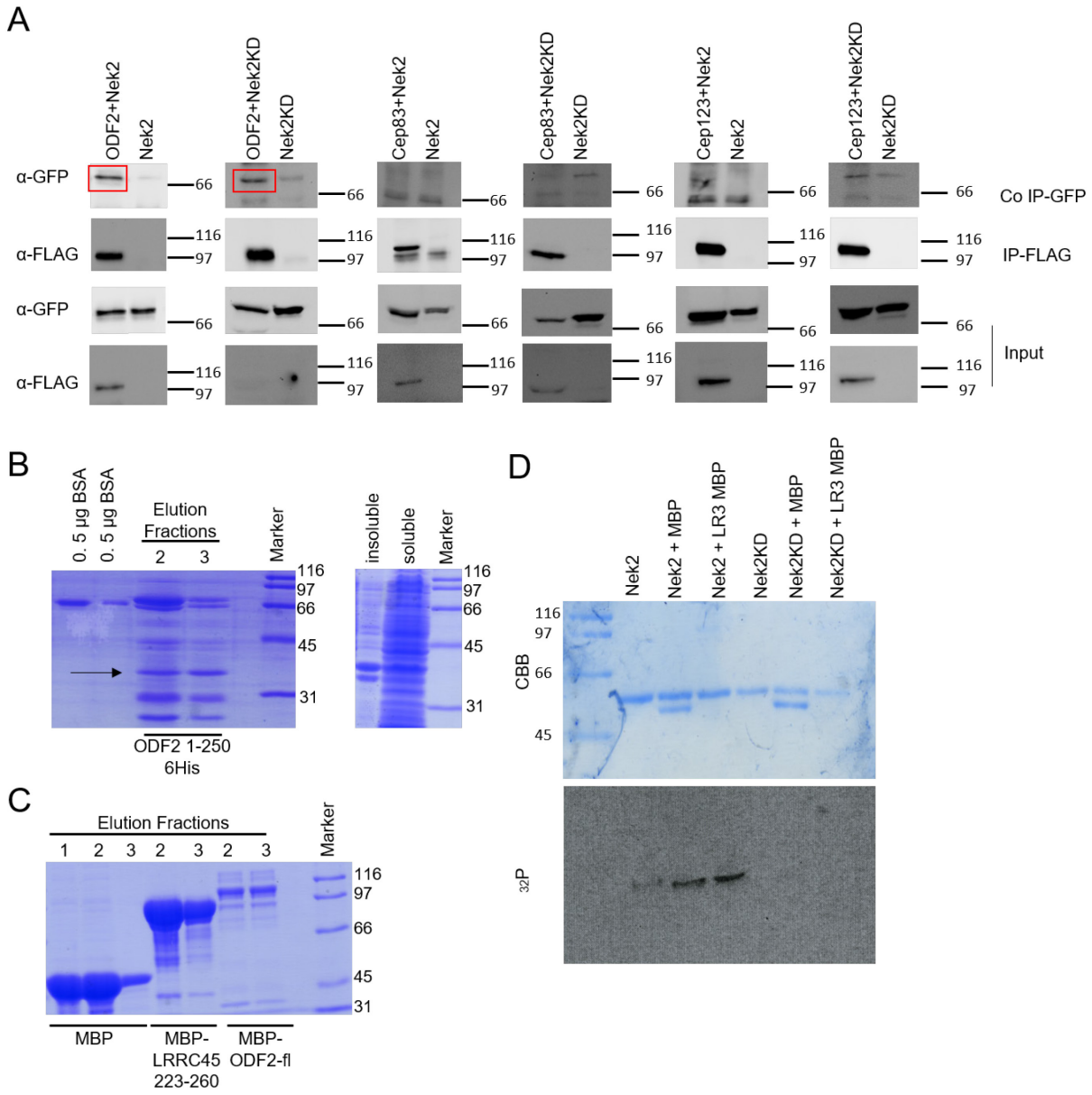

Figure 48. Nek2 interacts with ODF2. (A) HEK293T cells were transiently co-transfected with the indicated constructs fused to FLAG and GFP tagged Nek2. Immunoprecipitations (IP) were performed using anti-FLAG agarose and interacting proteins were detected by immunoblot. Not shown: Likewise, no interaction of Nek2/Nek2-KD with SCLT1 and Cep164 was observed. Note, ODF2-FLAG expression was not detectable at the loaded protein amount in the input for Nek2-KD Co-IP. ODF2 and Nek2 Co-IP vs. the control (only Nek2) were separated on the membrane and aligned for the figure. (B) Coomassie Brilliant Blue-stained SDS-PAGE gels showing the expression and purification of ODF2 1-250 6-His. Note, the kept elution fractions are not pure but contain the expected fragment of the fusion protein (33.17 kDa), which is seen in the soluble and insoluble extract after induction. (C) Purification of the negative control MBP (~50 kDa), positive control LRRC45 223-260-MPB (~100 kDa) and MBP-ODF2 full length (fl) (~140kDa). (D) Purified Nek2-FLAG and either catalytic active (Nek2) or kinase-dead (Nek2-KD) were incubated alone or with truncated LRRC45 223-260-MBP fusion (LR-C). MBP was used as a negative control. Samples were subjected to SDS-PAGE followed by autoradiography (32 P) and Coomassie Brilliant blue staining (CBB). Expected sizes LR-C-MBP ~100 kDa, Nek-FLAG ~55 kDa, MBP 50 kDa.

Because the Nek2-dependent release of appendages could also be mediated by an indirect interaction and does not necessarily require direct phosphorylation of the

released appendages, the interaction studies need to be complemented with an unbiased strategy. Therefore, I created cell lines expressing Nek2 and Nek2-KD BirA fusion constructs under the control of an inducible promotor for proximity-dependent biotinylation (BioID). The fusion constructs are expressed and can be used in follow-up studies (Figure 49).

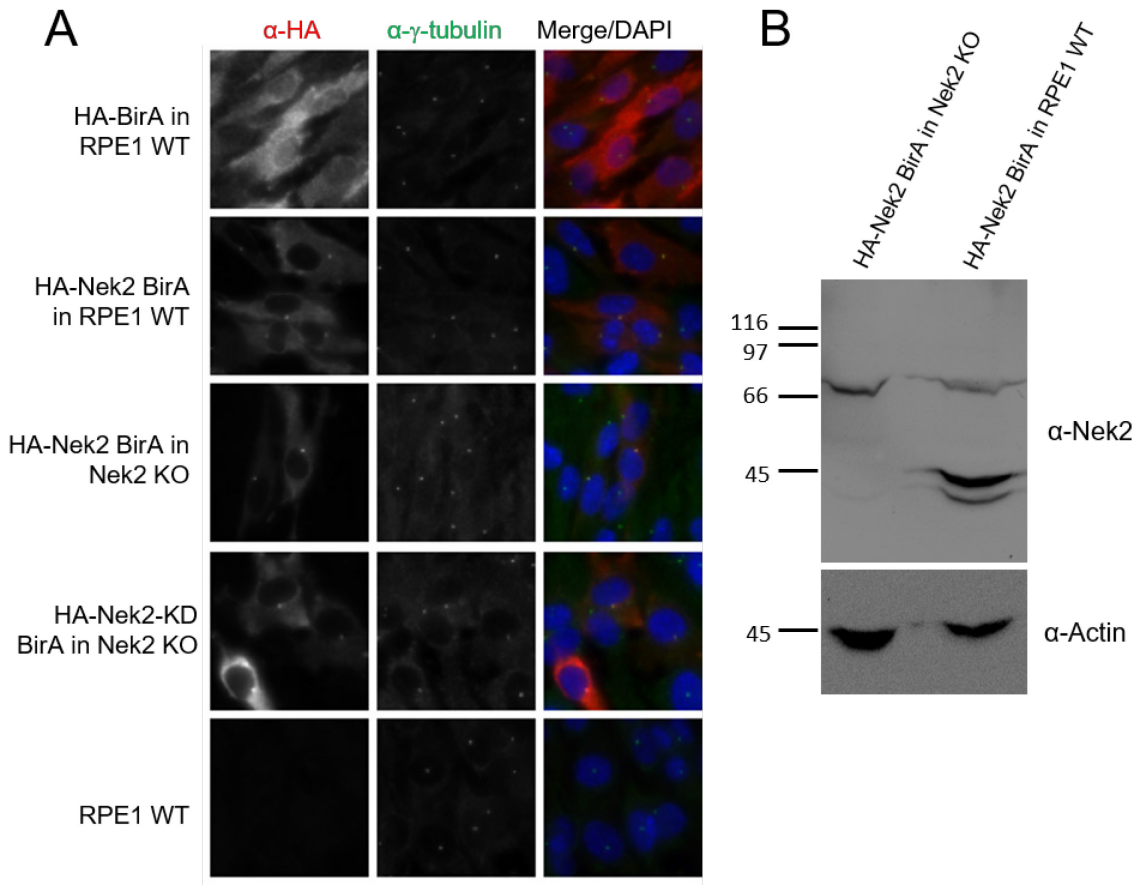

Figure 49. Doxycycline-inducible HA-BirA-Nek2 cell lines were generated. (A) Representative images showing fixed indicated cell lines upon doxycycline induction γ-tubulin was used as a centrosome reference and DAPI stained the DNA. A specific antibody against Nek2 was used to visualize the fusion constructs in western-blot. (B) Western-blot showing expression of the fusion constructs Nek2-BirA-HA in Nek2 Ko and RPE1 WT cells. Sizes: Nek2 ~ 44 kDa, BirA-HA 33 kDa, Fusion 77 kDa. Actin was used as a loading control.

Interestingly, in the yeast two-hybrid assay an interaction of WT Nek2 with full-length versions was only observed in both directions for ODF2, Cep83 and the positive control LRRC45 (Figure 47, Table 4). Additionally, a co-precipitation was only seen with ODF2 (Figure 48A). Hence, it is tempting to speculate that Nek2 phosphorylates core components that are not released during mitosis, resulting in the release of adherent distal appendages versus direct phosphorylation of those (Figure 50).

It could still be that the other interactions seen in the yeast two-hybrid are too transient to be captured via Co-IP in the used conditions. This issue can be solved by follow-up studies using BioID, SILAC and kinase assays.

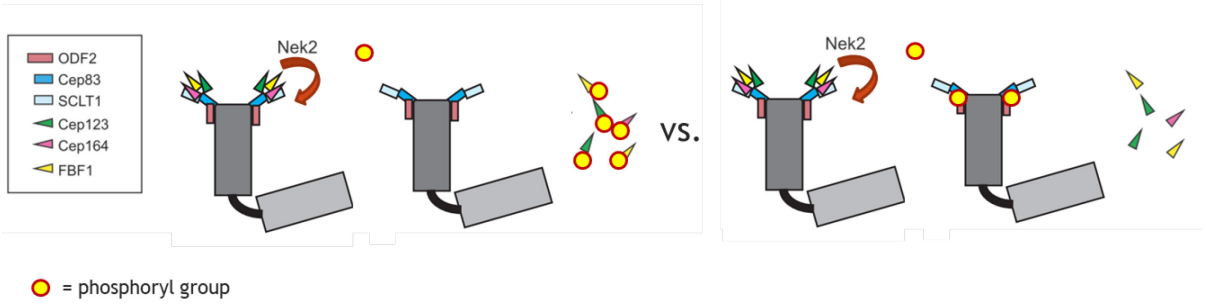

Figure 50. Scheme for potential models for Nek2 dependent appendage phosphorylation. Appendages, which are released upon mitotic entry, could either be directly phosphorylated by Nek2 (left) or the release could be triggered by phosphorylation of a core component (ODF2/Cep83) that are required for their assembly (Introduction part 1.2., Figure 2). It is not yet verified if shown appendages are true phosphorylation targets of Nek2.

3.4 Generation of an RPE1 ODF2 KO cell line

As mentioned in the last section, one possibility for appendage regulation via Nek2 could be phosphorylation of the appendage core component ODF2. According to this hypothesis, Nek2 activity might be needed to e.g. change the confirmation of ODF2 upon phosphorylation, leading to the disassembly of adjected appendages like Cep164. Interaction of ODF2 and Nek2 was shown before by proximity label mass spectrometry (Gupta et al., 2015) and could be captured in this study via Co-Ip (Figure 48). However, it is not clarified if distal appendages are dependent on ODF2. This would be the prerequisite for the above-mentioned hypothesis.

ODF2 was proposed to be required for distal appendage establishment in mouse embryonic stem cells (Ishikawa et al., 2005; Tateishi et al., 2013) and Figure 51A. In contrast, distal appendage assembly was not affected upon depletion of ODF2 in RPE1 cells (Kuhns et al. 2013, Tanos et al. 2013). To test whether this phenotype is a result of incomplete depletion using siRNA and if distal appendages require ODF2 in RPE1, I performed analysis in ODF2 KO cells. I used CRISPR/Cas9 to produce an ODF2 KO cell line and investigated whether ODF2 regulates distal appendage formation and influences the behavior of distal appendages by Nek2 in RPE1 cells (Figure 51-53). I designed a guide RNA to target Exon 6 of human ODF2, which is the first coding Exon in the most prominent isoform cenexin1 in somatic cells (Figure 51B). KO was achieved in both alleles leading to premature stop codons as revealed by sequencing (Figure 51C). Western-blot and immunofluorescence verified complete KO (Figure 51D).

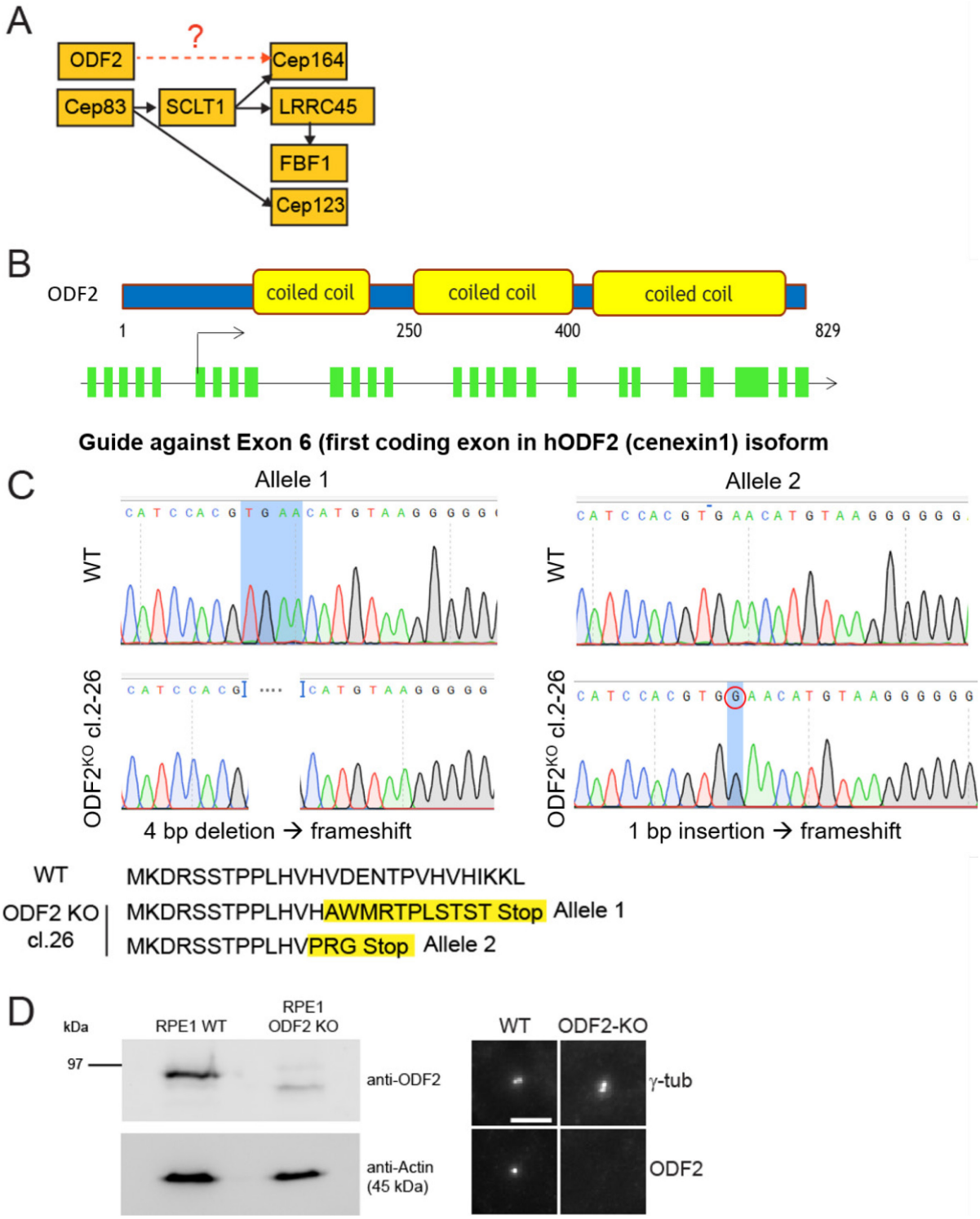

Figure 51. Creation of an RPE1 ODF2 KO cell line. (A) Hierarchy of distal appendages as previously published (Kurtulmus et al., 2018; Tanos et al., 2013). The dependency of Cep164 on ODF2 is controversial (Ishikawa et al., 2005; Tateishi et al., 2013; Kuhns et al., 2013, Tanos et al. 2013). (B) Schematic representation of the ODF2 KO strategy using CRISPR Cas9 targeting exon 6, the first coding exon for the hODF2 (cenexin 1) isoform. (C) Sequencing results and resulting frameshift mutations led to a premature stop of translation. (D) Western-blot using total cell lysate and representative images of fixed RPE1 WT and RPE1 ODF2 KO cells. A specific antibody against ODF2 was used to visualize the loss of the proteins in the ODF2 KO cell line. Actin was used as a loading control. γ-tubulin was used as a centrosome reference and DAPI stained the DNA. Scale bar is 5 µm.

3.4.1 ODF2 knockout does not affect distal appendage assembly and ciliation

To investigate whether ODF2 regulates distal appendage formation and influences the behavior of distal appendages by Nek2 in RPE1 cells, I analyzed these questions in the generated CRISPR/Cas9 ODF2 KO cell line (Figure 52 and 53). The lack of ODF2 disrupts subdistal appendage formation, as confirmed by EM (Figure 52C), and led to a drastic reduction of centriolin and Cep128 centrosomal levels (Figure 52A and B) (Ishikawa et al., 2005; Mazo et al., 2016; Tateishi et al., 2013), confirming a functional KO.

In contrast, the levels of Cep164, Cep123, LRRC45, FBF1, Cep83, and SCLT1 at interphase centrosomes remained unchanged in the absence of ODF2 in comparison to WT cells (Figure 52D). ODF2 KO cells were proficient in cilia formation (Figure 52E), showing that distal appendages were functional. In contrast to previous data (Ishikawa et al. 2005, Tateishi et al. 2013, Kuhns et al. 2013), no significant decrease in ciliation was observed after 24 or 48 h of serum starvation. Likewise, cilia length was not affected (Figure 52F). This data shows that neither Cep164 nor the other distal appendages require ODF2 for their assembly.

3.4.2 Regulation of distal appendages by Nek2 does not require ODF2

Finally, I wanted to confirm the assumption that Nek2 dependent mitotic release of appendages is independent of ODF2. In theory, if ODF2 is required for this process, normally released appendages should also stay asymmetric in ODF2 KO cells, like in Nek2 KO cells. Cep164, Cep123, and LRRC45 centrosomal levels decreased during mitosis in ODF2 KO cells similarly to WT cells (Figure 53A), indicating that ODF2 is not required for distal appendage regulation. In agreement with this conclusion, centrosomal appendage levels still decreased in interphase upon Nek2 overexpression in ODF2 depleted cells (Figure 53B-D). Furthermore, Cep164, Cep123, and LRRC45 persisted at the mother centriole during mitosis upon Nek2 knockdown in ODF2 KO cells (Figure 53E and F). Together, these analyses show that ODF2 is dispensable for distal appendage formation and regulation by Nek2 in RPE1 cells.

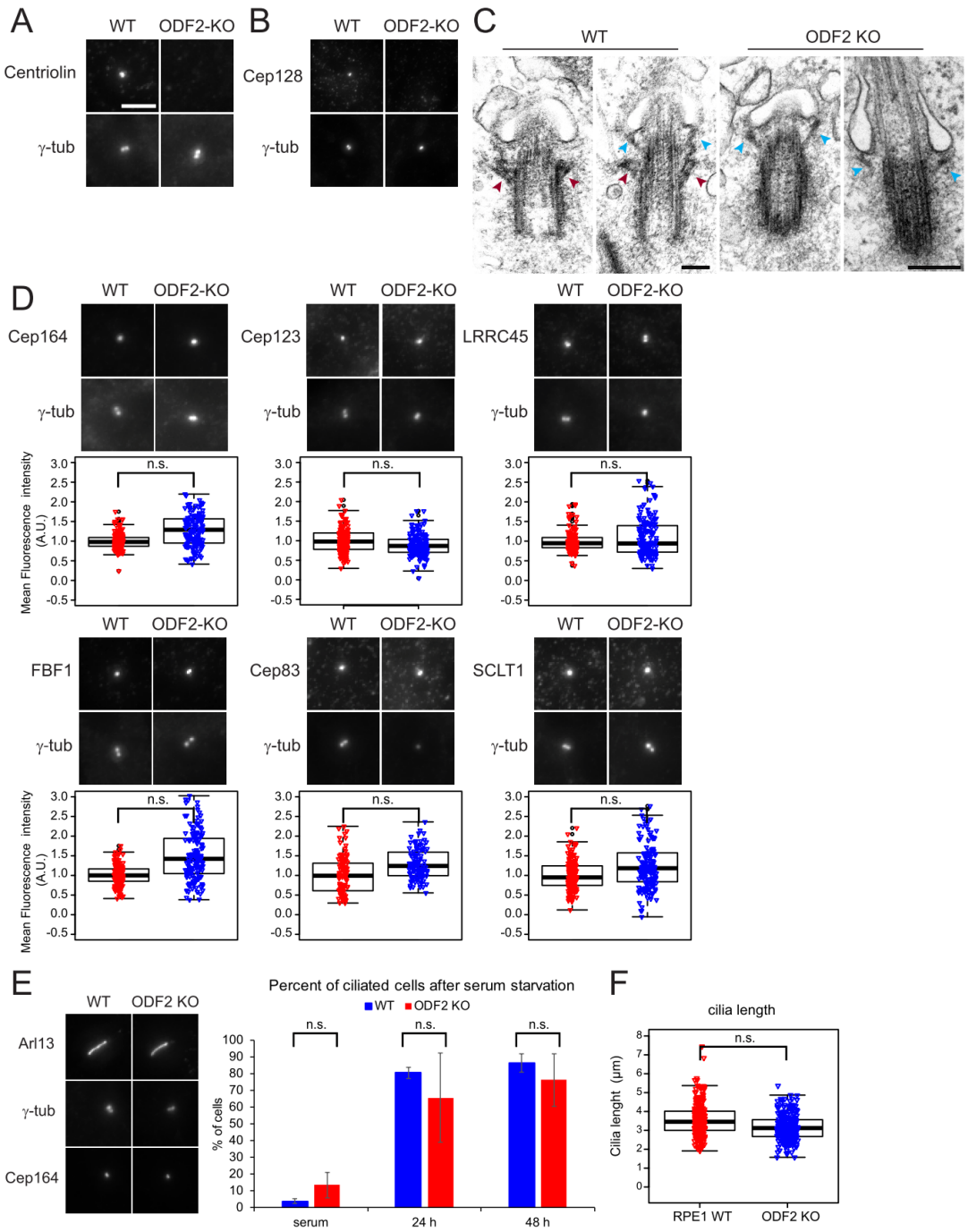

Figure 52. Distal appendages are not affected after ODF2 KO. Representative images of fixed RPE1 WT and RPE1 ODF2 KO cells. Specific antibodies against Centriolin (A) and Cep128 (B) were used to visualize the loss of these proteins in the ODF2 KO cell line. γ-tubulin was used as a centrosome reference. Scale bar is 5 µm. (C) Electron micrographs showing longitudinal serial sections of RPE1 WT and ODF2 KO cells. Cells were serum starved for 48 h before fixation for trans-mission electron microscopy (TEM) analysis. Red arrows indicate subdistal appendages, blue arrows show distal appendages. Early stages of ciliogenesis are shown. Scale bar is 200 nm. Serial sections and electron microscopy were performed by Annett Neuner (ZMBH, Heidelberg). (D) Representative images showing fixed RPE1 WT and RPE1 ODF2 KO interphase cells using the indicated antibodies for distal appendage proteins. γ-tubulin served as a marker for centrosomes. Whisker-Box plots show the normalized quantification of appendage signal at the centrosome in RPE1 WT and ODF2 KO cells. 50 cells were analyzed per staining and cell type in each of three independent experiments. Cumulative data from three experiments is shown. (E) Representative images of fixed RPE1 WT and RPE1 ODF2 KO interphase cells. Specific antibodies were used to visualize cilia marked by Arl13B and the appendage Cep164 in the ODF2 KO cell line. γ-tubulin served as a marker for centrosomes. Bar graphs show the average of two independent experiments +/- standard derivation of ciliated cells in fixed samples using

Arl13B as a cilia maker after 0, 24 and 48 h of serum starvation. N=248, 190, 194 RPE1 WT and N= 78, 244, 265 ODF2 KO cells were quantified for 0, 24 and 48 h of starvation, respectively. (F) Whisker-Box plot shows quantification of ciliary length in RPE1 WT vs ODF2 KO cells upon 48 h of serum starvation. Plot shows cumulative data from three independent experiments. In total, 224 and 248 cilia were measured in RPE1 WT and ODF2 KO cells, respectively.
Significance levels: ns P > 0.05, *: P ≤ 0.05, **: P ≤ 0.01, ***:P ≤ 0.001, ****: P ≤ 0.0001.

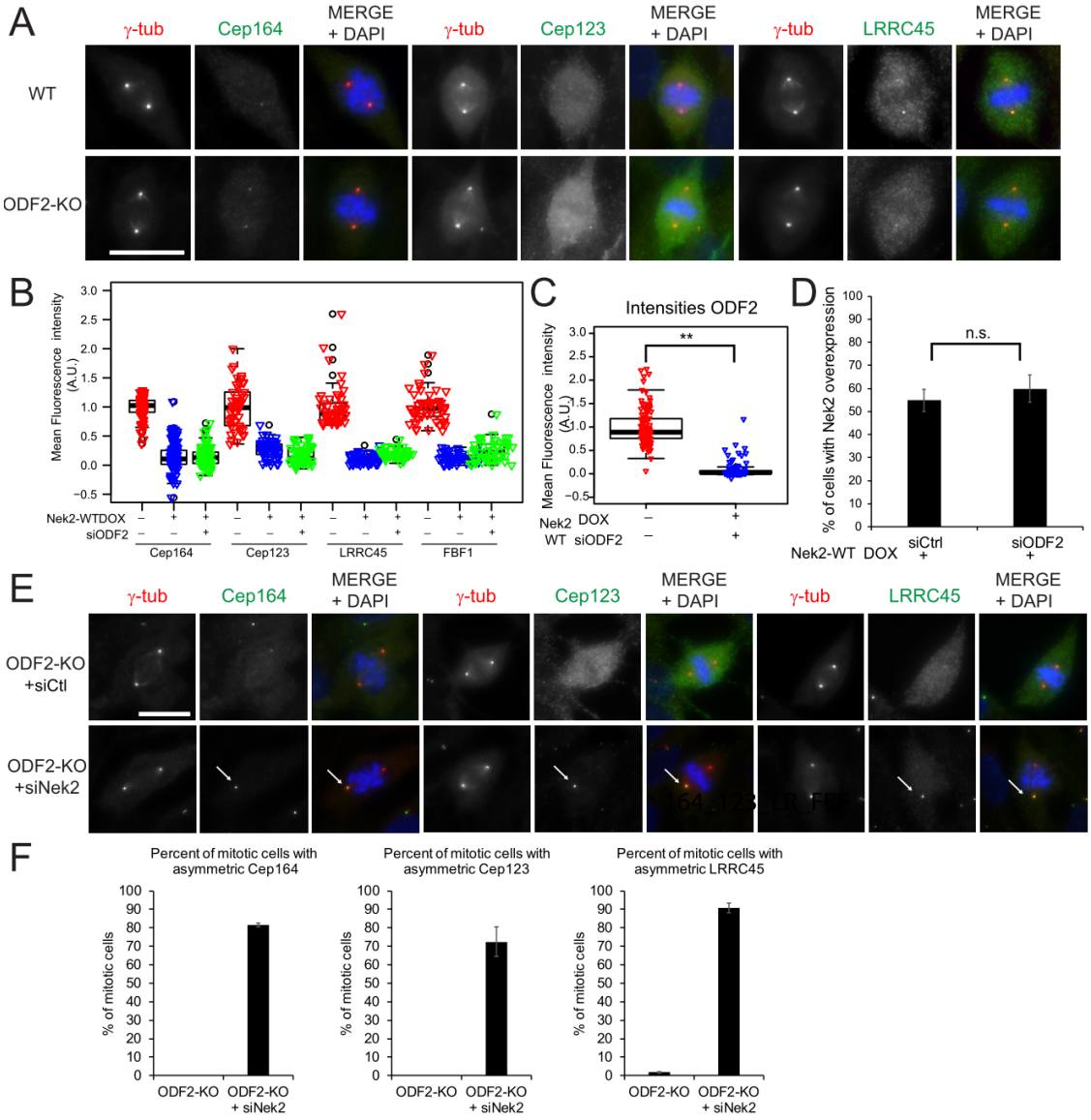

Figure 53. Nek2 induced centrosomal appendage release is independent of ODF2. (A) Representative images of mitotic RPE1 WT and RPE1 ODF2 KO cells using the indicated antibodies for distal appendage proteins. γ-tubulin (red) and DAPI (blue) served as markers for centrosomes and nuclei, respectively. Scale bar is 20 µm. (B) Box/dot plots show quantification of the indicated appendage intensities with and without doxycycline (DOX) inducible Nek2-WT overexpression upon control (Ctrl) or ODF2 siRNA. N=150 cells per condition for Cep164 and N=50 per condition for the other appendages. (C) Box/dot plot shows quantification of ODF2 intensity upon control (Ctrl) or ODF2 siRNA for the experiment shown in Figure 53B. N=98 cells per condition. (D) Quantification of Nek2-WT overexpressing cells identified by the mNeonGreen signal to show efficient overexpression in Figure 53B. N=229 of Ctrl and N=265 of siODF2 cells were quantified, respectively. Bar graphs show the average of two independent experiments +/- standard derivation (E) Representative images of mitotic RPE1 ODF2 KO cells using the indicated antibodies upon control (Ctrl) and Nek2 siRNA. γ-tubulin (red) and DAPI (blue) served as markers for centrosomes and nuclei, respectively. Scale bar is 20 µm. (F) Quantification of mitotic cells with asymmetric appendage signal during mitosis for the indicated proteins. For siCtrl N=128,72,116 and for siNek2 N=108,62,72 mitotic cells were quantified for Cep164, Cep123, and LRRC45, respectively in two independent experiments.
Significance levels: ns P > 0.05, *: P ≤ 0.05, **: P ≤ 0.01, ***:P ≤ 0.001, ****: P ≤ 0.0001.

4. Discussion

4.1 Centrosomal appendages and associated proteins display common dynamics during mitosis in stem- and differentiated cells

In previous studies, appendage proteins were intensively studied regarding their localization and assembly hierarchy on interphase centrosomes (Kashihara et al., 2019; Kurtulmus et al., 2018; Mazo et al., 2016; Tanos et al., 2013; Yang et al., 2018). However, only uncomplete analysis about their dynamics and regulation during mitosis exist (De Harven and Dustin, 1960; Graser et al., 2007; Kong et al., 2014; Schmidt et al., 2012; Sillibourne et al., 2013; Tanos et al., 2013; Vorobjev and Chentsov, 1982). Further, it needed to be solved if different types of mitotic behavior can be identified for specific subsets of appendages, if centrosome asymmetry can be observed between older and younger centrosome during mitosis and whether this influences the cell fate of the resulting daughter cells. Additionally, distal appendages are essential for initial steps of ciliation (Graser et al., 2007; Schmidt et al., 2012; Tanos et al., 2013, Yang et al. 2018). Consequently, solving their cell cycle specific regulation will help also to understand how ciliogenesis and hence signaling during development and tissue maintenance are coordinated with the cell cycle.

In this study, I systematically analyzed the behavior of key centrosome appendages and other centrosome components throughout the cell cycle in the differentiated and ciliating RPE1 cell line versus HSPCs and the hematopoietic cell line KG1a, which displays progenitor-like properties (results part 3.1.). A subset of appendages was drastically reduced on mitotic centrosomes, while core components stayed at the older centrosome.

As previously reported (Kong et al., 2014; Schmidt et al., 2012; Sillibourne et al., 2013), the levels of Cep164 and Cep123 at the mother centriole were drastically reduced prior to mitosis in RPE1 cells, KG1a cells and HSPCs. Additionally, the binding partner of Cep164, TTBK2, was lost from centrosomes prior to mitosis. Likewise, LRRC45 was released from mitotic centrosomes in all analyzed cell types. Conversely, Cep164 was found associated with the centrioles throughout mitosis in U2OS cells and mouse apical progenitors (Graser et al., 2007; Paridaen et al., 2013), indicating cell type -and interspecies specific differences.

FBF1 remained at the mother centrosome in RPE1 cells, as reported previously for IMCD3 cells (Wei et al. 2013), while it had decreased levels in mitotic hematopoietic cells like shown before in HeLa cells (Kong et al. 2014). This indicates a cell-type

specific regulation of this appendage protein. In the analysis of Bowler et al. (2019), FBF1 levels were reduced in half of the RPE1 population. This phenotype was not detected in this study and might be due to clonal differences in the cultured RPE1 cell lines or different analysis methods.

Notably, even decades ago, ultrastructural analysis has suggested that the subdistal appendages are lost from the mother centriole in late G2 and reappear in G1 (Vorobjev and Chentsov, 1982). Consistent with a previous study (Gromley et al., 2003), Centriolin staining diminished at centrosomes during mitosis in all here analyzed cell types. In previous analysis, Centriolin also concentrated at the midbody in RPE1 cells, pointing towards its role in cytokinesis (Gromley et al., 2003; Gromley et al., 2005). I could not observe this pattern in the analyzed cell types in this study. The midbody staining observed by Gromley et al. was specific, as it was reduced upon siRNA targeting Centriolin. Hence, the epitope of the antibody used in this study may not recognize Centriolin at that region or dissimilarities are due to different fixation methods.

In one of the initial studies of Ninein, its signal declined from mitotic centrosomes and total Ninein protein levels were reduced during mitotic phases (Chen et al., 2003). In *Drosophila* stem cells, Ninein localizes asymmetrically on centrosomes, yet is not required for their asymmetric division (Zheng et al., 2016). Asymmetric Ninein localization was also shown in radial glial progenitor cells of the mouse and in rat embryos (Paridaen et al., 2013; Shinohara et al., 2013; Wang et al., 2009) and depletion of this protein resulted in disruption of asymmetric centrosome segregation and depletion of progenitors (Wang et al., 2009). In contrast to studies using neuronal progenitors (Wang et al., 2009; Paridaen et al., 2013; Shinohara et al., 2013), Ninein was not asymmetric in HSPCs and decreased like in the other analyzed non-progenitor cell types in this study. Skin progenitor cells and other polarized tissues in the mouse were reported to require Ninein for proper spindle orientation and cortical microtubule organization (Chen et al., 2014; Lecland et al., 2019). One explanation could be that asymmetric Ninein is only required in specific polarized progenitors, in which oriented division towards niche cells were reported (Yamashita, 2009). Non-polar hematopoietic progenitors may do not display asymmetric distribution of Ninein because they are not dependent on tight regulation of spindle orientation towards their niche. The discrepancy of the asymmetric Ninein pattern (Paridaen et al., 2013; Wang et al., 2009) versus the release during mitosis detected in this study and (Chen et al., 2003) might

also arise from the use of GFP tagged Ninein versus the use of a specific antibody against the endogenous protein. The tagged Ninein used by Paridaen et al. (2013) and Wang et al. (2009) may behave differently than the endogenous protein. Further, the differences could also be a result of species-specific variability as these studies were done in mice. Of note, although Wang et al. (2009) suggested that asymmetric inheritance of the old mother centriole is crucial for the maintenance of the cortical progenitor character, a more recent study failed to detect any correlation of daughter cell fate and centrosome inheritance in granule neuron progenitors in the developing cerebellum (Chatterjee et al., 2018).

The here found centrosome asymmetry of ODF2 throughout mitosis is in line with previous analysis in RPE1 cells (Kong et al., 2014). Likewise association of SCLT1 and Cep83 with mitotic centrioles in all here analyzed cell types is consistent with previous analysis in HeLa cells (Kong et al., 2014).

Bowler et al. (2019) also observed the removing of outer appendage components like Cep164 and maintaining of inner appendage components. The biological significance of the pre-mitotic removal of specific appendages remained uncertain in previous analysis.

Notably, the mitotic behavior of appendage proteins reflects the hierarchical network of their assembly: The assembly of appendage proteins, which were released from the centrosome in mitosis (Cep164, Cep123, LRRC45), was shown to be dependent on the components that stay on the mother centrosome in mitosis (Cep83 and SCLT1) (Kurtulmus et al., 2018; Tanos et al., 2013).

I propose that distal components can be sub-divided into two groups: a stable core composed of Cep83 and SCLT1 and regulated core. The stable core might play a structural role of appendage assembly and is needed for quick re-assembly in the next cell cycle. The pre-mitotic loss of the outer regulated core contributes to cilia disassembly prior to mitosis. Further, it reduces the age gap between the two centrosomes after mitosis to prevent unequal ciliation and signaling in the two new daughter cells (further discussed in part 4.5).

Collectively, these data suggest a common regulation of appendage dynamics with some cell-type specific components, like FBF1. Centrosome asymmetry during mitosis, which can be captured by visualizing ODF2, SCLT1 or Cep83, seems not preliminary dedicated to stem cells, as it was seen in the here analyzed progenitor and differentiated cells. Still, the asymmetry of an appendage complex could be used as a

scaffold to unequally capture cell fate components, which are only expressed in stem cells. Examples for components specifically expressed in stem cells with asymmetric inheritance are CD133/prominin or Numb (Görgens et al., 2014; Kechad et al., 2012). Of note, no difference between RPE1 cells and HSPCs or KG1a cells was observed regarding the mitotic behavior of other centrosomal components and ciliary regulators like CP110, TTBK2 or Arl13B, except the ciliary localization of Arl13B as hematopoietic cells do not form cilia. The reason of cilia absence in hematopoietic cells is not known and, for example, CSPP1, a protein that is important for cilia localization of Arl13 (Akizu et al., 2014; Tuz et al., 2014), is still expressed in the hematopoietic lineage (BloodSpot database). Yet, cilia genes like Arl13B are mutated in some leukemia patients, pointing towards cilia independent roles of these proteins that may be involved in the deregulation of signaling or division in leukemia (Coppe et al., 2017). An Arl13B localization preserved in hematopoietic cells is at the midbody. Some HSPCs and KG1a cells kept the midbody on one daughter cell after division. This phenomenon was also observed in MDCK cells and here may have other significance than the timing of cilia formation (Bernabé-Rubio et al., 2016). Another function of the midbody remnant in symmetrically dividing progenitors is the enrichment of CD133 particles for an extracellular release (Dubreuil et al., 2007). Similarly, HSPCs could use this as a system to balance symmetric versus asymmetric divisions via CD133 distribution.

4.2 Centrosome inheritance does not regulate cell fate in HSPCs

In the first part of this study, I observed that a subset of appendages displays asymmetry and another subset is released during mitosis. Therefore, three main questions arose: Can the visible age asymmetry of centrosomes be correlated with asymmetric divisions in human HSPCs? How is the removal of outer appendage during mitosis regulated? And what is the physiological significance of removing a subset of appendages during mitosis? In this passage, I will discuss my results addressing the first question (results part 3.2.).

In the model organism *Drosophila* and in mouse progenitor cells, the kind of centrosome (young or old) inherited is connected with cell fate in several developmental contexts (Conduit and Raff, 2010; Delgehyr et al., 2005; Januschke et al., 2011; Paridaen et al., 2013; Salzmann et al., 2014; Wang et al., 2009; Yamashita et al., 2007). However, the roles of centrosome inheritance in human HSPC division and mechanistic insights have not been investigated. I showed that mother and

daughter centrosomes can be distinguished by ODF2 staining during mitosis in HSPCs. The next prerequisite to elaborate if this asymmetry has a role in ACD was to find an asymmetrically segregating stem cell marker in HSPCs.

I could not detect asymmetric segregation of Numb and Notch in human HSPCs, which was published for mouse HSCs (Wu et al., 2007). The study of Wu et al. used a mouse transgenic Notch reporter line that expresses GFP under the control of a Notch-responsive promoter (Duncan et al., 2005). Asymmetric Notch signaling might not coincide with asymmetric Notch or Numb protein segregation in hematopoietic cells, although asymmetric Numb protein segregation was observed in this study and in mouse cerebral progenitors (Shen et al., 2002; Wu et al., 2007). Conversely, another study using HSPCs overexpressing a Numb fusion protein cultured on OP9 stromal cells could not confirm asymmetric segregation of Numb (Ting et al., 2012).

Of note, my screen was based on immunofluorescence analysis of fixed samples using HSPCs after three days of culture, of which only a small percentage are quiescent HSCs (Shin et al., 2018). Numb/Notch may already be downregulated in the progenitor population and only present in quiescent HSCs. Alternatively, asymmetric Notch might not be captured by the antibodies used in this study or is restricted to mouse HSCs due to interspecies variability. Further research is required to clarify this topic. The functional relevance of asymmetric Numb segregation in HSCs remains to be demonstrated. Although the study of Wu et al. (2007) gave indirect evidence for the relevance of their reporter by the observation that GFP+ cells have lower NUMB expression level than GFP- cells, the asymmetric segregation of Numb was not directly linked to future daughter cell fates. Also, conditional deletion of Notch1 does not affect HSC-maintenance *in vivo* (Mancini et al., 2005).

I also preliminary analyzed CDC42 in HSPCs and KG1a cells (not shown) because of its reported asymmetry in HSCs (Florian et al., 2012; Florian et al., 2018), which could not be reproduced in this study. Florian et al. (2012, 2018) found that with aging the frequency of polar HSCs defined by a polar distribution of tubulin and CDC42 in the cytoplasm decreases. These studies further found that the polarity status before mitosis influences asymmetric versus symmetric divisions. Aged apolar HSCs favored self-renewing symmetric divisions, while young polar HSCs favored asymmetric divisions (Florian et al., 2018). I did not perform an in-depth analysis of CDC42 because I could not observe a clear asymmetry in HSPCs derived from cord blood or peripheral blood. However, a careful analysis of CDC42 in HSCs from cord blood

compared to peripheral blood-derived HSCs from healthy aged donors could reveal if the CDC42 asymmetry observed by Florian et al. (2018) is mouse specific or also influences asymmetric divisions in humans HSPCs.

In summary, I could not replicate the findings of asymmetric protein segregation in the mouse system in human HSPCs. In contrast, I could reproduce the asymmetric segregation of proteins published for human HSPCs by the group of Bernd Giebel, namely the tetraspanin CD63 and progenitor marker CD133 (Beckmann et al., 2007; Görgens et al., 2014).

Beckmann et al. (2007) revealed that *in vitro* cultured HSPCs expressing low CD63 levels are more immature due to a higher amount of long-term culture initiating cells. Although a direct functional correlation is missing, this result could suggest that CD63 segregates to the differentiating daughter. Endosomes were also found to segregate asymmetrically in *C. elegans* embryos (Andrews and Ahringer, 2007). This hints towards the assumption that during mitosis the segregation of certain endosomes needs to be controlled. A link between the endosomal compartment and mechanisms governing ACDs was discovered in *Drosophila*. Here, they are responsible for different Notch signaling in the two daughter cells of dividing sensory organ precursors. The Notch receptor and its ligand Delta are found mostly in intracellular vesicles, called SARA endosomes, which segregate in a higher number to the signaling posterior daughter cells (Coumailleau et al., 2009). Little is known about the role of lysosomes (marked by CD63) in HSPCs and the functional relevance of their asymmetric segregation remains unclear. In this study, a preliminary correlation of CD63 segregation with centrosome asymmetry defined by ODF2, gave contradictory results in HSPCs and KG1a cells, which needs further clarification.

Hence, I continued the in-depth analysis of centrosome asymmetry and asymmetric cell fate with the most promising marker for ACD in human HSPCs, namely CD133. According to the revised model, CD133 positive multipotent progenitors give rise to CD133 positive lympho-myeloid and CD133 negative erythro-myeloid progenitors (Görgens et al., 2014). Asymmetric segregation in ~30% of HSPCs could be confirmed and was subsequently correlated with ODF2 asymmetry using imaging flow cytometry in cooperation with the group of Bernd Giebel. We failed to observe a clear-cut tendency of CD133 with ~60% segregation to the daughter cell with the older (ODF2 high) centrosome. The analysis is still preliminary and increasing the sample size and optimizing the system could reveal if the segregation is random or not. A clearer bias

between 70 and 90% of old/young centrosome segregation to the more primitive cell was observed in the previous studies using polarized *Drosophila* and mouse progenitor cells (Salzmann et al., 2014; Wang et al., 2009; Yamashita et al., 2007). Interestingly, it was shown that HSC differentiation promotes the release of CD133 containing vesicles via the endocytic-exocytic pathway (Bauer et al., 2011). Thus, CD133 loss must not essentially occur via ACD. It still remains to be seen whether ACD is involved at other branching points of the human hematopoietic tree, for example at the HSC level (Murke et al., 2015).

Furthermore, when we disrupted centrosome asymmetry by ODF2 shRNA, differentiation capability of CD34 positive MPs was not affected. However, the knockdown was incomplete. For clarification a full KO of ODF2 would be needed, which is not feasible with primary human HSPCs.

The results shown here raise the question if centrosome asymmetry is only required for ACD in highly polarized stem cells, for example in the developing brain, where spindle orientation towards the niche must be tightly controlled, and not in non-polar HSPCs. On the other hand, in mouse HSCs, loss of the protein Lis1 disrupted spindle positioning, the inheritance of cell fate determinants and spindle positioning (Zimdahl et al., 2014).

Therefore, it would be important to know if oriented divisions also occur in the human hematopoietic system. So far it is not possible to access HSC divisions in a living human. In cooperation with the group of Motomu Tanaka, a system to study oriented divisions real-time *in vitro* with a niche model was established. We used ICAM-1, which is expressed by niche cells and binds to LFA-1A expressed by HSPCs (Gunji et al., 1992). Here, I observed oriented (vertical) divisions, in which one daughter cell remained attached to the ICAM-1 coated surface in 23% of the cells. Those vertical divisions might reflect ACDs, like they were observed in other stem cell systems with only one of the daughter contacting the niche. Thereby, only one of the daughter cells receives signals from the niche, which could impact on the asymmetric outcome of the cells (Yamashita et al., 2010). Interestingly, the amount of vertical divisions observed in this study fits the published values for asymmetric division in HSCs *in vitro* (20-30%) (Beckmann et al., 2007; Görgens et al., 2014; Huang et al., 1999).

Oriented divisions were only recapitulated in the leukemic cell line K562, but not KG1a cells. One explanation for this observation could be that, in contrast to KG1a, K562 cells are still able to differentiate in response to various chemical reagents (Koiso et

al., 2000). Oriented types of division might be limited to cells with the ability to further differentiate and hence need to divide asymmetrically in contrast to already differentiated cells, where the two daughter cells after division are always equal.

To investigate if the observed oriented divisions are not an artifact but really reflect unequal divisions, further experiments are needed. First, visualization of Integrin distribution on the two daughter cells using a surface antibody against LFA-1A and live cell imaging could show if the detachment of one cell is due to an asymmetric distribution of ICAM-1 receptors. Further, ICAM-1 coated surfaces can be used as a tool to study oriented divisions by combining the analysis of division axis with differential protein segregation, e.g. CD133, and ODF2 asymmetry and spindle orientation on both daughter cells. Though, this analysis is hardly feasible because transduction of primary cells is needed for visualization of ODF2, which was not effectively achieved in our hands. Instead, cells could be treated with centrinone to deplete centrosomes or nocodazole to affect spindle formation to test the requirement of centrosomes and their role in spindle orientation for oriented divisions. If vertical divisions fail under these circumstances, they require centrosomes. Another question to ask is if the mode of HSPC division can be manipulated by e.g., decreasing ICAM-1 density.

Future studies could then explore if differing ICAM-1 concentration on niche cells are used *in vivo* to control asymmetric versus symmetric divisions. Moreover, surface staining of different differentiation markers in long term live cell imaging could clarify if the division axis in the niche links to the cell fate decisions of stem or progenitor cells. In the future, this tool could be used to study oriented divisions by combining the analysis of division axis with differential protein segregation in healthy versus leukemic donor HSPCs to analyze the process and its potential deregulation in cancer mechanistically.

4.3 Nek2 regulates appendages

I aimed to unravel the mechanism and functional relevance of the pre-mitotic release of distal appendages (results part 3.3.). I proposed that Nek2 is involved in the release of appendages for several reasons. First, this study showed that the release of appendages in the G2/M transition is concomitant with the accumulation of Nek2 at the centrosome (Fry et al., 1998, Kim et al., 2015; Spalluto et al., 2012). Second, besides its localization at the proximal ends of both mother and daughter centrioles (Fry et al.,

1998), Nek2 also localizes to the distal ends of the centriole and the basal body at S/G2 phase (Kim et al., 2015; Spalluto et al., 2012). This study further defined the distal localization of Nek2 using super-resolution microscopy and found that it co-localizes with the distal appendage Cep164. Lastly, Nek2 is also required for the centrosomal release upon mitotic entry for another mother centriole-specific protein, namely Nlp, which is prematurely displaced from interphase centrosome upon overexpression of Nek2 (Rapley et al., 2005).

This study showed that overexpression of active Nek2 but not kinase-dead Nek2 prematurely displace distal appendages in interphase, indicating that this process is a direct or indirect phosphorylation-dependent event mediated by Nek2. Conversely, in Nek2 KO cells, appendages remained associated with the older centrosome during mitosis. As proteasome inhibition did not prevent the release of distal appendages upon Nek2 overexpression, I reason that displacement rather than local degradation underlies the regulation of distal appendages by Nek2. This assumption is further supported by the observation that only the centrosomal and not the overall Cep164 protein levels decreased during mitosis (Schmidt et al., 2012).

It was shown that the distal pool of Nek2 accumulates at S/G2 phase (Spalluto et al. 2012, Kim et al. 2015), aligned with its action on appendages and Nlp. I wanted to test if the proximal linker pool is also required for Nek2's action on appendages by depleting the proximal pool of Nek2 using C-Nap1 siRNA (Panic et al., 2015; Spalluto et al., 2012). Depletion of C-Nap1 did not perturb the release of Cep164, Cep123, FBF1 and the distal fraction of LRRC45 upon Nek2 overexpression. Therefore, I conclude that the distal but not the proximal pool of Nek2 is required for the displacement of appendages. Recruitment of Nek2 to the proximal and distal pool of centrioles may occur via separate mechanisms since C-Nap1 appears to be required specifically for Nek2-recruitment to proximal ends. Likewise, our own unpublished data indicates that the distal localization of Nek2 could be dependent on appendages. The distal pool of Nek2 seems not relevant for ciliation, as siRNA of C-Nap1 did not affect ciliation (Graser et al., 2007). Yet, distal appendage proteins, which are released during mitosis have been functionally linked to ciliogenesis (Graser et al., 2007; Schmidt et al., 2012; Tanos et al., 2013).

Of note, levels of FBF1 decreased on mitotic centrosomes of HSPCs and KG1a cells, but not in RPE1. Still, FBF1 levels were decreased in RPE1 interphase cells upon ectopic Nek2-WT overexpression. Our unpublished data shows that centrosomal

localization and intensity of FBF1 were not affected by siRNA mediated depletion of Cep164, Cep123 or double depletion. This is in agreement with published results (Tanos et al., 2013). Hence, the loss of FBF1 upon Nek2 overexpression cannot be explained as a secondary effect due to the loss of these appendages. As overexpression of Nek2 is artificial, it could still be that the centrosomal reduction of FBF1 in interphase is a secondary effect of overexpression. The levels of this protein decreased not only as shown here in mitotic hematopoietic cells, but also in HeLa cells (Kong et al., 2014). Other studies using IMCD3 and RPE1 cells observed FBF1 remaining at the mother centrosome during mitosis (Kong et al., 2014; Wei et al., 2013). Using RPE1 cells, Bowler et al. (2019) found bipartite FBF1 behavior: In half of the population, its levels on the mother centrosome remained interphase levels, while the other half lost FBF1 from both mitotic centrosomes. These data indicate cell type-specific regulation of FBF1 dynamics and suggest clonal variability within the same cell line. I did not test if the release of FBF1 in hematopoietic cells is dependent on Nek2. Therefore, another kinase may control FBF1 levels in a cell type specific context. Another possibility could be that Nek2 initially functions to release FBF1 and this might be prevented by secondary pathways in a cell type or environmental specific context.

Nek2 is overexpressed in several forms of cancer, including breast cancer (Hayward et al., 2004; Zhou et al., 2013; Cappello et al., 2014). Here, I detected a higher percentage of interphase cells with reduced Cep164 levels in breast epithelial and breast cancer cells with reported elevated Nek2 levels (Kim et al., 2015; Neve et al., 2006; Yuan et al., 2010) compared to RPE1 cells. Depleting Nek2 could rescue this phenotype, implying that Nek2 is indeed the cause of reduced centrosomal Cep164 in these cells. Notable, in this analysis, Nek2 centrosomal or total cell levels were not significantly higher in the MCF10A derived cell lines compared to RPE1 cells. Thus, disturbed or increased activity rather than augmented levels of Nek2 could causes premature Cep164 release in interphase in the analyzed breast cell lines.

This hypothesis could be tested by, for example, using a phospho-specific antibody against Nek2, a kinase assay measuring autophosphorylated Nek2 in the cell lines, or indirectly by probing against phosphorylated C-Nap1 (Mardin et al., 2010) in G2 cells. However, for these tests synchronization of the used cell lines must be established, which was not realized during this study.

Notably, loss of ciliation is associated with multiple types of cancer (Emoto et al., 2014; Hassounah et al., 2013; Nobutani et al., 2014). Kim et al. (2015) reported that Nek2

and Kif24 depletion recued the cilia-less phenotype in in the MCF10 cell line series, thereby reducing proliferation. As my data indicate that Nek2 level or activity affect centrosome composition in MCF10 derived cells lines it is tempting to speculate that the decrease of centrosomal Cep164 may also promote the unciliated phenotype and thus might be one underlying mechanism that contributes to cilia loss in tumors overexpressing Nek2. It remains to be elucidated if disturbance of cilia assembly by both, the increased inhibition of assembly via the Kif24 pathway (Kim et al. 2015) and the Cep164 reduction lead to tumor progression.

If this will be proofed, screening for the appendage and/or cilia phenotype in cancer patients could be a diagnostic tool for targeted therapy using Nek2 inhibitors in those cancer types displaying reduction of appendages and cilia compared to healthy tissues.

Further, my results show that Nek2 dependent appendage release does not require PLK1. Rapley et al. (2005) showed that Nek2 and PLK1 work synergistically to displace Nlp from the centrosome during mitosis. In contrast to Nlp (Rapley et al., 2005), distal appendages were not displaced from interphase centrosomes upon overexpression of hyperactive PLK1. The recent study of Bowler et al. (2019) displayed that treatment of HeLa and mIMCD3 cells with Plk1 inhibitor BI2536 prevented Cep164 removal from the mother centrosome in some prophase or prometaphase cells. In this study, PLK1 inhibition on top of Nek2 overexpression did interfere with the Nek2 dependent release of distal appendages in RPE1 cells, suggesting that this process is primarily dependent on Nek2. However, a minor contribution of PLK1 for pre-mitotic distal appendage removal cannot be excluded.

It is likely that pre-mitotic removal of outer distal and subdistal appendages occurs through partly independent mechanisms. In this study, Centriolin, but not Ninein remained asymmetric in Nek2 KO cells. This suggests that the action of an additional kinase, like PLK1 in the case of Nlp (Rapley et al, 2005), might be required for the mitotic release of Ninein. Therefore, it is possible that Ninein, like Nlp (Rapley et al., 2005), needs priming of PLK1. Quantification of Ninein and Centriolin levels upon overexpression of hyperactive PLK1 could solve this question. Similar to Nlp and in contrast to distal appendages, Ninein protein levels might be cell-cycle dependent regulated by APC-mediated protein degradation (Wang and Zhan, 2007). Ninein levels at the centrosome were decreased, however not significantly, upon proteasome inhibition combined with Nek2 overexpression. To uncover if total Ninein levels

fluctuate in a cell cycle dependent manner, western blot analysis after synchronization is needed.

Overall, my data indicates that pre-mitotic appendage release is primarily dependent on Nek2 but the additional involvement of other mitotic kinases, especially for subdistal appendages cannot be fully excluded.

4.4 Impairment of ciliogenesis upon Nek2 overexpression correlates with reduction of distal appendages

This study provides evidence that Nek2 dependent appendage release affects ciliation independent to the pathway via Kif24 upon ectopic Nek2 overexpression (Kim et al., 2015). Kim et al. (2015) identified that Nek2 regulates cilia assembly by the phosphorylation of Kif24, which stimulates its microtubule depolymerizing activity (Kim et al., 2015). Here, overexpression of Nek2 resulted in a reduction of ciliated cells as described earlier (DeVaul et al., 2017; Kim et al., 2015; Spalluto et al., 2012). My study now found that those cells which were unciliated upon Nek2 overexpression had lower levels of the subdistal appendage protein Cep164. Further, the level of Nek2 overexpression correlated with the decline in cilia formation.

According to my hypothesis, Nek2 influences appendage levels at the centrosome and, in turn, this disturbs ciliation. Nek2 KO did not affect interphase appendage levels. In line with this and a previous study using Nek2 siRNA treatment (Spalluto et al., 2012), ciliation was not affected in interphase Nek2 KO cells. In contrast, Kim et al. (2015) observed an increase of ciliation in Nek2 depleted cells. However, using the same siRNA in Nek2 KO cells, I observed an additional increase in ciliation, pointing towards an off-target effect.

As Cep164 removal by Nek2 was not affected upon depletion of Kif24 in the Nek2 overexpressing cell line, and similarly Cep164 levels were not affected by overexpression of Kif24, I conclude that appendage loss and Kif24 overstimulation are independent results of Nek2 overexpression. These results indicate that the centrosomal release of appendages upon Nek2 overexpression additionally promotes the ciliation phenotype independent of Kif24.

Published data lead to the conclusion that Nek2 regulates cilia assembly rather than cilia disassembly. When cells were serum starved before Nek2 overexpression, the effect on ciliation and appendage levels was prevented. In the basal body, appendages could be guarded against Nek2 by the ciliary membrane and other components of the

cilium. Notably, Nek2 levels drastically decrease in G1 and G0 upon serum starvation (this study, Spalluto et al., 2012, Kim et al., 2015). Here, even the overexpressed Nek2-mNeongreen decreased in serum-starved cells. This is likely because Nek2 is destroyed by the proteasome, dependent upon the APC/C–Cdc20 ubiquitin ligase upon mitotic entry, persisting until throughout G1 and G0 (Hames et al., 2001). Hence, the diminishment of Nek2 overexpression by serum starvation could explain that the decrease of Cep164 levels was not as drastic compared to growing cells, even if cells were serum starved after overexpression. Together, ciliation analysis in this study and data of Kim et al. (2015) and DeVaul et al. (2017) showed that Nek2 acts to prevent assembly and nucleation of new cilia but does not disassemble fully formed cilia, while others proposed Nek2 to function in cilia disassembly before mitosis (Spalluto et al., 2012).

Additional to Nek2 and PLK1, cilium disassembly and resorption are mainly activated by Aurora A, which stimulates HDAC6-mediated deacetylation and destabilization of microtubules (Pugacheva et al., 2007). Regulation of ciliation by Nek2 was shown to be independent of the Aurora A pathway in assembling cilia (Kim et al. 2015, DeVaul et al. 2017). However, both kinases seem to be required for the resorption of cilia and Aurora A and Nek2 functionally interact in cilia reabsorption in ARPE-19 cells (DeVaul et al. 2017). This study did not analyze if Aurora A influences appendage release together or independent of Nek2. Because Cep164 levels did not decrease in already assembled cilia in a Nek2 dependent manner this process is likely timely independent of Aurora A activity (Pugacheva et al., 2007). Therefore, I did not further test the involvement of Aurora A in appendage removal.

In summary, Nek2-dependent appendage release is a further explanation of why ciliation is decreased after Nek2 overexpression. Particularly, the appendage release upon the G2/M transition is likely a fail-safe mechanism to prevent ciliogenesis before mitosis, parallel to the Nek2-Kif24 pathway.

4.5 A ciliary remnant in mitotic Nek2 KO cells leads to the asymmetric inheritance of ciliary signaling components and asynchronous cilium reassembly

One major question that evolved during this study was the physiological relevance of Nek2 mediated distal appendage release. It is tempting to hypothesize that the removal of distal appendages during the G2/M phase represents an additional fail-safe barrier for cilia formation. To find the consequence of perturbed appendage release and the reason why a subset of appendages should be released in normal mitosis, I analyzed the cilia marker Arl13B in mitotic Nek2 KO cells. Although cilia resorption is dependent on the cell type and environmental context (Ford et al., 2018), this organelle is believed to be incompatible with a mitotic spindle and is usually absorbed prior to mitosis.

It was shown before that siRNA mediated depletion of Nek2 compromised the cells ability to resorb cilia (Spalluto et al., 2012). However, the previous analysis only identified cells in G2 and prophase with a mitotic remnant, while in this study using Nek2 KO cells the cilia remnant of ciliary membrane persisted throughout mitosis.

This study showed for the first time that impeded appendage release in Nek2 KO cells is the cause for a ciliary remnant in mitotic cells. The Arl13B positive remnant docked at the mother centriole in a Cep164-dependent manner and was not present upon Cep164 depletion. Live cell imaging revealed that the remnant emerged from previously ciliated cells that shortened the cilium to a remnant and elongated it after cytokinesis. This resulted in asynchronous cilium reassembly in the daughter cell bearing the remnant versus the daughter inheriting the younger centrosome.

Mechanistically, I showed that the mitotic ciliary remnant is not caused by CP110 removal triggered by recruitment of TTBK2 due to remanence of Cep164 on the mother centrosome. CP110 and TTBK2 did not localize differentially in Nek2 KO cells compared to WT cells with CP110 still being present on mitotic centrosomes in Nek2 KO cells and TTBK2 still being released. More likely, as the remnant bearing cells were ciliated before, the persistence of Cep164, which is a key requirement for ciliary vesicle docking (Schmidt et al., 2012), might not allow the cilium to fully disassemble. In conclusion, this is normally prevented by Nek2 dependent pre-mitotic removal of Cep164 from the mother centrosome. The live cell imaging data further strengthens the point that the remnant is caused by incomplete disassembly and not de-novo assembly.

It has been revealed previously that RPE1 cells which inherit the older mother centriole tend to initiate primary cilium assembly ahead of the other daughter cell that inherited the younger mother centriole (Anderson and Stearns, 2009). On the one hand, loss of outer appendages that regulate ciliogenesis like Cep164 and Cep123 could assure timely cilia resorption. On the other hand, maintenance of inner structural components like Cep83 for the restoration of the appendage complex in the next cell cycle, could balance the age gap and associated functions between the two centrosomes in differentiated cells.

In parallel to this study, Bowler et al. (2019) found impeded Cep164 removal and cilia resorption in mIMCD3 cells after PLK1 or Aurora A inhibition. In contrast to this study using Nek2 KO cells, the ciliary marker became absent after NEB (Bowler et al., 2019). The authors concluded that Cep164 removal is not necessary for cilia resorption. This milder phenotype observed after PLK1 or Aurora A could point to a major role of Nek2 for this process, because in this study the mitotic remnant was observed throughout mitosis upon KO or depletion of Nek2.

However, although PLK1 involvement is minor in RPE1 cells according to this study, cell type and species-specific differences in appendage and ciliation regulation cannot be excluded. IMCD3 kidney epithelial cells display surfaced cilia, while RPE1 cells usually build submerged cilia (Galati et al., 2016; Mazo et al., 2016). The mitotic remnant might be restricted to cells building submerged cilia and be incompatible for cells, which require surface protrusion of the cilium. It is likely that the pre-mitotic removal of distal appendages by Nek2 per se is also required for cells building surfaced cilia. Here, Nek2-dependent appendage removal could be involved in the mechanism allowing the detachment of the basal body from the plasma membrane. It was shown that this process involves regulation of INPP5E, which interacts with several regulators of ciliary dynamics including Aurora A, Arl13b, and Cep164 (Humbert et al., 2012; Plotnikova et al., 2015). Phua et al. (2017) demonstrated that, early in ciliary disassembly, INPP5E is displaced from the membrane. This triggers actin polymerization at the site primary cilia, which they suggest excises cilia tips (Phua et al., 2017). However, this mechanism does likely not account for the complete disassembly of the cilium since tubulin was not found in the decapitated ciliary fragments (Phua et al., 2017). Therefore, the axoneme must be disassembled by other means, like depolymerization by MT-depolymerizing kinesins and detachment of Cep164 to prevent docking of residual membrane, both which are dependent on Nek2

(this study and Kim et al., 2015). This Nek2-dependent regulation of cilia detachment in turn could be important for correct spindle orientation. A role of cilia in spindle positioning was shown previously in Kidney cells: Deletion of IFT20 and Kif3a resulted in misoriented spindles and concurrent cilia loss causing epithelial cyst formation (Jonassen et al., 2008; Patel et al., 2008). This suggests that persistence of cilia membrane into late G2/M may affect the positioning of the mitotic spindle and future plane of cell division.

Importantly, this study showed that the daughter cell that inherited the older centrosome and the ciliary membrane remnant grows the primary cilium prematurely. Further, the mitotic cilia remnant caused the asymmetric inheritance of the ciliary signaling component Smo, one of the hedgehog pathway components. Asynchronous cilium growth has consequences for cell fate determination by allowing sister cells to differentially detect environmental signals (Figure 54).

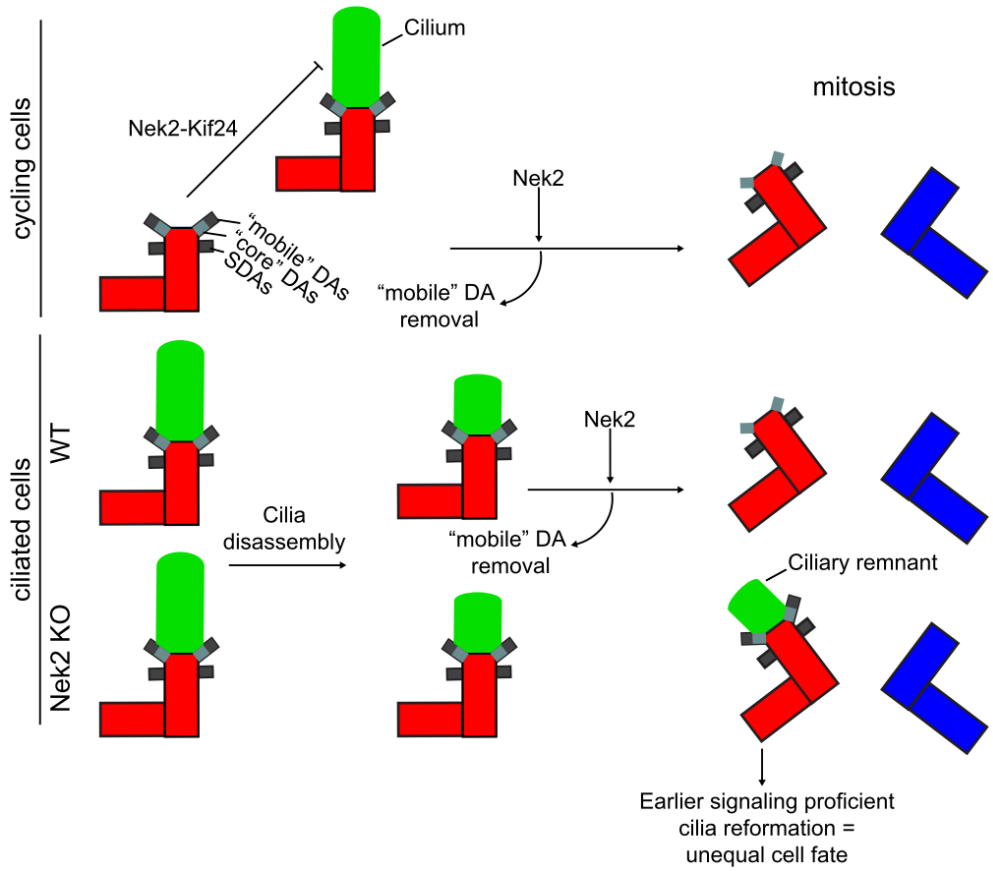

Figure 54. Prevented distal appendage release in mitotic Nek2 KO cells results in a ciliary remnant and earlier cilia reformation after mitosis. In cycling cells, the Nek2-Kif24 pathway ensures the inhibition of assembly, while "mobile" distal appendages (DAs), which are required for cilia vesicle docking, are removed by Nek2 before mitosis. In ciliated cells, cilia are disassembling before mitosis, e.g. by Aurora A activation (Pugacheva et al. 2007) and Nek2-Kif24 dependent inhibition of re-assembly (Kim et al. 2015). In WT cells, the displacement of "mobile" DAs prevents ciliary vesicle attachment in mitosis. In Nek2 KO cells, maintenance of DAs results in a ciliary remnant with the consequence of premature primary cilia reformation. Asynchronous cilia reformation gives the two progenies unequal signaling proficiency and can result in unequal cell fate.

Therefore, a ciliary remnant during mitosis might be restricted to stem cells, which divide asymmetrically and therefore need a tool to respond contrarily to environmental signaling. Interestingly, specific stem cells keep a ciliary remnant on the older centrosome. In neural stem cells, the older mother centriole and its associated ciliary remnant usually segregate to the stem cell in an asymmetric division and the cell receiving the remnant makes a cilium first and is responsive to Sonic hedgehog ligand (Paridaen et al., 2013). Further, the centrosomal association of ciliary membrane in dividing neural stem cells decreases at late neurogenesis concomitant with differentiation (Paridaen et al., 2013). Thus, the Nek2 mediated release of specific appendage proteins during mitosis in differentiated cells could serve as a mechanism to ensure equal behavior of daughter cells.

Such a ciliary remnant in neuronal stem cells (Paridaen et al., 2013) could be regulated by Nek2 levels and hence asymmetry of outer distal appendages may define stem cell vs. differentiated state in stem cells. To test the idea if low Nek2 levels in neuronal stem cells define Cep164 asymmetry and remnant inheritance, a co-staining of the ciliary membrane marker Arl13B and Cep164 should be performed. If the remnant coincides with asymmetric Cep164 in mitotic stem cells, it would be interesting to follow if this phenotype can be correlated with Nek2 levels in dividing cells using a knock-in cell line. This is not unlikely, because asymmetric Cep164 was also observed in the cilia remnant bearing neuronal progenitors studied by Paridaen et al. (2013). So far, manipulation of neuronal stem cells was ineffective in our hands. Yet, it might be promising to team up with a group experienced in manipulating these cells. Notably, not only the level but also the activity of Nek2 should be considered in asymmetrically dividing stem cells. A study comparing the kinome under- or overrepresented in hESCs, based on the incidence of specific phosphorylations, Nek2 was even found overrepresented in hESCs (Van Hoof et al., 2009). If Nek2 controls unequal cell fate, it is likely restricted to certain polarized stem cell types like neuronal progenitors.

Future analysis can reveal if and how Nek2 regulated remnant inheritance controls differential signaling and cell fate in adult stem cells and during development.

4.6 Regulation of distal appendages by Nek2 does not require the subdistal appendage ODF2

Nek2 coimmunoprecipitated with ODF2 in this study and both proteins were found in close proximity in a study using BioID (Gupta et al., 2015). Therefore, I reasoned that the release of outer distal appendages might occur via ODF2 phosphorylation. Phosphorylation of an inner structural appendage like ODF2 or Cep83 could induce a conformational change leading to the expulsion of outer appendages. However, a prerequisite for this assumption is that the assembly of outer distal appendages is dependent on ODF2. Still, the dependency of Cep164 on ODF2 is controversial (Ishikawa et al., 2005; Kuhns et al., 2013; Tanos et al., 2013; Tateishi et al., 2013). In mouse testis, embryonal carcinoma (F9) ODF2 KO cells, distal appendages, subdistal appendages, and primary cilia were lost from the mother centriole (Ishikawa et al. 2005). A follow-up study, using the same mouse cell line found that distal appendages and cilia were lost in the full mutant and mutants lacking the C-terminal part of ODF2, while the N-terminus was indispensable for cilia formation and distal appendage formation (Tateishi et al. 2013). Depletion of ODF2 in RPE1 cells did not affect distal appendage assembly but had reduced capability of cilia formation (Kuhns et al. 2013, Tanos et al. 2013). In contrast, another study using RPE1 ODF2 KO cells could neither detect any difference in cilia formation after serum starvation nor in cilia length (Mazo et al., 2016).

To investigate whether the retention of distal appendages observed by Kuhns et al. (2013) was due to incomplete depletion using siRNA, I produced an RPE1 ODF2 KO cell line using CRISPR/Cas9 (results part 3.4.). Similar to ODF2 depletion in RPE1 cells, formation of distal appendages was not affected in ODF2 KO cells (Kuhns et al., 2013; Tanos et al., 2013), demonstrating interspecies variability in appendage regulation between human and mouse cell. The treatment of RPE1 WT and ODF2 KO cells with ODF2 siRNA equally decreased ciliogenesis by 20-30% [(Kuhns et al., 2013) and our unpublished observation]. I thus propose that off-target effects of the siRNA rather than compensatory mechanisms triggered by ODF2 KO might account for the discrepancy in results regarding ciliation in this study and Kuhns et al. (2013). Lastly, the release of Cep164, Cep123, and LRRC45 during mitosis and upon Nek2 overexpression was not affected in ODF2 KO and depleted cells, respectively. This showed that ODF2 is dispensable for distal appendage regulation by Nek2.

Why are distal appendages dependent on ODF2 in one species but not in another? One could assume that ODF2 performs partly different functions in different species or tissues, or the expression of different ODF2 isoforms or differences in the amino acid sequences in different species result in different functions. ODF2 was first identified as the main protein component of the sperm tail cytoskeleton, the outer dense fibers, and then shown to be a component of the centrosomal scaffold in chicken (Nakagawa et al., 2001). In this initial study in isolated chicken centrosomes and human cell lines, ODF2 was found to be localized at the distal end of the mother centriole overlapping with Ninein. This suggests that in chicken, like in human cells, ODF2 is a primary subdistal component. However, initial studies in rat suggested that expression pattern of ODF2 is related to the initiation of the flagella formation (Sun et al., 2002). As motile cilia and flagella have nearly identical structures, it could be that a role of ODF2 in building or maintenance cilia/flagella is restricted to different tissues, for example sperms and tissues with motile cilia.

Another possibility could be that the different functions detected are due to differently expressed ODF2 isoforms. In mouse two related ODF2 cDNA clones were isolated which are the result of alternative splicing: ODF2 and Cenexin1 (Hüber and Hoyer-Fender, 2007). However, RT-PCR analyses revealed that isoforms are not restricted to specific tissues (Hüber and Hoyer-Fender, 2007). ODF2 is the main isoform in testicular tissue and Cenexin1, the isoform analyzed and targeted in this study and named here as “ODF2” (results, 3.4.), is the main isoform in other tissues analyzed so far. Cenexin1, containing an additional sequence at the C-terminus, localizes to basal bodies in cultured mammalian cells. In ODF2 KO mouse F9 cells lacking both isoforms, but exogenously expressing one or both of these proteins, it was shown that Cenexin1, but not the shorter ODF2 isoform, was necessary to induce ciliogenesis (Chang et al., 2013). Further, mice with truncated ODF2, missing the essential C-terminal part required for ciliogenesis, cough and sneeze due to primary ciliary dyskinesia (Kunimoto et al., 2012).

These results reinforce a role for the Cenexin1 isoform of ODF2 for cilia formation in mice but not humans. The dependency of distal appendages and ciliation in mice versus humans could result from sequence differences of the mainly expressed ODF2 isoform Cenexin1. Human and mouse ODF2 (cenexin1 isoform) share 97.3% sequence identity. To test if this small difference in amino acid composition accounts for the difference of cilia and distal appendage dependency, one could re-express

human versus mouse ODF2 in F9 ODF2 KO cells and test if only the mouse version can recue the loss of distal appendages and ciliation to finally resolve the discrepancy observed here and in mice F9 cells.

4.7 Future perspectives

What is the real contribution of appendages in ACD? The initial analysis in HSPCs suggest that appendage asymmetry may not be essential for non-polarized cells. However, the functional analysis of Nek2 in RPE1 cells revealed that Nek2 could be a player involved in the decision of unequal versus equal outcome of cells. This study showed that Nek2 regulates the pre-mitotic release of appendages, which contributes to cilia disassembly in mitosis and prevents asymmetric cilia inheritance. Analysis of Nek2 levels, remnant formation and Cep164 asymmetry in different stem cell types, different tissues and species as described in 4.5. could reveal if Nek2 induced asymmetry of normally released distal appendages affects unequal cell fate. This regulation is maybe only required in specific polarized stem cells like neuronal stem cells or epithelial cells versus non-polarized stem cells. Thereby, this regulation could serve as a cell-type specific control of timely cilia reformation.

Distal centrosome appendages may represent novel targets of Nek2. Still, it is unclear whether the mechanism of pre-mitotic release is indirect or via direct phosphorylation. The appendage constructs purified and ready for purification generated in this study (5.1.7., Table 8) can be used for kinase assays with Nek2. Additionally, the here generated cell lines expressing inducible Nek2-BirA can be used to unbiasedly identify Nek2 phosphorylation targets. In parallel, SILAC can be performed analyzing differential phosphorylation in RPE1 WT and Nek2 KO cells incubated in medium containing light and heavy amino acids, respectively. Overlaps can subsequently be verified in kinase assays.

To expose whether potential hits are involved in Nek2 dependent appendage regulation phosphomimetic and phosphodead mutants must be generated. If appendage release can be reserved in the phosphodead mutant the phosphorylation would expectedly be relevant for Nek2 dependent regulation of appendage behavior. Notably, pre-mitotic appendage release can also be mediated by a known Nek2 substrate. Kif24 and ODF2 can be excluded according to this study. Another target, ß-catenin, is phosphorylated and stabilized at mitotic centrosomes (Bahmanyar et al., 2008; Mbom et al., 2014). One could speculate that β-catenin stability may be

necessary for some functions, such as removal of the linker proteins and appendages before mitosis.

This study lays the ground for further exploration of the pathway by which Nek2 regulates appendage behavior. Furthermore, Nek2 is overexpressed in many cancer types (Hayward et al., 2004; Zhou et al., 2013; Cappello et al., 2014; Fang and Zhang, 2016). Understanding how Nek2 regulates appendages and in which cancer types Nek2 overexpression affects appendages could help to develop targeted drugs and cancer screenings to identify in which patients inhibition of Nek2 has clinical implications.

5. Materials and Methods

5.1 Materials

5.1.1 Chemicals

Suppliers for chemicals are noted separately in the respective protocols in the Methods section.

5.1.2 Antibiotics

Antibiotics used for mammalian cell and bacteria culture were:

Ampicillin 100 µg/mL (100 mg/mL stock in H_2O)

Kanamycin 25 µg/mL (25 mg/mL stock in H_2O)

Chloramphenicol 30 µg/mL (30 mg/mL stock in ethanol)

G418 800 µg/mL (200 mg/mL stock in H_2O)

Puromycin 3 µg/ml (10 mg/ml stock in H_2O)

Doxycyclin 250 ng/mL (10 mg/mL stock in H_2O)

5.1.3 General buffers and solutions

Frequently used buffers:

- Enhanced chemiluminescence (ECL) solution 1: 100 mM Tris-HCl, pH 8.5, 25 mM Luminol (3-aminophthalydrazide), 2.5 mM p-Coumaric acid
- ECL solution 2: 100 mM Tris-HCl, pH 8.5, 61.5 µl H_2O_2 (30%), filled with H_2O to 100 ml. ECL solution 1 and 2 were stored in the dark at 4°C and mixed 1:1 just before usage.
- Mini-prep solution I: 50 mM glucose, 25 mM Tris-HCl pH 8.0, 10 mM ethylendiaminetetraacetic acid (EDTA), 10 µg/mL RNAse I (Sigma Aldrich)
- Mini-prep solution II: 0.2 M NaOH, 1% weight per volume (w/v) SDS
- Mini-prep solution III: 3 M potassium acetate 11.5% volume per volume (v/v) acetic acid
- Phosphate buffered saline (PBS): 10 mM Na_2HPO_4, 1.76 mM KH_2PO_4, 2.7 mM KCl, 137 mM NaCl, pH 7.2, autoclaved for molecular biology
- PBS-T: PBS, 0.01% (v/v) Tween 20
- SDS-Running buffer: 25 mM Tris, 192 mM Glycine, 0.1% (w/v) SDS
- 5x SDS-sample buffer: 250 mM Tris-HCl, pH 6.8, 10% (w/v) SDS, 50% (v/v) glycerol, 0.05% (w/v) Bromphenol-Blue, 1% β-mercaptoethanol

- Semi-dry blotting buffer: 25 mM Tris, 192 mM Glycine, 0.025% (w/v) SDS, 20% (v/v) Methanol
- Ponceau S: 0.2% Ponceau S, 3% TCA
- TAE buffer: 40 mM Tris-HCl, pH 8.3, 20 mM acetic acid, 1 mM EDTA
- TY agar medium: 1 L TY medium, autoclaved, 20 g agar
- TY medium: 10 g Bacto tryptone autoclaved, 10 g Yeast extract, 5 g NaCl
- YPD medium: 10 g Bacto yeast extract (Difco, Lawrence, Kansas, USA), 20 g Bacto peptone (Difco, Lawrence, Kansas, USA), 20 g Glucose filled to 1 l with H_2O, autoclaved
- YPD-agar plates 1 l YPD, 20 g agar, autoclaved
- SC medium: 6.7 g Bacto yeast nitrogen base without amino acids, 20 g Glucose, 2 g Drop-out amino acid mix, filled to 1 l with H_2O and autoclaved
- SC plates: 6.7 g Bacto yeast nitrogen base without amino acids, 20 g Glucose, 2 g Drop-out amino acid mix, filled to 500 ml with H_2O mixed with 20 g Bacto agar (Difco, Lawrence, Kansas, USA) in 500 ml H_20, autoclaved separately
- SC selection plates: To 36.7 g of the drop-out amino acids mix were added the following amino acids: 2 g histidine, 4 g leucine

Other buffers and solutions compositions are described with the respective method.

5.1.4 siRNA oligos

Table 5. small interfering RNAs (siRNAs) used in this study

Name	Target sequence (5'-3')	Reference	Supplier
Luciferase	AACGTACGCGGAATACTTCGA	(Knodler et al., 2010), siControl	Dharmacon ON-Target plus/ Ambion Silencer Select
siCep164	CAGGTGACATTTACTATTTCA	(Graser et al., 2007)	Ambion Silencer Select
siODF2	AAAGACTAATGGAGCAACAAG	(Soung et al., 2009)	Ambion Silencer Select
siNek2-1	GAUGCAAUUUGGUCAUUAAUU	(Kim et al., 2015)	Dharmacon ON-TARGETplus
siNek2-2	GAAAGGCAAUACUUAGAUGUU	(Kim et al., 2015)	Dharmacon ON-TARGETplus
siKif24-1	GGAACACCCTGGAGAATAGTT	(Kobayashi et al., 2011)	Dharmacon ON-TARGETplus
siKif24-2	GAGTTGAGCTCTCCTTTGGTT	(Kobayashi et al., 2011)	Dharmacon ON-TARGETplus
siC-Nap1-1	GAGCAGAGCUACAGCGAAU	(Panic et al. 2015)	Dharmacon ON-TARGETplus
siC-Nap1-3	AAGCUGACGUGGUGAAUAA	(Panic et al. 2015)	Dharmacon ON-TARGETplus

The two named siRNAs for Nek2, Kif24 and C-Nap1 were always used in a mixture. All siRNA oligonucleotide duplexes were ordered from Life Technologies in a lyophilized form, dissolved in RNAse free H_2O to a stock concentration of 20 µM and stored at -80°C.

5.1.5 shRNA sequences

Table 6. Small hairpin RNAs (shRNAs) used in this study

Name	Forward oligo	Reverse oligo
shRNA ODF2 for LEGO-G	CCGGGACTGCTGAGTATTCCGCATT CTCGAGAATGCGGAATACTCAGCAG TCTTTTTG	AATTCAAAAAGACTGCTGAGTATTCCGCATT CTCGAGAATGCGGAATACTCAGCAGTC
shRNA ODF2 for pCl2	CGCGTCCCCGACTGCTGAGTATTCC GCATTTTCAAGAGAAATGCGGAATA CTCAGCAGTCTTTTGGAAT	CGATTTCCAAAAGACTGCTGAGTATTCCGCAT TTCTCTTGAAAATGCGGAATACTCAGCAGTC GGGGA

5.1.6 gRNA sequences

Table 7. Guide RNA (gRNA) used in this study

Name	Forward oligo	Reverse oligo
gRNA ODF2	CACCGTCCCCCCTTACATGTTCACG	AAACCGTGAACATGTAAGGGGGGAC

5.1.7 Plasmids

Table 8. Plasmids used in this study

Plasmid	Vector	Source
FLAG	pCMV-3Tag-1A	Agilent Technologies
FLAG-Cep164	pCMV-3Tag-1B	(Schmidt et al. 2012)
Flag-Nek2	pCMV-3Tag-1A	This study
Flag-Nek2-KD	pCMV-3Tag-1A	This study
FLAG-Cep83	pCMV-3Tag-1A	This study
FLAG-Cep123	pCMV-3Tag-1A	This study
FLAG-ODF2	pCMV-3Tag-1A	This study
pCMV-HA-SCLT1	pCMV	Kind gift from B. Cerikan
pCL6IEG	pCL6IEG	Kind gift from H. Hanenberg
pCL6IEG –Nek2	pCL6IEG	This study
pCL6IEG –Nek2-KD	pCL6IEG	This study
LeGO G	LeGO G	(Weber et al., 2008)
LeGO-G ODF2 shRNA Nr.3	LeGO G	This study
pCL2-EG	pCL2-EG	Kind gift from H. Hanenberg
pCL2-EG ODF2 shRNA Nr.3	pCL2-EG	This study
pRetroX-TRE3G	pRetroX-TRE3G	TakaraBio
pRetroX-TRE3G- BirA-HA	pRetroX-TRE3G	(Chen et al., 2017)
pRetroX-Tre3G-Nek2-BirA	pRetroX-TRE3G	This study
pRetroX-Tre3G-Nek2KD-BirA	pRetroX-TRE3G	This study

PLK1-pRetroX-TRE3G-mNeonGreen	pRetroX-TRE3G	Kind gift from S. Hata
PLK1-T210D-pRetroX-TRE3G-mNeonGreen	pRetroX-TRE3G	This study
gRNA ODF2 in pX458	pX458	This study
AcGFP1-C1-Kif24	AcGFP1-C1	(Miyamoto et al., 2015)
pRDS28	Modified PMM5	(Geissler et al., 1996; Kurtulmus et al., 2018)
pRDS29	Modified PMM6	(Geissler et al., 1996; Kurtulmus et al., 2018)
pRDS28 Nek2	pRDS28	This study
pRDS29 Nek2	pRDS29	This study
pRDS28 Nek2-KD	pRDS28	This study
pRDS29 Nek2-KD	pRDS29	This study
pRDS28 Nek2-C	pRDS28	This study
pRDS29 Nek2-C	pRDS29	This study
pMM5 Cep164-C	pMM5	(Schmidt et al. 2012)
pMM5 Cep164-C	pMM6	(Schmidt et al. 2012)
pMM5 Cep164-N	pMM56	(Schmidt et al. 2012)
pMM5 Cep164 fl	pMM5	(Schmidt et al. 2012)
pRDS28 ODF2 frag 1 (1-250)	pRDS28	This study
pRDS29 ODF2 frag 1 (1-250)	pRDS29	This study
pRDS28 ODF2 frag 2 (200-450)	pRDS28	This study
pRDS29 ODF2 frag 2 (200-450)	pRDS29	This study
pRDS28 ODF2 frag 3 (400-806)	pRDS28	This study
pRDS29 ODF2 frag 3 (400-806)	pRDS29	This study
pRDS28 ODF2 fl	pRDS28	This study
pRDS29 ODF2 fl	pRDS29	This study
pRDS28 FBF1 fl	pRDS28	This study
pRDS28 FBF1 fl	pRDS29	This study
pRDS28 FBF1-C (481-830)	pRDS28	(Kurtulmus et al. 2018)
pRDS29 FBF1-C (481-830)	pRDS29	(Kurtulmus et al. 2018)
pRDS28 FBF1-N (1-480)	pRDS28	(Kurtulmus et al. 2018)
pRDS29 FBF1-N (1-480)	pRDS29	(Kurtulmus et al. 2018)
pRDS28-Cep123-1 (1-230)	pRDS28	(Kurtulmus et al. 2018)
pRDS29-Cep123-1 (1-230)	pRDS29	(Kurtulmus et al. 2018)

pRDS28-Cep123-2 (220-352)	pRDS28	(Kurtulmus et al. 2018)
pRDS29-Cep123-2 (220-352)	pRDS29	(Kurtulmus et al. 2018)
pRDS28-Cep123-3 (353-506)	pRDS28	(Kurtulmus et al. 2018)
pRDS29-Cep123-3 (353-506)	pRDS29	(Kurtulmus et al. 2018)
pRDS28-Cep123-4 (507-781)	pRDS28	(Kurtulmus et al. 2018)
pRDS29-Cep123-4 (507-781)	pRDS29	(Kurtulmus et al. 2018)
pRDS28-Cep123-5 fl	pRDS28	(Kurtulmus et al. 2018)
pRDS29-Cep123-5 fl	pRDS29	(Kurtulmus et al. 2018)
pRDS28-LRRC45-1 (108-670)	pRDS28	(Kurtulmus et al. 2018)
pRDS29-LRRC45-1 (108-670)	pRDS29	(Kurtulmus et al. 2018)
pRDS28-LRRC45-2 (167-670)	pRDS28	(Kurtulmus et al. 2018)
pRDS29-LRRC45-2 (167-670)	pRDS29	(Kurtulmus et al. 2018)
pRDS28-LRRC45-3 (223-670)	pRDS28	(Kurtulmus et al. 2018)
pRDS29-LRRC45-3 (223-670)	pRDS29	(Kurtulmus et al. 2018)
pRDS28-LRRC45-4 (fl)	pRDS28	(Kurtulmus et al. 2018)
pRDS29-LRRC45-4 (fl)	pRDS29	(Kurtulmus et al. 2018)
pRDS28-Cep83-1 (1-160)	pRDS28	(Kurtulmus et al. 2018)
pRDS29-Cep83-1 (1-160)	pRDS29	(Kurtulmus et al. 2018)
pRDS28-Cep83-2 (161-426)	pRDS28	(Kurtulmus et al. 2018)
pRDS29-Cep83-2 (161-426)	pRDS29	(Kurtulmus et al. 2018)
pRDS28-Cep83-3 (427-701)	pRDS28	(Kurtulmus et al. 2018)
pRDS29-Cep83-3 (427-701)	pRDS29	(Kurtulmus et al. 2018)
pRDS28-Cep83-4 (fl)	pRDS28	(Kurtulmus et al. 2018)
pRDS29-Cep83-4 (fl)	pRDS29	(Kurtulmus et al. 2018)
pRDS29-SCLT1 (1-178)	pRDS29	(Kurtulmus et al. 2018)
pRDS29-SCLT1 (179-553)	pRDS29	(Kurtulmus et al. 2018)
pRDS28-SCLT1 (554-688)	pRDS28	(Kurtulmus et al. 2018)
pRDS29-SCLT1 (554-688)	pRDS29	(Kurtulmus et al. 2018)
pRDS28-SCLT1 fl	pRDS29	(Kurtulmus et al. 2018)
pet28-a ODF2 frag 1(1-250)	pet28-a	This study
pet28-a ODF2 frag 2(200-450)	pet28-a	This study
ODF2 fl in pet28-a	pet28-a	This study
pet28-a Cep83-1 (1-160)	pet28-a	This study
pet28-a Cep83-2 (161-426)	pet28-a	This study
pet28-a Cep83-4 (fl)	pet28-a	This study
pet28-a Cep123-2 (220-352)	pet28-a	This study
pet28-a Cep123-3 (353-506)	pet28-a	This study
pet28-a Cep123-4 (507-781)	pet28-a	This study
pet28-a Cep123-5 fl	pet28-a	This study
pet28-a SCLT1 frag 1 (1-178)	pet28-a	This study

pet28-a SCLT1 fl	pet28-a	This study
pMAL-c2X	pMAL-c2X	This study
pMAL-c2X SCLT1-1 (1-178)	pMAL-c2X	This study
pMAL-c2X Cep123-4 (507-781)	pMAL-c2X	This study
pMAL-c2X ODF2 fl	pMAL-c2X	This study
pMAL-c2X Cep123 fl	pMAL-c2X	This study
pMAL-c2X Cep123-3 (353-506)	pMAL-c2X	This study
pMAL-c2X LRRC45-3(223-670)	pMAL-c2X	This study
pMAL-c2X ODF2-3 (400-806)	pMAL-c2X	This study
pMAL-c2X Cep83 fl	pMAL-c2X	This study

5.1.8 Primers

Primers were ordered from Sigma-Aldrich. They were obtained in desalted, lyophilized form, were dissolved in H_2O (100 µM) and stored at -20°C. All primers relevant to this study are found with their respective sequences in the Primer collection of the Pereira laboratory. If they were used for the purpose of cloning, they are referred to in description of the plasmid the Bacteria collection of the Pereira laboratory.

5.1.9 *Escherichia coli* (*E.coli*) strains

- DH5α: deoR endA1 gyrA96 hsdR17 (rκ-mκ-) recA1 relA1 supE44 thi-1Δ(lacZYA-argFV169) φ80δlacZΔM15 F- λ-
- BL21 (DE3) pLysS Rosetta: F- ompT hsdSB(RB- mB-) gal dcm λ(DE3 [lacI lacUV5-T7 gene 1 ind1 sam7 nin5]) pLysSRARE (CamR)
- Stabl3: F– mcrB mrr hsdS20(rB–, mB–) recA13 supE44 ara-14 galK2 lacY1 proA2 rpsL20(StrR) xyl-5 λ– leu mtl-1

5.1.10 Yeast strains

- SGY37 : MATa ura3-52:: URA3-levA-op-lacZ trpl his3 lelu2
- YPH500: MATα ura3-52::URA3-lexA-op-LacZ trp1 his3 leu2

5.1.11 Mammalian cell lines

- RPE1 human telomerase immortalized retinal pigment epithelial 1 cell line
- HEK293T human embryonic kidney cell line 293T

- GP2-293 cell line stably expresses the viral gag and pol proteins. HEK293 derivative.
- MCF10A Michigan Cancer Foundation-10A, human immortalized epithelial mammary-gland cell line, (kind gift from C. Conrad and K. Jechow (Heidelberg), originally obtained from the Barbara Ann Karmanos Cancer Institute (Detroit, MI, USA))
- MCF10CA1d.cl1 Michigan Cancer Foundation-10CA1d, human immortalized and transformed epithelial mammary-gland cell line (kind gift from C. Conrad and K. Jechow (Heidelberg), originally obtained from the Barbara Ann Karmanos Cancer Institute (Detroit, MI, USA))
- MCF10AT1k.cl2 Michigan Cancer Foundation-10CA1d, human immortalized and transformed epithelial mammary-gland cell line (kind gift from C. Conrad and K. Jechow (Heidelberg), originally obtained from the Barbara Ann Karmanos Cancer Institute (Detroit, MI, USA))
- KG1a human acute myeloid leukemia (derivative of KG-1) (Koeffler and Golde, 1978)
- K562 human immortalized lymphoblast chronic myelogenous leukemia (CML)
- HSPCs human primary CD34+ cells isolated from cord or peripheral blood

Table 9. Stable cell lines used in this study

Name	Cell line background	Source
RPE1 Tet3G	RPE1	Kind gift of E. Schiebel
mNeonGreen-Nek2A	RPE1 Tet3G	Kind gift of A. Pastor Peidro
mNeonGreen-Nek2A-KD	RPE1 Tet3G	Kind gift of A. Pastor Peidro
Nek2 KO cells	RPE1	Kind gift of M. Panic and A. Pastor Peidro
Nek2 KO with Tet3G	RPE1 Tet3G Nek2 KO	Kind gift of A. Pastor Peidro
mNeonGreen-Nek2A in Nek2 KO	RPE1 Tet3G Nek2 KO	Kind gift of A. Pastor Peidro
C-Nap1 KO	RPE1	(Panic et al., 2015)
ODF2 KO	RPE1	This study
mNeonGreen- PLK1-T210D	RPE1	This study
mArl13bGFP + γ-tubulin-mRuby2	RPE1	
mArl13bGFP + γ-tubulin-mRuby2 in Nek2 KO	RPE1 Nek2 KO	This study
mSMO-eGFP	RPE1 Tet3G	This study
mSMO-eGFP in Nek2 KO	RPE1 Tet3G Nek2 KO	This study
BirA-HA	RPE1 Tet3G	This study
Nek2-BirA-HA	RPE1 Tet3G	This study
Nek2-BirA-HA in Nek2 KO	RPE1 Tet3G Nek2 KO	This study
Nek2-KD-BirA-HA in Nek2 KO	RPE1 Tet3G Nek2 KO	This study

5.1.12 Antibodies

Table 10. Primary antibodies used in this study

Antibody	Species	Source	dilution
Anti-Cep 164 N	Guinea pig	Schmidt. et al. 2012	1:500 (IF)
Anti-Cep123 N	Guinea pig	(Kurtulmus et al., 2018)	1:250 (IF)
Anti-LRRC45	Guinea pig	(Kurtulmus et al., 2018)	1:400 (IF)
Anti-CCDC4/Cep83	Rabbit	Sigma # HPA038161	1:250 (IF)
Anti-FBF1	Rabbit	Sigma# HPA023677	1:250 (IF, MeOH)
Anti-SCLT1	Rabbit	Sigma#HPA036561	1:250 (IF)
Anti-ODF2 (gly1-4)	Guinea pig	(Kuhns et al., 2013)	1:500 (IF, MeOH)
Anti-ODF2	Rabbit	(Kuhns et al., 2013)	1:500 (WB)
Anti-Ninein (pep3)	Rabbit	Lab stock	1:250 (IF, MeOH)
Anti-Centriolin	Rabbit	Kind gift of E. Schiebel	1:100 (IF)
Anti-Centrobin	Rabbit	Sigma #HPA023321	1:500 (IF)
Anti-CP110	Rabbit	Biomol #A301343A	1:300 (IF)
Anti-Cep97	Rabbit	Bethyl Laboratories, #A301-947A	1:300 (IF, MeOH)
Anti-TTBK2	Rabbit	Sigma, #HPA018113	1:1000 (IF, MetOH)
Anti-ARL13B	Rabbit	Acris, #17711-1-AP	1:500 (IF)
Anti-γ tubulin	Rabbit	Sigma, #T5192	1:500 (IF)
Anti-γ tubulin (GTU88)	Mouse	Sigma, #T6557	1:500 (IF)
Anti-PCM-1	Rabbit	Kind gift of Oliver Gruss (Bärenz et al., 2013)	1:1000 (IF)
Anti-Rootletin	Rabbit	root-N (Panic et al., 2015)	1:100 (IF)
Anti-Numb	Rabbit	Abcam, #14140	1:50 (IF)
Anti-Numb	Mouse	DSHB/ CMnb-1-s	1:6 (IF)
Anti-hNotch2	Mouse	DSHB/ C651.6DbHN-s	1:6 (IF)
Anti-Notch1	Mouse	DSHB/ bTAN20-s	1:10 (IF)
Anti-CD63	Mouse	BD Biosciences, #556019	1:400 (IF)
Anti-CD53	Mouse	BD Biosciences, #555506	1:400 (IF)
Anti-CD133 (HC7)-PE	Mouse	(Görgens et al., 2014)	1:50 (IF, live cell imaging)
Anti-ß Catenin	Rabbit	Abcam, # ab6302	1:500 (IF)
Anti-Nek2	Mouse	BD Biosciences, #610593	1:100 (IF), 1:500 (WB)
Anti-Nek2	Mouse	Santa Cruz, #D-8 sc-55601	I1:250 (IF), 1:500 (WB)
Anti-Actin	Mouse	Chemicon/Millipore MAB1501	1:1000 (WB)
Anti-Cofilin	Rabbit	Abcam, #ab42824	1:3000 (WB)
Anti-GFP	Mouse	Roche, #11814460001	1:800 (IF, WB)
Anti-FLAG	Rabbit	Sigma-Aldrich, F7425	1:5000 (WB)
Anti-nuclear pore complex mAB414	Mouse	Abcam, ab24609	1:2000 (IF)
Anti-HA	Mouse	Lab stock, 12CA5	1:10 (WB)
Anti-Cep128	Rabbit	Abcam, #ab118797	1:500 (IF)

Table 11. Secondary antibodies used in this study

Antibody	Species	Source	dilution
Anti-mouse Horseradish peroxidase (HRP)	Goat	Dianova	1:5000

Anti-rabbit (HRP)	Goat	Dianova	1:5000
Anti-guinea pig (HRP)	Goat	Dianova	1:5000
Anti-mouse Alexa488	Goat	Molecular Probes	1:500
Anti-rabbit Alexa488	Goat	Molecular Probes	1:500
Anti-mouse Alexa488	Goat	Molecular Probes	1:500
Anti-guinea pig Alexa488	Goat	Molecular Probes	1:500
Anti-mouse Alexa594	Goat	Molecular Probes	1:500
Anti-guinea pig Alexa594	Goat	Molecular Probes	1:500
Anti-rabbit Alexa546	Goat	Molecular Probes	1:500
Anti-rat Alexa546	Goat	Molecular Probes	1:500
Anti-mouse Alexa647	Goat	Molecular Probes	1:200
Anti-rabbit Alexa647	Goat	Molecular Probes	1:200
Anti-guinea pig Alexa647	Goat	Molecular Probes	1:200

Secondary antibodies for immunofluorescence analysis were coupled to Alexa Fluor 488, 546, 594, or 647 dyes (Thermo Fisher Scientific). Antibodies for Western blot analysis were coupled to horseradish peroxidase (Dianova).

Table 12. Antibodies used for FACS Analysis

For the MPP sort

antigen	Fluorochrom	Clone	Source
CD10	PE-CF594	HI10a	BD Biosciences
CD34	APC- AF750	581	Beckman Coulter
CD45	BV510	HI30	BD Biosciences
CD45RA	BV711	HI100	BioLegend
CD56	PerCP-Cy5.5	B159	BD Biosciences
CD66b	PerCP-Cy5.5	G10F5	BD Biosciences
CD133	APC	AC133	Miltenyi Biotec
CD38	BV786	HIT2	BD Biosciences
CD19	FITC	4G7	BD Biosciences
CD3	PerCP-Cy5.5	SK7	BD Biosciences

For the analysis of the kinetics

antigen	Fluorochrom	Clone	Company
CD10	PE-CF594	HI10a	BD Biosciences
CD34	APC- AF750	581	Beckman Coulter
CD45	BV510	HI30	BD Biosciences
CD45RA	BV711	HI100	BioLegend
CD133	APC	AC133	Miltenyi Biotec
CD38	BV786	HIT2	BD Biosciences

5.2 Methods

5.2.1 Molecular biology

5.2.1.1 DNA amplification by polymerase chain reaction (PCR)

The polymerase chain reaction (PCR) was used to amplify fragments of DNA from plasmid DNA. The reaction is based on the sequence specific annealing of two oligonucleotides, referred to as primers, to the DNA template. The sequence of the primers binds to the complementary strands of the template. The region between the

primers defines the DNA fragment that is amplified during the PCR. If needed for subcloning, overhangs containing restriction sites, followed by 3-4 nucleotides to enhance enzyme cleaving, were added to the primer sequence on the 5' site and, if needed for in-frame cloning, extra nucleotides were added on the 3' site of the primer. The initial step of increasing the temperature to 95°C is called denaturation, which induces the separation of the complementary DNA strands. The subsequent annealing step enables the binding of the primers to the DNA template. The annealing temperature of the two primers was calculated depending on their A/T and G/C content using the formula n(A, T) x 2°C + n(C, G) x 4°C. Afterwards, the temperature is changed to meet the temperature optimum of the used DNA polymerase (here 72°C) for the extension step. During this step, the polymerase is catalyzing the extension of both primers in 5´-> 3´direction using deoxynucleosid 5´-triphosphate (dNTPs) present in the reaction mix as a substrate. After completion, each DNA strand has been replicated once and is present as double stranded DNA. The reaction continues by repeating cycles of the described temperature changes until the desired degree of amplification is accomplished.

PCR reactions were run in a Thermocycler T-Personal (Biometra, Göttingen, Germany). The following reaction set up was used, respectively for the Pfu (Stratagene) or Q5 (NEB) kinase:

Q5	**Pfu**	
1-2 ng	20-50 ng	**DNA template**
0.5 µM	0.2 µM	**forward primer**
0.5 µM	0.2 µM	**reverse primer**
1x	1x	**Pfu/Q5-Polymerase buffer**
0.2 mM	0.2 mM	**dNTPs**
1 U	1.25 U	**Pfu Turbo DNA Polymerase**
To final volume of 50 µl	To final volume of 50 µl	**demin. H_2O**

Optionally, in tricky PCR reactions, Dimethyl sulfoxide (DMSO) was added to a final concentration of 2% (v/v) to prevent the formation of secondary structures in the DNA template. DMSO decreases the melting point of the primers, so if high DMSO concentrations are used, the annealing temperature must be lowered. Mg^{2+} concentration was increased if needed to raise the Tm (and thus also the annealing temperature) by acting as a catalyst for the polymerase and shielding the negatively charged backbone of the DNA, thereby decreasing the electrostatic repulsion between the DNA strands.

The thermocycler was programmed as follows:

Q5 Polymerase		**Pfu Polymerase**	
98°C	30 s	**95°C**	2 min
98°C	10 s (30 cycles)	**95°C**	30 s (30 cycles)
Primer Tm +3°C	30 s	**Primer Tm -5°C**	30 s
72°C	30 s/kb	**72°C**	1 min/kb
72°C	2 min	**72°C**	10 min

2-5 µl of the PCR reaction were analyzed on an agarose gel.

For sub-cloning, the fragment of correct size was excised, extracted (5.2.1.4.), digested with restriction enzymes (5.2.1.6.) and ligated into the destination plasmid (5.2.1.7.).

5.2.1.2 Cloning of PCR products with CloneJET PCR Cloning Kit

In cases it was necessary to enhance cloning efficiency of a PCR fragment into a vector, the CloneJET PCR Cloning Kit (Thermo Scientific) was used. Blunt-end PCR products generated by a proofreading DNA polymerase were directly ligated with the linearized pJET1.2/blunt cloning vector following the manufacturer's protocol.

5.2.1.3 Agarose gel electrophoresis

DNA fragments were separated according to their size using gels with 0.8-2% agarose in TAE buffer. Higher agarose concentrations are used to separate smaller fragments, while lower agarose concentrations are used to separate bigger DNA fragments. Before loading, samples were mixed with 1/5 volume of 6x DNA loading dye [0.25% (w/v) Bromophenol blue, 0.25% (w/v) Xylen cyanol FF, 15% (w/v) Ficoll 400 (Pharmacia, Sweden)] or 6x Gel loading Dye Purple (NEB). As standard marker, the 1 kb TrackIt™ ladder from Invitrogen or the 1 kb Plus DNA Ladder (N3200) from NEB were used. Gels were run at 100 V for analytical gels or at 50 V for preparative gels and subsequently stained with 1 ng/ml ethidium bromide in water for 10 minutes. After de-staining in water, bands were detected by UV-illumination and documented with a gel documentation system (Biometra, Analytik Jena).

5.2.1.4 DNA extraction from agarose gels

Excised bands were transferred to Eppendorf vials, weighed and DNA was purified with provided spin columns using the QIAquick gel extraction kit (Qiagen) or NucleoSpin® Gel- and PCR clean up kit (Macherey and Nagel) following the manufacturer's instructions. The kits are based on the principle of ion exchange

chromatography and use the differential adsorption of DNA to a chromatography matrix with changing pH-values to separate DNA from contaminants. The kit's spincolumns use a silica membrane as a matrix to adsorb DNA in aqueous solution with pH-values below 7.5, while solutions with higher pH-value lead to the elution of DNA. After loading the DNA to the columns, a series of wash steps in low pH-buffers remove contaminants. The elution of purified DNA follows with H_2O or EB buffer.

5.2.1.5 Determination of DNA concentration

DNA concentrations in solutions were determined with the Nanodrop ND-1000 Spectrophotometer (Nanodrop Wilmington, DE) by loading the 2 µl onto the device and comparing it´s absorbance to the buffer control. In order to calculate the DNA concentration, the device determines the absorbance of the loaded sample across wavelengths and calculates based on the absorbance at λ=260nm and λ=280nm the DNA concentration and purity based on the Beer-Lambert law are as follows:

$E_\lambda = -\log I_1/I_0 = c \times d \times e_\lambda$

E_λ Extinction, I_1 Intensity of transmitted light, I_0 Intensity of, c Concentration in µg/ml, d Travel length of light, e_λ Molar extinction coefficient depending on λ (DNA:λ260= 50 µg/ml; RNA:λ280 = 40 µg/ml)

The purity of DNA in the sample is thereby assessed by the ratio of absorbance. A λ260/λ280 ratio of 1.8 is pure for DNA, while a ratio of 2.0 is supposed to be pure RNA. Lower ratios indicate the presence of proteins, phenol or other contaminants that absorb at 280 nm.

5.2.1.6 Restriction digestion of DNA

The digestion of DNA is a controlled reaction catalyzed by specific enzymes referred to as restriction endonuclease. DNA was digested to generate DNA fragments for cloning, linearize integration plasmids and identify positive clones. Digests were carried out in the appropriate buffer system of the enzyme manufacturer (New England Biolabs, Beverly, USA). For a typical analytic restriction, 0.2-0.5 µg of DNA was digested in a final volume of 20 µl with 2-5 U restriction enzymes (NEB) and incubated for 1.5 h at the recommended temperature. For preparative plasmid and PCR fragment digestions, 1-5 µg of DNA was digested in a final volume of 50 µl with 10-20 U restriction enzyme and incubated for 4-12 h. Before ligation, the digested DNA was purified from the reaction mixture by PCR purification using the QIAquick PCR

Purification Kit according to the manufacturer's instructions. Digested DNA was analyzed by agarose gel electrophoresis.

5.2.1.7 Ligation of DNA into plasmid vectors

During the ligation reaction two linearized, double stranded DNA molecules, referred to as insert and backbone are connected via cohesive ends to produce a circularized DNA molecule. The ATP dependent enzyme T4- ligase catalyzes the reaction. Therefore, 50 ng of vector plus insert DNA as calculated by the NEBioCalculator according to the size of the vector and insert in a 1:3 ratio were mixed. The reaction was mixed with 1x T4 ligase buffer (NEB, includes ATP), H_2O and 1 µl (400 U) T4-Ligase (NEB) in a total volume of 20 µl and incubated either for 1-2 h at RT or at 16°C overnight. To stop the reaction and inactivate the ligase, the solution was incubated for 10 min at 65°C. 2-20 µL were transformed into *E. coli* DH5α. For cloning of plasmids constructed earlier in this thesis (before 2017), ligations were performed with 10 U T4 DNA ligase (Epicentre, Madison, USA). There, 50-200 ng of linearized vector was mixed with the insert in a 1:3 molar ratio, Epicentre ligase buffer (1x), 1.25 mM ATP, water and 10 U T4 DNA ligase in a total volume of 10 µl and incubated for 4 h at RT.

5.2.1.8 Dephosphorylation of DNA

If needed for tricky ligations, linearized plasmids were dephosphorylated before ligation to prevent their re-ligation. The reaction impacts the efficiency of the ligation reaction by reducing the frequency of false positive clones during selection to a minimum. For the reaction 1-5 µg of DNA were mixed with 10x Antarctic Phosphatase buffer (NEB) and 5 U of Antarctic Phosphatase (NEB) in a total volume of 20 µl and subsequently incubated for 15 min at 37°C.

5.2.1.9 Generation of shRNA expression constructs

For ligation into the MluI/ClaI linearized vector pCL2EGw.THPC (kind gift from Helmut Hanenberg) shRNA oligos were design according to the following scheme:

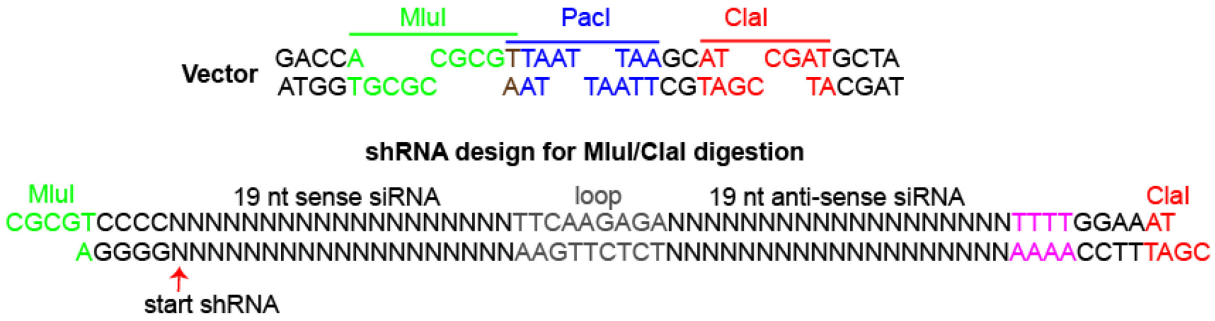

Figure 55. Design of shRNA oligos for ligation into pCL2EGw.THPC via MluI/ClaI restriction sites [adapted from Paula Rio (2005), group of Helmut Hanenberg].

For the generation of shRNA containing plasmids, first the two respective shRNA oligos were annealed. Therefore, 2.5 µl of each oligo (1 µg/µl) were mixed with 5 µl NEB 2.1. buffer and 40 µl water to a final volume of 50 µl. The mixture was heated up for 5 min. at 95°C in a heating block. Then the heating block was switched off and the mixture was cooled down to room temperature (RT) in the heating block covered with aluminum foil. shRNA oligos were cloned into the vector pCL2EGw.THPC via MluI/ClaI restriction sites. Therefore, 150 ng MluI/ClaI linearized vector, 2 µl freshly annealed oligos, 2 µl 10x T4 ligation buffer, 1.25 mM ATP, water and 10 U T4 ligase were mixed in a total volume of 20 µl and the ligation was incubated at 16°C O/N before transformation into competent DH5α. Positive clones were identified via restriction using the enzyme PacI and another single cutter, because the restriction site of PacI in pCL2EGw.THPC lies between the MluI and ClaI site and should be destroyed after successful ligation. Consequently, positive clones will result in a linearized plasmid. Positive clones were confirmed by sequencing using the primer H1.Forward. The shRNAs used for HSPCs were cloned according to the scheme in Figure 54, except the shRNA used for transduction of KG1a cells. In this case, ODF2 shRNA oligos were annealed using the same protocol, but designed with the forward overhang CCGG (AgeI site), loop CTCGAG, and reverse overhang 3'TTTTTG plus AATTCAAAAA (contains EcoRI site) and ligated into pLKO.1. via AgeI and EcoRI. U6 and shRNA were PCR amplified from positive pLKO.1. clones, subcloned in pJET and from there finally subcloned into the LEGO-G vector via XbaI and XhoI restriction for virus production.

5.2.1.10 Generation of gRNA and Cas9 expression constructs

gRNA was used for generating the ODF2 KO clone. To identify target sequences the online tool at http://crispr.mit.edu/ was used. Target sequences with the highest scores

and at the first exons were used. Three sequences were chosen, but homozygous KO was just achieved with the following oligos: Exon 2, first exon of ODF2 isoform 9 a.k.a. cenexin-1 (NM_002540.4) CACCGTCCCCCCTTACATGTTCACG and AAACCGTGAACATGTAA-GGGGGGAC. Following scheme was used to design gRNAs for cloning into BbsI linearized PX458 vector containing Cas9 from S. pyogenes with 2A-EGFP:

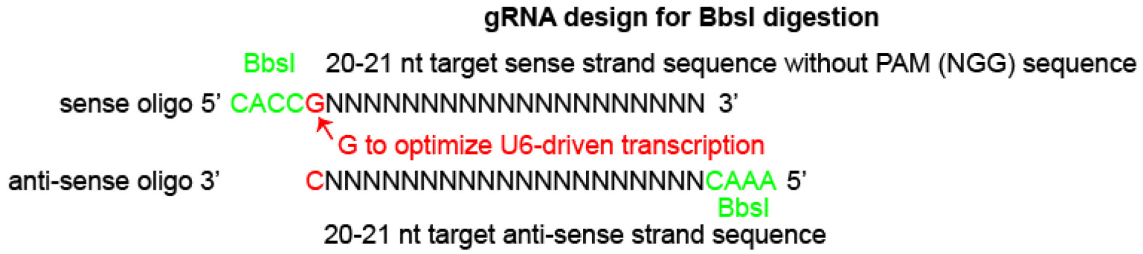

Figure 56. gRNA design for ligation into PX458 via BbsI.

For expression of gRNAs and Cas9, the two oligos containing the forward and reverse guide sequences were annealed by incubating 1 µl of each oligo (100 µM) with 0.5 µl T4 Polynucleotide kinase (New England Biolabs #M0201S) and 1 µl 10X ligation buffer (NEB) in a total of 10 µl for 30 min at 37°C, afterwards incubating the mixture at 95°C for 5 min and subsequent cooling to 25°C at a cooling rate of 5°C/min. Annealed oligos (1 µl from 1:200 diluted annealing reaction) were ligated into BbsI digested PX458 (50 ng) using the standard NEB T4 ligase protocol. Colony PCR (5.2.1.15.) of the targeted region using the forward guide oligo and the primer PX335_seq_R reverse as primers and the NEB OneTaq Polymerase was performed.

10µM	oligo forw.	1.25 µl
10 µM	PX335_seq-R	1.25 µl
2 mM	dNTPs	2.5 µl
2.5 µl	10x PCR buffer 3*	2.5 µl
0.2 µl	Taq Polymerase	0.2 µl
	H_2O	To 25 µl

*500 mMTris-HCL (pH 9.2), 160 mM $(NH_4)_2SO_4$, 22.5 mM $MgCl_2$, 20% DNSO, 1% Triton-X100

The thermocycler for colony PCR was programmed as follows:

95°C	5 min
95°C	1 min (30 cycles)
55°C	1 min

72°C	20 s
72°C	2 min

PCR products were analyzed on an 1.5% agarose gel. The expected size is around 0.3 kb. Positive colonies were amplified from backup plates and plasmids were purified and confirmed by sequencing.

5.2.1.11 Generation of chemically competent *E. coli*

Chemically competent *E. coli* cells were used for transformation by heat shock. To make chemically competent *E. coli*, a 250 ml culture was inoculated with an overnight pre-culture and grown at 18°C with shaking to an optical density at 600 nm (OD 600) of 0.6. The culture was pelleted by centrifugation at 1,000 g at 4°C and the pellet was gently resuspended in 1/3 of the original volume in chilled FTB (10 mM PIPES, 55 mM $MnCl_2$, 15 mM $MgCl_2$, 250 mM KCl). After incubation on ice for 10 min, the cells were again pelleted at 1,000 g and the pellet was resuspended in 1/12 of the original volume in cooled FTP [10 mM MOPS, 75 mM $CaCl_2$, 10 mM RbCl, 12% (w/v) glycerol]. After the addition of 7% DMSO, the cells were incubated for 10 min on ice and snap-frozen in liquid nitrogen to be stored at -80°C.

5.2.1.12 Heat shock transformation of chemically competent E. coli

An aliquot in chemo competent DH5α was thawed for 30 min on ice and mixed with 0.1-1 µg of DNA. After 30 min on ice, bacteria were heat shocked for 90 s at 42° and incubated on ice for 2 min. Next, 900 µL of TY-medium without antibiotics was added and cells were incubated shaking for 1h at 37°C. Afterwards the solution was plated on an agar plate containing the antibiotic required for selection and incubated over night at 37°C.

5.2.1.13 Preparation of *E.coli* glycerol stocks

Glycerol stocks are prepared to store successfully transformed bacteria and are used to circumvent the transformation reaction when more DNA of a previously cloned plasmid is needed. Glycerol stocks can be used directly to streak out a bit of the frozen stock on a plate containing the appropriate selection antibiotic(s) for inoculation of single colonies from this plate. To prepare a glycerol stock, 700 µl bacteria culture were mixed with 700 µl of 50% glycerol solution and frozen/stored at -80°C.

5.2.1.14 Isolation of plasmid DNA from *E. coli*

Colonies were inoculated in TY-medium supplemented with the appropriate antibiotics and grown under shaking overnight at 37 °C. Cells were pelleted for 2 min at 14,000 rpm and plasmid isolation was performed using the Qiagen Plasmid Mini Kit buffers (Qiagen, Hilden, Germany) combined with Genaxxon bioscience DNA purification columns (#S5313.0050) or for larger amounts with the NucleoBond® Midi/Maxi Kits plus NucleoBond® Finalizer (Macherey-Nagel) according to the manufacturer's protocols. The composition of the Mini Kit buffers can be found in the Materials section. The isolated plasmids were analyzed by restriction digestion and agarose gel electrophoresis.

The silica membrane used as a matrix in the columns is optimized to adsorb DNA in aqueous solution with pH-values below 7.5, while solutions with higher pH-value lead to the elution of DNA. After lysis of the bacteria and of plasmid DNA to the columns, a series of wash steps in low pH-buffers remove contaminants, which is followed by the elution of purified DNA with H_2O or EB buffer.

5.2.1.15 Colony PCR

To screen larger number of colonies for positive transformants, colony PCR was used instead of plasmid isolation and control digestion. Therefore, colonies were picked up and dissolved in a PCR master mix containing primer flanking the region of interest in the cloning vectors and Taq polymerase. Transformants were picked with a sterile toothpick and re-streaked on selective plates to isolate plasmids out of new inoculations from positive PCR results.

The following reaction set up was used per reaction/colony (following the protocol from CloneJET PCR Cloning Kit):

1 colony	DNA template
0.2 µM	forward primer
0.2 µM	reverse primer
1x	Taq-Polymerase buffer
0.2 mM	dNTPs
1.5 mM	$MgSO_4$
0.5 U	Taq DNA Polymerase
To final volume of 20 µl	demin. H_2O

The thermocycler was programmed as follows:

95°C	3 min
94°C	30 s (25 cycles)
60°C	30 s
72°C	1 min/kb

PCR reactions were analyzed on an agarose gel.

5.2.1.16 Precipitation of DNA

To precipitate DNA, 1/10 volume of 3 M sodium acetate (3M, PH 5.2) and 1/10 volumes 100% cold ethanol were added. The solution was mixed, incubated at -20°C for 1-24 h and centrifuged at 14,000 rpm for 30 min at 4°C. The precipitate was washed in 1 ml cold 70% ethanol and centrifuges at 14,000 rpm for 5 min at 4°C. The supernatant was removed, and the pellet air-dried and resuspended in 20 µl EB or H_2O.

5.2.1.17 Sequencing of DNA

DNA plasmids were sent for sequencing at GATC Biotech – Eurofins Genomics (Ebersberg, Germany). The sequencing results were manually analyzed using Snapgene Viewer.

5.2.1.18 RT-PCR

WT and siKif24 cells were detached from 6-well plates (Sarstedt TC Dish) using Trypsin-EDTA (Sigma-Aldrich) and centrifuged to form a cell pellet. RNA was isolated using the RNeasy Mini Kit (Qiagen Cat No./ID: 74104) according to manufacturer's directions (Part I). Total RNA was quantified on the Nanodrop ND-1000 Spectrophotometer (Nanodrop Wilmington, DE). Quantitative real-time PCR (RT-qPCR) was performed with 100 ng RNA using One-Step SYBR ®PrimeScriptTM RT-PCR Kit II (Takara, Perfect Real Time #RR086A) with ROX reference dye on the Applied Biosystems 7300 Real-Time PCR System according to the manufacturer's protocols. This method detects the fluorescence produced during the amplification process by the addition of SYBR Green, which binds to the double strand DNA that is synthesized by the polymerase in the reaction mix. Thereby, quantity and melting point of the amplified DNA can be measured. Forward and reverse primer pairs were reconstituted in Nuclease-Free Water. Results were exported to Microsoft Excel for analysis. All the corresponding RT-qPCR data was analyzed using the ΔΔCT method and normalized against GAPDH (housekeeping gene). The Ct (cycle threshold) is defined as the number of cycles required for the fluorescent signal to cross the

threshold (exceeds background level). Ct levels are inversely proportional to the amount of target nucleic acid in the sample. ΔCT was calculated by subtracting the Ct of GAPDH from the Ct of the gene of interest (Kif24), for each treatment (WT versus siKif24). ΔΔCT is considered as the subtraction of the ΔCT of the WT sample from the siKif24 sample. Since all calculations are in logarithm base 2, the value of 2^-ΔΔCt needs to be calculated the to get the expression fold change. The RQ value (fold change) was calculated by using the formula 2^(-ΔΔCT).

5.2.2 Yeast two-hybrid

5.2.2.1 Yeast transformation

A 5 ml preculture was grown overnight at 30°C in the appropriate medium, diluted to OD600 0.2 in 50 ml and grown to OD600 0.6-0.8. Cells were harvested by centrifugation at 3,200 rpm for 2 min at RT followed by one wash with 45 ml H_2O and one wash in 25 ml LiSorb (100 mM Lithium acetate, 10 mM Tris-HCl pH 8, 1 mM EDTA pH 8, 1 M Sorbitol). Once all residual LiSorb was removed by an additional centrifugation step, cells were resuspended in 300 µl LiSorb and 35 µl carrier DNA (Salmon Sperm, Invitrogen, Karlsruhe, Germany) that had been denatured at 95°C for 5 min and cooled on ice. Competent yeast cells were used immediately or aliquoted and frozen at -80°C. For each transformation reaction 50 µl of competent cells were mixed with 1-3 µl plasmid DNA and incubated for 15 min at RT. next, 300 µl LiPEG (100 mM Lithium acetate, 10 mM Tris-HCl pH 8, 1 mM EDTA pH 8, 40% PEG3350) were added and the mixture was briefly vortexed, followed by 15 min incubation at RT. After adding 35 µl DMSO and vortexing, the transformation reaction was heat shocked at 42°C for 15 min. The cells were centrifuged at 3,200 rpm for 3 min, resuspended in 200 µl PBS, plated onto selective plates and incubated at 30°C.

5.2.2.2 Yeast two-hybrid

The yeast two-hybrid system is used to detect protein-protein interactions. It was originally introduced by (Fields and Song, 1989) and is based on the fact that transcription factors are composed of two functional domains required for their function, the DNA binding domain (BD) and the DNA activation domain (AD). In the yeast two-hybrid system, one ORF is fused to the BD of the transcription factor Gal4 (referred to as Gal4), while the other is fused to the AD of Gal4 (referred to as LexA). If those two chimeric proteins are co-expressed in yeast, the functional transcription

factor is only reconstituted if the two fusion constructs come together and interact. Therefore, upon interaction of both proteins, the transcription of the reporter gen by Gal4 is activated. In this case *lacZ* (β-galactosidase) was used as reporter gene. Full-length and truncations of interest were cloned into yeast two-hybrid frame modified vectors pMM5 and pMM6 (Schramm et al., 2001). Those bait and prey constructs were first transformed in two different yeast strains that have opposing mating types before mating and selected according to their auxotrophy markers. The *S. cerevisiae* strain YPH500 (mat-alpha) is auxotrophic for the amino acid histidine, and the strain SGY37 (mat-a) is auxotrophic for leucin. The yeast strain SGY37 also carries the LacZ reporter gene. Activation of the reporter gene lacZ leads to the expression of β-galactosidase, which is detected by adding its substrate X-Gal (5-bromo-4-chloro-3-indolyl-β-D-galactoside). β-galactosidase metabolizes X-Gal, producing a blue dye after oxidation. A pool of colonies from the single transformation plates were picked and streaked as individual lines on selection plates. Transformants of LexA fusion proteins were then mated with the Gal4 fusion proteins on non-selective plates for 2 days, and next the diploid strains were selected on double selection plates. For these steps, replica plating was used to transfer yeast colonies from one plate to another. Here, a sterile velvet was taut over a plastic block and the original plate was then turned upside down and pressed gently onto the velvet. Then, a new plate was pressed onto the velvet to transfer the yeast colonies to the new plate and plates were subsequently incubated at 30°C.

Two-three days after selection, the plates were covered with overlay solution containing 0.25 M NaPi buffer pH 7.0, 0.1% SDS, 10 mM KCl, 1mM MgCl2, 0.4% low melting agarose, and 0.04% X-Gal heated to 40-50°C. Development of blue color was observed and recorded. The assay with the complete set of genes was repeated two times independently.

5.2.3 Cell culture

5.2.3.1 Cultivation and preservation of mammalian cells

All cell lines were grown at 37°C under 5% CO2. h-TERT-immortalized Retinal Pigment Epithelial (RPE1, ATCC, CRL-4000, USA) cells were grown in DMEM/F12 (Sigma Aldrich) supplemented with 10% fetal bovine serum (FBS, Biochrom), 2 mM L-glutamine (Thermo Fischer Scientific) and 0.348% sodium bicarbonate (Sigma Aldrich). RPE1 Nek2 KO cells (clone 18 and 27) were generated by M. Panic (Elmar

Schiebel, ZMBH, University of Heidelberg, Germany). The rescue cell line RPE1 Nek2 KO clone 27 with Tet3G pRetrox-Tre3G-mNeonGreen-Nek2A and RPE1 Tet3G pRetrox-Tre3G -mNeonGreen-Nek2A WT/KD cell lines were made by A. Pastor-Peidro (Elmar Schiebel, ZMBH, University of Heidelberg, Germany). HEK293T cells (ATCC CRL-3216) and GP2-293 (Takara Bio) were cultured in DMEM High Glucose supplemented with 10% FBS. MCF10A, MCF10CA1d.cl1, and MCF10AT1k.cl2 were a courtesy of C. Conrad and K. Jechow (Heidelberg) and originally obtained from the Barbara Ann Karmanos Cancer Institute (Detroit, MI, USA). MCF10A, MCF10A and MCF10AT1 cell lines were maintained in DMEM/F-12 supplemented with 0.1 µg/ml cholera toxin, 10 µg/ml insulin, 0.5 µg/ml hydrocortisone, 0.02 µg/ml epidermal growth factor (EGF) and 5% horse serum. KG1a (ATCC® CCL-246.1™) and primary CD34+ cells (HSPCs) were provided by the Department of Internal Medicine V, University Hospital Heidelberg (A. Lenze, A.D. Ho, P. Wuchter, P. Horn, C. Pabst). KG1a cells were cultured in RPMI-1640 with 2 mM L-glutamine and 10% FBS. Primary HSPCs were cultured in Stemline II Haematopoietic Cell Expansion Medium (Sigma), supplemented with L-Glutamine (2 mmol/l, Thermo Fischer Scientific), TPO (100 ng/ml, R&D systems), SCF (100 ng/ml, R&D systems), G-CSF (100 ng/ml, R&D systems) and FLT3-L (500 ng/mL, R&D systems). HSPCs were expanded for 4 days after isolation on retronectin coated dishes (Takara, T100B Recombinant Human Fibronectin Fragment). The coating was performed by incubating the dish (cellstar greiner bio-one suspension culture plate) for 2 h at 37°C with retronectin at a final concentration of 20 µg/ml in PBS (Sigma-Aldrich), followed by washing in PBS. For experiments performed in cooperation with the group of Bernd Giebel, HSPCs were cultured in IMDM with 20% FBS and 10 ng/ml Flt3L,10 ng/ml SCF as well as 10 ng/ml TPO.

5.2.3.2 Isolation of hematopoietic stem and progenitor cells

All experiments involving the use of human HSPCs were approved by the Ethics Committee of the Medical Faculty, University of Heidelberg, Germany and performed after obtaining informed consent from all voluntary donors in accordance with relevant guidelines and regulations. Human HSPCs were derived from umbilical cord blood (CB) or from healthy allogeneic stem cell donors. The latter had received a mobilization regimen with G-CSF (10 µg/kg bw per day subcutaneously for 5 days) and a sample of 60 ml of peripheral blood (PB) was taken for this study prior to leukapheresis. HSC

were isolated as previously described (Ludwig et al., 2014; Wein et al., 2010). Briefly, mononuclear cells (MNCs) were isolated by density gradient centrifugation using the Ficoll–Hypaque technique (Merck KGaA, Darmstadt, Germany). CD34+ cells from the MNC fraction were enriched by labeling with magnetic microbeads and sorted twice using an affinity column with the AutoMACS system (all Miltenyi Biotec GmbH, Bergisch-Gladbach, Germany).

5.2.3.3 Induction of ciliogenesis

RPE1 cells were incubated in serum-free medium for 48-72 h to induce cilia formation as indicated in the respective figure legend. Nek2 KO cells were serum starved for 24 h, followed by 24 h serum re-stimulation to stimulate the formation of a ciliary remnant. For the same purpose, mSMO-eGFP was induced via doxycycline for 24 h, followed by 24 h serum starvation and 24h serum-re-stimulation. SAG (0.4 µM, Tocris, Cat. No. 4366) treatment was combined with the serum re-stimulation for 24 h. MCF10A, -AT and -CA1 cells were grown for 7 days in confluence to induce ciliogenesis.

5.2.3.4 Proteasome inhibition

Proteasome inhibition was induced by incubating the cells with MG132 (Biozol, SMQ-SIH-537) for 4 h at a final concentration of 20 µM. PLK1 inhibition was achieved using BI-2536 at a concentration of 200 nM for 1 h. Because cells without Plk1 activity arrest in prometaphase (Mardin et al., 2011), inhibition was confirmed by quantifying cells in prometaphase after treatment.

5.2.3.5 PLK1 inhibition

PLK1 inhibition was achieved using BI-2536 at a concentration of 200 nM for 1 h. Because cells without Plk1 activity arrest in prometaphase (Mardin et al., 2011), inhibition was confirmed by quantifying cells in prometaphase after treatment.

5.2.3.6 Transfection

RPE1 cells were transiently transfected with plasmid DNA by either electroporation using the NEPA21 transfection system (Nepa Gene) or using Fugene 6 (Promega) according to the manufacturer's protocol (Fugene 6 /DNA 3:1 ratio) and fixed 24-48 h after transfection. In case the NEPA21 transfection system was used, $1x10^6$ cells were transfected with 10 µg DNA in a total volume of 100 µl (filled up with Optimem) using the following parameter:

Poring Pulse						Transfer Pulse					
V	Length (ms)	Interval (ms)	No.	D. Rate (%)	Polarity	V	Length (ms)	Interval (ms)	No.	D. Rate (%)	Polarity
150	**5**	50	**2**	10	+	20	50	50	5	40	+/-

Transient transfection in HEK293T and GP2-293 cells was performed using Polyethyleneimine (PEI 25000, Polysciences). Therefore, HEK293T cells were grown in 10 cm dishes (Sarstedt TC Dish) until 80% confluency and were transfected with a 3:1 ratio of PEI:DNA (6 µg DNA and 18 µl PEI). DNA and PEI were mixed before in Optimem in a final volume of 750 µl. The mixture was incubated for 20 min at RT and added drop wise to the cells. Eight-12 hours after transfection, the medium was changed. 48 h after transfection, cells were harvested (5.2.5.1.).

5.2.3.7 siRNA-mediated protein depletion

Transfections of siRNA were performed using Lipofectamine RNAiMAX transfection reagent (Thermo Fischer Scientific) according to the manufacturer's instructions. Cells were analyzed 48-72 h after the initial transfection. All siRNAs used in this study were used in 50 nM final concentration.

5.2.3.8 Generation of cell lines via viral transduction

Stable cell lines expressing L13-Arl13bGFP (Larkins et al 2011) were generated using lentiviral transduction. Therefore, HEK293T cells were transiently transfected with L13-Arl13bGFP (24 µg), pMDG2 (Addgene) (12 µg), and pSPAX2 (12 µg) in a 15 cm dish (Sarstedt TC Dish) at 60% confluency using a 1:3 DNA:PEI ratio. Forty-eight h after transfection, the supernatant was supplemented with 4 µg/ml polybrene and used to transduce RPE1 WT and Nek2 KO cells.

RPE1 cells with inducible expression of proteins of interest were constructed as previously described (Vlijm et al., 2018). Tet3G pRetroX-TRE3G with mSMO-eGFP, mNeonGreen-PLK1, mNeonGreen-PLK1-T210D and pQCXIZ TUBG1-mRuby2 (γ-tubulin-mRuby2) in L13-Arl13bGFP RPE1 or Nek2 KO cells were generated via retroviral transduction. The gene of interest (6 µg) was co-transfected with the envelope vector pMDG2 (6 µg) per well in a 6-well plate into an HEK293-based retroviral packaging cell line (GP2-293, Clontech) using PEI at 60% confluency. Media was changed after 24 h and after 48 h, the virus-containing media was harvested and filtered using a 0.45 µM filter (Millipore). Four parts of filtered virus medium were

supplemented with two parts fresh media, one part FBS and 4 µg/ml Polybrene (Sigma). Cells pre-seeded in a 6-well plate were infected by adding the virus-containing solution three times sequentially for 6 h. Cells were split 24 h after the first transduction. GFP and mRuby-positive cells were selected by fluorescence-activated cell sorting (BD FACS-ARIA II SORP).

5.2.3.9 Transduction of hematopoietic cells

HSPCs were transduced in cooperation with the group of Bernd Giebel. For HSPC transduction the foamy virus system was used (kind gift from Helmut Hanenberg, University Clinic Düsseldorf). The envelope plasmid pPE01 codes the foamy virus envelope (Mergia and Heinkelein, 2003). In brief, for generation of the foamy virus, HEK293T cells with 60% confluency in T-175 flasks were transfected with 22.5 µg of the helper plasmid pNL-BH (for HIV1 gag/pol/rev), 3.5 µg pPE01, and 22.5 µg shRNA or overexpression construct, mixed with 240 µl of 1 mg/ml PEI solution in 3 ml DMEM high glucose. The mixture was incubated for 30 minutes before adding it to the flask with 6 ml DMEM high glucose, 15% FBS, 1.5% PBS. Twenty-four h after transfection the medium was changed to DMEM high glucose supplemented 10% FBS and 10 mM sodium butyrate to induce the CMV promotor for 8 h. Afterwards the medium was replaced by fresh medium, which was harvested after 18-22 h. The virus containing supernatant was filtered through a 0.45 µm filter (Millipore) and centrifuged at 26,000 g at 4°C for 90 min. The supernatant was discarded, and the pellet resuspended in 2 ml N-2-hydroxyethylpiperazine-N'-2-ethanesulfonic (HEPES) buffered medium (20 % FBS in IMDM), aliquoted and stored at -80°C until use.

For transduction, 1-2x10^5 HSPCs (one day after isolation) were plated on retronectin coated plates containing HSPC medium (IMDM with 20% FBS and 10 ng/ml Flt3L,10 ng/ml SCF as well as 10 ng/ml TPO) and 100 µl concentrated virus was added and incubated overnight at 37°C and 5% CO_2.

KG1a cells were transduced with lentivirus containing shRNA (produced as described in 5.2.3.8.). In this case, viral supernatant was concentrated using Lenti-X^{TM} according to the manufacturer's instructions. Cells were seeded on retronectin coated dishes (5.2.3.1.) one day before transduction and 50 µl virus was added aiming a titer >1x10^7 IU/ml in the presence of 4 µg/ml polybrene. Medium was changed 24 h after transduction and positive cells were pooled by FACS sorting for GFP positive cells before being processed in an experiment.

5.2.3.10 Induction of inducible expression

Expression of Tet-on-inducible constructs (Retro-X Tet-On 3G Inducible Expression System, Clontech Laboratories, Inc) was induced by the addition of doxycycline (Sigma-Aldrich) at a concentration of 10 ng/ml for 24 h and 72 h in case ciliation was induced by serum starvation for additional 48 h.

5.2.3.11 Rescue experiments

In the rescue cell line Nek2 KO with Tet3G pRetrox-Tre3G-mNeonGreen-Nek2A, Nek2A expression was induced by the addition of doxycycline at a concentration of 1 ng/ml for 24 h to allow a weaker Nek2 expression. Higher Nek2 expression arrests cells in prometaphase and leads to

5.2.3.12 Generation of Crispr Cas KO cells

RPE1 ODF2 knockout clones were generated by transfecting $1x10^6$ cells with 15 µg of the gRNA containing plasmid (gRNA cloned into PX458 as described in 5.2.1.10.) using the electroporation NEPA21 Transfection System (Nepa Gene) according to the manufacturer's instructions. Forty-eight h after transfection, GFP positive cells were single sorted in 96-well plates containing 50% normal and 50% conditioned medium (BD FACS-ARIA II SORP). After expansion, genomic DNA of the clones was extracted according to the manufacturer's protocol (GeneJET Genomic DNA Purification Kit, Thermo Scientific). PCR of the targeted region was conducted using primers flanking this region. Successful KO was confirmed by sequencing of the PCR product. Additionally, the PCR products were subcloned into pJET using the CloneJET PCR Cloning Kit and 3-6 isolated plasmids with insert were sent for sequencing.

5.2.3.13 Fluorescence-activated cell sorting (FACS)

For the creation of cell lines with tagged fusion constructs or KO cell lines, positive clones were bulk or single sorted, in the case of the ODF2 KO cell line using FACS. For processing by cell sorting, cells of a 10 cm dish were trypsinized, centrifuged (1000 rpm, 5 min), washed once with PBS and after another centrifugation resuspended in 500 µl PBS. Sorting of the cells was performed by the FACS Core Facility of the University Clinic Heidelberg, led by Volker Eckstein, with a BD FACS-ARIA II SORP.

5.2.3.14 Analysis of the differentiation potential of HSPCs using FACS

The analysis of HSPC differentiation was performed within the cooperation with the group of Bernd Giebel. CD34+ cells were isolated from umbilical cord blood using Ficoll Gradient Centrifugation (Biocoll-Trennlösung, Biochrom) followed by CD34 MACS Isolation (MBC CD34 Micro Bead Kit human, Miltenyi Biotec). Cells were sorted for MPPs ($Lin^-CD34^+CD45^{int}CD133^+CD45RA^-$), using the antibodies listed in Table 5. One day after isolation, cells were transduced with GFP, the ODF2 shRNA or the Nek2 overexpression constructs and cultured in HSPC medium (IMDM with 20% FBS and 10 ng/ml Flt3L,10 ng/ml SCF as well as 10 ng/ml TPO) and analyzed flow cytometrically on day 3, 7 and 12 after transduction.

For the flow cytometric analysis cells were extracellular labeled with fluorochrome conjugated antibodies. Cells were stained in media or PBS with 16 % v/v Brilliant Stain Buffer (BD). The buffer already contains BSA, so no additional protein was added. The applied antibodies were used in a 1:25 dilution and incubated for 30 min on 4°C in the dark. Afterwards surplus antibodies were washed off with PBS via centrifugation (900 g 5 min) and the cells were resuspended in a smaller volume for measuring. For the discrimination of dead cells 7-AAD is added in a dilution of 1:12.5 during the antibody staining. All measurements were performed on an ARIA IIIu (BD Biosciences). The analysis of the data was performed with FlowJO (Version 10.4.1, BD Biosciences). In the flow cytometric analysis, the composition of the MP, LM, EM and LP populations were characterized using the antibodies listed in Table 7. Additionally, the GFP+ frequency of the transduced cells was followed to identify impacts of the inserted constructs on the proliferation rate. In parallel, the granulocyte, macrophage and erythrocyte differentiation capacity of the transduced cells was studied. For this purpose, GFP+ LM (CD34+CD45intCD133+CD45RA+) and EM (CD34+CD45intCD133-CD45RA-) were sorted into the CFC assay during the flow cytometric read-out on day 3 post transduction.

5.2.3.15 Colony forming cell (CFC) assay

For colony-forming cell (CFC) assays, 200 sorted cells (LM and EM on day 3 of cultivation) were seeded into 1 ml MethoCult H4434 (StemCell Technologies) and divided on two wells (500 µl each) of a 24-well plate (Greiner Bio-One). After 12-14 days the M-, G-, E- and Mix-CFUs were counted (M: macrophage, G: granulocyte, E:

erythrocyte, Mix: having M, G and E). The analysis of HSPC differentiation was performed within the cooperation with the group of Bernd Giebel.

5.2.3.16 Preparation of ICAM-1 supported membranes

ICAM-1 coated membranes were prepared in cooperation with the group of Motomu Tanaka by Judith Thoma. Chamber slides were prepared by sealing microscopic grade 256 x 75 mm^2 glass slides from Gerhard Menzel GmbH (Braunschweig,Germany) to bottomless plastic fluidic channels (m-Slide $VI^{0.4}$) from Ibidi (Martinsried, Germany). Preparation of supported membranes was performed as described previously (Burk et al., 2015). Briefly, stock solution of lipids in $CHCL_3$ (5 mg/mL) were mixed to obtain 0.5 mg/ml SOPC with 2 mol% DOGS-NTA. With the maximum concentration of lipid anchors in the matrix lipids of 2 mol% DOGS-NTA lipid anchor distance is ~5.7 nm. Stock solutions of lipids were injected into the glass vials. After evaporation of $CHCl_3$ under a gentle nitrogen stream and storage under vacuum overnight, the lipids were re-suspended in HBS buffer (150 mM NaCl, 10 mM Hepes, pH 7.4) in a concentration of 0.5 mg/ml and sonicated for at least 60 min to obtain small unilamellar vesicles (SUVs). To remove any residual titanium particles, vesicle suspensions were for 10 min at 13400 g. Thereafter, SUV suspensions (0.5 mg/ml) were stored at 4°C for up to 2 weeks. The supported lipid bilayer was obtained by vesicle fusion. SUV suspension was injected into the channel slide and incubated for 30 min at 40°C, followed by rinsing with Ni^{2+} buffer (2 mM $NiCl_2.6H_2O$, 150 mM NaCl, 10 mM Hepes, pH 7.4) to remove excess SUVs. Supported membranes were incubated with Ni^{2+} buffer to saturate the NTA-group with nickel cations. Then, every channel was rinsed with 20 ml HBS buffer. The His-tagged protein was added at a concentration of 200 nM and the sample was packed in aliminium foil and incubated overnight at 4°C.

The HIS-tagged protein concentration for saturation of lipid anchors was calculated by dividing the area of the channel through the area of the anchor and is further determined by $n_{protein} > 10 \times n_{anchors} = 0.03$ nmol for ICAM-1. Thus, the protein concentration needed for saturation is 1.5 µg in 30 µl ($V_{channel}$) = 0.05 mg/ml per channel. Before imaging, excess proteins were removed by rinsing with 20 ml preheated medium per channel, and the samples were equilibrated at 37°C.

5.2.4 Microscopy and image analysis

5.2.4.1 Cell fixation and immunofluorescence staining

RPE1 cells were grown on coverslips (No. 1.5, Thermo Fischer Scientific) and fixed in ice-cold methanol at -20 ºC for 5 min or pre-fixed with 3% PFA for 3 min prior to methanol fixation to conserve fluorescence in cell lines containing fluorophore-tagged proteins. Cells were blocked with blocking solution containing 3% IgG-free BSA (Jackson ImmunoResearch), 0.1% Triton X100 (Sigma Aldrich) in PBS for 30 minutes and incubated with primary antibodies dissolved in blocking solution for 1 h at RT. All antibody solutions were centrifuged at full speed at 4°C for 3 minutes before adding the supernatant to avoid antibody aggregates and unspecific staining. After washing with PBS, the cells were incubated with conjugated secondary antibodies together with 4'6-diamidino-2-phenylindole (DAPI) (Sigma-Aldrich) dissolved in blocking solution for 1 h at RT. Coverslips were mounted with Mowiol (EMD Millipore).

For the staining of hematopoietic suspension cells, cells were fixed as described above in suspension and washing steps with PBS were performed by centrifugation (5 min, 1500 rpm at RT). After fixation and washing steps, cells were resuspended in an appropriate volume of blocking solution (for $1x10^6$ cells ~200 µl), incubated for 30 min at RT and then a ~ 20 µl drop of cell suspension was dried per well on an 18 well teflon coated slide (HTC supercured, Thermo Scientific). While aliquoting the drops, cell density was monitored using a light microscope and the amount of cell suspension was adjusted until the wished density was achieved. The slides with cell suspension were dried in a laminar flow hood. Dried cells were resuspended with a drop of water and after removal of water stained as described above.

5.2.4.2 Immunofluorescence microscopy

Images were acquired as Z stacks (4.5 µm in 16 steps) using Zeiss Axio Observer Z1 equipped with 63x NA 1.4 Plan-Apochromat oil immersion objective, and AxioCam MRm CCD camera using the ZEN software.

5.2.4.3 Live cell imaging

For live cell imaging, cells were seeded in cellview culture dishes (Greiner bio-one) and imaged for 21 to 24 h. Images were acquired as Z stacks using Zeiss Axio Observer Z1 equipped with 63x NA 1.4 Plan-Apochromat oil immersion objective, and AxioCam MRm CCD camera using ZEN software. For the staining of sirTubulin in live

cell imaging in the SMO-eGFP cell lines 20 nM sirTubulin and 5 µM verapamil were added to the medium 3 h before imaging.

For imaging of CD133 stained HSPCs, ~700,000 cells were seeded in a retronectin coated µ-Dish (ibidi, Westfield Medical, uncoated) containing Stemline II + cytokines after 3 days of expansion under the same condition isolation. Before imaging, cells were pelleted at 1800 rpm for 10 min and resuspended in medium containing 1:50 HC7-PE and incubated at 4°C for 30 min. After washing with PBS via centrifugation, cells were resuspended in Stemline II medium + cytokines and 1:20,000 HC7-PE using Zeiss Axio Observer as above.

For imaging of HSPCs, KG1a- and K562 cells on ICAM-1 coated channel slides (5.2.4.16.), HSPCs were expanded on retronectin coated wells for 2-3 days before imaging and ~100,000 cells were seeded each in ICAM-1 coated channels. Slides with cells were incubated at 37°C for 1-1.5 h to ensure adhesion of the cells. Phase contrast imaging was performed for 12-13.6 hours, all 70 seconds, on a Keyence BZ-9000 (Keyence, Osaka, Japan) microscope, equipped with a Plan Fluor 40x/0.6 air objective. Imaging on the Keyence microscope was recorded by Rainer Saffrich.

5.2.4.4 3D SIM

For 3D-SIM, cells were processed for immunofluorescence microscopy as described above, except that cells were mounted in Prolong Gold antifade reagent (Molecular Probes). Samples were analyzed with 3D-SIM Nikon Ti inverted microscope equipped with three lasers (488, 561 and 647 nm), a Nikon Apo TIRF 100×1.49 NA oil immersion objective and an Andor iXon3 DU-897E single-photon detection EMCCD camera. After image capture, raw images were reconstructed in the NIS-Elements program of the microscope to obtain 3D-SIM images.

5.2.4.5 Image processing and analysis

Images were processed in ImageJ and Illustrator CS5 (Adobe). For figures the maximum projection of representative images using FiJi (Schindelin et al., 2012) was generated. Image brightness and contrast were adjusted equally in Fiji. Quantification of fluorescence intensity was performed using maximum projection of images using Fiji. In a Fiji macro, an area around the centrosome (judged by γ tubulin staining) of 25 square pixels and near the centrosome of 49 square pixels (background) was defined. For background subtraction, first the mean background intensity was calculated.

Therefore, the integrated intensity measurement of the centrosome area was subtracted from the integrated intensity measurement of the background area and divided through the subtraction of the background area minus the centrosome area. This value was subtracted from the mean intensity of the centrosome area to get the mean value with background subtraction. Intensity measurements from replicate experiments were normalized to the average of each repetition and combined. Statistical tests were performed in Excel (Microsoft) and R (https://www.r-project.org/). The data was plotted as box plots using R (Synergy Software) or bar graphs using Excel. Colocalization of signals in 3D-SIM images was analyzed using the Plot Profile tool in Fiji and graphs were normalized and plotted in Excel.

5.2.4.6 Statistical analysis

For statistical analyses two-tailed Student's t-tests were applied using the average of each repetition. Significance probability values are: ns: $P > 0.05$, *: $P \leq 0.05$, **: $P \leq 0.01$, ***:$P \leq 0.001$, ****: $P \leq 0.0001$. The sampling sizes for quantifications are indicated in the respective figure legends.

5.2.4.7 Cell cycle-related analysis

Mitotic cells were identified by immunofluorescence microscopy based on their chromosome morphology (condensed chromosomes). Cells with non-condensed chromosomes and split centrioles ($d > 4$ µm) were classified as in the G2 phase of the cell cycle. Inter-centrosomal distances were measured manually using Fiji. If methanol fixation had to be used in hematopoietic cells, nuclear morphology could not be preserved. In this case, prometaphase and metaphase cells were only distinguished by the distance between the two centrosomes and spindle morphology. The intensity of the two mitotic centrosomes was measured and calculated as described in Image Processing and Analysis. The values for the second centrosome were set to zero in interphase because just one centrosome and appendage signal exists in this cell cycle phase. Measurements were normalized to the normalized to the average of interphase. Centrosome 1 mean intensity of interphase was tested for significant difference with centrosome 1 mean intensity during mitotic phases using two-tailed Student t-test for the average values of all repetitions. Results show the average ± standard derivation of the performed repetitions.

5.2.4.8 Measurement of cilia length

Arl13B marked cilia were measured from base (centrosome marked) to tip, using the Measure Plugin in the Fiji software.

5.2.4.9 Imaging flow cytometry

For imaging flow cytometric analysis, cells were prefixed in 0.5% PFA (in medium) for 5 minutes at RT. Cells were transferred into a falcon and PBS was added to the maximal volume to dilute the fixation and cells were harvested by centrifugation (900 g 5 min). Next, 10^8 cells per staining were resuspended in 500 µl methanol and washed with PBS (all washing steps by filling up the falkon with PBS and centrifugation at 500 g 5 min) and resuspended in 50 µl blocking solution (3% BSA in PBS + 0.1% TritonX100). After incubation for 30 min at RT, CD133 (HC7-PE) (1:50) and CD34 (1:22.5) staining was performed by resuspending the cells in blocking solution including the diluted antibody. After two washings with PBS, cells were resuspended in blocking buffer with ODF2 and γ-tubulin antibodies and incubated for 1 h at 37°C. Antibody solutions were centrifuged at full speed at 4°C for 3 minutes before adding the supernatant to avoid antibody aggregates and unspecific staining. After two washing steps, cells were resuspended in 100 µl blocking solution with secondary antibodies and DAPI. After 45 minutes incubation at RT on a rotator, cells were washed two times and resuspended in 60 µl PBS and measured.

Data was recorded on the ImageStream X Mark II (AMNIS) (ISX; Amnis/MilliporeSigma) equipped with 5 lasers (70 mW 375 nm, 100 mW 488 nm, 200mW 561 nm, 150 mW 642 nm, 70 mW 785 nm (SSC), a 96-well autosampler and an EDF option using a 60× objective with an NA of 0.9 and a DOF of 2.5 µm. All lasers were set to maximum powers, middle flow rate and SSC off settings were used as described in (Görgens et al., 2019). Data was analyzed using the IDEAS software (version 6.1.). A compensation file was created by recording of single stainings and uploaded as compensation matrix in the IDEAS software. Table 13 shows the compensation matrix for channel 1 (brightfield), channel 2 (ODF2 Alexa Fluor 488), channel 3 (HC7-PE), channel 4 (CD34-ECD), channel 7 (DAPI), and channel 11 (γ-tubulin Alexa Fluor 647).

Table 12. Compensation matrix used for AMNIS analysis

	Ch01	Ch02	CH03	Ch04	Ch07	Ch11
Ch01	1	0.028	0.039	0.047	0.004	0.005
Ch02	0.052	1	0.072	0.052	0.012	0.005
Ch03	0	0.123	1	0.241	0.004	0.005
Ch04	0	0.057	0.462	1	0.004	0.005
Ch07	0.026	0	0	0.008	1	0.061
Ch11	0	0	0.006	0.033	0.01	1

Following data acquisition, different “masks”, defined as the algorithm, which selects pixels within an image based on their intensity and localization, were used in the IDEAS software. In the final analysis, a gating strategy was established to first, identify dividing cells, based on their morphology and DAPI, second, measure the intensity o CD133 in each daughter cell and third, correlate the CD133 intensity within the ODF2 high and ODF2 low daughter cell. Therefore, the following steps were conducted:

Identification of mitotic cells

Step 1: The Aspect Ratio was plotted versus the Area of the brightfield image. The gate was set to exclude small debris (very low Area) and cell aggregates (high Area).

Step 2: To exclude non-focused cells, first the gradient RMS feature was used for the phase contrast channel to produce a histogram of the cells selected in step 1. This feature enumerates changes of pixel values in the image to measure the focus quality of an image. A threshold was set to exclude non-focused cells.

Step 3: Next, Intensity of channel 4 (CD34) was plotted against the DAPI signal to identify events positive for CD34 and high DAPI. High DAPI signal specifies the G2/M population.

Step 4: The Threshold 50% Area of the DAPI channel was plotted against the Bright Detail Intensity of the DAPI channel to identify cells with condensed nuclei. Condensed nuclei have a high Bright Detail Intensity.

Step 5: The brightfield Contrast was plotted versus the Threshold 50% Area of DAPI to discriminate mitotic cells from apoptotic cells. The gate should include cells with higher Threshold 50% Area of DAPI but low brightfield contrast. Mitotic and polarized cells will be found in the resulting population.

Identification of Anaphase and Telophase cells

Step 6: The Spot Count of the LevelSet Mask for the DAPI channel was used to identify events with two nuclei. Two DAPI spots are found in Anaphase-, Telophase cells and cell duplets.

Step 7: The Aspect Ratio Intensity for components having two nuclear spots of the LevelSet Mask was plotted for each component. Thereby cells with low nucleus Aspect Ratio were gated. This further excluded coincidence events of two nuclei.

Step 8: Next, the Ratio_Area_Comp1/2 was plotted for each component. In Ana- and Telophase cells, both daughter compartments are of similar size, in contrast to cells duplets. Thereby Comp Ratios between 0.8 and 1.5 were gated to eliminate false positives.

Step 9: Anaphase and Telophase events were separated by plotting the symmetry of the DAPI channel versus the circularity of the brightfield image. Telophase cells have higher symmetry but lower circularity.

Correlation of centrosome age and CD133 distribution

Step 10: The H Entropy Mean of the γ-tubulin channel was plotted versus the H Entropy Mean of the ODF2 channel. Thereby, cells with unsharp/granular centrosome signal (high H Entropy Mean) could be excluded from the gate.

Step 11: The Spot Count of the Threshold Mask for the γ-tubulin channel was used to identify events with two or three γ-tubulin signals. Three γ-tubulin spots were not excluded because γ-tubulin sometimes displays an additional signal at the midbody of telophase cells.

Step 12: The Watershed and Components Mask was used to separate the two CD133 compartments and measure CD133 intensity for each daughter cell separately. The daughter cells were separated by the DAPI channel using the Watershed Mask. The Component Mask for each daughter cell ranked the intensity for the CD133 channel. The X-axis shows the intensity for CD133 in one daughter and the Y-axis CD133 intensity for the other daughter cell. Thereby cells with higher CD133 intensity in one of the two daughter cells can be distinguished. The mask was used for the population of Telophase cells with 2-3 γ-tubulin signals and is named Intensity_Component(1/2, Intensity, watershed(DAPI channel), CD133 channel, Ascending)_CD133 channel.

Step 13: Finally, the Bright Detail Intensity R3 feature was used in combination with the Watershed and Component Mask to measure ODF2 intensity in each compartment and rank it to an ODF2 high and ODF2 low compartment. Then CD133 intensity was plotted for each compartment. In the resulting graph shown in Figure 23, daughter cells with high CD133 intensity in the ODF2 high compartment can be distinguished from daughter cells with high CD133 intensity in the ODF2 low compartment. The final Mask/Feature combination applied for the population of Telophase cells with 2-3 γ-tubulin signals was Intensity_Component(1/2, Bright Detail Intensity R3, Wathershed(DAPI channel), ODF2 channel, Descending)_CD133 channel. The distribution of CD133 segregation to the ODF2 high and low compartment was calculated by diagonally splitting the plot with a triangular gate.

5.2.4.10 EM

Transmission electron microscopy was performed by Annett Neuner (ZMBH, Heidelberg). Cells were grown on coverslips and fixed using 2.5% glutaraldehyde in 0.1 M Na cacodylate buffer, pH 7.2, at RT for 30 min. The cells were subsequently washed with 0.1 M Na cacodylate buffer and postfixed with 2% osmium tetroxide in Na cacodylate buffer for 1 h on ice. The samples were washed and contrasted in 0.5% uranyl acetate overnight. The samples were subsequently washed and gradually dehydrated by immersing them in a graded ethanol solution from 50, 70, to 90% and finally two times in 100% ethanol. Dehydrated cells were embedded in Epoxy medium using Epoxy Embedding kit (Fluka) and serial sections were generated using Reichert Ultracut S Microtome (Leica Instruments). Sections were post-stained with 2% uranyl acetate (in 70% methanol) and lead citrate. Finally, serial sections were viewed using a CM120 electron microscope (Phillips Electronics), operated at 120 kV, and images obtained by a Keen view CCD camera (Soft imaging systems).

5.2.5 Protein biochemical and immunological techniques

5.2.5.1 Harvesting of mammalian cells

Cells were washed once with chilled PBS and scraped from the dish in PBS. The suspension was transferred to a Falcon tube and the cells were pelleted at 1,000 rpm for 5 minutes at 4°C. The supernatant was discarded, and the cell pellet was resuspended in PBS and washed by another centrifugation step. After removing the

supernatant, the pellet was either directly processed or snap-frozen in ice and stored at -80°C.

5.2.5.2 SDS-Polyacrylamide gel electrophoresis (PAGE)

Proteins were separated according to their sizes by SDS-PAGE gels. The Bio-Rad Mini-PROTEAN II gel system was used for running acrylamide gels of 6, 8, 10, and 12% according to the expected size of the proteins. The higher the molecular weight of the protein was, the lower the acrylamide concentration was chosen. Acrylamide solution for separating gel (5 ml/gel) and stacking gel (2 ml/gel) were prepared as follows:

Table 13. Pipetting scheme for one separating and stacking gel.

Gel constituent	Separating gel				Stacking gel
% Acrylamide	6	8	10	12	4
ml H2O	2.68	2.38	2	1.7	1.55
ml of 30% acrylamide	1	1.3	1.68	2	0.325
ml of 1.5 M Tris-HCl, pH 8.8	1.25	1.25	1.25	1.25	-
ml of 0.5 M Tris-HCl, pH 6.8	-	-	-	-	0.625
µl of 10% SDS	50	50	50	50	25
µl of 10% APS	25	25	25	25	12.5
µl of TEMED	5	5	5	5	2.5

Before running 1/5 per sample of 5x SDS sample buffer was added to the sample and heated for 5 min at 95°C, except when Urea buffer was used (see 5.2.5.3. for lysis methods). Mini gels were run in SDS-running buffer at 20 mA per gel. Prestained (Bio-Rad) or unstained molecular markers (Fermentas) were used as protein standard. Separated proteins were either stained with Coomassie Brilliant Blue, Colloidal Coomassie or transferred onto a nitrocellulose or PVDF membrane (GE Healthcare, Amersham).

5.2.5.3 Lysis methods for detection by western-blot

As a standard lysis procedure for RPE1 and HEK cells processed for western-blot analysis, cell pellets, harvested from an 80-90% confluent 10 cm dish, were resuspended in 100 µl 1x SDS sample buffer. One µl Benzonase (Merck Millipore) was added per sample and samples were incubated at 37°C for 30 min, subsequently heated at 95°C for 5 min and centrifuged full speed at RT for 2 min before loading on an SDS-PAGE gel.

For detection of the PLK1-WT and -T210D mNeonGreen fusion constructs Urea lysis was used. Therefore, an 80-90% confluent dish of the cell lines was washed once with PBS. Next, 500 µl 8M Urea (in H_2O) plus 1/1000 Benzonase were pipetted on the dish and distributed evenly. After 1 h at RT, detached cells in the Urea buffer were collected and 1/5 SDS sample buffer was added before loading.
For the RPE1 cell lines with inducible Nek2-BirA-HA fusions, cell pellets were lysed in 350 µl BIPA buffer (20 mM Tris/HCl pH 7.5, 120 mM NaCl, 1 mM EDTA, 1 mM Ethylene glycol-bis(2-aminoethylether)-N,N,N′,N′-tetraacetic acid (EGTA), 1 mM plus Complete EDTA-free protease inhibitor cocktail [Roche]). Total extracts were incubated at 4°C for 30 min and centrifuged at 20,000 g for 15 min and 1/5 SDS sample buffer was added before heating and loading.

5.2.5.4 Semi-dry immunoblot

Semi-dry immunoblot was used routinely for protein detection. After SDS-PAGE, the separating gel, a nitrocellulose membrane (GE Healthcare, Amersham) and 6 Whatman 3MM papers were immersed in semi-dry blotting buffer. A sandwich, comprising 3 Whatman papers, the nitrocellulose membrane, the SDS-PAGE gel and another 3 Whatman papers, was assembled between the two electrodes of a semi-dry blotting apparatus. The standard blotting conditions was 110 mA for 1.5 h with constant amperage and maximum voltage set to 190 V. Transferred proteins were visualized by staining with Ponceau S solution for 2 minutes. Membranes were blocked with 5% milk in PBS-T for 0.5 h at RT or overnight at 4°C and then incubated with the primary antibody diluted in 3% milk/PBS-T at RT for 1-2 h or at 4°C overnight. The membrane was washed 3 times in PBS-T before incubating with the secondary antibody diluted in 3% milk/PBS-T for 1-2 h. The membrane was washed 3 times with PBS-T and the western-blots were probed with the enhanced chemiluminescence (ECL) solution 1 and 2 or ECL-plus (Thermo Scientific) for 90 s for visualization. The signals were detected on a Biometra UV Transilluminator (Analytic Jena).

5.2.5.5 Wet immunoblot

To detect Kif24-GFP and PLK1-mNeongreen by western-blot, tank blotting on a PVDF membrane (GE Healthcare, Amersham) was performed. The PVDF membrane was activated in methanol for 2 minutes and then rinsed in chilled Borat buffer (1.25 g Boric acid and 0.3725 g EDTA dissolved in 1 l H_2O, pH 8.8). Separating gel, 6 Whatman

paper, and two tissues were also immersed in chilled Borat buffer. The blotting sandwich covered by the two tissues on each site was assembled between the two electrodes of the tank blot system (Bio-Rad). Blotting was performed at 350 mA constant for 2.5 h. The apparature was cooled during the whole transfer and blotting was performed in a cool room (4°C). The membrane was blocked and stained as nitrocellulose membranes.

5.2.5.6 Membrane stripping

Stripping was used occasionally for the detection of more than one protein on the same membrane. For removal of antibodies after the first probing the nitrocellulose membrane was incubated in 25 ml stripping buffer [0.2 M Glycine, pH 2.5, 1% (w/v) SDS] for 1 h at RT. After washing the membrane several times with PBS-T, it was blocked again and re-probed with the following antibody.

5.2.5.7 Detection of proteins with Coomassie Brilliant Blue

Coomassie Brilliant Blue staining was used to stain proteins in SDS-PAGE. The gel was incubated in Coomassie staining solution [0.25% Coomassie Brilliant Blue R-250 (AppliChem), 10% (v/v) acetic acid, 40% (v/v) ethanol] for 1 hour with gentle tumbling on a rotator. The gel was briefly rinsed in H_2O and destained overnight in destaining solution (7.5% (v/v) acetic acid, 25% (v/v) isopropanol).

5.2.5.8 Detection of proteins with Colloidal Coomassie

Proteins in SDS-PAGE gels were detected with Colloidal Coomassie when a more sensitive method was required for example, for kinase assays. The gel was stained in Colloidal Coomassie staining solution [10% (w/v) $(NH4)_2So_4$, 2% (v/v) H_3PO_4, 0,1-0,12% (w/v) coomassie G250, 20% (v/v) Methanol] for 24-48 h. Unbound color was removed by several washes with H_2O.

5.2.5.9 Co-immunoprecipitations

HEK cells, seeded in 15 cm dishes, were co- and single transfected with 4.5 µg Nek2-GFP fusion constructs and FLAG tagged appendage constructs and harvested two days after tnsfection. Pellets were lysed in 600 µl BIPA-buffer (20 mM Tris/HCl pH 7.5, 120 mM NaCl, 1 mM EDTA, 1 mM EGTA, 1 mM plus Complete EDTA-free protease inhibitor cocktail [Roche]) for 30 min on ice. Total extracts were centrifuged for 15 min

at 21,000 g at 4°C. FLAG M2 beads (Sigma-Aldrich) were washed twice in BIPA buffer. Agerose beads were washed by 2 min centrifugation at 1000 rpm. In case magnetic beads were used, a magnetic rack was used for the washing steps. The supernatant was transferred to the beads and incubated rotating at 4°C for 2 h, while a 20 µl sample of the supernatant from the total lysate was kept for later analysis. Beads with bound protein were washed 5 times with BIPA buffer and proteins were eluted in SDS sample buffer at 95°C for 5 min and subjected to SDS-PAGE.

5.2.5.10 Determination of protein concentrations

Protein concentrations cell lysates prepared in BIPA-buffer or Urea buffer were determined by the Bradford-assay in comparison to an BSA standard following the manufacturer's protocol (Sigma-Aldrich). The lysates were diluted 1:10 in H_2O. For purified proteins, a defined volume of a bacterially expressed and purified protein was subjected to SDS-PAGE with succeeding Coomassie Brilliant Blue staining. The protein concentration was then estimated based on an BSA standard subjected to the same gel.

5.2.5.11 Expression and purification of fusion proteins from *E. coli*

For purification of MBP-fusion proteins (MBP, ODF2fl-MBP, and LRRC45$_{AA223-260}$-MBP) from *E. coli* fusion constructs were transformed in BL21(DE3) pLysS Rosetta *Escherichia coli* (*E. coli*) cells. Single colonies were grown in TY plates containing the appropriate antibiotics. Five to six colonies were grown in a pre-culture of 20 ml at 30°C overnight. Lactose was dissolved to a concentration of 252 g/l in water and filter sterilized. One ml from the pre-culture was added to 500 ml TY medium with antibiotics and 35 ml of the lactose solution were added. After 16 h incubation at 23°C, OD_{600} was between 1.2 and 1.5 and cells were harvested by centrifugation (15 min, 4,000 rpm, 4°C). The cell pellet was resuspended in 30 ml water, transferred into a 50 ml falcon tube followed by another centrifugation (15 min, 4,000 rpm, 4°C). 1/100 1 mM PMSF was added to the pellet and it was stored at -80°C. All purification steps were performed on ice using cooled solutions. The cell pellet was resuspended in 10 ml lysis buffer [50 mM HEPES pH 7, 200 mM NaCl, 2 mM $MgCl_2$, 1 mM DTT, 1 mg/ml Lysozyme (Sigma-Aldrich) plus Complete EDTA-free protease inhibitor cocktail (Roche)], followed by ultra-sonication (Bandelin Sonopuls) on ice for 15 rounds (40% output, 30 s pulsed, cycle 3). Tween20 was added to the lysate (final concentration 1%), followed by

incubation for 30 min on ice. The cell lysate was cleared by centrifugation at 21,000 g at 4°C. The supernatant was transferred to a new vial and 500 µl Amylose resin (New England Biolabs) that was equilibrated by three washes with lysis buffer (centrifugation for 3 min at 2000 rpm) was added. Binding to the Amylose resin was allowed by incubation for 2 h at 4°C on a rotating wheel. The beads were collected and separated from the flow-through by centrifugation (3 minutes, 2,000 rpm, 4 ºC) and washed twice with lysis buffer. A disposable 3 ml plastic column (Thermo Scientific) was washed once with water and twice with lysis buffer, before beads were loaded to the column with the bottom outlet capped. The cap was removed and flow through collected. Beads were washed by adding lysis buffer to the column until no more protein was present. The presence of protein was checked by regularly taking a 10 µl sample and adding 50 µl Bradford solution (Sigma). Proteins were eluted in MBP-column buffer (10 mM maltose, 50 mM HEPES pH 7, 200 mM NaCl, 2 mM MgCl2, 1 mM DTT) in 500 µl fractions with 3 min incubation times. For qualitative analysis of the purification aliquots of total lysate, insoluble fractions, cleared lysates, flow through, and 10 µl of each elution were loaded on an SDS-PAGE gel and stained with Coomassie Blue. The fractions with the highest concentration were chosen and changed into a buffer suitable for kinase assays (50 mM HEPES pH 7, 5 mM $MnCl_2$, 10 mM $MgCl_2$, 10% glycerol) using G25 Sephadex columns (GE Healthcare) according to the manufacturer's instructions. Aliquots of 50 µl were stored at -80°C.

His-fusion proteins ($ODF2_{AA1-250}$-His) were expressed and harvested as described for MBP fusion proteins. Pellets were resuspended in 2-5 ml/wet weight lysis buffer [50 mM NaH_2PO_4, 300 mM NaCl, 20 mM Imidazole, 10 mM ß-mercaptoethanol, 0.1 mM $MgCl_2$, 1 mg/ml Lysozyme plus Complete EDTA-free protease inhibitor cocktail (Roche), pH8] and sonicated as described for MBP fusions. Tween20 was added to a final concentration of 1% and the lysate was incubated for 30 min on ice. The cell lysate was cleared by centrifugation at 21,000 g at 4°C. The cleared lysate was added to 1 ml of Ni-NTA agarose (Quiagen) that was previously equilibrated by 3 washes (1 min 1000 rpm) in lysis buffer. The lysate and slurry mixture were incubated on a rotating for 1.5 h at 4ºC. After incubation, the beads were centrifuged and resuspended in 10 ml lysis buffer. The slurry was loaded on an equilibrated disposable plastic column (Thermo Scientific) and washes were performed as described for MBP proteins. Proteins were eluted in His-elution buffer (50 mM NaH_2PO_4, 300 mM NaCl, 250 mM Imidazole) in 500 µl fractions with 2 min incubation times. The aliquots were analyzed

by SDS-PAGE and the fractions with the highest concentration were chosen and changed into kinase assay buffer as described for MBP fusions.

5.2.5.12 Purification of FLAG tagged NEK2 kinase from HEK cells

Six plates of 70-80% confluent 15 cm dishes of HEK cells were transfected with 4.5 µg Nek2-WT-Flag and Nek2-KD-Flag fusion constructs, respectively. Two days after transfection, cells were harvested, and pellets were resuspended in 500 µl lysis buffer [50 mM HEPES pH 7.5, 100 mM NaCl, 5 mM $MnCl_2$, 10 mM $MgCl_2$, 5 mM KCl, 5 mM EGTA, 5 mM EDTA, 0.1% Nonident P40 plus Complete EDTA-free protease inhibitor cocktail (Roche)] per dish. After incubation for 30 min on ice, the total cell lysate was cleared by centrifugation (21,000 g, 15 min, 4°C). M2 Magnetic beads (Sigma) were washed two times with lysis buffer and 60 µl beads slurry was added per 500 µl cleared lysate. Nek2 fusion constructs were allowed to bind to the beads by incubation for 2 h at 4°C rotating. Beads were washed three times with lysis buffer and two times with kinase buffer (5.2.5.13.) without ATP. Beads were stored with minimal residual kinase buffer at -80°C. Of note, functional kinase was detected by its autophosphorylation only by using previously frozen but not freshly prepared beads.

5.2.5.13 In vitro kinase assay

An ATP/µCi P^{32} mix was prepared by mixing 0.5 µl 4 mM ATP with 0.2 µl µCi P^{32} (1 µl= 10 µCi) per tube. Two µl of substrate (~2 µg protein) and 5 µl M2-Flag-Nek2 kinase beads were mixed together with 0.7 µl of the ATP mix per reaction in kinase buffer (50 mM HEPES pH 7, 5 mM $MnCl_2$, 10 mM $MgCl_2$, 1 mM NaF, 4 mM ß-glycerolphosphate, 10 % glycerol) in a total volume of 20 µl. The reactions were incubated with light shaking for 30 minutes at 30°C. 2x SDS sample buffer was added to each sample to stop the kinase reaction before boiling at 95°C for 5 minutes. The samples were subjected to SDS- PAGE, dried under vacuum, followed by autoradiography and Coomassie Colloidal Blue staining. Gels were dried in a gel dryer (Bio-Rad) at 85°C for 30 min and then exposed to a phosphoimager screen (Fujifilm) over night. Radioactivity was detected by the Fujifilm Film BAS 1800-II imaging system.

6. References

Abdelhamed, Z. A., Wheway, G., Szymanska, K., Natarajan, S., Toomes, C., Inglehearn, C. and Johnson, C. A. (2013). Variable expressivity of ciliopathy neurological phenotypes that encompass Meckel–Gruber syndrome and Joubert syndrome is caused by complex de-regulated ciliogenesis, Shh and Wnt signalling defects. *Hum. Mol. Genet.* **22**, 1358–1372.

Adams, M., Simms, R. J., Abdelhamed, Z., Dawe, H. R., Szymanska, K., Logan, C. V., Wheway, G., Pitt, E., Gull, K., Knowles, M. A., et al. (2012). A meckelin–filamin A interaction mediates ciliogenesis. *Hum. Mol. Genet.* **21**, 1272–1286.

Afroz, T., Perez-Berlanga, M. and Polymenidou, M. (2019). Structural Transition, Function and Dysfunction of TDP-43 in Neurodegenerative Diseases. *Chimia (Aarau).* **73**, 380–390.

Afzelius, B. A. (1976). A human syndrome caused by immotile cilia. *Science* **193**, 317–9.

Agbu, S. O., Liang, Y., Liu, A. and Anderson, K. V (2018). The small GTPase RSG1 controls a final step in primary cilia initiation. *J. Cell Biol.* **217**, 413–427.

Akizu, N., Silhavy, J. L., Rosti, R. O., Scott, E., Fenstermaker, A. G., Schroth, J., Zaki, M. S., Sanchez, H., Gupta, N., Kabra, M., et al. (2014). Mutations in CSPP1 Lead to Classical Joubert Syndrome. *Am. J. Hum. Genet.* **94**, 80–86.

Anderson, R. G. (1972). The three-dimensional structure of the basal body from the rhesus monkey oviduct. *J. Cell Biol.* **54**, 246–265.

Anderson, R. G. and Brenner, R. M. (1971). The formation of basal bodies (centrioles) in the Rhesus monkey oviduct. *J. Cell Biol.* **50**, 10–34.

Anderson, C. T. and Stearns, T. (2009). Centriole Age Underlies Asynchronous Primary Cilium Growth in Mammalian Cells. *Curr. Biol.* **19**, 1498–1502.

Andrews, R. and Ahringer, J. (2007). Asymmetry of Early Endosome Distribution in C. elegans Embryos. *PLoS One* **2**, e493.

Aughsteen, A. A. (2001). The ultrastructure of primary cilia in the endocrine and excretory duct cells of the pancreas of mice and rats. *Eur. J. Morphol.* **39**, 277–83.

Bahe, S., Stierhof, Y.-D., Wilkinson, C. J., Leiss, F. and Nigg, E. A. (2005). Rootletin forms centriole-associated filaments and functions in centrosome cohesion. *J. Cell Biol.* **171**, 27–33.

Bahmanyar, S., Kaplan, D. D., DeLuca, J. G., Giddings, T. H., O'Toole, E. T., Winey, M., Salmon, E. D., Casey, P. J., Nelson, W. J. and Barth, A. I. M. (2008). ß-Catenin is a Nek2 substrate involved in centrosome separation. *Genes Dev.* **22**, 91–105.

Bärenz, F., Inoue, D., Yokoyama, H., Tegha-Dunghu, J., Freiss, S., Draeger, S., Mayilo, D., Cado, I., Merker, S., Klinger, M., et al. (2013). The centriolar satellite protein SSX2IP promotes centrosome maturation. *J. Cell Biol.* **202**, 81 LP – 95.

Barral, D. C., Garg, S., Casalou, C., Watts, G. F. M., Sandoval, J. L., Ramalho, J. S., Hsu, V. W. and Brenner, M. B. (2012). Arl13b regulates endocytic recycling traffic. *Proc. Natl. Acad. Sci. U. S. A.* **109**, 21354–21359.

Baudoin, J.-P., Viou, L., Launay, P.-S., Luccardini, C., Espeso Gil, S., Kiyasova, V., Irinopoulou, T., Alvarez, C., Rio, J.-P., Boudier, T., et al. (2012). Tangentially migrating neurons assemble a primary cilium that promotes their reorientation to the cortical plate. *Neuron* **76**, 1108–1122.

Bauer, N., Wilsch-Bräuninger, M., Karbanová, J., Fonseca, A.-V., Strauss, D., Freund,

D., Thiele, C., Huttner, W. B., Bornhäuser, M. and Corbeil, D. (2011). Haematopoietic stem cell differentiation promotes the release of prominin-1/CD133-containing membrane vesicles--a role of the endocytic-exocytic pathway. *EMBO Mol. Med.* **3**, 398–409.

Beckmann, J., Scheitza, S., Wernet, P., Fischer, J. C. and Giebel, B. (2007). Asymmetric cell division within the human hematopoietic stem and progenitor cell compartment: identification of asymmetrically segregating proteins. *Blood* **109**, 5494–5501.

Beneden, E. van (1876). *Contributions à l'histoire de la vésicule germinative et du premier noyau embryonnaire*. [Brussels]: [F. Hayes].

Benmerah, A. (2013). The ciliary pocket. *Curr. Opin. Cell Biol.* **25**, 78–84.

Berdnik, D., Torok, T., Gonzalez-Gaitan, M. and Knoblich, J. A. (2002). The endocytic protein alpha-Adaptin is required for numb-mediated asymmetric cell division in Drosophila. *Dev. Cell* **3**, 221–231.

Bergen, L. G., Upshall, A. and Morris, N. R. (1984). S-phase, G2, and nuclear division mutants of Aspergillus nidulans. *J. Bacteriol.* **159**, 114–119.

Bernabé-Rubio, M., Andrés, G., Casares-Arias, J., Fernández-Barrera, J., Rangel, L., Reglero-Real, N., Gershlick, D. C., Fernández, J. J., Millán, J., Correas, I., et al. (2016). Novel role for the midbody in primary ciliogenesis by polarized epithelial cells. *J. Cell Biol.* **214**, 259–273.

Bernhard, W. and de Harven, E. (1960). L'ultrastructure du centriole et d'autres éléments de l'appareil achromatique. In *Vierter Internationaler Kongress für Elektronenmikroskopie / Fourth International Conference on Electron Microscopy / Quatrième Congrès International de Microscopie Électronique*, pp. 217–227. Berlin, Heidelberg: Springer Berlin Heidelberg.

Berns, M. W., Rattner, J. B., Brenner, S. and Meredith, S. (1977). The role of the centriolar region in animal cell mitosis. A laser microbeam study. *J. Cell Biol.* **72**, 351–67.

Bertran, M. T., Sdelci, S., Regué, L., Avruch, J., Caelles, C. and Roig, J. (2011). Nek9 is a Plk1-activated kinase that controls early centrosome separation through Nek6/7 and Eg5. *EMBO J.* **30**, 2634–2647.

Bloecher, A., Venturi, G. M. and Tatchell, K. (2000). Anaphase spindle position is monitored by the BUB2 checkpoint. *Nat. Cell Biol.* **2**, 556–558.

Bornens, M. (2002). Centrosome composition and microtubule anchoring mechanisms. *Curr. Opin. Cell Biol.* **14**, 25–34.

Boveri, T. (1888). Zellen-Studien, v. 02.

Bowler, M., Kong, D., Sun, S., Nanjundappa, R., Evans, L., Farmer, V., Holland, A., Mahjoub, M. R., Sui, H. and Loncarek, J. (2019). High-resolution characterization of centriole distal appendage morphology and dynamics by correlative STORM and electron microscopy. *Nat. Commun.* **10**, 993.

Briscoe, J. and Thérond, P. P. (2013). The mechanisms of Hedgehog signalling and its roles in development and disease. *Nat. Rev. Mol. Cell Biol.* **14**, 416–429.

Bryan Tsou, M.-F. and Stearns, T. (2006). *Tsou, M. F. & Stearns, T. Mechanism limiting centrosome duplication to once per cell cycle. Nature 442, 947-951.OpenURL*.

Burk, A. S., Monzel, C., Yoshikawa, H. Y., Wuchter, P., Saffrich, R., Eckstein, V., Tanaka, M. and Ho, A. D. (2015). Quantifying adhesion mechanisms and dynamics of human hematopoietic stem and progenitor cells. *Sci. Rep.* **5**, 9370.

Cajánek, L. and Nigg, E. A. (2014). Cep164 triggers ciliogenesis by recruiting Tau tubulin kinase 2 to the mother centriole. *Proc. Natl. Acad. Sci.* **111**, E2841–E2850.

Cano, D. A., Murcia, N. S., Pazour, G. J. and Hebrok, M. (2004). Orpk mouse model of polycystic kidney disease reveals essential role of primary cilia in pancreatic tissue organization. *Development* **131**, 3457–67.

Cantagrel, V., Silhavy, J. L., Bielas, S. L., Swistun, D., Marsh, S. E., Bertrand, J. Y., Audollent, S., Attié-Bitach, T., Holden, K. R., Dobyns, W. B., et al. (2008). Mutations in the cilia gene ARL13B lead to the classical form of Joubert syndrome. *Am. J. Hum. Genet.* **83**, 170–179.

Cappello, P., Blaser, H., Gorrini, C., Lin, D. C. C., Elia, A. J., Wakeham, A., Haider, S., Boutros, P. C., Mason, J. M., Miller, N. A., et al. (2014). Role of Nek2 on centrosome duplication and aneuploidy in breast cancer cells. *Oncogene* **33**, 2375–2384.

Carvajal-Gonzalez, J. M., Roman, A.-C. and Mlodzik, M. (2016). Positioning of centrioles is a conserved readout of Frizzled planar cell polarity signalling. *Nat. Commun.* **7**, 11135.

Chaki, M., Airik, R., Ghosh, A. K., Giles, R. H., Chen, R., Slaats, G. G., Wang, H., Hurd, T. W., Zhou, W., Cluckey, A., et al. (2012). Exome capture reveals ZNF423 and CEP164 mutations, linking renal ciliopathies to DNA damage response signaling. *Cell* **150**, 533–548.

Chang, J. T., Palanivel, V. R., Kinjyo, I., Schambach, F., Intlekofer, A. M., Banerjee, A., Longworth, S. A., Vinup, K. E., Mrass, P., Oliaro, J., et al. (2007). Asymmetric T lymphocyte division in the initiation of adaptive immune responses. *Science* **315**, 1687–1691.

Chang, J., Seo, S. G., Lee, K. H., Nagashima, K., Bang, J. K., Kim, B. Y., Erikson, R. L., Lee, K.-W., Lee, H. J., Park, J.-E., et al. (2013). Essential role of Cenexin1, but not Odf2, in ciliogenesis. *Cell Cycle* **12**, 655–662.

Chatterjee, A., Chinnappa, K., Ramanan, N. and Mani, S. (2018). *Centrosome Inheritance Does Not Regulate Cell Fate in Granule Neuron Progenitors of the Developing Cerebellum*.

Chen, C.-H., Howng, S.-L., Cheng, T.-S., Chou, M.-H., Huang, C.-Y. and Hong, Y.-R. (2003). Molecular characterization of human ninein protein: two distinct subdomains required for centrosomal targeting and regulating signals in cell cycle. *Biochem. Biophys. Res. Commun.* **308**, 975–983.

Chen, C.-T., Hehnly, H., Yu, Q., Farkas, D., Zheng, G., Redick, S. D., Hung, H.-F., Samtani, R., Jurczyk, A., Akbarian, S., et al. (2014). A Unique Set of Centrosome Proteins Requires Pericentrin for Spindle-Pole Localization and Spindle Orientation. *Curr. Biol.* **24**, 2327–2334.

Chen, N.-P., Uddin, B., Hardt, R., Ding, W., Panic, M., Lucibello, I., Kammerer, P., Ruppert, T. and Schiebel, E. (2017). Human phosphatase CDC14A regulates actin organization through dephosphorylation of epithelial protein lost in neoplasm. *Proc. Natl. Acad. Sci.* **114**, 5201 LP – 5206.

Choi, B.-K., Dayaram, T., Parikh, N., Wilkins, A. D., Nagarajan, M., Novikov, I. B., Bachman, B. J., Jung, S. Y., Haas, P. J., Labrie, J. L., et al. (2018). Literature-based automated discovery of tumor suppressor p53 phosphorylation and inhibition by NEK2. *Proc. Natl. Acad. Sci.* **115**, 10666 LP – 10671.

Choksi, S. P., Lauter, G., Swoboda, P. and Roy, S. (2014). Switching on cilia: transcriptional networks regulating ciliogenesis. *Development* **141**, 1427 LP – 1441.

Chrétien, D., Buendia, B., Fuller, S. D. and Karsenti, E. (1997). Reconstruction of the

Centrosome Cycle from Cryoelectron Micrographs. *J. Struct. Biol.* **120**, 117–133.

Christensen, S. T., Pedersen, S. F., Satir, P., Veland, I. R. and Schneider, L. (2008). The primary cilium coordinates signaling pathways in cell cycle control and migration during development and tissue repair. *Curr. Top. Dev. Biol.* **85**, 261–301.

Ciruna, B., Jenny, A., Lee, D., Mlodzik, M. and Schier, A. F. (2006). Planar cell polarity signalling couples cell division and morphogenesis during neurulation. *Nature* **439**, 220–224.

Civin, C. I., Strauss, L. C., Brovall, C., Fackler, M. J., Schwartz, J. F. and Shaper, J. H. (1984). Antigenic analysis of hematopoiesis. III. A hematopoietic progenitor cell surface antigen defined by a monoclonal antibody raised against KG-1a cells. *J. Immunol.* **133**, 157–165.

Cizmecioglu, O., Arnold, M., Bahtz, R., Settele, F., Ehret, L., Haselmann-Weiß, U., Antony, C. and Hoffmann, I. (2010). Cep152 acts as a scaffold for recruitment of Plk4 and CPAP to the centrosome. *J. Cell Biol.* **191**, 731 LP – 739.

Clement, C. A., Ajbro, K. D., Koefoed, K., Vestergaard, M. L., Veland, I. R., Henriques de Jesus, M. P. R., Pedersen, L. B., Benmerah, A., Andersen, C. Y., Larsen, L. A., et al. (2013). TGF-β Signaling Is Associated with Endocytosis at the Pocket Region of the Primary Cilium. *Cell Rep.* **3**, 1806–1814.

Conduit, P. T. and Raff, J. W. (2010). Cnn Dynamics Drive Centrosome Size Asymmetry to Ensure Daughter Centriole Retention in Drosophila Neuroblasts. *Curr. Biol.* **20**, 2187–2192.

Conduit, S. E., Ramaswamy, V., Remke, M., Watkins, D. N., Wainwright, B. J., Taylor, M. D., Mitchell, C. A. and Dyson, J. M. (2017). A compartmentalized phosphoinositide signaling axis at cilia is regulated by INPP5E to maintain cilia and promote Sonic Hedgehog medulloblastoma. *Oncogene* **36**, 5969.

Coppe, A., Andersson, E. I., Binatti, A., Gasparini, V. R., Bortoluzzi, S., Clemente, M., Herling, M., Maciejewski, J., Mustjoki, S. and Bortoluzzi, S. (2017). Genomic landscape characterization of large granular lymphocyte leukemia with a systems genetics approach. *Leukemia* **31**, 1243–1246.

Corbit, K. C., Aanstad, P., Singla, V., Norman, A. R., Stainier, D. Y. R. and Reiter, J. F. (2005). Vertebrate Smoothened functions at the primary cilium. *Nature* **437**, 1018–1021.

Cortés, C. R., McInerney-Leo, A. M., Vogel, I., Rondón Galeano, M. C., Leo, P. J., Harris, J. E., Anderson, L. K., Keith, P. A., Brown, M. A., Ramsing, M., et al. (2016). Mutations in human C2CD3 cause skeletal dysplasia and provide new insights into phenotypic and cellular consequences of altered C2CD3 function. *Sci. Rep.* **6**, 24083.

Cottee, M. A., Muschalik, N., Johnson, S., Leveson, J., Raff, J. W. and Lea, S. M. (2015). The homo-oligomerisation of both Sas-6 and Ana2 is required for efficient centriole assembly in flies. *Elife* **4**, e07236–e07236.

Coumailleau, F., Fürthauer, M., Knoblich, J. A. and González-Gaitán, M. (2009). Directional Delta and Notch trafficking in Sara endosomes during asymmetric cell division. *Nature* **458**, 1051–1055.

D'Aquino, K. E., Monje-Casas, F., Paulson, J., Reiser, V., Charles, G. M., Lai, L., Shokat, K. M. and Amon, A. (2005). The Protein Kinase Kin4 Inhibits Exit from Mitosis in Response to Spindle Position Defects. *Mol. Cell* **19**, 223–234.

Dawe, H. R., Smith, U. M., Cullinane, A. R., Gerrelli, D., Cox, P., Badano, J. L., Blair-Reid, S., Sriram, N., Katsanis, N., Attie-Bitach, T., et al. (2007). The Meckel-Gruber Syndrome proteins MKS1 and meckelin interact and are required for primary cilium

formation. *Hum. Mol. Genet.* **16**, 173–186.

Dawe, H. R., Adams, M., Wheway, G., Szymanska, K., Logan, C. V, Noegel, A. A., Gull, K. and Johnson, C. A. (2009). Nesprin-2 interacts with meckelin and mediates ciliogenesis via remodelling of the actin cytoskeleton. *J. Cell Sci.* **122**, 2716–26.

Dawson, P. J., Wolman, S. R., Tait, L., Heppner, G. H. and Miller, F. R. (1996). MCF10AT: a model for the evolution of cancer from proliferative breast disease. *Am. J. Pathol.* **148**, 313–319.

De-Thé, G. (1964). CYTOPLASMIC MICROTUBULES IN DIFFERENT ANIMAL CELLS. *J. Cell Biol.* **23**, 265–75.

De Harven, E. and Dustin, P. J. (1960). *Etude au microscope électronique de la stathmocinése chez le rat.*

Delgehyr, N., Sillibourne, J. and Bornens, M. (2005). Microtubule nucleation and anchoring at the centrosome are independent processes linked by ninein function. *J. Cell Sci.* **118**, 1565–1575.

Deng, Y.-Z., Cai, Z., Shi, S., Jiang, H., Shang, Y.-R., Ma, N., Wang, J.-J., Guan, D.-X., Chen, T.-W., Rong, Y.-F., et al. (2018). Cilia loss sensitizes cells to transformation by activating the mevalonate pathway. *J. Exp. Med.* **215**, 177–195.

DeVaul, N., Koloustroubis, K., Wang, R. and Sperry, A. O. (2017). A novel interaction between kinase activities in regulation of cilia formation. *BMC Cell Biol.* **18**, 33.

Dhar, D. K., Ganguly, K. C., Alam, S., Hossain, A., Sarker, U. K., Das, B. K. and Haque, M. J. (2009). Kartagener's Syndrome. *Mymensingh Med. J.* **18**, 75–9.

Dictenberg, J. B., Zimmerman, W., Sparks, C. A., Young, A., Vidair, C., Zheng, Y., Carrington, W., Fay, F. S. and Doxsey, S. J. (1998). Pericentrin and gamma-tubulin form a protein complex and are organized into a novel lattice at the centrosome. *J. Cell Biol.* **141**, 163–174.

Doxsey, S. J. (2001). Centrosomes as command centres for cellular control. *Nat. Cell Biol.* **3**, E105-8.

Doxsey, S. J., Stein, P., Evans, L., Calarco, P. D. and Kirschner, M. (1994). Pericentrin, a highly conserved centrosome protein involved in microtubule organization. *Cell* **76**, 639–50.

Dubreuil, V., Marzesco, A.-M., Corbeil, D., Huttner, W. B. and Wilsch-Brauninger, M. (2007). Midbody and primary cilium of neural progenitors release extracellular membrane particles enriched in the stem cell marker prominin-1. *J. Cell Biol.* **176**, 483–495.

Duncan, A. W., Rattis, F. M., DiMascio, L. N., Congdon, K. L., Pazianos, G., Zhao, C., Yoon, K., Cook, J. M., Willert, K., Gaiano, N., et al. (2005). Integration of Notch and Wnt signaling in hematopoietic stem cell maintenance. *Nat. Immunol.* **6**, 314–322.

Dzhindzhev, N. S., Tzolovsky, G., Lipinszki, Z., Schneider, S., Lattao, R., Fu, J., Debski, J., Dadlez, M. and Glover, D. M. (2014). Plk4 Phosphorylates Ana2 to Trigger Sas6 Recruitment and Procentriole Formation. *Curr. Biol.* **24**, 2526–2532.

Egeberg, D. L., Lethan, M., Manguso, R., Schneider, L., Awan, A., Jørgensen, T. S., Byskov, A. G., Pedersen, L. B. and Christensen, S. T. (2012). Primary cilia and aberrant cell signaling in epithelial ovarian cancer. *Cilia* **1**, 15.

Emoto, K., Masugi, Y., Yamazaki, K., Effendi, K., Tsujikawa, H., Tanabe, M., Kitagawa, Y. and Sakamoto, M. (2014). Presence of primary cilia in cancer cells correlates with

prognosis of pancreatic ductal adenocarcinoma. *Hum. Pathol.* **45**, 817–825.

Endicott, S. J., Basu, B., Khokha, M. and Brueckner, M. (2015). The NIMA-like kinase Nek2 is a key switch balancing cilia biogenesis and resorption in the development of left-right asymmetry. *Development*.

Eto, M., Elliott, E., Prickett, T. D. and Brautigan, D. L. (2002). Inhibitor-2 regulates protein phosphatase-1 complexed with NimA-related kinase to induce centrosome separation. *J. Biol. Chem.* **277**, 44013–44020.

Ezratty, E. J., Stokes, N., Chai, S., Shah, A. S., Williams, S. E. and Fuchs, E. (2011). A role for the primary cilium in Notch signaling and epidermal differentiation during skin development. *Cell* **145**, 1129–41.

Fang, Y. and Zhang, X. (2016). Targeting NEK2 as a promising therapeutic approach for cancer treatment. *Cell Cycle* **15**, 895–907.

Faragher, A. J. and Fry, A. M. (2003). Nek2A kinase stimulates centrosome disjunction and is required for formation of bipolar mitotic spindles. *Mol. Biol. Cell* **14**, 2876–2889.

Field, M. C. and Carrington, M. (2009). The trypanosome flagellar pocket. *Nat. Rev. Microbiol.* **7**, 775–786.

Fields, S. and Song, O. (1989). A novel genetic system to detect protein-protein interactions. *Nature* **340**, 245–246.

Fisch, C. and Dupuis-Williams, P. (2011). Ultrastructure of cilia and flagella - back to the future! *Biol. cell* **103**, 249–270.

Flemming, W. (1875). *Studien in der entwicklungsgeschichte der Najaden,*. Prag.

Florian, M. C., Dorr, K., Niebel, A., Daria, D., Schrezenmeier, H., Rojewski, M., Filippi, M.-D., Hasenberg, A., Gunzer, M., Scharffetter-Kochanek, K., et al. (2012). Cdc42 activity regulates hematopoietic stem cell aging and rejuvenation. *Cell Stem Cell* **10**, 520–530.

Florian, M. C., Klose, M., Sacma, M., Jablanovic, J., Knudson, L., Nattamai, K. J., Marka, G., Vollmer, A., Soller, K., Sakk, V., et al. (2018). Aging alters the epigenetic asymmetry of HSC division. *PLOS Biol.* **16**, e2003389.

Fong, K.-W., Choi, Y.-K., Rattner, J. B. and Qi, R. Z. (2008). CDK5RAP2 Is a Pericentriolar Protein That Functions in Centrosomal Attachment of the γ-Tubulin Ring Complex. *Mol. Biol. Cell* **19**, 115–125.

Ford, M. J., Yeyati, P. L., Mali, G. R., Keighren, M. A., Waddell, S. H., Mjoseng, H. K., Douglas, A. T., Hall, E. A., Sakaue-Sawano, A., Miyawaki, A., et al. (2018). A Cell/Cilia Cycle Biosensor for Single-Cell Kinetics Reveals Persistence of Cilia after G1/S Transition Is a General Property in Cells and Mice. *Dev. Cell* **47**, 509-523.e5.

Fry, A. M. (2002). The Nek2 protein kinase: a novel regulator of centrosome structure. *Oncogene* **21**, 6184–6194.

Fry, A. M., Schultz, S. J., Bartek, J. and Nigg, E. A. (1995). Substrate specificity and cell cycle regulation of the Nek2 protein kinase, a potential human homolog of the mitotic regulator NIMA of Aspergillus nidulans. *J. Biol. Chem.* **270**, 12899–12905.

Fry, A. M., Mayor, T., Meraldi, P., Stierhof, Y. D., Tanaka, K. and Nigg, E. A. (1998). C-Nap1, a novel centrosomal coiled-coil protein and candidate substrate of the cell cycle-regulated protein kinase Nek2. *J. Cell Biol.* **141**, 1563–74.

Fry, A. M., Arnaud, L. and Nigg, E. A. (1999). Activity of the human centrosomal kinase, Nek2, depends on an unusual leucine zipper dimerization motif. *J. Biol. Chem.* **274**,

16304–16310.

Fry, A. M., O'Regan, L., Sabir, S. R. and Bayliss, R. (2012). Cell cycle regulation by the NEK family of protein kinases. *J. Cell Sci.* **125**, 4423–4433.

Fu, W., Asp, P., Canter, B. and Dynlacht, B. D. (2014). Primary cilia control hedgehog signaling during muscle differentiation and are deregulated in rhabdomyosarcoma. *Proc. Natl. Acad. Sci.* **111**, 9151 LP – 9156.

Fu, J., Hagan, I. M. and Glover, D. M. (2015). The centrosome and its duplication cycle. *Cold Spring Harb. Perspect. Biol.* **7**, a015800.

Gabriel, E., Wason, A., Ramani, A., Gooi, L. M., Keller, P., Pozniakovsky, A., Poser, I., Noack, F., Telugu, N. S., Calegari, F., et al. (2016). CPAP promotes timely cilium disassembly to maintain neural progenitor pool. *EMBO J.* **35**, 803–819.

Galati, D. F., Mitchell, B. J. and Pearson, C. G. (2016). Subdistal Appendages Stabilize the Ups and Downs of Ciliary Life. *Dev. Cell* **39**, 387–389.

Gambarotto, D., Pennetier, C., Ryniawec, J. M., Buster, D. W., Gogendeau, D., Goupil, A., Nano, M., Simon, A., Blanc, D., Racine, V., et al. (2019). Plk4 Regulates Centriole Asymmetry and Spindle Orientation in Neural Stem Cells. *Dev. Cell*.

Garcia-Gonzalo, F. R. and Reiter, J. F. (2012). Scoring a backstage pass: mechanisms of ciliogenesis and ciliary access. *J. Cell Biol.* **197**, 697–709.

Garcia-Gonzalo, F. R. and Reiter, J. F. (2017). Open Sesame: How Transition Fibers and the Transition Zone Control Ciliary Composition. *Cold Spring Harb. Perspect. Biol.* **9**, a028134.

Gasic, I., Nerurkar, P. and Meraldi, P. (2015). Centrosome age regulates kinetochore-microtubule stability and biases chromosome mis-segregation. *Elife* **4**, e07909.

Geissler, S., Pereira, G., Spang, A., Knop, M., Soues, S., Kilmartin, J. and Schiebel, E. (1996). The spindle pole body component Spc98p interacts with the gamma-tubulin-like Tub4p of Saccharomyces cerevisiae at the sites of microtubule attachment. *EMBO J.* **15**, 3899–3911.

Gerdes, J. M., Davis, E. E. and Katsanis, N. (2009). The Vertebrate Primary Cilium in Development, Homeostasis, and Disease. *Cell* **137**, 32–45.

Gheghiani, L., Loew, D., Lombard, B., Mansfeld, J. and Gavet, O. (2017). PLK1 Activation in Late G2 Sets Up Commitment to Mitosis. *Cell Rep.* **19**, 2060–2073.

Goetz, S. C. and Anderson, K. V. (2010). The primary cilium: a signalling centre during vertebrate development. *Nat. Rev. Genet.* **11**, 331–344.

Goetz, S. C., Liem, K. F. J. and Anderson, K. V (2012). The spinocerebellar ataxia-associated gene Tau tubulin kinase 2 controls the initiation of ciliogenesis. *Cell* **151**, 847–858.

Goggolidou, P. (2014). Wnt and planar cell polarity signaling in cystic renal disease. *Organogenesis* **10**, 86–95.

Golsteyn, R. M., Mundt, K. E., Fry, A. M. and Nigg, E. A. (1995). Cell cycle regulation of the activity and subcellular localization of Plk1, a human protein kinase implicated in mitotic spindle function. *J. Cell Biol.* **129**, 1617 LP – 1628.

Gomez-Ferreria, M. A., Rath, U., Buster, D. W., Chanda, S. K., Caldwell, J. S., Rines, D. R. and Sharp, D. J. (2007). Human Cep192 Is Required for Mitotic Centrosome and Spindle Assembly. *Curr. Biol.* **17**, 1960–1966.

Gómez-Orte, E., Sáenz-Narciso, B., Moreno, S. and Cabello, J. (2013). Multiple functions of the noncanonical Wnt pathway. *Trends Genet.* **29**, 545–553.

Görgens, A., Ludwig, A. K., Möllmann, M., Krawczyk, A., Dürig, J., Hanenberg, H., Horn, P. A. and Giebel, B. (2014). Multipotent hematopoietic progenitors divide asymmetrically to create progenitors of the lymphomyeloid and erythromyeloid lineages. *Stem Cell Reports*.

Görgens, A., Bremer, M., Ferrer-Tur, R., Murke, F., Tertel, T., Horn, P. A., Thalmann, S., Welsh, J. A., Probst, C., Guerin, C., et al. (2019). Optimisation of imaging flow cytometry for the analysis of single extracellular vesicles by using fluorescence-tagged vesicles as biological reference material. *J. Extracell. Vesicles* **8**, 1587567.

Gould, R. R. and Borisy, G. G. (1977). The pericentriolar material in Chinese hamster ovary cells nucleates microtubule formation. *J. Cell Biol.* **73**, 601–615.

Gradilone, S. A., Radtke, B. N., Bogert, P. S., Huang, B. Q., Gajdos, G. B. and LaRusso, N. F. (2013). HDAC6 Inhibition Restores Ciliary Expression and Decreases Tumor Growth. *Cancer Res.* **73**, 2259–2270.

Graser, S., Stierhof, Y.-D., Lavoie, S. B., Gassner, O. S., Lamla, S., Le Clech, M. and Nigg, E. A. (2007). Cep164, a novel centriole appendage protein required for primary cilium formation. *J. Cell Biol.* **179**, 321–330.

Gromley, A., Jurczyk, A., Sillibourne, J., Halilovic, E., Mogensen, M., Groisman, I., Blomberg, M. and Doxsey, S. (2003). A novel human protein of the maternal centriole is required for the final stages of cytokinesis and entry into S phase. *J. Cell Biol.* **161**, 535–545.

Gromley, A., Yeaman, C., Rosa, J., Redick, S., Chen, C.-T., Mirabelle, S., Guha, M., Sillibourne, J. and Doxsey, S. J. (2005). Centriolin anchoring of exocyst and SNARE complexes at the midbody is required for secretory-vesicle-mediated abscission. *Cell* **123**, 75—87.

Gu, Z., Zhou, W., Huang, J., Yang, Y., Wendlandt, E., Xu, H., He, X., Tricot, G. and Zhan, F. (2014). Nek2 Is a Novel Regulator of B Cell Development and Immunological Response. *Biomed Res. Int.* **2014**, 1–11.

Gunji, Y., Nakamura, M., Hagiwara, T., Hayakawa, K., Matsushita, H., Osawa, H., Nagayoshi, K., Nakauchi, H., Yanagisawa, M. and Miura, Y. (1992). Expression and function of adhesion molecules on human hematopoietic stem cells: CD34+ LFA-1- cells are more primitive than CD34+ LFA-1+ cells. *Blood* **80**, 429 LP – 436.

Gupta, A. and Kitagawa, D. (2018). Ultrastructural diversity between centrioles of eukaryotes. *J. Biochem.* **164**, 1–8.

Gupta, G. D., Coyaud, E., Goncalves, J., Mojarad, B. A., Liu, Y., Wu, Q., Gheiratmand, L., Comartin, D., Tkach, J. M., Cheung, S. W. T., et al. (2015). A Dynamic Protein Interaction Landscape of the Human Centrosome-Cilium Interface. *Cell* **163**, 1484–1499.

Habib, S. J., Chen, B.-C., Tsai, F.-C., Anastassiadis, K., Meyer, T., Betzig, E. and Nusse, R. (2013). A localized Wnt signal orients asymmetric stem cell division in vitro. *Science* **339**, 1445–1448.

Hamada, H. (2016). *Roles of Motile and Immotile Cilia in Left-Right Symmetry Breaking*.

Hames, R. S. and Fry, A. M. (2002). Alternative splice variants of the human centrosome kinase Nek2 exhibit distinct patterns of expression in mitosis. *Biochem. J.* **361**, 77–85.

Hames, R. S., Wattam, S. L., Yamano, H., Bacchieri, R. and Fry, A. M. (2001). APC/C-

mediated destruction of the centrosomal kinase Nek2A occurs in early mitosis and depends upon a cyclin A-type D-box. *EMBO J.* **20**, 7117–27.

Hames, R. S., Crookes, R. E., Straatman, K. R., Merdes, A., Hayes, M. J., Faragher, A. J. and Fry, A. M. (2005). Dynamic recruitment of Nek2 kinase to the centrosome involves microtubules, PCM-1, and localized proteasomal degradation. *Mol. Biol. Cell* **16**, 1711–1724.

Hamze-Komaiha, O., Sarr, S., Arlot-Bonnemains, Y., Samuel, D. and Gassama-Diagne, A. (2016). SHIP2 Regulates Lumen Generation, Cell Division, and Ciliogenesis through the Control of Basolateral to Apical Lumen Localization of Aurora A and HEF 1. *Cell Rep.* **17**, 2738–2752.

Han, Y.-G., Kim, H. J., Dlugosz, A. A., Ellison, D. W., Gilbertson, R. J. and Alvarez-Buylla, A. (2009). Dual and opposing roles of primary cilia in medulloblastoma development. *Nat. Med.* **15**, 1062–1065.

Hanks, S. K. and Hunter, T. (1995). Protein kinases 6. The eukaryotic protein kinase superfamily: kinase (catalytic) domain structure and classification. *FASEB J.* **9**, 576–96.

Hardy, T., Lee, M., Hames, R. S., Prosser, S. L., Cheary, D.-M., Samant, M. D., Schultz, F., Baxter, J. E., Rhee, K. and Fry, A. M. (2014). Multisite phosphorylation of C-Nap1 releases it from Cep135 to trigger centrosome disjunction. *J. Cell Sci.* **127**, 2493 LP – 2506.

Hassounah, N. B., Nagle, R., Saboda, K., Roe, D. J., Dalkin, B. L. and McDermott, K. M. (2013). Primary cilia are lost in preinvasive and invasive prostate cancer. *PLoS One* **8**, e68521.

Hassounah, N. B., Nunez, M., Fordyce, C., Roe, D., Nagle, R., Bunch, T. and McDermott, K. M. (2017). Inhibition of Ciliogenesis Promotes Hedgehog Signaling, Tumorigenesis, and Metastasis in Breast Cancer. *Mol. Cancer Res.* **15**, 1421–1430.

Haycraft, C. J., Banizs, B., Aydin-Son, Y., Zhang, Q., Michaud, E. J. and Yoder, B. K. (2005). Gli2 and Gli3 Localize to Cilia and Require the Intraflagellar Transport Protein Polaris for Processing and Function. *PLoS Genet.* **1**, e53.

Hayward, D. G., Clarke, R. B., Faragher, A. J., Pillai, M. R., Hagan, I. M. and Fry, A. M. (2004). The centrosomal kinase Nek2 displays elevated levels of protein expression in human breast cancer. *Cancer Res.* **64**, 7370–6.

He, R., Huang, N., Bao, Y., Zhou, H., Teng, J. and Chen, J. (2013). LRRC45 is a centrosome linker component required for centrosome cohesion. *Cell Rep.* **4**, 1100–1107.

Helps, N. R., Luo, X., Barker, H. M. and Cohen, P. T. (2000). NIMA-related kinase 2 (Nek2), a cell-cycle-regulated protein kinase localized to centrosomes, is complexed to protein phosphatase 1. *Biochem. J.* **349**, 509–518.

Hildebrandt, F., Attanasio, M. and Otto, E. (2009). Nephronophthisis: Disease Mechanisms of a Ciliopathy. *J. Am. Soc. Nephrol.* **20**, 23–35.

Hirsch, H. R. (1977). The dynamics of repetitive asymmetric cell division. *Mech. Ageing Dev.* **6**, 319–32.

Hoggatt, J., Kfoury, Y. and Scadden, D. T. (2016). Hematopoietic Stem Cell Niche in Health and Disease. *Annu. Rev. Pathol. Mech. Dis.* **11**, 555–581.

Horvitz, H. R. and Herskowitz, I. (1992). Mechanisms of asymmetric cell division: two Bs or not two Bs, that is the question. *Cell* **68**, 237–55.

Huang, P. and Schier, A. F. (2009). Dampened Hedgehog signaling but normal Wnt signaling in zebrafish without cilia. *Development* **136**, 3089–3098.

Huang, S., Law, P., Francis, K., Palsson, B. O. and Ho, A. D. (1999). Symmetry of Initial Cell Divisions Among Primitive Hematopoietic Progenitors Is Independent of Ontogenic Age and Regulatory Molecules. *Blood* **94**, 2595 LP – 2604.

Huang, N., Xia, Y., Zhang, D., Wang, S., Bao, Y., He, R., Teng, J. and Chen, J. (2017). Hierarchical assembly of centriole subdistal appendages via centrosome binding proteins CCDC120 and CCDC68. *Nat. Commun.* **8**, 15057.

Huangfu, D. and Anderson, K. V. (2005). Cilia and Hedgehog responsiveness in the mouse. *Proc. Natl. Acad. Sci.* **102**, 11325–11330.

Huangfu, D., Liu, A., Rakeman, A. S., Murcia, N. S., Niswander, L. and Anderson, K. V (2003). Hedgehog signalling in the mouse requires intraflagellar transport proteins. *Nature* **426**, 83–7.

Hüber, D. and Hoyer-Fender, S. (2007). Alternative splicing of exon 3b gives rise to ODF2 and Cenexin. *Cytogenet. Genome Res.* **119**, 68–73.

Huisman, S. M. and Segal, M. (2005). Cortical capture of microtubules and spindle polarity in budding yeast - where's the catch? *J. Cell Sci.* **118**, 463 LP – 471.

Humbert, M. C., Weihbrecht, K., Searby, C. C., Li, Y., Pope, R. M., Sheffield, V. C. and Seo, S. (2012). ARL13B, PDE6D, and CEP164 form a functional network for INPP5E ciliary targeting. *Proc. Natl. Acad. Sci. U. S. A.* **109**, 19691–19696.

Hung, H.-F., Hehnly, H. and Doxsey, S. (2016). The Mother Centriole Appendage Protein Cenexin Modulates Lumen Formation through Spindle Orientation. *Curr. Biol.* **26**, 793–801.

Hurd, T. W. and Hildebrandt, F. (2011). Mechanisms of nephronophthisis and related ciliopathies. *Nephron. Exp. Nephrol.* **118**, e9-14.

Hutterer, A. and Knoblich, J. A. (2005). Numb and alpha-Adaptin regulate Sanpodo endocytosis to specify cell fate in Drosophila external sensory organs. *EMBO Rep.* **6**, 836–842.

Ibrahim, R., Messaoudi, C., Chichon, F. J., Celati, C. and Marco, S. (2009). Electron tomography study of isolated human centrioles. *Microsc. Res. Tech.* **72**, 42–48.

Inaba, H., Goto, H., Kasahara, K., Kumamoto, K., Yonemura, S., Inoko, A., Yamano, S., Wanibuchi, H., He, D., Goshima, N., et al. (2016). Ndel1 suppresses ciliogenesis in proliferating cells by regulating the trichoplein-Aurora A pathway. *J. Cell Biol.* **212**,.

Inoko, A., Matsuyama, M., Goto, H., Ohmuro-Matsuyama, Y., Hayashi, Y., Enomoto, M., Ibi, M., Urano, T., Yonemura, S., Kiyono, T., et al. (2012). Trichoplein and Aurora A block aberrant primary cilia assembly in proliferating cells. *J. Cell Biol.* **197**, 391–405.

Ishikawa, H., Kubo, A., Tsukita, S. and Tsukita, S. (2005). Odf2-deficient mother centrioles lack distal/subdistal appendages and the ability to generate primary cilia. *Nat. Cell Biol.* **7**, 517–524.

Izawa, I., Goto, H., Kasahara, K. and Inagaki, M. (2015). Current topics of functional links between primary cilia and cell cycle. *Cilia* **4**,.

Izumi, H. and Kaneko, Y. (2012). Evidence of asymmetric cell division and centrosome inheritance in human neuroblastoma cells. *Proc. Natl. Acad. Sci.*

Januschke, J., Llamazares, S., Reina, J. and Gonzalez, C. (2011). Drosophila neuroblasts retain the daughter centrosome. *Nat. Commun.*

Jenkins, P. M., McEwen, D. P. and Martens, J. R. (2009). Olfactory cilia: linking sensory cilia function and human disease. *Chem. Senses* **34**, 451–64.

Jenks, A. D., Vyse, S., Wong, J. P., Kostaras, E., Keller, D., Burgoyne, T., Shoemark, A., Tsalikis, A., de la Roche, M., Michaelis, M., et al. (2018). Primary Cilia Mediate Diverse Kinase Inhibitor Resistance Mechanisms in Cancer. *Cell Rep.* **23**, 3042–3055.

Jensen, V. L. and Leroux, M. R. (2017). Gates for soluble and membrane proteins, and two trafficking systems (IFT and LIFT), establish a dynamic ciliary signaling compartment. *Curr. Opin. Cell Biol.* **47**, 83–91.

Jeong, Y., Lee, J., Kim, K., Yoo, J. C. and Rhee, K. (2007). Characterization of NIP2/centrobin, a novel substrate of Nek2, and its potential role in microtubule stabilization. *J. Cell Sci.* **120**, 2106–2116.

Jonassen, J. A., San Agustin, J., Follit, J. A. and Pazour, G. J. (2008). Deletion of IFT20 in the mouse kidney causes misorientation of the mitotic spindle and cystic kidney disease. *J. Cell Biol.* **183**, 377–384.

Jones, D. G. and Rosamond, J. (1990). Isolation of a novel protein kinase-encoding gene from yeast by oligodeoxyribonucleotide probing. *Gene* **90**, 87–92.

Jones, C., Roper, V. C., Foucher, I., Qian, D., Banizs, B., Petit, C., Yoder, B. K. and Chen, P. (2008). Ciliary proteins link basal body polarization to planar cell polarity regulation. *Nat. Genet.* **40**, 69–77.

Joo, K., Kim, C. G., Lee, M.-S., Moon, H.-Y., Lee, S.-H., Kim, M. J., Kweon, H.-S., Park, W.-Y., Kim, C.-H., Gleeson, J. G., et al. (2013). CCDC41 is required for ciliary vesicle docking to the mother centriole. *Proc. Natl. Acad. Sci. U. S. A.* **110**, 5987–5992.

Kashihara, H., Chiba, S., Kanno, S. ichiro, Suzuki, K., Yano, T. and Tsukita, S. (2019). Cep128 associates with Odf2 to form the subdistal appendage of the centriole. *Genes to Cells* **24**, 231–243.

Ke, Y.-N. and Yang, W.-X. (2014). Primary cilium: an elaborate structure that blocks cell division? *Gene* **547**, 175–185.

Kechad, A., Jolicoeur, C., Tufford, A., Mattar, P., Chow, R. W. Y., Harris, W. A. and Cayouette, M. (2012). Numb is Required for the Production of Terminal Asymmetric Cell Divisions in the Developing Mouse Retina. *J. Neurosci.* **32**, 17197 LP – 17210.

Kellogg, D. R., Moritz, M. and Alberts, B. M. (1994). The centrosome and cellular organization. *Annu. Rev. Biochem.* **63**, 639–674.

Kim, S. and Tsiokas, L. (2011). Cilia and cell cycle re-entry: more than a coincidence. *Cell Cycle* **10**, 2683–2690.

Kim, J., Krishnaswami, S. R. and Gleeson, J. G. (2008). CEP290 interacts with the centriolar satellite component PCM-1 and is required for Rab8 localization to the primary cilium. *Hum. Mol. Genet.* **17**, 3796–3805.

Kim, T.-S., Park, J.-E., Shukla, A., Choi, S., Murugan, R. N., Lee, J. H., Ahn, M., Rhee, K., Bang, J. K., Kim, B. Y., et al. (2013). Hierarchical recruitment of Plk4 and regulation of centriole biogenesis by two centrosomal scaffolds, Cep192 and Cep152. *Proc. Natl. Acad. Sci. U. S. A.* **110**, E4849-57.

Kim, S., Lee, K., Choi, J. H., Ringstad, N. and Dynlacht, B. D. (2015). Nek2 activation of Kif24 ensures cilium disassembly during the cell cycle. *Nat. Commun.*

Kinzel, D., Boldt, K., Davis, E. E., Burtscher, I., Trumbach, D., Diplas, B., Attie-Bitach, T., Wurst, W., Katsanis, N., Ueffing, M., et al. (2010). Pitchfork regulates primary cilia

disassembly and left-right asymmetry. *Dev. Cell* **19**, 66–77.

Kitagawa, D., Vakonakis, I., Olieric, N., Hilbert, M., Keller, D., Olieric, V., Bortfeld, M., Erat, M. C., Fluckiger, I., Gonczy, P., et al. (2011). Structural basis of the 9-fold symmetry of centrioles. *Cell* **144**, 364–375.

Klinger, M., Wang, W., Kuhns, S., Barenz, F., Drager-Meurer, S., Pereira, G. and Gruss, O. J. (2014). The novel centriolar satellite protein SSX2IP targets Cep290 to the ciliary transition zone. *Mol. Biol. Cell* **25**, 495–507.

Knodler, A., Feng, S., Zhang, J., Zhang, X., Das, A., Peranen, J. and Guo, W. (2010). Coordination of Rab8 and Rab11 in primary ciliogenesis. *Proc. Natl. Acad. Sci. U. S. A.* **107**, 6346–6351.

Kobayashi, T., Tsang, W. Y., Li, J., Lane, W. and Dynlacht, B. D. (2011). Centriolar kinesin Kif24 interacts with CP110 to remodel microtubules and regulate ciliogenesis. *Cell* **145**, 914–925.

Kobayashi, T., Kim, S., Lin, Y.-C., Inoue, T. and Dynlacht, B. D. (2014). The CP110-interacting proteins Talpid3 and Cep290 play overlapping and distinct roles in cilia assembly. *J. Cell Biol.* **204**, 215–229.

Kobayashi, T., Nakazono, K., Tokuda, M., Mashima, Y., Dynlacht, B. D. and Itoh, H. (2017). HDAC2 promotes loss of primary cilia in pancreatic ductal adenocarcinoma. *EMBO Rep.* **18**, 334–343.

Koeffler, H. P. and Golde, D. W. (1978). Acute myelogenous leukemia: a human cell line responsive to colony-stimulating activity. *Science* **200**, 1153–1154.

Koefoed, K., Veland, I. R., Pedersen, L. B., Larsen, L. A. and Christensen, S. T. (2014). Cilia and coordination of signaling networks during heart development. *Organogenesis* **10**, 108–125.

Kogerman, P., Grimm, T., Kogerman, L., Krause, D., Undén, A. B., Sandstedt, B., Toftgård, R. and Zaphiropoulos, P. G. (1999). Mammalian Suppressor-of-Fused modulates nuclear–cytoplasmic shuttling of GLI-1. *Nat. Cell Biol.* **1**, 312–319.

Kohlmaier, G., Lončarek, J., Meng, X., McEwen, B. F., Mogensen, M. M., Spektor, A., Dynlacht, B. D., Khodjakov, A. and Gönczy, P. (2009). Overly Long Centrioles and Defective Cell Division upon Excess of the SAS-4-Related Protein CPAP. *Curr. Biol.* **19**, 1012–1018.

Koiso, Y., Nakajima, O., Matsumura, D., Fujimoto, Y. and Hashimoto, Y. (2000). *Chemical Control of Cell Differentiation of Human Myeloleukemia K562 Cell Line*.

Kokuryo, T., Yokoyama, Y., Yamaguchi, J., Tsunoda, N., Ebata, T. and Nagino, M. (2019). NEK2 Is an Effective Target for Cancer Therapy With Potential to Induce Regression of Multiple Human Malignancies. *Anticancer Res.* **39**, 2251–2258.

Kong, D., Farmer, V., Shukla, A., James, J., Gruskin, R., Kiriyama, S. and Loncarek, J. (2014). Centriole maturation requires regulated Plk1 activity during two consecutive cell cycles. *J. Cell Biol.* **206**, 855 LP – 865.

Korinek, W. S., Copeland, M. J., Chaudhuri, A. and Chant, J. (2000). Molecular Linkage Underlying Microtubule Orientation Toward Cortical Sites in Yeast. *Science (80-.).* **287**, 2257 LP – 2259.

Kraatz, S., Guichard, P., Obbineni, J. M., Olieric, N., Hatzopoulos, G. N., Hilbert, M., Sen, I., Missimer, J., Gonczy, P. and Steinmetz, M. O. (2016). The Human Centriolar Protein CEP135 Contains a Two-Stranded Coiled-Coil Domain Critical for Microtubule Binding. *Structure* **24**, 1358–1371.

Krien, M. J., Bugg, S. J., Palatsides, M., Asouline, G., Morimyo, M. and O'Connell, M. J. (1998). A NIMA homologue promotes chromatin condensation in fission yeast. *J. Cell Sci.* **111 (Pt 7)**, 967–76.

Kuhns, S., Schmidt, K. N., Reymann, J., Gilbert, D. F., Neuner, A., Hub, B., Carvalho, R., Wiedemann, P., Zentgraf, H., Erfle, H., et al. (2013). The microtubule affinity regulating kinase MARK4 promotes axoneme extension during early ciliogenesis. *J. Cell Biol.* **200**, 505–522.

Kunimoto, K., Yamazaki, Y., Nishida, T., Shinohara, K., Ishikawa, H., Hasegawa, T., Okanoue, T., Hamada, H., Noda, T., Tamura, A., et al. (2012). Coordinated Ciliary Beating Requires Odf2-Mediated Polarization of Basal Bodies via Basal Feet. *Cell* **148**, 189–200.

Kurtulmus, B., Wang, W., Ruppert, T., Neuner, A., Cerikan, B., Viol, L., Dueñas-Sánchez, R., Gruss, O. J. and Pereira, G. (2016). WDR8 is a centriolar satellite and centriole-associated protein that promotes ciliary vesicle docking during ciliogenesis. *J. Cell Sci.* **129**,.

Kurtulmus, B., Yuan, C., Schuy, J., Neuner, A., Hata, S., Kalamakis, G., Martin-Villalba, A. and Pereira, G. (2018). LRRC45 contributes to early steps of axoneme extension. *J. Cell Sci.* jcs.223594.

Latta, H., Maunsbach, A. B. and Madden, S. C. (1961). CILIA IN DIFFERENT SEGMENTS OF THE RAT NEPHRON. *J. Biophys. Biochem. Cytol.* **11**, 248 LP – 252.

Lawo, S., Hasegan, M., Gupta, G. D. and Pelletier, L. (2012). Subdiffraction imaging of centrosomes reveals higher-order organizational features of pericentriolar material. *Nat. Cell Biol.* **14**, 1148–1158.

Lecland, N., Hsu, C.-Y., Chemin, C., Merdes, A. and Bierkamp, C. (2019). Epidermal development requires ninein for spindle orientation and cortical microtubule organization. *Life Sci. Alliance* **2**, e201900373.

Lee, J. J., von Kessler, D. P., Parks, S. and Beachy, P. A. (1992). Secretion and localized transcription suggest a role in positional signaling for products of the segmentation gene hedgehog. *Cell* **71**, 33–50.

Lee, L., Tirnauer, J. S., Li, J., Schuyler, S. C., Liu, J. Y. and Pellman, D. (2000). Positioning of the Mitotic Spindle by a Cortical-Microtubule Capture Mechanism. *Science (80-.).* **287**, 2260 LP – 2262.

Lee, K. H., Johmura, Y., Yu, L.-R., Park, J.-E., Gao, Y., Bang, J. K., Zhou, M., Veenstra, T. D., Yeon Kim, B. and Lee, K. S. (2012). Identification of a novel Wnt5a-CK1varepsilon-Dvl2-Plk1-mediated primary cilia disassembly pathway. *EMBO J.* **31**, 3104–3117.

Lee, J., Yi, S., Eun Kang, Y., Chang, J., Tae Kim, J., Joung Sul, H., Ok Kim, J., Kim, J., Kim, J., Maria Porcelli, A., et al. (2016). *Defective ciliogenesis in thyroid hürthle cell tumors is associated with increased autophagy*.

Leigh, M. W., Pittman, J. E., Carson, J. L., Ferkol, T. W., Dell, S. D., Davis, S. D., Knowles, M. R. and Zariwala, M. A. (2009). Clinical and genetic aspects of primary ciliary dyskinesia/Kartagener syndrome. *Genet. Med.* **11**, 473–87.

Lengefeld, J., Hotz, M., Rollins, M., Baetz, K. and Barral, Y. (2017). *Budding yeast Wee1 distinguishes spindle pole bodies to guide their pattern of age-dependent segregation*.

Liakopoulos, D., Kusch, J., Grava, S., Vogel, J. and Barral, Y. (2003). Asymmetric loading of Kar9 onto spindle poles and microtubules ensures proper spindle alignment. *Cell* **112**, 561–74.

Lin, F., Hiesberger, T., Cordes, K., Sinclair, A. M., Goldstein, L. S. B., Somlo, S. and Igarashi, P. (2003). Kidney-specific inactivation of the KIF3A subunit of kinesin-II inhibits renal ciliogenesis and produces polycystic kidney disease. *Proc. Natl. Acad. Sci.* **100**, 5286–5291.

Lindemann, C. B. and Lesich, K. A. (2010). Flagellar and ciliary beating: the proven and the possible. *J. Cell Sci.* **123**, 519–528.

Lopes, C. A. M., Prosser, S. L., Romio, L., Hirst, R. A., O'Callaghan, C., Woolf, A. S. and Fry, A. M. (2011). Centriolar satellites are assembly points for proteins implicated in human ciliopathies, including oral-facial-digital syndrome 1. *J. Cell Sci.* **124**, 600–612.

Loskutov, Y. V, Griffin, C. L., Marinak, K. M., Bobko, A., Margaryan, N. V, Geldenhuys, W. J., Sarkaria, J. N. and Pugacheva, E. N. (2018). LPA signaling is regulated through the primary cilium: a novel target in glioblastoma. *Oncogene* **37**, 1457–1471.

Lu, H., Toh, M. T., Narasimhan, V., Thamilselvam, S. K., Choksi, S. P. and Roy, S. (2015a). A function for the Joubert syndrome protein Arl13b in ciliary membrane extension and ciliary length regulation. *Dev. Biol.* **397**, 225–236.

Lu, Q., Insinna, C., Ott, C., Stauffer, J., Pintado, P. A., Rahajeng, J., Baxa, U., Walia, V., Cuenca, A., Hwang, Y.-S., et al. (2015b). Early steps in primary cilium assembly require EHD1/EHD3-dependent ciliary vesicle formation. *Nat. Cell Biol.* **17**, 228–240.

Ludwig, A., Saffrich, R., Eckstein, V., Bruckner, T., Wagner, W., Ho, A. D. and Wuchter, P. (2014). Functional potentials of human hematopoietic progenitor cells are maintained by mesenchymal stromal cells and not impaired by plerixafor. *Cytotherapy* **16**, 111–121.

Mackenzie, I. R. A. and Rademakers, R. (2008). The role of transactive response DNA-binding protein-43 in amyotrophic lateral sclerosis and frontotemporal dementia. *Curr. Opin. Neurol.* **21**, 693–700.

Mahjoub, M. R., Montpetit, B., Zhao, L., Finst, R. J., Goh, B., Kim, A. C. and Quarmby, L. M. (2002). The FA2 gene of Chlamydomonas encodes a NIMA family kinase with roles in cell cycle progression and microtubule severing during deflagellation. *J. Cell Sci.* **115**, 1759–68.

Malicki, J. J. and Johnson, C. A. (2017). The Cilium: Cellular Antenna and Central Processing Unit. *Trends Cell Biol.* **27**, 126–140.

Mardin, B. and Schiebel, E. (2012). *Breaking the ties that bind: New advances in centrosome biology*.

Mardin, B. R., Lange, C., Baxter, J. E., Hardy, T., Scholz, S. R., Fry, A. M. and Schiebel, E. (2010). Components of the Hippo pathway cooperate with Nek2 kinase to regulate centrosome disjunction. *Nat. Cell Biol.*

Mardin, B. R., Agircan, F. G., Lange, C. and Schiebel, E. (2011). Plk1 controls the Nek2A-PP1γ Antagonism in centrosome disjunction. *Curr. Biol.*

Marion, V., Stoetzel, C., Schlicht, D., Messaddeq, N., Koch, M., Flori, E., Danse, J. M., Mandel, J.-L. and Dollfus, H. (2009). Transient ciliogenesis involving Bardet-Biedl syndrome proteins is a fundamental characteristic of adipogenic differentiation. *Proc. Natl. Acad. Sci.* **106**, 1820 LP – 1825.

Marumoto, T., Hirota, T., Morisaki, T., Kunitoku, N., Zhang, D., Ichikawa, Y., Sasayama, T., Kuninaka, S., Mimori, T., Tamaki, N., et al. (2002). Roles of aurora-A kinase in mitotic entry and G2 checkpoint in mammalian cells. *Genes Cells* **7**, 1173–1182.

Mazo, G., Soplop, N., Wang, W.-J., Uryu, K. and Tsou, M.-F. B. (2016). Spatial Control of Primary Ciliogenesis by Subdistal Appendages Alters Sensation-Associated Properties

of Cilia. *Dev. Cell* **39**, 424–437.

Mbom, B. C., Siemers, K. A., Ostrowski, M. A., Nelson, W. J. and Barth, A. I. M. (2014). Nek2 phosphorylates and stabilizes β-catenin at mitotic centrosomes downstream of Plk1. *Mol. Biol. Cell* **25**, 977–991.

Mennella, V., Keszthelyi, B., McDonald, K. L., Chhun, B., Kan, F., Rogers, G. C., Huang, B. and Agard, D. A. (2012). Subdiffraction-resolution fluorescence microscopy reveals a domain of the centrosome critical for pericentriolar material organization. *Nat. Cell Biol.* **14**, 1159–1168.

Menzl, I., Lebeau, L., Pandey, R., Hassounah, N. B., Li, F. W., Nagle, R., Weihs, K. and McDermott, K. M. (2014). Loss of primary cilia occurs early in breast cancer development. *Cilia* **3**, 7.

Mergia, A. and Heinkelein, M. (2003). Foamy virus vectors. *Curr. Top. Microbiol. Immunol.* **277**, 131–159.

Miller, F. R., Santner, S. J., Tait, L. and Dawson, P. J. (2000). MCF10DCIS.com xenograft model of human comedo ductal carcinoma in situ. *J. Natl. Cancer Inst.* **92**, 1185–1186.

Miyamoto, T., Hosoba, K., Ochiai, H., Royba, E., Izumi, H., Sakuma, T., Yamamoto, T., Dynlacht, B. D. and Matsuura, S. (2015). The Microtubule-Depolymerizing Activity of a Mitotic Kinesin Protein KIF2A Drives Primary Cilia Disassembly Coupled with Cell Proliferation. *Cell Rep.* **10**, 664–673.

Moens, P. B. and Rapport, E. (1971). Spindles, spindle plaques, and meiosis in the yeast Saccharomyces cerevisiae (Hansen). *J. Cell Biol.* **50**, 344–361.

Molla-Herman, A., Ghossoub, R., Blisnick, T., Meunier, A., Serres, C., Silbermann, F., Emmerson, C., Romeo, K., Bourdoncle, P., Schmitt, A., et al. (2010). The ciliary pocket: an endocytic membrane domain at the base of primary and motile cilia. *J. Cell Sci.* **123**, 1785–95.

Morin, X. and Bellaiche, Y. (2011). Mitotic spindle orientation in asymmetric and symmetric cell divisions during animal development. *Dev. Cell* **21**, 102–119.

Moritz, M. and Agard, D. A. (2001). Gamma-tubulin complexes and microtubule nucleation. *Curr. Opin. Struct. Biol.* **11**, 174–81.

Moritz, M., Braunfeld, M. B., Sedat, J. W., Alberts, B. and Agard, D. A. (1995). Microtubule nucleation by γ-tubulin-containing rings in the centrosome. *Nature* **378**, 638–640.

Moritz, M., Braunfeld, M. B., Guénebaut, V., Heuser, J. and Agard, D. A. (2000). Structure of the γ-tubulin ring complex: a template for microtubule nucleation. *Nat. Cell Biol.* **2**, 365–370.

Moser, J. J., Fritzler, M. J. and Rattner, J. B. (2009). Primary ciliogenesis defects are associated with human astrocytoma/glioblastoma cells. *BMC Cancer* **9**, 448.

Moyer, T. C. and Holland, A. J. (2019). PLK4 promotes centriole duplication by phosphorylating STIL to link the procentriole cartwheel to the microtubule wall. *Elife* **8**, e46054.

Murke, F., Castro, V. S., Giebel, B. and Görgens, A. (2015). Concise Review: Asymmetric Cell Divisions in Stem Cell Biology. *Symmetry* **7**,.

Nachury, M. V. (2018). The molecular machines that traffic signaling receptors into and out of cilia. *Curr. Opin. Cell Biol.* **51**,.

Nachury, M. V, Loktev, A. V, Zhang, Q., Westlake, C. J., Peranen, J., Merdes, A.,

Slusarski, D. C., Scheller, R. H., Bazan, J. F., Sheffield, V. C., et al. (2007). A core complex of BBS proteins cooperates with the GTPase Rab8 to promote ciliary membrane biogenesis. *Cell* **129**, 1201–1213.

Nachury, M. V, Seeley, E. S. and Jin, H. (2010). Trafficking to the ciliary membrane: how to get across the periciliary diffusion barrier? *Annu. Rev. Cell Dev. Biol.* **26**, 59–87.

Nakagawa, Y., Yamane, Y., Okanoue, T., Tsukita, S. and Tsukita, S. (2001). Outer Dense Fiber 2 Is a Widespread Centrosome Scaffold Component Preferentially Associated with Mother Centrioles: Its Identification from Isolated Centrosomes. *Mol. Biol. Cell* **12**, 1687–1697.

Nakazawa, Y., Hiraki, M., Kamiya, R. and Hirono, M. (2007). SAS-6 is a cartwheel protein that establishes the 9-fold symmetry of the centriole. *Curr. Biol.* **17**, 2169–2174.

Neve, R. M., Chin, K., Fridlyand, J., Yeh, J., Baehner, F. L., Fevr, T., Clark, L., Bayani, N., Coppe, J.-P., Tong, F., et al. (2006). A collection of breast cancer cell lines for the study of functionally distinct cancer subtypes. *Cancer Cell* **10**, 515–527.

Nielsen, B. S., Malinda, R. R., Schmid, F. M., Pedersen, S. F., Christensen, S. T. and Pedersen, L. B. (2015). PDGFR and oncogenic mutant PDGFR D842V promote disassembly of primary cilia through a PLC - and AURKA-dependent mechanism. *J. Cell Sci.* **128**, 3543–3549.

Nigg, E. A. and Raff, J. W. (2009). Centrioles, centrosomes, and cilia in health and disease. *Cell* **139**, 663–678.

Nigg, E. A. and Stearns, T. (2011). The centrosome cycle: Centriole biogenesis, duplication and inherent asymmetries. *Nat. Cell Biol.* **13**, 1154–60.

Nobutani, K., Shimono, Y., Yoshida, M., Mizutani, K., Minami, A., Kono, S., Mukohara, T., Yamasaki, T., Itoh, T., Takao, S., et al. (2014). Absence of primary cilia in cell cycle-arrested human breast cancer cells. *Genes Cells* **19**, 141–152.

O'regan, L., Blot, J. and Fry, A. M. (2007). Mitotic regulation by NIMA-related kinases. *Cell Div.* **2**, 25.

Oakley, B. R. and Morris, N. R. (1983). A mutation in Aspergillus nidulans that blocks the transition from interphase to prophase. *J. Cell Biol.* **96**, 1155–1158.

Ocbina, P. J. R., Tuson, M. and Anderson, K. V. (2009). Primary Cilia Are Not Required for Normal Canonical Wnt Signaling in the Mouse Embryo. *PLoS One* **4**, e6839.

Ohta, M., Ashikawa, T., Nozaki, Y., Kozuka-Hata, H., Goto, H., Inagaki, M., Oyama, M. and Kitagawa, D. (2014). Direct interaction of Plk4 with STIL ensures formation of a single procentriole per parental centriole. *Nat. Commun.* **5**, 5267.

Olsen, B. (2005). Nearly all cells in vertebrates and many cells in invertebrates contain primary cilia. *Matrix Biol.* **24**, 449–450.

Osmani, S. A., May, G. S. and Morris, N. R. (1987). Regulation of the mRNA levels of nimA, a gene required for the G2-M transition in Aspergillus nidulans. *J. Cell Biol.* **104**, 1495 LP – 1504.

Ou, Y. Y., Mack, G. J., Zhang, M. and Rattner, J. B. (2002). CEP110 and ninein are located in a specific domain of the centrosome associated with centrosome maturation. *J. Cell Sci.* **115**, 1825–1835.

Paintrand, M., Moudjou, M., Delacroix, H. and Bornens, M. (1992). Centrosome organization and centriole architecture: their sensitivity to divalent cations. *J. Struct. Biol.* **108**, 107–128.

Panic, M., Hata, S., Neuner, A. and Schiebel, E. (2015). The Centrosomal Linker and Microtubules Provide Dual Levels of Spatial Coordination of Centrosomes. *PLoS Genet.*

Paridaen, J. T. M. L., Wilsch-Brauninger, M. and Huttner, W. B. (2013). Asymmetric inheritance of centrosome-associated primary cilium membrane directs ciliogenesis after cell division. *Cell* **155**, 333–344.

Park, T. J., Mitchell, B. J., Abitua, P. B., Kintner, C. and Wallingford, J. B. (2008). Dishevelled controls apical docking and planar polarization of basal bodies in ciliated epithelial cells. *Nat. Genet.* **40**, 871–879.

Patel, V., Li, L., Cobo-Stark, P., Shao, X., Somlo, S., Lin, F. and Igarashi, P. (2008). Acute kidney injury and aberrant planar cell polarity induce cyst formation in mice lacking renal cilia. *Hum. Mol. Genet.* **17**, 1578–1590.

Pedersen, L. B. and Rosenbaum, J. L. (2008). Intraflagellar transport (IFT) role in ciliary assembly, resorption and signalling. *Curr. Top. Dev. Biol.* **85**, 23–61.

Pereira, G. and Schiebel, E. (2005). Kin4 Kinase Delays Mitotic Exit in Response to Spindle Alignment Defects. *Mol. Cell* **19**, 209–221.

Pereira, G. and Yamashita, Y. M. (2011). Fly meets yeast: checking the correct orientation of cell division. *Trends Cell Biol.* **21**, 526–33.

Pereira, G., Höfken, T., Grindlay, J., Manson, C. and Schiebel, E. (2000). The Bub2p spindle checkpoint links nuclear migration with mitotic exit. *Mol. Cell* **6**, 1–10.

Pereira, G., Tanaka, T. U., Nasmyth, K. and Schiebel, E. (2001). Modes of spindle pole body inheritance and segregation of the Bfa1p-Bub2p checkpoint protein complex. *EMBO J.* **20**, 6359–70.

Pereira, G., Manson, C., Grindlay, J. and Schiebel, E. (2002). Regulation of the Bfa1p–Bub2p complex at spindle pole bodies by the cell cycle phosphatase Cdc14p. *J. Cell Biol.* **157**, 367–379.

Perry, J. M., He, X. C., Sugimura, R., Grindley, J. C., Haug, J. S., Ding, S. and Li, L. (2011). Cooperation between both Wnt/{beta}-catenin and PTEN/PI3K/Akt signaling promotes primitive hematopoietic stem cell self-renewal and expansion. *Genes Dev.* **25**, 1928–1942.

Phua, S. C., Chiba, S., Suzuki, M., Su, E., Roberson, E. C., Pusapati, G. V., Setou, M., Rohatgi, R., Reiter, J. F., Ikegami, K., et al. (2017). Dynamic Remodeling of Membrane Composition Drives Cell Cycle through Primary Cilia Excision. *Cell* **168**,.

Piatti, S., Venturetti, M., Chiroli, E. and Fraschini, R. (2006). The spindle position checkpoint in budding yeast: the motherly care of MEN. *Cell Div.* **1**, 2.

Piel, M., Meyer, P., Khodjakov, A., Rieder, C. L. and Bornens, M. (2000). The respective contributions of the mother and daughter centrioles to centrosome activity and behavior in vertebrate cells. *J. Cell Biol.* **149**, 317–330.

Plotnikova, O. V, Pugacheva, E. N. and Golemis, E. A. (2009). Primary cilia and the cell cycle. *Methods Cell Biol.* **94**, 137–160.

Plotnikova, O. V, Nikonova, A. S., Loskutov, Y. V, Kozyulina, P. Y., Pugacheva, E. N. and Golemis, E. A. (2012). Calmodulin activation of Aurora-A kinase (AURKA) is required during ciliary disassembly and in mitosis. *Mol. Biol. Cell* **23**, 2658–70.

Plotnikova, O. V., Seo, S., Cottle, D. L., Conduit, S., Hakim, S., Dyson, J. M., Mitchell, C. A. and Smyth, I. M. (2015). INPP5E interacts with AURKA, linking phosphoinositide signaling to primary cilium stability. *J. Cell Sci.* **128**, 364–372.

Pugacheva, E. N., Jablonski, S. A., Hartman, T. R., Henske, E. P. and Golemis, E. A. (2007). HEF1-dependent Aurora A activation induces disassembly of the primary cilium. *Cell* **129**, 1351–1363.

Rapley, J., Baxter, J. E., Blot, J., Wattam, S. L., Casenghi, M., Meraldi, P., Nigg, E. A. and Fry, A. M. (2005). Coordinate Regulation of the Mother Centriole Component Nlp by Nek2 and Plk1 Protein Kinases. *Mol. Cell. Biol.* **25**, 1309–1324.

Reina, J. and Gonzalez, C. (2014). When fate follows age: unequal centrosomes in asymmetric cell division. *Philos. Trans. R. Soc. B Biol. Sci.* **369**, 20130466–20130466.

Reiter, J. F. and Leroux, M. R. (2017). Genes and molecular pathways underpinning ciliopathies. *Nat. Rev. Mol. Cell Biol.* **18**, 533–547.

Reiter, J. F., Blacque, O. E. and Leroux, M. R. (2012). The base of the cilium: roles for transition fibres and the transition zone in ciliary formation, maintenance and compartmentalization. *EMBO Rep.* **13**, 608–618.

Rellos, P., Ivins, F. J., Baxter, J. E., Pike, A., Nott, T. J., Parkinson, D.-M., Das, S., Howell, S., Fedorov, O., Shen, Q. Y., et al. (2007). Structure and regulation of the human Nek2 centrosomal kinase. *J. Biol. Chem.* **282**, 6833–42.

Ren, B., Cam, H., Takahashi, Y., Volkert, T., Terragni, J., Young, R. A. and Dynlacht, B. D. (2002). E2F integrates cell cycle progression with DNA repair, replication, and G(2)/M checkpoints. *Genes Dev.* **16**, 245–256.

Ringo, D. L. (1967). Flagellar motion and fine structure of the flagellar apparatus in Chlamydomonas. *J. Cell Biol.* **33**, 543–571.

Rohatgi, R. and Snell, W. J. (2010). The ciliary membrane. *Curr. Opin. Cell Biol.* **22**, 541–546.

Rohatgi, R., Milenkovic, L. and Scott, M. P. (2007). Patched1 Regulates Hedgehog Signaling at the Primary Cilium. *Science (80-.).* **317**, 372–376.

Rüthnick, D. and Schiebel, E. (2016). Duplication of the Yeast Spindle Pole Body Once per Cell Cycle. *Mol. Cell. Biol.* **36**, 1324 LP – 1331.

Salisbury, J. L. (2003). Centrosomes: coiled-coils organize the cell center. *Curr. Biol.* **13**, R88-90.

Salzmann, V., Chen, C., Chiang, C.-Y. A., Tiyaboonchai, A., Mayer, M. and Yamashita, Y. M. (2014). Centrosome-dependent asymmetric inheritance of the midbody ring in Drosophila germline stem cell division. *Mol. Biol. Cell* **25**, 267–75.

Sanchez-Madrid, F. and Serrador, J. M. (2009). Bringing up the rear: defining the roles of the uropod. *Nat. Rev. Mol. Cell Biol.* **10**, 353–359.

Sánchez, I. and Dynlacht, B. D. (2016). Cilium assembly and disassembly. *Nat. Cell Biol.* **18**,.

Santner, S. J., Dawson, P. J., Tait, L., Soule, H. D., Eliason, J., Mohamed, A. N., Wolman, S. R., Heppner, G. H. and Miller, F. R. (2001). Malignant MCF10CA1 cell lines derived from premalignant human breast epithelial MCF10AT cells. *Breast Cancer Res. Treat.* **65**, 101–110.

Schindelin, J., Arganda-Carreras, I., Frise, E., Kaynig, V., Longair, M., Pietzsch, T., Preibisch, S., Rueden, C., Saalfeld, S., Schmid, B., et al. (2012). Fiji: an open-source platform for biological-image analysis. *Nat. Methods* **9**, 676–682.

Schmidt, T. I., Kleylein-Sohn, J., Westendorf, J., Le Clech, M., Lavoie, S. B., Stierhof, Y.-D. and Nigg, E. A. (2009). Control of Centriole Length by CPAP and CP110. *Curr.*

Biol. **19**, 1005–1011.

Schmidt, K. N., Kuhns, S., Neuner, A., Hub, B., Zentgraf, H. and Pereira, G. (2012). Cep164 mediates vesicular docking to the mother centriole during early steps of ciliogenesis. *J. Cell Biol.*

Schmidt, M., Rohe, A., Platzer, C., Najjar, A., Erdmann, F. and Sippl, W. (2017). Regulation of G2/M Transition by Inhibition of WEE1 and PKMYT1 Kinases. *Molecules* **22**,.

Schneider, L., Clement, C. A., Teilmann, S. C., Pazour, G. J., Hoffmann, E. K., Satir, P. and Christensen, S. T. (2005). PDGFRalphaalpha signaling is regulated through the primary cilium in fibroblasts. *Curr. Biol.* **15**, 1861–6.

Schöckel, L., Möckel, M., Mayer, B., Boos, D. and Stemmann, O. (2011). Cleavage of cohesin rings coordinates the separation of centrioles and chromatids. *Nat. Cell Biol.* **13**, 966.

Schraml, P., Frew, I. J., Thoma, C. R., Boysen, G., Struckmann, K., Krek, W. and Moch, H. (2009). Sporadic clear cell renal cell carcinoma but not the papillary type is characterized by severely reduced frequency of primary cilia. *Mod. Pathol.* **22**, 31–36.

Schramm, C., Janke, C. and Schiebel, E. (2001). Molecular dissection of yeast spindle pole bodies by two hybrid, in vitro binding, and co-purification. *Methods Cell Biol.* **67**, 71–94.

Seeger-Nukpezah, T., Little, J. L., Serzhanova, V. and Golemis, E. A. (2013). Cilia and cilia-associated proteins in cancer. *Drug Discov. Today. Dis. Mech.* **10**, e135–e142.

Seeley, E. S. and Nachury, M. V (2010). The perennial organelle: assembly and disassembly of the primary cilium. *J. Cell Sci.* **123**, 511 LP – 518.

Seeley, E. S., Carriere, C., Goetze, T., Longnecker, D. S. and Korc, M. (2009). Pancreatic Cancer and Precursor Pancreatic Intraepithelial Neoplasia Lesions Are Devoid of Primary Cilia. *Cancer Res.* **69**, 422–430.

Seo, S., Zhang, Q., Bugge, K., Breslow, D. K., Searby, C. C., Nachury, M. V and Sheffield, V. C. (2011). A novel protein LZTFL1 regulates ciliary trafficking of the BBSome and Smoothened. *PLoS Genet.* **7**, e1002358.

Sharma, N., Kosan, Z. A., Stallworth, J. E., Berbari, N. F. and Yoder, B. K. (2011). Soluble levels of cytosolic tubulin regulate ciliary length control. *Mol. Biol. Cell* **22**, 806–816.

Shen, Q., Zhong, W., Jan, Y. N. and Temple, S. (2002). Asymmetric Numb distribution is critical for asymmetric cell division of mouse cerebral cortical stem cells and neuroblasts. *Development* **129**, 4843 LP – 4853.

Shillingford, J. M., Murcia, N. S., Larson, C. H., Low, S. H., Hedgepeth, R., Brown, N., Flask, C. A., Novick, A. C., Goldfarb, D. A., Kramer-Zucker, A., et al. (2006). The mTOR pathway is regulated by polycystin-1, and its inhibition reverses renal cystogenesis in polycystic kidney disease. *Proc. Natl. Acad. Sci. U. S. A.* **103**, 5466–71.

Shin, J., Wyman, S. K., Dewitt, M. A., Bray, N. L., Vu, J. and Corn, J. E. (2018). Controlled cycling and quiescence enables homology directed repair in engraftment-enriched adult hematopoietic stem and progenitor cells. *bioRxiv* 301176.

Shinin, V., Gayraud-Morel, B., Gomes, D. and Tajbakhsh, S. (2006). Asymmetric division and cosegregation of template DNA strands in adult muscle satellite cells. *Nat. Cell Biol.* **8**, 677–687.

Shinohara, H., Sakayori, N., Takahashi, M. and Osumi, N. (2013). Ninein is essential for

the maintenance of the cortical progenitor character by anchoring the centrosome to microtubules. *Biol. Open* **2**, 739 LP – 749.

Siller, S. S., Sharma, H., Li, S., Yang, J., Zhang, Y., Holtzman, M. J., Winuthayanon, W., Colognato, H., Holdener, B. C., Li, F.-Q., et al. (2017). Conditional knockout mice for the distal appendage protein CEP164 reveal its essential roles in airway multiciliated cell differentiation. *PLOS Genet.* **13**, e1007128.

Sillibourne, J. E., Hurbain, I., Grand-Perret, T., Goud, B., Tran, P. and Bornens, M. (2013). Primary ciliogenesis requires the distal appendage component Cep123. *Biol. Open* **2**, 535–545.

Simons, M., Gloy, J., Ganner, A., Bullerkotte, A., Bashkurov, M., Krönig, C., Schermer, B., Benzing, T., Cabello, O. A., Jenny, A., et al. (2005). Inversin, the gene product mutated in nephronophthisis type II, functions as a molecular switch between Wnt signaling pathways. *Nat. Genet.* **37**, 537–543.

Singh, M., Chaudhry, P. and Merchant, A. A. (2016). Primary cilia are present on human blood and bone marrow cells and mediate Hedgehog signaling. *Exp. Hematol.* **44**, 1181-1187.e2.

Sorokin, S. (1962). CENTRIOLES AND THE FORMATION OF RUDIMENTARY CILIA BY FIBROBLASTS AND SMOOTH MUSCLE CELLS. *J. Cell Biol.* **15**, 363 LP – 377.

Sorokin, S. P. (1968). Reconstructions of Centriole Formation and Ciliogenesis in Mammalian Lungs. *J. Cell Sci.* **3**,.

Soung, N.-K., Park, J.-E., Yu, L.-R., Lee, K. H., Lee, J.-M., Bang, J. K., Veenstra, T. D., Rhee, K. and Lee, K. S. (2009). Plk1-Dependent and -Independent Roles of an ODF2 Splice Variant, hCenexin1, at the Centrosome of Somatic Cells. *Dev. Cell* **16**, 539–550.

Spalluto, C., Wilson, D. I. and Hearn, T. (2012). Nek2 localises to the distal portion of the mother centriole/basal body and is required for timely cilium disassembly at the G2/M transition. *Eur. J. Cell Biol.*

Spektor, A., Tsang, W. Y., Khoo, D. and Dynlacht, B. D. (2007). Cep97 and CP110 Suppress a Cilia Assembly Program. *Cell* **130**, 678–690.

Stearns, T. and Kirschner, M. (1994). In vitro reconstitution of centrosome assembly and function: the central role of gamma-tubulin. *Cell* **76**, 623–37.

Steinman, R. M. (1968). An electron microscopic study of ciliogenesis in developing epidermis and trachea in the embryo ofXenopus laevis. *Am. J. Anat.* **122**, 19–55.

Stevens, N. R., Dobbelaere, J., Brunk, K., Franz, A. and Raff, J. W. (2010). Drosophila Ana2 is a conserved centriole duplication factor. *J. Cell Biol.* **188**, 313–323.

Sugiyama, N., Tsukiyama, T., Yamaguchi, T. P. and Yokoyama, T. (2011). The canonical Wnt signaling pathway is not involved in renal cyst development in the kidneys of inv mutant mice. *Kidney Int.* **79**, 957–965.

Sumara, I., Gime, J. F., Gerlich, D., Hirota, T., Kraft, C., Torre, C. De, Ellenberg, J. and Peters, J. (2004). Roles of Polo-like Kinase 1 in the Assembly of Functional Mitotic Spindles. **14**, 1712–1722.

Sun, X. D., Yu, Z. R., Ma, J., Ge, Y. H., Li, S., Xue, S. P. and Han, D. S. (2002). [Characterization of expression of the centrosomal protein, Cenexin, in rat spermatogenesis]. *Shi Yan Sheng Wu Xue Bao* **35**, 21–25.

Sun, T.-Y., Wang, H.-Y., Kwon, J.-W., Yuan, B., Lee, I.-W., Cui, X.-S. and Kim, N.-H. (2017). Centriolin, a centriole-appendage protein, regulates peripheral spindle migration

and asymmetric division in mouse meiotic oocytes. *Cell Cycle* **16**, 1774–1780.

Suzuki, T. and Chiba, S. (2005). Notch Signaling in Hematopoietic Stem Cells. *Int. J. Hematol.* **82**, 285–294.

Tanaka, M. and Sackmann, E. (2005). Polymer-supported membranes as models of the cell surface. *Nature* **437**, 656–663.

Tang, C.-J. C., Fu, R.-H., Wu, K.-S., Hsu, W.-B. and Tang, T. K. (2009). CPAP is a cell-cycle regulated protein that controls centriole length. *Nat. Cell Biol.* **11**, 825–831.

Tanos, B. E., Yang, H. J., Soni, R., Wang, W. J., Macaluso, F. P., Asara, J. M. and Tsou, M. F. B. (2013). Centriole distal appendages promote membrane docking, leading to cilia initiation. *Genes Dev.*

Tateishi, K., Yamazaki, Y., Nishida, T., Watanabe, S., Kunimoto, K., Ishikawa, H. and Tsukita, S. (2013). Two appendages homologous between basal bodies and centrioles are formed using distinct Odf2 domains. *J. Cell Biol.* **203**, 417–425.

Thauvin-Robinet, C., Lee, J. S., Lopez, E., Herranz-Pérez, V., Shida, T., Franco, B., Jego, L., Ye, F., Pasquier, L., Loget, P., et al. (2014). The oral-facial-digital syndrome gene C2CD3 encodes a positive regulator of centriole elongation. *Nat. Genet.* **46**, 905–911.

Ting, S. B., Deneault, E., Hope, K., Cellot, S., Chagraoui, J., Mayotte, N., Dorn, J. F., Laverdure, J.-P., Harvey, M., Hawkins, E. D., et al. (2012). Asymmetric segregation and self-renewal of hematopoietic stem and progenitor cells with endocytic Ap2a2. *Blood* **119**, 2510–2522.

Tollenaere, M. A. X., Mailand, N. and Bekker-Jensen, S. (2015). Centriolar satellites: key mediators of centrosome functions. *Cell. Mol. Life Sci.* **72**, 11–23.

Tsang, W. Y., Bossard, C., Khanna, H., Peränen, J., Swaroop, A., Malhotra, V. and Dynlacht, B. D. (2008). CP110 Suppresses Primary Cilia Formation through Its Interaction with CEP290, a Protein Deficient in Human Ciliary Disease. *Dev. Cell* **15**, 187–197.

Tsou, M.-F. B., Wang, W.-J., George, K. A., Uryu, K., Stearns, T. and Jallepalli, P. V (2009). Polo kinase and separase regulate the mitotic licensing of centriole duplication in human cells. *Dev. Cell* **17**, 344–354.

Tucker, R. W., Pardee, A. B. and Fujiwara, K. (1979). Centriole ciliation is related to quiescence and DNA synthesis in 3T3 cells. *Cell* **17**, 527–535.

Tukachinsky, H., Lopez, L. V and Salic, A. (2010). A mechanism for vertebrate Hedgehog signaling: recruitment to cilia and dissociation of SuFu-Gli protein complexes. *J. Cell Biol.* **191**, 415–428.

Tuz, K., Bachmann-Gagescu, R., O'Day, D. R., Hua, K., Isabella, C. R., Phelps, I. G., Stolarski, A. E., O'Roak, B. J., Dempsey, J. C., Lourenco, C., et al. (2014). Mutations in CSPP1 cause primary cilia abnormalities and Joubert syndrome with or without Jeune asphyxiating thoracic dystrophy. *Am. J. Hum. Genet.* **94**, 62–72.

Uto, K., Nakajo, N. and Sagata, N. (1999). Two Structural Variants of Nek2 Kinase, Termed Nek2A and Nek2B, Are Differentially Expressed inXenopusTissues and Development. *Dev. Biol.* **208**, 456–464.

Valdés-Sánchez, L., De la Cerda, B., Diaz-Corrales, F. J., Massalini, S., Chakarova, C. F., Wright, A. F. and Bhattacharya, S. S. (2013). ATR localizes to the photoreceptor connecting cilium and deficiency leads to severe photoreceptor degeneration in mice. *Hum. Mol. Genet.* **22**, 1507–1515.

Valente, E. M., Logan, C. V, Mougou-Zerelli, S., Lee, J. H., Silhavy, J. L., Brancati, F., Iannicelli, M., Travaglini, L., Romani, S., Illi, B., et al. (2010). Mutations in TMEM216 perturb ciliogenesis and cause Joubert, Meckel and related syndromes. *Nat. Genet.* **42**, 619–625.

van Breugel, M., Hirono, M., Andreeva, A., Yanagisawa, H., Yamaguchi, S., Nakazawa, Y., Morgner, N., Petrovich, M., Ebong, I.-O., Robinson, C. V, et al. (2011). Structures of SAS-6 suggest its organization in centrioles. *Science* **331**, 1196–1199.

Van Hoof, D., Muñoz, J., Braam, S. R., Pinkse, M. W. H., Linding, R., Heck, A. J. R., Mummery, C. L. and Krijgsveld, J. (2009). Phosphorylation Dynamics during Early Differentiation of Human Embryonic Stem Cells. *Cell Stem Cell* **5**, 214–226.

Veleri, S., Manjunath, S. H., Fariss, R. N., May-Simera, H., Brooks, M., Foskett, T. A., Gao, C., Longo, T. A., Liu, P., Nagashima, K., et al. (2014). Ciliopathy-associated gene Cc2d2a promotes assembly of subdistal appendages on the mother centriole during cilia biogenesis. *Nat. Commun.* **5**, 4207.

Vestergaard, M. L., Awan, A., Warzecha, C. B., Christensen, S. T. and Andersen, C. Y. (2016). Immunofluorescence Microscopy and mRNA Analysis of Human Embryonic Stem Cells (hESCs) Including Primary Cilia Associated Signaling Pathways. *Methods Mol. Biol.* **1307**, 123–40.

Vlijm, R., Li, X., Panic, M., Rüthnick, D., Hata, S., Herrmannsdörfer, F., Kuner, T., Heilemann, M., Engelhardt, J., Hell, S. W., et al. (2018). STED nanoscopy of the centrosome linker reveals a CEP68-organized, periodic rootletin network anchored to a C-Nap1 ring at centrioles. *Proc. Natl. Acad. Sci.* **115**,.

Vorobjev, I. A. and Chentsov, Y. (1982). Centrioles in the cell cycle. I. Epithelial cells. *J. Cell Biol.* **93**, 938–949.

Vorobjev, I. A. and Nadezhdina, E. S. (1987). The centrosome and its role in the organization of microtubules. *Int. Rev. Cytol.* **106**, 227–93.

Wagner, W., Ansorge, A., Wirkner, U., Eckstein, V., Schwager, C., Blake, J., Miesala, K., Selig, J., Saffrich, R., Ansorge, W., et al. (2004). Molecular evidence for stem cell function of the slow-dividing fraction among human hematopoietic progenitor cells by genome-wide analysis. *Blood* **104**, 675–686.

Wallingford, J. B., Rowning, B. A., Vogeli, K. M., Rothbächer, U., Fraser, S. E. and Harland, R. M. (2000). Dishevelled controls cell polarity during Xenopus gastrulation. *Nature* **405**, 81–85.

Wang, L. and Dynlacht, B. D. (2018). The regulation of cilium assembly and disassembly in development and disease. *Development* **145**, dev151407.

Wang, Y. and Zhan, Q. (2007). Cell cycle-dependent expression of centrosomal ninein-like protein in human cells is regulated by the anaphase-promoting complex. *J. Biol. Chem.* **282**, 17712–9.

Wang, Y., Hu, F. and Elledge, S. J. (2000). The Bfa1/Bub2 GAP complex comprises a universal checkpoint required to prevent mitotic exit. *Curr. Biol.* **10**, 1379–82.

Wang, X., Tsai, J.-W., Imai, J. H., Lian, W.-N., Vallee, R. B. and Shi, S.-H. (2009). Asymmetric centrosome inheritance maintains neural progenitors in the neocortex. *Nature* **461**, 947.

Wang, W.-J., Soni, R. K., Uryu, K. and Tsou, M.-F. B. (2011). The conversion of centrioles to centrosomes: essential coupling of duplication with segregation. *J. Cell Biol.* **193**, 727–739.

Wang, L., Failler, M., Fu, W. and Dynlacht, B. D. (2018). A distal centriolar protein network controls organelle maturation and asymmetry. *Nat. Commun.* **9**, 3938.

Wang, X., Chen, K., Liu, H., Huang, Z., Chen, X. and Yin, L. (2019). Prognostic significance of NEK2 in human solid tumors: a systematic review and meta-analysis. *Biosci. Rep.* **39**,.

Weber, U. and Mlodzik, M. (2017). APC/C Fzr/Cdh1 -Dependent Regulation of Planar Cell Polarity Establishment via Nek2 Kinase Acting on Dishevelled. *Dev. Cell* **40**, 53–66.

Weber, K., Bartsch, U., Stocking, C. and Fehse, B. (2008). A multicolor panel of novel lentiviral "gene ontology" (LeGO) vectors for functional gene analysis. *Mol. Ther.* **16**, 698–706.

Wei, Q., Xu, Q., Zhang, Y., Li, Y., Zhang, Q., Hu, Z., Harris, P. C., Torres, V. E., Ling, K. and Hu, J. (2013). Transition fibre protein FBF1 is required for the ciliary entry of assembled intraflagellar transport complexes. *Nat. Commun.* **4**, 2750.

Wein, F., Pietsch, L., Saffrich, R., Wuchter, P., Walenda, T., Bork, S., Horn, P., Diehlmann, A., Eckstein, V., Ho, A. D., et al. (2010). N-cadherin is expressed on human hematopoietic progenitor cells and mediates interaction with human mesenchymal stromal cells. *Stem Cell Res.* **4**, 129–139.

Westlake, C. J., Baye, L. M., Nachury, M. V, Wright, K. J., Ervin, K. E., Phu, L., Chalouni, C., Beck, J. S., Kirkpatrick, D. S., Slusarski, D. C., et al. (2011). Primary cilia membrane assembly is initiated by Rab11 and transport protein particle II (TRAPPII) complex-dependent trafficking of Rabin8 to the centrosome. *Proc. Natl. Acad. Sci.* **108**, 2759 LP – 2764.

Wheatley, D. N., Wang, A. M. and Strugnell, G. E. (1996). Expression of primary cilia in mammalian cells. *Cell Biol. Int.* **20**, 73–81.

Wheway, G., Abdelhamed, Z., Natarajan, S., Toomes, C., Inglehearn, C. and Johnson, C. A. (2013). Aberrant Wnt signalling and cellular over-proliferation in a novel mouse model of Meckel–Gruber syndrome. *Dev. Biol.* **377**, 55–66.

Wheway, G., Nazlamova, L. and Hancock, J. T. (2018). Signaling through the Primary Cilium . *Front. Cell Dev. Biol.* **6**, 8.

Whitfield, M. L., Sherlock, G., Saldanha, A. J., Murray, J. I., Ball, C. A., Alexander, K. E., Matese, J. C., Perou, C. M., Hurt, M. M., Brown, P. O., et al. (2002). Identification of genes periodically expressed in the human cell cycle and their expression in tumors. *Mol. Biol. Cell* **13**, 1977–2000.

Wiese, C. and Zheng, Y. (2000). A new function for the γ -tubulin ring complex as a microtubule minus-end cap. *Nat. Cell Biol.* **2**, 358–364.

Wilson, E. B. (1925). *The cell in development and heredity.* New York: Macmillan.

Wolpert, L. (1988). Stem cells: a problem in asymmetry. *J. Cell Sci. Suppl.* **10**, 1–9.

Woodruff, J. B., Wueseke, O. and Hyman, A. A. (2014). Pericentriolar material structure and dynamics. *Philos. Trans. R. Soc. Lond. B. Biol. Sci.* **369**,.

Wright, J. H., Munar, E., Jameson, D. R., Andreassen, P. R., Margolis, R. L., Seger, R. and Krebs, E. G. (1999). Mitogen-activated protein kinase kinase activity is required for the G₂/M transition of the cell cycle in mammalian fibroblasts. *Proc. Natl. Acad. Sci.* **96**, 11335 LP – 11340.

Wu, M., Kwon, H. Y., Rattis, F., Blum, J., Zhao, C., Ashkenazi, R., Jackson, T. L., Gaiano, N., Oliver, T. and Reya, T. (2007). Imaging Hematopoietic Precursor Division

in Real Time. *Cell Stem Cell* **1**, 541–554.

Xu, Q., Zhang, Y., Wei, Q., Huang, Y., Hu, J. and Ling, K. (2016). Phosphatidylinositol phosphate kinase PIPKIγ and phosphatase INPP5E coordinate initiation of ciliogenesis. *Nat. Commun.* **7**, 10777.

Yamashita, Y. M. (2009). Regulation of asymmetric stem cell division: spindle orientation and the centrosome. *Front. Biosci. (Landmark Ed.* **14**, 3003–3011.

Yamashita, Y. M., Mahowald, A. P., Perlin, J. R. and Fuller, M. T. (2007). Asymmetric Inheritance of Mother Versus Daughter Centrosome in Stem Cell Division. *Science (80-.).* **315**, 518–521.

Yamashita, Y. M., Yuan, H., Cheng, J. and Hunt, A. J. (2010). Polarity in stem cell division: asymmetric stem cell division in tissue homeostasis. *Cold Spring Harb. Perspect. Biol.* **2**, a001313–a001313.

Yang, J., Liu, X., Yue, G., Adamian, M., Bulgakov, O. and Li, T. (2002). Rootletin, a novel coiled-coil protein, is a structural component of the ciliary rootlet. *J. Cell Biol.* **159**, 431–440.

Yang, T. T., Chong, W. M., Wang, W.-J., Mazo, G., Tanos, B., Chen, Z., Tran, T. M. N., Chen, Y.-D., Weng, R. R., Huang, C.-E., et al. (2018). Super-resolution architecture of mammalian centriole distal appendages reveals distinct blade and matrix functional components. *Nat. Commun.* **9**, 2023.

Yao, Y., Su, J., Zhao, L., Luo, N., Long, L. and Zhu, X. (2019). NIMA-related kinase 2 overexpression is associated with poor survival in cancer patients: a systematic review and meta-analysis. *Cancer Manag. Res.* **11**, 455–465.

Yasar, B., Linton, K., Slater, C. and Byers, R. (2017). Primary cilia are increased in number and demonstrate structural abnormalities in human cancer. *J. Clin. Pathol.* **70**, 571 LP – 574.

Ye, X., Zeng, H., Ning, G., Reiter, J. F. and Liu, A. (2014). C2cd3 is critical for centriolar distal appendage assembly and ciliary vesicle docking in mammals. *Proc. Natl. Acad. Sci.* **111**, 2164–2169.

Yeh, E., Skibbens, R. V, Cheng, J. W., Salmon, E. D. and Bloom, K. (1995). Spindle dynamics and cell cycle regulation of dynein in the budding yeast, Saccharomyces cerevisiae. *J. Cell Biol.* **130**, 687–700.

Yin, H., Pruyne, D., TC, H. and Bretscher, A. (2000). Myosin V orientates the mitotic spindle in yeast. *Nature* **406**, 1013–1015.

Yoshiba, S., Tsuchiya, Y., Ohta, M., Gupta, A., Shiratsuchi, G., Nozaki, Y., Ashikawa, T., Fujiwara, T., Natsume, T., Kanemaki, M., et al. (2019). HsSAS-6-dependent cartwheel assembly ensures stabilization of centriole intermediates. *J. Cell Sci.*

Yoshimura, S.-I., Egerer, J., Fuchs, E., Haas, A. K. and Barr, F. A. (2007). Functional dissection of Rab GTPases involved in primary cilium formation. *J. Cell Biol.* **178**, 363–369.

Yuan, K., Frolova, N., Xie, Y., Wang, D., Cook, L., Kwon, Y.-J., Steg, A. D., Serra, R. and Frost, A. R. (2010). Primary cilia are decreased in breast cancer: analysis of a collection of human breast cancer cell lines and tissues. *J. Histochem. Cytochem.* **58**, 857–870.

Zeng, H., Jia, J. and Liu, A. (2010). Coordinated Translocation of Mammalian Gli Proteins and Suppressor of Fused to the Primary Cilium. *PLoS One* **5**, e15900.

Zhang, Y., Wang, W., Wang, Y., Huang, X., Zhang, Z., Chen, B., Xie, W., Li, S., Shen, S. and Peng, B. (2018). NEK2 promotes hepatocellular carcinoma migration and invasion through modulation of the epithelial-mesenchymal transition. *Oncol. Rep.* **39**, 1023–1033.

Zhao, X., Pak, E., Ornell, K. J., Pazyra-Murphy, M. F., MacKenzie, E. L., Chadwick, E. J., Ponomaryov, T., Kelleher, J. F. and Segal, R. A. (2017). A Transposon Screen Identifies Loss of Primary Cilia as a Mechanism of Resistance to SMO Inhibitors. *Cancer Discov.* **7**, 1436–1449.

Zheng, Y., Wong, M. L., Alberts, B. and Mitchison, T. (1998). Purification and assay of gamma tubulin ring complex. *Methods Enzymol.* **298**, 218–28.

Zheng, Y., Mennella, V., Marks, S., Wildonger, J., Elnagdi, E., Agard, D. and Megraw, T. L. (2016). The Seckel syndrome and centrosomal protein Ninein localizes asymmetrically to stem cell centrosomes but is not required for normal development, behavior, or DNA damage response in Drosophila. *Mol. Biol. Cell* **27**, 1740–1752.

Zhou, W., Yang, Y., Xia, J., Wang, H., Salama, M. E., Xiong, W., Xu, H., Shetty, S., Chen, T., Zeng, Z., et al. (2013). NEK2 induces drug resistance mainly through activation of efflux drug pumps and is associated with poor prognosis in myeloma and other cancers. *Cancer Cell* **23**, 48–62.

Zhu, F., Lawo, S., Bird, A., Pinchev, D., Ralph, A., Richter, C., Müller-Reichert, T., Kittler, R., Hyman, A. A. and Pelletier, L. (2008). The Mammalian SPD-2 Ortholog Cep192 Regulates Centrosome Biogenesis. *Curr. Biol.* **18**, 136–141.

Zimdahl, B., Ito, T., Blevins, A., Bajaj, J., Konuma, T., Weeks, J., Koechlein, C. S., Kwon, H. Y., Arami, O., Rizzieri, D., et al. (2014). Lis1 regulates asymmetric division in hematopoietic stem cells and in leukemia. *Nat. Genet.* **46**, 245–52.

Zou, C., Li, J., Bai, Y., Gunning, W. T., Wazer, D. E., Band, V. and Gao, Q. (2005). Centrobin. *J. Cell Biol.* **171**, 437 LP – 445.

7. Abbreviations

3D-SIM	3D-structural illumination microscopy
A.U.	arbitrary unit
ACD	asymmetric cell division
AcGFP	*Aequorea coerulescens* GFP
AD	activation domain
ADPKD	autosomal dominant polycystic kidney disease
ALMS	Alström syndrome;
APC/C	anaphase-promoting complex/cyclosome
ARL13B	ADP-ribosylation factor-like protein 13B
BBS	Bardet-Biedl syndrome
BBSome	Bardet–Biedl syndrome complex bp base pair
BD	binding domain
C-Nap1	centrosomal Nek2-associated protein 1
C2cd3	C2 Calcium Dependent Domain Containing 3
CaM	calcium-calmodulin
CC	coiled-coil
CC2D2A	Coiled-Coil and C2 Domain Containing 2A
CCDCs	Coiled-Coil Domain-Containing Proteins
Cdk5	Cyclin dependent kinase 5
CDK5RAP2	Cdk5 regulatory subunit associated protein 2
CFC	colony forming cell
CML	chronic myelogenous leukemia
Co-IP	Co-immuno-precipitation
COC	centrosome orientation checkpoint
CP110	centriolar coiled-coil protein of 110 kDa
CPAP	Centrosomal P4.1-associated protein
DA	distal appendage
DAPI	4'6-diamidino-2-phenylindole
DMSO	Dimethyl sulfoxide
DNA	deoxyribonucleic acid
dNTP	deoxynucleosid 5´-triphosphate
DOX	doxycycline
Dvl	Dishevelled

Dvl2	Dishevelled 2
E. coli	*Escherichia coli*
ECL	enhanced chemiluminescence
EDTA	ethylendiaminetetraacetic acid
EGFP	enhanced GFP
EGTA	Ethylene glycol-bis(2-aminoethylether)-N,N,N′,N′-tetraacetic acid
EM	electron microscopy
EMs	erythro-myeloid progenitors
EVS	Ellis-van Creveld Syndrome
FBF1	fas-binding factor 1
FBS	fetal bovine serum
fGSCs	female germline stem cells
G0	exit of G1
G1	gap phase 1
G2	gap phase 2
GEF	guanine exchange factor
GFP	green fluorescent protein
GliA	Gli activator form
gRNA	Guide RNA
HEK293	Human embryonic kidney cells 293
HeLa	Henrietta Lacks
HEPES	N-2-hydroxyethylpiperazine-N'-2-ethanesulfonic
Hh	Hedgehog
HRP	Horseradish peroxidase
HSPCs	hematopoietic stem and progenitor cells
IFT	intraflagellar transport
INPP5E	phosphatidylinositol 5-phosphatase
IPTG	isopropyl-β
JATD	Jeune asphyxiating thoracic dystrophy
JBTS	Joubert syndrome;
KD	kinase-dead
kDa	kilo Dalton
KO	knockout

LCA	Leber congenital amaurosis
LMs	lympho-myeloid
LP	late progenitors
LZ	leucine zipper
MARK4	MAP/microtubule affinity-regulating kinase 4
mGSCs	male germline stem cells
mRNA	Messenger RNA
MKS	Meckel-Gruber syndrome
MPPs	multipotent progenitors
mRNA	messenger RNA
MTOC	microtubule-organizing center
Ndel1	nuclear distribution element-like 1
NEB	nuclear envelope breakdown
Nek2	never in mitosis A-related kinase 2
NIMA	Never in mitosis A
Nlp	ninein-like protein
NPHP	Nephronophthisis
ODF2	outer dense fiber protein 2
OFD	Oro-facial-digital syndrome
OFD1	oral-facial-digital syndrome 1
PCM	pericentriolar matrix
PCP	planar cell polarity
PCR	polymerase chain reaction
PI4P	phosphatidylinositol 4-phosphate
Pifo	Pitchfork
PIPKIγ	PtdIns kinase
PKD	Polycystic kidney disease
PLK1	polo-like kinase 1
PLK4	Polo-like kinase 4
PtdIns	Phosphatidylinositol
RNA	Ribonucleic acid
RNAi	RNA interference
RP	retinitis pigmentosa
RPE1	retinal pigment epithelial

SAS6	abnormal protein 6 homolog
SCLT1	Sodium channel and clathrin linker 1
SDA	subdistal appendage
Shh	Sonic Hedgehog
shRNA	Short hairpin RNA
siRNA	small interfering RNA
SLS	Senior-Løken syndrome
Smo	Smoothened
SPB	spindle pole body
SPOC	spindle position checkpoint
SRPS	Short Rib-Polydactyly Syndrome
STIL	SCL-interrupting locus protein
SuFu	Suppressor of Fused
TGF-β	transforming factor beta
TMEM	transition zone transmembrane proteins
TTBK2	Tau tubulin kinase 2
USH	Usher syndrome
v/v	volume per volume
w/v	weight per volume
WDR8	WD repeat-containing protein 8
WT	wild type

Poster presentations

Linda Viol, Anthony Ho, Patrick Wuchter, Gislene Pereira
“Analysis of centrosome asymmetry in hematopoietic stem cells”
31st Klenk Symposium 2015, Cologne, Germany, September 27-29, 2015

Linda Viol, Florian Murke, Bernd Giebel, Patrick Wuchter, Gislene Pereira
“Analysis of centrosome asymmetry in hematopoietic stem cells”
EMBO Conference Centrosomes and Spindle Pole Bodies, Heidelberg, Germany, September 24-27, 2017

Linda Viol, Ana Pastor Peidro, Patrick Wuchter, Florian Murke, Bernd Giebel, Gislene Pereira
“Regulation of the behavior of centrosomal proteins during mitosis”
EMBO Workshop Cilia 2018, Copenhagen, Denmark, October 2-5, 2018

Acknowledgement

I would like to thank Prof. Dr. Gislene Pereira for the opportunity to pursue my doctoral studies in her lab and the technical and scientific support throughout the years of my PhD. Thank you for the discussions and constructive ideas that contributed to the development and progress of this project.

I wish to express my gratitude to my Thesis Advisory Committee, Prof. Dr. Gislene Pereira, Prof. Dr. Elmar Schiebel and Prof. Dr. Alwin Krämer for the constructive feedback on the progress of my work and helpful suggestions regarding future directions. Additionally, I want to thank my Thesis Advisory Committee and Dr. Steffen Lemke for willing to be my Examination Commission members.

I am thankful to all my colleagues for scientific and non-scientific help and nice moments inside and outside the lab. I am grateful to Ayse Caysadi, Bahtiyar Kurtulmus and Ricardo Costa Pereira de Carvalho for training me when I first joined the lab. I want to thank Astrid Hofman and Dorothee Albrecht for excellent technical assistance. I thank Prof. Dr. Schiebel and his whole lab for scientific support through our shared meetings and for sharing cell lines and reagents and patiently answering my questions. I am grateful to Annett Neuner for the EM-Analysis of my project.

My gratitude also goes to Prof. Dr. Bernd Giebel and Florian Murke, who both made the HSPC analysis of this project possible. Thank you for nice collaboration and facilitation of my experiments in Essen as well as shared reagents. I further thank Prof. Dr. Motomu Tanaka and Judith Thoma for facilitating the ICAM-1 analysis.

I wish to express my gratitude to Anthony D. Ho, Patrick Wuchter, Patrick Horn and Caroline Pabst for providing hematopoietic primary cells and Angela Lenze for purification of CD34+ HSPCs. I want to thank HBIGS for the training and support they delivered as well as all the Core facilities that I had the luck to make use of.

I would like to thank my friends Mariama Mbengue and Jessica Velten for proofreading this thesis. I wish to thank all my friends, members of the “Sandwich Club”, “Beer Bench” and Christoph Pille, with whom I shared the whole period of my PhD, for the mental support and the balance they created between my work and personal life.

A big thank you goes to Jonathan Nees for his love, support and patience, without which this work would not have been possible.

Finally, I am grateful to my family and especially my parents. You always supported and encouraged me. Thank you!